

# **Formation, Activity and Growth of Copper Nanoparticles in Methanol Synthesis Catalysts**

Vorming, Activiteit en Groei van Kopernanodeeltjes in Katalysatoren voor de Synthese van Methanol

*(met een samenvatting in het Nederlands)*

Proefschrift

ter verkrijging van de graad van doctor aan de Universiteit Utrecht op gezag van de rector magnificus, prof.dr. G.J. van der Zwaan, ingevolge het besluit van het college voor promoties in het openbaar te verdedigen op woensdag 18 mei 2016 des middags te 2.30 uur

door

Roy van den Berg

geboren op 16 maart 1988 te Nijkerk

Promotoren: Prof. dr. ir. K. P. de Jong  
Prof. dr. P. E. de Jongh

This thesis was accomplished with financial support from Haldor Topsøe A/S.

# **Formation, Activity and Growth of Copper Nanoparticles in Methanol Synthesis Catalysts**

Author: Roy van den Berg

Title: Formation, Activity and Growth of Copper Nanoparticles in Methanol Synthesis Catalysts

ISBN: 978-94-6233-278-2

Printed by: Gildeprint – The Netherlands

Cover by: Koen Leenders, Buitengewoon Concept

Figures metallic nanoparticles with permission from Elsevier reproduced from: van Helden, P.; Ciobîcă, I. M.; Coetzer, R. L. J. *Catal. Today* **2016**, *261*, 48-59

## Contents

<b>Chapter 1</b>	General Introduction	7
<b>Chapter 2</b>	Revealing the Formation of Copper Nanoparticles from a Homogeneous Solid Precursor by Electron Microscopy	21
<b>Chapter 3</b>	Effect of Particle Size on the Activity of Supported Cu and CuZn catalysts in the Methanol Synthesis	65
<b>Chapter 4</b>	Support Functionalization to Retard Ostwald Ripening in Copper Methanol Synthesis Catalysts	109
<b>Chapter 5</b>	Impact of the Synthesis Route of Supported Copper Catalysts on the Performance in the Methanol Synthesis Reaction	143
<b>Chapter 6a</b>	Summary, Concluding Remarks and Outlook	161
<b>Chapter 6b</b>	Nederlandse Samenvatting	167
	List of Publications	174
	Acknowledgments	177
	About the Author	181



## **Chapter 1**

### **General Introduction**

## Methanol

Methanol is one of the essential building blocks in the petrochemical industry due to its versatility to convert it to a wide range of valuable products, such as formaldehyde, methyl tert-butyl ether (MTBE), acetic acid, methyl methacrylate (MMA), dimethyl terephthalate (DMT), dimethyl ether (DME), ethanol and olefins (Figure 1.1).<sup>1</sup> Moreover, methanol receives currently a lot of attention as a potential fuel or energy carrier in a more sustainable energy system, since methanol can form a closed cycle involving (artificial) photosynthesis, has a relatively high volumetric and gravimetric energy density, and is liquid at room temperature making it convenient for transportation.<sup>2</sup> At the moment, most of the methanol is produced from 'synthesis gas' or in short 'syngas', which is a mixture of  $H_2$  and  $CO$ , and possibly  $CO_2$ . Syngas is primarily produced from oil, coal and natural gas, but can also be produced from biomass, waste or even  $CO_2$  and  $H_2O$  using solar or wind energy.<sup>1a, 3</sup> Syngas chemistry thus allows shifting between carbon sources depending on the economic and political situation, while methanol can be converted in almost everything. Syngas conversion to methanol therefore presents an alternative route for products that are traditionally made from oil. The wide availability of shale gas in North America and coal and natural gas in China, and the increase in demand for methanol-derived products, have therefore boosted the global annual methanol production from about 40 million tons in 2008 to about 65 million tons in 2013.<sup>1b, 4</sup> Especially China is expanding its production capacity and consequently global methanol demand is expected to increase to about 105 million tons in 2023.<sup>4-5</sup>

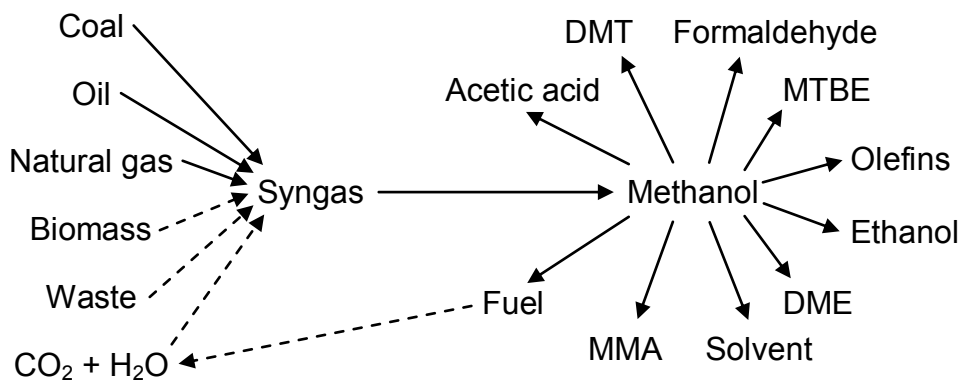


**Figure 1.1** The main routes to produce methanol from natural resources via syngas and the main applications of methanol. A dashed line indicates that the route is technically feasible but not yet applied at large scale.

The conversion of syngas to methanol is governed by the hydrogenation of CO and CO<sub>2</sub>, and the (reverse) water gas shift reaction (Eq. 1.1-1.3). Typical operating conditions are temperatures between 220 °C and 300 °C and pressures between 50 and 100 bar.<sup>1a, 6</sup> As the carbon conversion to methanol at thermodynamic equilibrium at these conditions is well below 70%, recycling of the syngas remaining after methanol condensation is required in industry.<sup>1a</sup> Table 1.1 shows the feed and equilibrium composition at the conditions used in this thesis, i.e. 260 °C, 40 bar.<sup>4</sup> Catalyst performances were investigated at conversions below the thermodynamic per-pass conversion limit, i.e. below 20%.

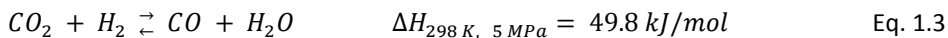
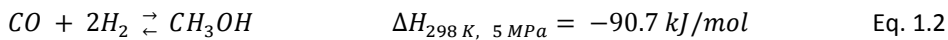
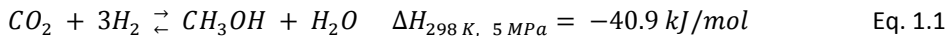


**Table 1.1.** Feed and equilibrium composition in mol% at the conditions used in this thesis, i.e. 260 °C, 40 bar.

	H <sub>2</sub> (%)	CO (%)	CO <sub>2</sub> (%)	CH <sub>3</sub> OH (%)	H <sub>2</sub> O (%)	Ar (%)	CO+CO <sub>2</sub> conversion (%)	Total moles
Feed	60.0	23.0	7.0	0.0	0.0	10.0	-	100
Equilibrium	51.4	17.7	8.1	10.3	0.3	12.1	28.5	82.8

### Catalyst

The catalyst used in industry for this process is Cu/ZnO/Al<sub>2</sub>O<sub>3</sub> with a respective weight ratio of about 55/30/15.<sup>6</sup> Copper is regarded as the active metal, zinc oxide as a chemical and structural promotor, and alumina as a structural promotor.<sup>1a</sup> The exact nature of the active site is still under debate and might be different for CO and CO<sub>2</sub> hydrogenation.<sup>1a, 6-7</sup> The conversion of syngas to methanol was for decades considered to be structure insensitive since a linear relationship was found between catalytic activity and exposed metallic copper surface area.<sup>8</sup> Based on the measured copper surface areas reported in these studies, the copper particles were estimated to be mostly larger than 10 nm. Density functional theory calculations and surface science experiments, however, suggest that the reaction is sensitive to the structure of the copper metal surface.<sup>7a, 9</sup> According to these studies higher Miller-index copper surfaces are more active than the most-densely packed Cu(111) surface. The fraction of different facets or surface atoms and thereby the fraction of specific surface sites typically alters upon nanosizing metal particles to a size below 10 nm.<sup>10</sup> The methanol synthesis activity and selectivity are therefore expected to depend on the size of the copper particles only below 10 nm.

Furthermore, it has been shown in more recent studies that the activity does not only depend on the exposed copper surface area but also on the presence of zinc, be it in the form of zinc oxide or zinc hydroxyl(phylo)silicate.<sup>7a, 8b-d, 9, 11</sup> No promotion by zinc has been observed for catalyst beds with a variety of arrangements of separate copper and zinc components, indicating that the promotion is not occurring via gas-phase processes or due to a bifunctional mechanism.<sup>12</sup> Many mechanistic models have been proposed in literature to explain the observed 'synergistic' effect of copper and zinc, including hydrogen spillover from zinc oxide to copper,<sup>12-13</sup> copper shape changes on zinc oxide supports,<sup>14</sup> zinc-induced defects in the copper structure,<sup>9, 15</sup> and the formation of either  $\text{Cu}^+$  or  $\text{Cu}^-$  species.<sup>16</sup> Recent work, however, indicates that the increase in activity for zinc-containing catalysts is due to the formation of (partially) reduced zinc species from zinc oxide or zinc silicate and subsequent migration to the metallic copper surface, increasing the surface specific activity.<sup>7a, 9, 17</sup> Since this process is affected by the thermodynamic stability of the zinc phases involved, it is expected to depend on the composition of the zinc-containing phase.

In the copper-catalysed methanol synthesis the product selectivity towards methanol is typically above 99%.<sup>1a</sup> The process can therefore be completely described by equations 1.1-1.3. For  $\text{Cu}/\text{ZnO}/\text{Al}_2\text{O}_3$  and  $\text{Cu}/\text{SiO}_2$  catalysts, the methanol synthesis reaction rate has shown to increase upon the addition of  $\text{CO}_2$  in the syngas feed, even at low concentrations.<sup>12, 18</sup> Isotopic labelling studies showed for these catalysts that the hydrogenation of  $\text{CO}_2$  is the main route by which methanol is formed.<sup>18c, 19</sup> Formate is considered to be the most abundant carbon-containing intermediate surface species during reaction.<sup>1a, 7b</sup>

### Deactivation

Although copper-based catalysts were already identified as very active and selective methanol synthesis catalysts as early as the 1920s and 1930s, they were not used on a large scale until the 1960s.<sup>1a</sup> The main reason for that was the poor stability of the catalysts, especially when the syngas was contaminated with sulphur species. New developments in the 1960s allowed careful purification of the syngas feed limiting sulphur poisoning. However, even in the absence of poisons, one-third of the initial activity is lost during the first 1000 h of operation, limiting the economic lifetime of an industrial catalyst.<sup>1a</sup> During reaction either the number of active sites or the intrinsic activity per active site thus decreases. Common deactivation mechanisms for supported metal catalysts include coking, oxidation, and particle growth.<sup>20</sup> Because only trace amounts of  $\text{CH}_4$  and  $\text{C}_2+$  molecules are produced during the methanol synthesis reaction, it can be concluded that under these conditions copper is not effective in forming carbon-carbon

bonds or breaking the final carbon-oxygen bond in CO or CO<sub>2</sub>. The contribution of coke formation to catalyst deactivation is therefore considered to be insignificant.<sup>1a</sup> The effect of oxidation on catalyst deactivation depends on the syngas composition. If the feed contains high CO<sub>2</sub> and low CO and H<sub>2</sub> concentrations, the copper surface might become inactive due to oxidation. Furthermore, zinc promotion might be affected by the feed composition since it has been observed in literature that the shape of the copper particles and the extent of zinc species migration to the copper surface depend on the gas atmosphere.<sup>14, 17a, 17b</sup> Although these processes can have an effect on the activity during the first hours of operation, they probably do not contribute to catalyst deactivation on longer time scales since they are expected to equilibrate within a few hours. The main mechanism for long-term deactivation is therefore considered to be growth of the copper particles.<sup>1a</sup>

### Particle growth

Since the activity of methanol synthesis catalysts depends on the exposed copper surface area, a high surface to volume ratio of the copper phase is essential for achieving high catalyst activities, which means that small copper particles are required. In the Cu/ZnO/Al<sub>2</sub>O<sub>3</sub> catalyst the copper particles are therefore initially about 7 nm.<sup>1a, 21</sup> However, the high surface to volume ratio for these particles inherently means that the contribution of the surface energy to the total energy of the particles is large. Consequently, smaller particles are in general thermodynamically less stable than larger particles, resulting in a thermodynamic driving force for particle growth. To avoid direct coalescence of the copper particles, ZnO and Al<sub>2</sub>O<sub>3</sub> act as spacers to physically separate the copper particles from each other.<sup>1a</sup> However, particle growth can still occur due to diffusion of entire particles followed by their coalescence, or by transport of metal species from one particle to another.<sup>22</sup>

The strong interaction between copper particles and supports such as ZnO, Al<sub>2</sub>O<sub>3</sub> and SiO<sub>2</sub> makes it unlikely for the particles to detach from the support surface at methanol synthesis conditions and particle diffusion therefore takes place across the surface of the support. The formation of metal species depends on the thermodynamic stability of the particle in comparison to the thermodynamic stability of the metal species.<sup>22c, 23</sup> The obtained concentration of metal species is higher in the vicinity of smaller and thereby less stable particles. As a result, a concentration gradient of metal species is established between particles with different sizes, leading to a net flux of metal species from smaller to larger particles and hence growth of larger particles at the expense of smaller particles – a process often referred to as Ostwald ripening.

### Chemical potential of a supported metal particle

In the case of a supported metal particle the Gibbs relation reads as follows:

$$dG = \mu_0 dN + \gamma_M dA + \gamma_S dA_S + \gamma_{MS} dA_{MS}$$

Eq. 1.4

where  $\mu_0$  is the chemical potential of the bulk (i.e. macroscopic) material, A is the area of the particle's free surface,  $A_S$  is the area of the support,  $A_{MS}$  is the area of the metal-support interface, and  $\gamma_M$ ,  $\gamma_S$  and  $\gamma_{MS}$  are the energies of the metal, support and metal-support interfaces, respectively (see Figure 1.2). The energy of a particle thus depends on:

- the contribution of the surface energies to the total energy and thus on the particle size
- the surface energies of the metal and the support which depend on the reaction conditions
- the adhesion of the metal particle to the support which depends on the chemical nature of the support
- the interface area between the particle and the support which depends on the surface energies and on the support geometry

The creation of the metal-support interface area occurs at the expense of the free support surface area and depends on the wetting of the particle. The different surface energies are related to the contact (or wetting) angle ( $\theta$ ) via the Young-Duprez relation:

$$\gamma_M \cos(\theta) = \gamma_S - \gamma_{MS}$$

Eq. 1.5

Taking these relations into account the chemical potential of the nanoparticle reads:

$$\mu = \left( \frac{\partial G}{\partial N} \right) = \mu_0 + \frac{2\gamma_M \Omega}{R}$$

Eq. 1.6

where  $\Omega$  is the volume occupied by an atom in the nanoparticle and R the radius of curvature, which differs from half of the apparent diameter for small contact angles. This equation is often referred to as the Gibbs-Thomson relation.<sup>22a, 24</sup> The size-dependency of the chemical potential of the metal phase becomes more pronounced for particles with small radii of curvature, i.e. below 10 nm.

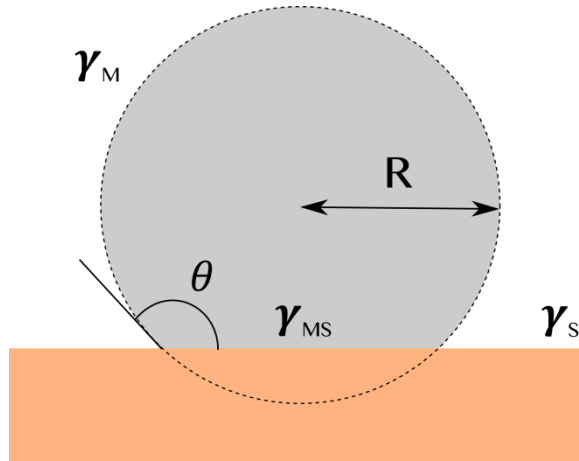


**Figure 1.2.** Sketch of a particle on a flat surface, with definition of the radius of curvature  $R$ , of the contact angle  $\theta$ , as well as of the surface energies  $\gamma$  of the metal (M), support (S), and metal-support (MS) interfaces.

Although the Gibbs relation provides a general description of the size-dependency of the chemical potential of the metal phase, it is important to note that for nanoparticles some of the underlying assumptions may no longer hold.<sup>24</sup> Firstly, the average coordination number of surface atoms decreases with decreasing particle size and results in a higher average metal surface energy. Secondly, the accuracy of the spherical approximation of the exposed metallic surface area decreases for smaller particles. Thirdly, for metallic particles with a size below ca. 2-3 nm, the local density of electronic states becomes size-sensitive and might influence the chemical potential of internal and external atoms. As a result, smaller (magic number) clusters of atoms can be thermodynamically more stable than larger clusters.

### Particle growth kinetics

In the case of particle growth via particle diffusion and coalescence (Figure 1.3), the coalescence step is irreversible due to the gain in free energy upon reducing the exposed metal surface area.<sup>22a</sup> For small particles (< 25 nm) coalescence occurs very fast compared to diffusion<sup>22a</sup> as is evidenced by the large increase in thermal stability upon the usage of supports or spacers. The rate-limiting step for most industrial supported metal catalysts in the diffusion-coalescence sequence is therefore particle diffusion.<sup>22a</sup> The probability for particles to meet each other and coalesce on a surface depends on the diffusion coefficient and the interparticle distances. The diffusion of the particles depends in turn on the size of the particles, the interaction with the support and the interaction with the reaction medium. The support geometry also plays a very important role as it affects the

interparticle surface distances and the interaction of the particle with the support. A particle on a concave surface is for instance more stable than a particle on a convex surface, resulting in different diffusion coefficients on both surfaces. Furthermore, particle migration might be physically restricted by the support due to for instance particle encagement or entrapment.<sup>11a, 25</sup>

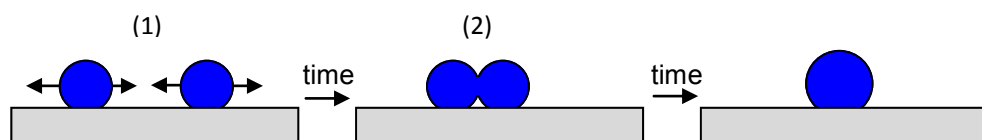


**Figure 1.3.** Schematic representation of particle growth due to particle diffusion (1) followed by particle coalescence (2). Metallic particles are shown in blue and the support material in grey.

In the case of Ostwald ripening (Figure 1.4), the net flux of metal species between particles is proportional to the gradient in metal species concentration at the respective particles and the diffusion coefficient of the metal species. Diffusion can occur via the liquid or gas phase, or via the support surface. In the former situation the diffusion coefficient of the metal species depends on the reaction medium and in the latter it depends also on their interaction with the support surface. The equilibrium concentration of metal species at a certain particle depends on the thermodynamic stability of the particle in comparison to the stability of the metal species. Single copper atoms have a very low thermodynamic stability at methanol synthesis reaction conditions and are therefore most likely not responsible for Ostwald ripening. Copper atoms can, however, be stabilized by adsorbates forming for instance  $\text{Cu}(\text{CO})_x$ , by interaction with the support, or by a combination of the two.<sup>26</sup> Copper adsorbate species diffusing over the support surface are often held responsible for Ostwald ripening in the methanol synthesis reaction.<sup>26</sup>

In summary, Ostwald ripening is governed by the gradient in metal species concentration between particles due to differences in the chemical potential of the particles which are primarily due to differences in particle size. The process is either reaction-limited or diffusion-limited.<sup>23</sup> In the former case either the detachment or attachment of metal species determines the rate of the process. Considering the attachment of metal species to be an exothermic process and the reverse endothermic, it is likely that the detachment of metal species is limiting the Ostwald ripening process rather than the attachment.

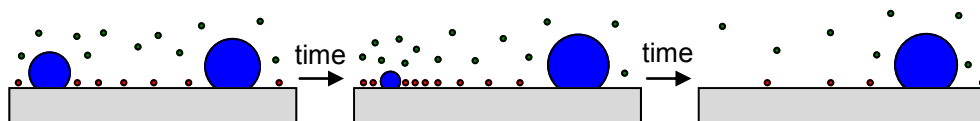


**Figure 1.4.** Schematic representation of particle growth due to Ostwald ripening. Metallic particles are shown in blue, the support material in grey, metal species diffusing over the surface in red and metal species diffusing in the reaction medium in green. Differences in metal species concentration lead to a net flux of metal species towards larger particles resulting in growth of larger particles at the expense of smaller particles.

As discussed above and shown in literature, parameters such as the reaction conditions,<sup>26</sup> the particle size (distribution),<sup>24, 27</sup> interparticle spacing,<sup>11a, 28</sup> support geometry<sup>25, 29</sup> and metal-support interaction<sup>23, 30</sup> all can have an influence on particle growth, irrespective of the mechanism. Furthermore, it has to be noted that not just the metal phase might change during reaction but also the support phase might change and thereby influence the metal particle growth. The support might for instance sinter resulting in decreased interparticle distances. Moreover, the chemical nature of the support surface might change during catalysis and thereby the interaction with the metal. All of the mentioned parameters influencing catalyst stability can also have a direct or indirect influence on catalyst activity and selectivity. In general, more active catalysts, with more and smaller particles on less support material, also deactivate faster due to particle growth. It is therefore of utmost importance to determine the influence of each of these parameters on activity, selectivity and stability to be able to engineer catalysts that are economically more attractive.

### Catalyst synthesis

Although the identification of the catalyst characteristics required for the optimal catalytic performance is very important, it is of no use if the catalyst containing these characteristics cannot be made at an industrial scale in an economically viable way. Two main routes are used in industry to prepare supported metal catalysts, i.e. precipitation and impregnation.<sup>31</sup> In precipitation, a metal precursor is deposited on a preformed support (deposition-precipitation) or precipitated together with a support precursor (co-precipitation). Subsequent drying, calcination and reduction result in the formation of metallic particles and in the case of a co-precipitate also in the formation of the support. In impregnation, a support is contacted with a metal solution and metallic particles are formed upon drying, calcination and reduction. The commercially used Cu/ZnO/Al<sub>2</sub>O<sub>3</sub> catalyst is made via the co-precipitation route.<sup>1a, 21</sup> It has been shown that every synthesis step can profoundly affect the properties of the final supported metal catalyst, e.g. the

particle spatial distribution by the temperature during drying,<sup>32</sup> the particle size by the space velocity and gas composition during heat treatment<sup>33</sup> and the oxidation state by the pressure of H<sub>2</sub> during reduction.<sup>17a</sup> To obtain control over the properties influencing the catalytic performance it is necessary to understand and control the evolution of the catalyst during synthesis.

### Scope of this thesis

The goal of the research described in this thesis is to investigate and control the processes involved in the synthesis of supported copper catalysts, the structural parameters required for maximum methanol synthesis activity, and the influence of different catalyst characteristics on copper particle growth. A fundamental understanding of these aspects is highly relevant for the optimization of methanol synthesis catalysts, but also for the rational design of supported metal catalysts in general as many physicochemical processes during synthesis and catalysis are similar. The synthesis of supported copper catalysts can act as a model system to investigate fundamental processes involved in the synthesis of supported metal catalyst such as nanoparticle formation. Secondly, copper-based methanol synthesis catalysts allow investigating the synergistic effect of two components and the effect of surface structure on catalyst activity which are relevant for many (bi)metallic systems. Lastly, the methanol synthesis reaction is a suitable model reaction to investigate the parameters influencing particle growth, as other deactivation mechanisms play an insignificant role in the long-term stability. This reaction therefore allows studying a process by which many catalysts, including cobalt and iron catalysts in the Fischer-Tropsch reaction,<sup>34</sup> platinum and palladium in the three-way catalyst,<sup>20, 35</sup> platinum in fuel cells,<sup>36</sup> and nickel catalysts in the methanation reaction,<sup>37</sup> deactivate.

### Outline

To obtain fundamental information about the processes involved in the synthesis and performance of copper-based methanol synthesis catalysts and the structural parameters influencing these processes, well-defined 3D model catalysts were synthesized, characterized with bulk and microscopy techniques, and their performance was investigated at industrially relevant conditions.

In **Chapter 2** the formation of copper nanoparticles during synthesis is studied with electron microscopy. A homogeneous solid precursor consisting of copper phyllosilicate is synthesized and subsequently reduced in the electron microscope in an H<sub>2</sub> atmosphere. Time-resolved TEM images were acquired during the formation of the copper nanoparticles which enabled the extraction of quantitative information about the nucleation and growth of individual nanoparticles.

In **Chapter 3** the influence of copper particle size, addition of zinc, and thermodynamic stability of the zinc phase on catalyst activity in the methanol synthesis reaction is investigated. 42 catalysts with average copper particle sizes in the range from 2 to 15 nm were synthesized on zinc-free supports, on supports incorporating zinc as zinc hydroxyl(phylo)silicate and on supports containing zinc oxide. Furthermore, catalyst series with similar copper particle sizes and varying zinc loading were synthesized to determine the minimum amount of zinc required to achieve maximum activity.

In **Chapter 4** the effects of the chemical nature of the support surface, particle size distribution and interparticle spacing on copper particle growth in the methanol synthesis reaction are independently from each other investigated. Stöber silica was functionalized with aminopropyl groups and similarly sized copper particles were deposited on the functionalized and unfunctionalized support. The effect of the surface functionalization on the metal-support interaction was studied by determining the contact angle between the metallic copper particles and the supports using electron microscopy. By varying the copper loading on unfunctionalized Stöber silica either the interparticle spacing or the particle size distribution was changed. The information obtained from the effects of these parameters on copper particle growth enabled to extract the mechanism by which the copper particles in these catalysts grow.

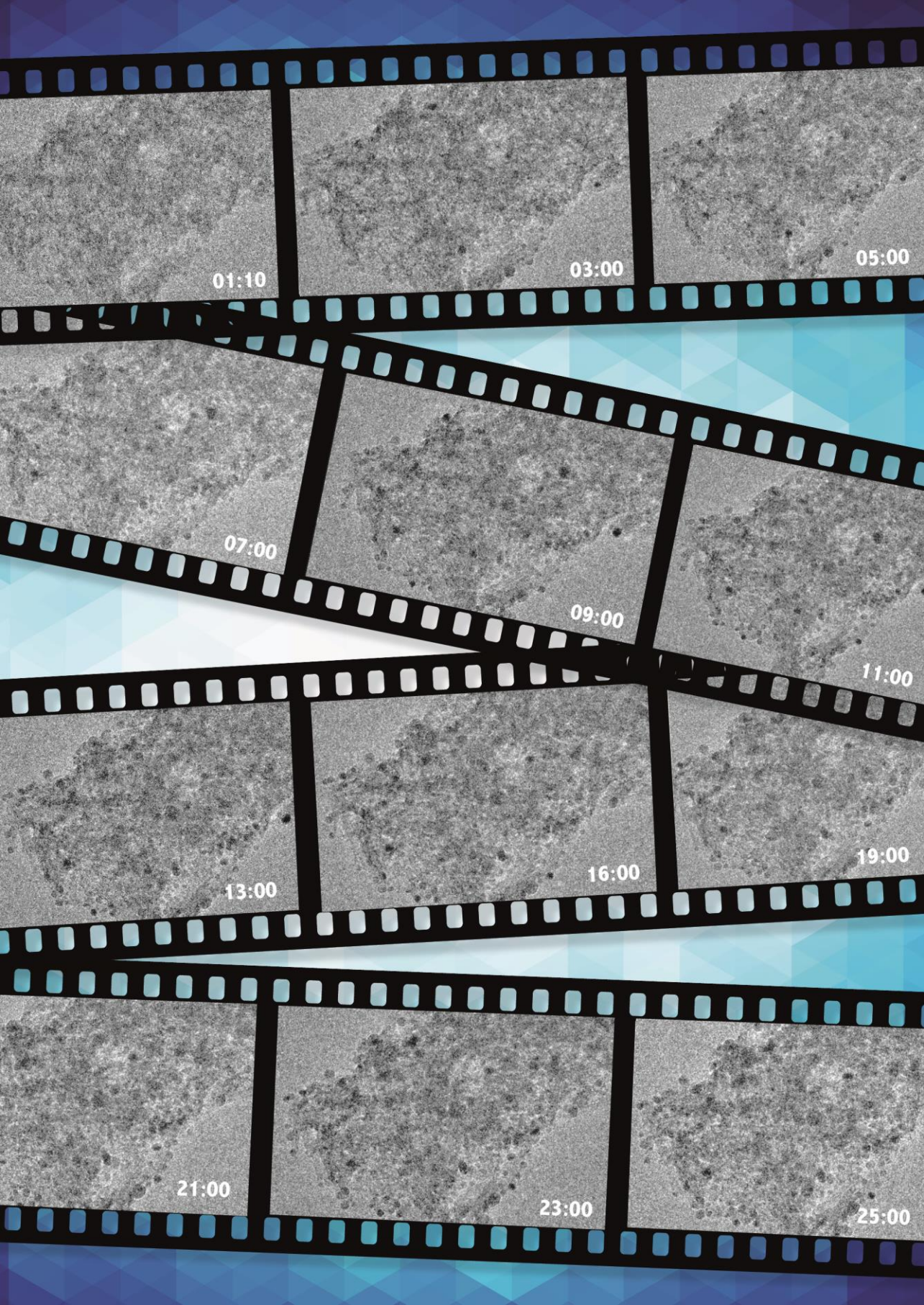
In **Chapter 5** the impact of the synthesis route on the support structure, the location of the copper particles therein, and the performance in the methanol synthesis reaction is investigated. Cu/SiO<sub>2</sub> catalysts with similar copper particle sizes and local copper weight loadings were synthesized via impregnation and via precipitation. Electron tomography was used to characterize the silica support structure and the location of the copper particles therein. Subsequently, the effect of these parameters on copper particle growth was determined.

In **Chapter 6** a summary of the thesis, concluding remarks and outlook are provided in both English and Dutch.

### References

- (1) (a) Hansen, J. B.; Højlund Nielsen, P. E. Methanol Synthesis. In *Handbook of Heterogeneous Catalysis*, Ertl, G.; Knözinger, H.; Schüth, F.; Weltkamp, J., Eds. Wiley-VCH: 2008; pp 2920-2949; (b) Bertau, M.; Offermans, H.; Plass, L.; Schmidt, F.; Wernicke, H. J. *Methanol: The Basic Chemical and Energy Feedstock of the Future*. Springer-Verlag: Heidelberg, 2014.
- (2) (a) Olah, G. A. *Angew. Chem. Int. Ed.* **2005**, *44*, 2636-2639; (b) Olah, G. A. *Angew. Chem. Int. Ed.* **2013**, *52*, 104-107.
- (3) Sutton, D.; Kelleher, B.; Ross, J. R. H. *Fuel Process. Technol.* **2001**, *73*, 155-173.
- (4) Yang, C.-J.; Jackson, R. B. *Energy Policy* **2012**, *41*, 878-884.
- (5) IHS Global Methanol Report 2014, [igpenenergy.com/products/methanol-overview/methanol/methanol](http://igpenenergy.com/products/methanol-overview/methanol/methanol), accessed 22-12-2015.
- (6) Waugh, K. C. *Catal. Lett.* **2012**, *142*, 1153-1166.
- (7) (a) Nakamura, J.; Choi, Y.; Fujitani, T. *Top. Catal.* **2003**, *22*; (b) Studt, F.; Behrens, M.; Kunkes, E. L.; Thomas, N.; Zander, S.; Tarasov, A.; Schumann, J.; Frei, E.; Varley, J. B.; Abild-Pedersen, F.; Nørskov, J. K.; Schlögl, R. *ChemCatChem* **2015**, *7*, 1105-1111.
- (8) (a) Chinchin, G. C.; Waugh, K. C.; Whan, D. A. *Appl. Catal.* **1986**, *25*, 101-107; (b) Robbins, J. L.; Iglesia, E.; Kelkar, C. P.; DeRites, B. *Catal. Lett.* **1991**, *10*, 1-10; (c) Kurtz, M.; Wilmer, H.; Genger, T.; Hinrichsen, O.; Muhler, M. *Catal. Lett.* **2003**, *86*, 77-80; (d) Burch, R.; Chappell, R. J. *Appl. Catal.* **1988**, *45*, 131-150; (e) Pan, W. X.; Cao, R.; Roberts, D. L.; Griffin, G. L. *J. Catal.* **1988**, *114*, 440-446.
- (9) Behrens, M.; Studt, F.; Kasatkin, I.; Kühn, S.; Hävecker, M.; Abild-Pedersen, F.; Zander, S.; Girgsdies, F.; Kurr, P.; Kniep, B.-L.; Tovar, M.; Fischer, R. W.; Nørskov, J. K.; Schlögl, R. *Science* **2012**, *336*, 893-897.
- (10) (a) van Hardeveld, R.; Hartog, F. *Surf. Sci.* **1969**, *15*, 189-230; (b) van Helden, P.; Ciobîcă, I. M.; Coetzer, R. L. *J. Catal. Today* **2016**, *261*, 48-59.
- (11) (a) Prieto, G.; Zečević, J.; Friedrich, H.; de Jong, K. P.; de Jongh, P. E. *Nat. Mater.* **2013**, *12*, 34-39; (b) Vesborg, P. C. K.; Chorkendorff, I.; Knudsen, I.; Balmes, O.; Nerlov, J.; Molenbroek, A. M.; Clausen, B. S.; Helveg, S. *J. Catal.* **2009**, *262*, 65-72.
- (12) Burch, R.; Golunski, S. E.; Spencer, M. S. *J. Chem. Soc. Faraday Trans.* **1990**, *86*, 2683-2691.
- (13) Burch, R.; Golunski, S. E.; Spencer, M. S. *Catal. Lett.* **1990**, *5*, 55-60.
- (14) Hansen, P. L.; Wagner, J. B.; Helveg, S.; Rostrup-Nielsen, J. R.; Clausen, B. S.; Topsøe, H. *Science* **2002**, *295*, 2053-2055.
- (15) Günter, M. M.; Ressler, T.; Bems, B.; Büscher, C.; Genger, T.; Hinrichsen, O.; Muhler, M.; Schlögl, R. *Catal. Lett.* **2001**, *71*, 37-44.
- (16) (a) Klier, K. *Adv. Catal.* **1982**, *31*, 243-313; (b) Frost, J. C. *Nature* **1988**, *334*, 577-580.
- (17) (a) Kuld, S.; Conradsen, C.; Moses, P. G.; Chorkendorff, I.; Sehested, J. *Angew. Chem. Int. Ed.* **2014**, *53*, 5941-5945; (b) Grunwaldt, J. D.; Molenbroek, A. M.; Topsøe, N. Y.; Topsøe, H.; Clausen, B. S. *J. Catal.* **2000**, *194*, 452-460; (c) Naumann d'Alnoncourt, R.; Xia, X.; Strunk, J.; Löffler, E.; Hinrichsen, O.; Muhler, M. *Phys. Chem. Chem. Phys.* **2006**, *8*, 1525-38; (d) Batyrev, E.; van den Heuvel, J.; Beckers, J.; Jansen, W.; Castricum, H. *J. Catal.* **2005**, *229*, 136-143; (e) Jansen, W.; Beckers, J.; v. d. Heuvel, J. C.; Denier v. d. Gon, A. W.; Bliet, A.; Brongersma, H. H. *J. Catal.* **2002**, *210*, 229-236.
- (18) (a) Rozovskii, A. Y.; Lin, G. I. *Top. Catal.* **2003**, *22*, 137-150; (b) Lee, J. S.; Lee, K. H.; Lee, S. Y.; Kim, Y. G. *J. Catal.* **1993**, *144*, 414-424; (c) Gotti, A.; Prins, R. J. *Catal.* **1998**, *178*, 511-519.
- (19) Yang, Y.; Mims, C. A.; Mei, D. H.; Peden, C. H. F.; Campbell, C. T. *J. Catal.* **2013**, *298*, 10-17.
- (20) Moulijn, J. A.; Diepen, A. E. V.; Kapteijn, F. *Science* **2001**, *212*, 3-16.
- (21) Baltes, C.; Vukojevic, S.; Schüth, F. *J. Catal.* **2008**, *258*, 334-344.
- (22) (a) Wynblatt, P.; Gjostein, N. A. *Prog. Solid State Chem.* **1976**, *9*, 21-58; (b) Ruckenstein, E.; Pulvermacher, B. *J. Catal.* **1973**, *29*, 224-245; (c) Lifshitz, I. M.; Slyozov, V. V. *J. Phys. Chem. Solids* **1961**, *19*, 35-50.

- (23) Ouyang, R.; Liu, J.-X.; Li, W.-X. *J. Am. Chem. Soc.* **2013**, *135*, 1760-1771.
- (24) Campbell, C. T.; Parker, S. C.; Starr, D. E. *Science* **2002**, *298*, 811-814.
- (25) (a) Arnal, P. M.; Comotti, M.; Schüth, F. *Angew. Chem. Int. Ed.* **2006**, *45*, 8224-8227; (b) Joo, S. H.; Park, J. Y.; Tsung, C. K.; Yamada, Y.; Yang, P.; Somorjai, G. A. *Nat. Mater.* **2009**, *8*, 126-131.
- (26) Rasmussen, D. B.; Janssens, T. V. W.; Temel, B.; Bligaard, T.; Hinnemann, B.; Helveg, S.; Sehested, J. *J. Catal.* **2012**, *293*, 205-214.
- (27) Datye, A. K.; Xu, Q.; Kharas, K. C.; McCarty, J. M. *Catal. Today* **2006**, *111*, 59-67.
- (28) (a) Morgenstern, K.; Rosenfeld, G.; Comsa, G. *Surf. Sci.* **1999**, *441*, 289-300; (b) Simonsen, S. B.; Chorkendorff, I.; Dahl, S.; Skoglundh, M.; Sehested, J.; Helveg, S. *J. Catal.* **2011**, *281*, 147-155.
- (29) (a) Prieto, G.; Shakeri, M.; de Jong, K. P.; de Jongh, P. E. *ACS Nano* **2014**, *8*, 2522-2531; (b) Laursen, A. B.; Højholt, K. T.; Lundegaard, L. F.; Simonsen, S. B.; Helveg, S.; Schüth, F.; Paul, M.; Grunwaldt, J. D.; Kegnæs, S.; Christensen, C. H.; Egeblad, K. *Angew. Chem. Int. Ed.* **2010**, *49*, 3504-3507.
- (30) (a) Cao, A.; Lu, R.; Veser, G. *Phys. Chem. Chem. Phys.* **2010**, *12*, 13499-510; (b) Wallace, W. T.; Min, B. K.; Goodman, D. W. *J. Mol. Catal. A: Chem.* **2005**, *228*, 3-10; (c) Campbell, C. T.; Sellers, J. R. V. *Faraday Discuss.* **2013**, *162*, 9.
- (31) (a) de Jong, K. P.; (Ed.). *Synthesis of solid catalysts*. Wiley-VCH: Weinheim, 2009; (b) Munnik, P.; de Jongh, P. E.; de Jong, K. P. *Chem. Rev.* **2015**, *115*, 6687-6718; (c) Schüth, F.; Hesse, M.; Unger, K. K. Precipitation and coprecipitation. In *Handbook of Heterogeneous Catalysis*, Ertl, G.; Knözinger, H.; Schüth, F.; Weitkamp, J., Eds. Wiley-VCH Verlag GmbH & Co. KGaA: Weinheim, 2008; (d) Behrens, M. *Catal. Today* **2015**, *246*, 46-54.
- (32) (a) Munnik, P.; de Jongh, P. E.; de Jong, K. P. *J. Am. Chem. Soc.* **2014**, *136*, 7333-7340; (b) Lekhal, A.; Glasser, B. J.; Khinast, J. G. *Chem. Eng. Sci.* **2001**, *56*, 4473-4487.
- (33) (a) Munnik, P.; Wolters, M.; Gabrielsson, a.; Pollington, S. D.; Headdock, G.; Bitter, J. H.; de Jongh, P. E.; de Jong, K. P. *J. Phys. Chem. C* **2011**, *115*, 14698-14706; (b) Sietsma, J. R.; Meeldijk, J. D.; den Breejen, J. P.; Versluijs-Helder, M.; van Dillen, A. J.; de Jongh, P. E.; de Jong, K. P. *Angew. Chem. Int. Ed.* **2007**, *46*, 4547-4549; (c) van de Loosdrecht, J.; Barradas, S.; Caricato, E. A.; Ngwenya, N. G.; Nkwanyana, P. S.; Rawat, M. A. S.; Sigwebela, B. H.; van Berge, P. J.; Visagie, J. L. *Top. Catal.* **2003**, *26*, 121-127.
- (34) van de Loosdrecht, J.; Botes, F. G.; Ciobica, I. M.; Ferreira, A.; Gibson, P.; Moodley, D. J.; Saib, A. M.; Visagie, J. L.; Weststrate, C. J.; Niemantsverdriet, J. W. Fischer-Tropsch Synthesis: Catalysts and Chemistry. In *Comprehensive Inorganic Chemistry II*, Reedijk, J.; Poeppelemeier, K., Eds. Elsevier: Oxford, 2013; Vol. 7, pp 525-557.
- (35) Simonsen, S. B.; Chorkendorff, I.; Dahl, S.; Skoglundh, M.; Sehested, J.; Helveg, S. *J. Am. Chem. Soc.* **2010**, *132*, 7968-7975.
- (36) Xin, H. L.; Mundy, J. A.; Liu, Z.; Cabezas, R.; Hovden, R.; Kourkoutis, L. F.; Zhang, J.; Subramanian, N. P.; Makharia, R.; Wagner, F. T.; Muller, D. A. *Nano Lett.* **2012**, *12*, 490-497
- (37) Munnik, P.; Velthoen, M. E. Z.; de Jongh, P. E.; de Jong, K. P.; Gommès, C. J. *Angew. Chem. Int. Ed.* **2014**, *126*, 9647-9651.



01:10

03:00

05:00

07:00

09:00

11:00

13:00

16:00

19:00

21:00

23:00

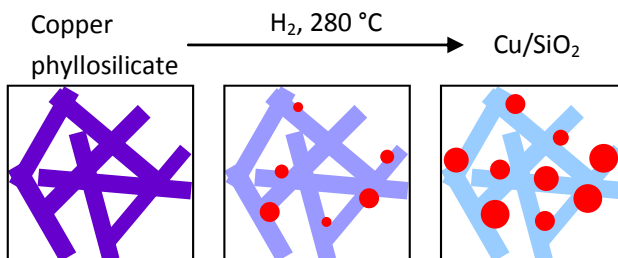
25:00

# Revealing the Formation of Copper Nanoparticles from a Homogeneous Solid Precursor by Electron Microscopy

Based on: van den Berg, R.; Elkjær, C. F.; Gommès, C. J.; Chorkendorff, I.; Sehested, J.; de Jongh, P. E.; de Jong, K. P.; Helveg, S. *J. Am. Chem. Soc.* **2016**, 138, 3433-3442

### Abstract

The understanding of processes leading to the formation of nanometer-sized particles is important for tailoring of their size, shape and location. The growth mechanisms and kinetics of nanoparticles from solid precursors are, however, often poorly described. Here we examine the formation of copper nanoparticles on a silica support during the reduction of copper phyllosilicate by  $H_2$  by means of transmission electron microscopy (TEM). Specifically, time-lapsed TEM image series acquired of the material during the reduction provide a direct visualization of the growth dynamics of an ensemble of individual nanoparticles and enable a quantitative evaluation of the nucleation and growth of the nanoparticles. This quantitative information is compared with kinetic models and found to be best described by a nucleation-and-growth scenario involving autocatalytic reduction of the copper phyllosilicate followed by diffusion-limited or reaction-limited growth of the copper nanoparticles. In this way, in situ observations made by electron microscopy provide mechanistic and kinetic insights into the formation of metallic nanoparticles, essential for the rational design of nanomaterials.



## Introduction

Nanometer-sized particles provide electronic, optical and catalytic properties that strongly depend on their size, shape and spatial arrangement. The synthesis of nanoparticles with predefined structural characteristics has therefore become an important research theme. Synthesis procedures include the aggregation of atomic species to form colloidal nanoparticles in liquid and the transformation of solid precursors by gas phase treatments to form supported nanoparticles.<sup>1</sup> In the latter case, precursors often consist of a metal salt impregnated on a support or of a co-precipitate of the metal oxide and support material. This approach is particularly beneficial for preparing nanoparticles at large scales for e.g. industrial catalytic processes.<sup>1a-c</sup> Despite the significant efforts devoted to optimize procedures for transforming solid precursors into supported nanoparticles, a fundamental understanding of the particle growth mechanisms and their relation with the growth kinetics is often limited.<sup>2</sup> As growth processes involve atom exchange at or across solid surfaces, observations made in situ at high spatial resolution would be beneficial for elucidating nanoparticle growth mechanisms.

In recent years, transmission electron microscopy (TEM) has become a powerful tool for visualizing nanoparticles at atomic resolution.<sup>3</sup> Studies of nanoparticles during exposure to gas or liquid environments are, however, hampered by the small mean free path of the electron beam in dense media. The introduction of differentially pumped vacuum systems and closed electron transparent cells provides a means to confine gas or liquid phases to the vicinity of the sample in the transmission electron microscope.<sup>4</sup> Hereby, TEM can be used to monitor nanoparticles in reactive environments by the acquisition of time-lapsed image series. This approach has resulted in new insights into the dynamical formation of nanoparticles in the liquid phase,<sup>5</sup> and, by gas phase treatment of impregnated support materials, in the solid phase.<sup>6</sup> However, the way in which nanoparticles grow in the solid phase by gas phase treatment of co-precipitated precursors has not been addressed so far although the homogeneity of these materials offer the possibility to obtain mechanistic and kinetic information that can be translated to large scale material synthesis.

Here we use TEM to examine the growth of an ensemble of Cu nanoparticles on SiO<sub>2</sub>, which results in a material that catalyzes the hydrogenation of carbon-oxygen bonds.<sup>7</sup> The nanoparticles and the silica support are formed in the electron microscope by reduction in H<sub>2</sub> of copper phyllosilicate, which is a precipitated solid precursor that consists of platelets with a homogeneous distribution of Cu<sup>2+</sup>.<sup>8</sup> To ensure that the TEM observations reflect processes inherent to the reduction treatment, the impact of the electron beam on the process was characterized and a beam-insensitive imaging scheme developed. By employing this optimized imaging scheme, time-resolved TEM images were acquired during the formation of the copper nanoparticles which enabled the extraction of quantitative

information about the nucleation and growth of individual copper nanoparticles. This dynamic information is compared to predictions made by kinetic models which allowed deriving a mechanism for the nanoparticle formation.

## Experimental Section

### Synthesis of copper phyllosilicate

Copper phyllosilicate can be synthesized by deposition precipitation of copper nitrate using ammonia evaporation<sup>7a, 7d, 9</sup> or urea hydrolysis<sup>8b</sup> and by using selective adsorption of  $[\text{Cu}(\text{NH}_3)_4]^{2+}$  on  $\text{SiO}_2$ .<sup>8a</sup> However, both deposition-precipitation and selective adsorption often lead to heterogeneous materials comprising unreacted silica, copper phyllosilicate, and other copper species like copper(II) oxide.<sup>8</sup> To obtain only the copper phyllosilicate phase for our material, the homogeneous deposition-precipitation procedure of van der Grift and coworkers was followed by a hydrothermal treatment.<sup>8b</sup>

Specifically, a mass of 20.1 g LUDOX-AS 30 (Sigma-Aldrich), 16.1 g  $\text{Cu}(\text{NO}_3)_2 \cdot 3\text{H}_2\text{O}$  (Acros Organics, 99% for analysis) and 12.1 g Urea (Acros Organics, 99.5% for analysis) were added to 1.7 L of demineralized water in a 2 L reaction vessel. The pH was adjusted to 2-3 with a few drops of  $\text{HNO}_3$  (Merck, 65% for analysis) to prevent premature hydrolysis of copper nitrate. The suspension was then heated to 90 °C in 1 h under stirring. At 90 °C, hydrolysis of urea led to an increase in pH resulting in the precipitation of  $\text{Cu}_2(\text{NO}_3)(\text{OH})_3$  and the formation of the  $[\text{Cu}(\text{OH})_2(\text{H}_2\text{O})_4]^0$  complex in solution. The well-stirred suspension was kept at 90 °C for 7 days to allow recrystallization of precipitated copper and silica, which resulted in the formation of copper phyllosilicate. The precipitate was obtained by hot filtration of the suspension. Thereafter, the precipitate was washed three times at room temperature with demineralized water, filtered and dried overnight at 60 °C. The yield was about 10 g, which is close to the intended dry copper phyllosilicate weight. A relatively high copper to silicon atomic ratio of 0.66 was chosen, corresponding to 41 wt% copper in the final  $\text{Cu}/\text{SiO}_2$  material. Lower copper loadings resulted in partly unreacted silica and a copper loading above 45 wt% resulted in the presence of copper oxide particles.<sup>7b</sup>

### Reduction in a plug-flow reactor

A mass of 0.3 g of the as-prepared copper phyllosilicate was reduced in a plug-flow reactor (diameter 1 cm) at 250 °C (heating rate 2 °C/min) in a flow of 30 mL/min of 20%  $\text{H}_2$  in Ar for 2½ h. After the reduction treatment, the reduced sample was passivated for 15 min at room temperature by slowly exposing the sample to a diluted air/ $\text{N}_2$  flow by creating a small leak

in the flow supply system. The sample was stored in a glove box containing an argon atmosphere.

### Characterization

X-ray diffraction was performed with a Bruker-Nonius D8 Advance X-ray diffractometer using Co-K<sub>α1,2</sub> ( $\lambda = 1.79026 \text{ \AA}$ ) radiation. For the reduced sample, the specimen holder was loaded in the glovebox and subsequently sealed to prevent exposure to air. Diffractograms of the material before and after reduction were obtained at room temperature from 20° to 70° (2 $\theta$ ). N<sub>2</sub> physisorption measurements were performed at -196 °C, using a Micromeritics Tristar 3000 apparatus. The BET method was used to calculate the specific surface area. Energy dispersive X-ray (EDX) spectroscopy was performed using a Technai 20FEG (FEI) electron microscope equipped with a field emission gun and with an EDAX Super Ultra Thin Window EDX detector. The as-prepared copper phyllosilicate was dispersed on a carbon coated Ni TEM grid (Agar 162 200 Mesh Ni) and this sample was introduced into the microscope using a low-background sample holder (Philips) with a 0.1 mm thick Be specimen support film and a Be ring to clamp the grid. EDX spectra were acquired of 22 regions of the sample using an electron beam diameter of 100 to 500 nm and of 6 regions by scanning a 0.3 – 1.2 nm wide electron beam along a line of 100 to 500 nm in length. The EDX spectra were quantified using the Tecnai Imaging and Analysis (TIA) software by using a detector correction of 0.977 and 0.997 and a k-factor of 1.000 and 1.757 for Si and Cu, respectively, on the integrated intensities of the Si-K and Cu-K signal. Temperature programmed reduction (TPR) was performed using an Autochem II ASAP 2910 from micromeritics. The H<sub>2</sub> concentration during the experiment was measured with a thermal conductivity detector. About 0.05 g copper phyllosilicate was placed on top of a quartz wool bed in a glass reactor tube. The sample was heated to 500 °C (5 °C/min) under a flow of 5% H<sub>2</sub>/Ar. Thermal gravimetric analysis (TGA) was performed with a Perkin-Elmer Pyris 1 apparatus. About 2.5 mg of copper phyllosilicate was heated to 500 °C under a flow of 2.5 mL/min 5% H<sub>2</sub>/Ar.

### Transmission electron microscopy

In situ observations by TEM were made using an image-aberration corrected Titan 80-300 ETEM (FEI Company).<sup>10</sup> The microscope was operated at a primary electron energy of 300 keV. Prior to the experiment, the image-aberration corrector was tuned using a cross-grating (Agar S106) and the spherical aberration coefficient was set in the range of -10 to -20  $\mu\text{m}$ . All quoted electron dose-rates were measured using the microscope's fluorescent screen. TEM grids were placed in a heating holder (Gatan model 628) for introduction into the electron microscope. TEM images were acquired with a bottom-mounted 2k  $\times$  2k

charged-coupled device (CCD) camera (Gatan US1000) and with the projection system set to an effective CCD pixel size between 0.37 and 0.56 nm.

The reduced Cu/SiO<sub>2</sub> was used as reference. A sample was prepared by grinding the powder and dispersing it on a stainless steel grid. The sample was re-reduced in 1 mbar H<sub>2</sub> at 250 °C (heating rate 30 °C/min) for 45 min. Under these conditions, TEM images of the sample were acquired using an electron dose-rate of 10 e<sup>-</sup>/(Å<sup>2</sup>s).

The as-prepared copper phyllosilicate was studied in three types of experiments in the electron microscope to address the effect of electron illumination and to establish conditions of negligible impact of the electron beam on the formation of copper particles. Specifically, experiment E1 addresses the effect of thermal reduction in H<sub>2</sub> without any electron beam illumination, experiment E2 addresses the effect of illuminating the sample in vacuum prior to a reduction treatment, and experiment E3 addresses the effect of the electron beam in H<sub>2</sub> with no thermally induced particle growth.

For the experiments E1-E3, samples of as-prepared copper phyllosilicate were prepared by grinding and dispersing the powder on stainless steel grids. Firstly, in experiment E1, separate samples were exposed to 1 mbar H<sub>2</sub> at 150 °C (4h), 200 °C (½ h), 250 °C (3h) and 280 °C (1 ¼ h) and subsequently imaged at the respective conditions or at base vacuum (1.9 • 10<sup>-6</sup> mbar) at room temperature. Secondly, in experiment E2, one sample was kept at base vacuum (2.3 • 10<sup>-5</sup> mbar) at room temperature and five distinct regions of copper phyllosilicate were illuminated at electron dose-rates of 1, 5, 10, 20 and 100 e<sup>-</sup>/(Å<sup>2</sup>s) for a total of ca. 2 min. Subsequently, the sample was exposed to 1 mbar H<sub>2</sub>, heated at 30 °C/min to 280 °C and held at that temperature for 75 min before it was heated further at 30 °C/min to 310 °C at which it was held for 30 min. Afterwards, the sample was cooled to room temperature in H<sub>2</sub> and the microscope was evacuated. Finally, the five areas were imaged in vacuum with a dose-rate of 20 e<sup>-</sup>/(Å<sup>2</sup>s). In addition, ten previously unilluminated regions were imaged as reference locations. Thirdly, in experiment E3, one sample was exposed to 1 mbar H<sub>2</sub> at 150 °C. Five distinct copper phyllosilicate regions were continuously illuminated at an electron dose-rate of 1, 5, 10, 20 or 100 e<sup>-</sup>/(Å<sup>2</sup>s), respectively, for 20 min while time-resolved series of TEM images were recorded. After the acquisition of these series, several distinct and previously unilluminated regions were located at 150 °C at base vacuum (1.4 • 10<sup>-6</sup> mbar) and TEM images were acquired at an electron dose-rate of 10 e<sup>-</sup>/(Å<sup>2</sup>s).

The information obtained from experiments E1-E3 enables an experimental procedure for the beam-insensitive experiments to be established (Figure 2.1). For these experiments, two samples were prepared by grinding and dispersing the as-prepared copper phyllosilicate on gold grids. In the microscope, the samples were exposed to 1 mbar H<sub>2</sub> and heated at 30 °C/min to 200 °C. At these conditions, regions of interest were identified with

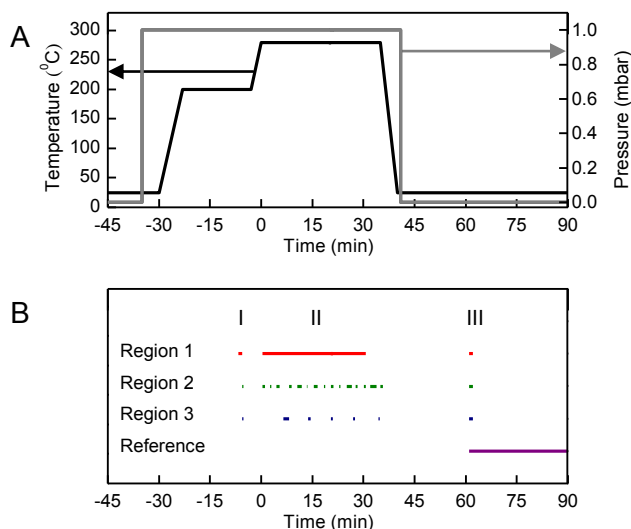


**Figure 2.1.** Procedure for TEM image acquisition during  $\text{H}_2$  reduction of the copper phyllosilicate. (A) Temporal profiles of temperature and  $\text{H}_2$  pressure in the experiment. Time  $t = 0$  min corresponds to the time at which the temperature reaches  $280^\circ\text{C}$ . (B) Scheme for electron illumination. The electron dose-rate:  $0.05 \text{ e}^-/(\text{\AA}^2\text{s})$  (before reduction (I)),  $1 \text{ e}^-/(\text{\AA}^2\text{s})$  (during reduction (II)) and  $5 \text{ e}^-/(\text{\AA}^2\text{s})$  (after reduction (III)). During reduction, region 1 (red) was continuously illuminated and Region 2 (green) and Region 3 (blue) were intermittently illuminated at time intervals of ca. 2 min and 6 min, respectively. After reduction, TEM images were acquired of regions 1-3 and at previously unilluminated regions (purple).

an electron dose-rate of  $0.05 \text{ e}^-/(\text{\AA}^2\text{s})$  and maximum illumination time of one minute per region. This short illumination prior to reduction had no detectable effect on the reduction process, as will be consistently shown in the Results & Discussion section. After 20 min, thermal drift of the heating holder subsided and the samples were further heated to  $280^\circ\text{C}$  (heating rate  $30^\circ\text{C}/\text{min}$ ). At those conditions, time-lapsed TEM images were recorded with an electron dose-rate of  $1 \text{ e}^-/(\text{\AA}^2\text{s})$ . Specifically, by operating the projection system corresponding to a CCD camera pixel size of  $0.56 \text{ nm}$  and a CCD illumination time of  $1 \text{ s}$ , the electron beam penetrating only the gas phase creates on average about 32 electrons per pixel with a standard deviation of about 8 electrons, resulting in a signal-to-noise ratio (SNR) of 4. Due to this low SNR, particles were only distinguishable in the present phyllosilicate materials at diameters larger than ca.  $3.4 \text{ nm}$  (6 pixels). In comparison the sample reduced in the plug-flow reactor was examined by TEM at illumination conditions with a corresponding SNR of about 25. It was shown that the particle size distribution for this sample is similar to the final distribution obtained in the electron microscope with a SNR of about 20 and that the lower cutoff particle size was  $3 \text{ nm}$ . Hence, the illumination

conditions employed during the reduction process were sufficient to monitor the growth of all the particles.

The time-lapsed images were acquired as outlined in the scheme in Figure 2.1: In one experiment, one region (Region 1) was continuously illuminated and images acquired with a CCD illumination time of 1 s and a frame rate of 1 per 5 s. In a second experiment, two distinct regions (Region 2 and Region 3), outside of each other's illuminated areas, were illuminated at intervals of ca. 2 and 6 min, respectively. The illumination persisted for approximately 45 seconds, for locating and focusing the sample region and subsequent image acquisition (2 s CCD illumination, see Figure 2.1B for the exact times each region was illuminated). In the intervening periods between successive electron illuminations, the electron beam was blanked off or moved to the other location. With this illumination scheme, the accumulated electron dose for Region 1, 2 and 3 was 1735, 620 and 230  $e^-/\text{\AA}^2$ , respectively. After 30 min at 1 mbar  $H_2$  at 280 °C the sample was cooled to room temperature and the microscope was evacuated to its base vacuum ( $1.9 \cdot 10^{-6}$  mbar). Under those conditions, TEM images were acquired of Region 1-3 as well as reference areas on the two samples at 5  $e^-/(\text{\AA}^2s)$ , which did not lead to any detectable changes to the sample.

### Image analysis

The time-resolved TEM image series provide information about the time for the first visual appearance of the copper particles and about the subsequent evolution of the copper particle size. For the different experiments, this information is evaluated by selecting 20 or 25 visually distinguishable particles in the last image of a time-series of images. The individual particles were tracked backwards in time in the earlier acquired images until the image of their first visual appearance. This tracking was possible because all of the particles remained immobile. In each image, the particle diameter (referred to as size) is determined by measuring the projected area manually with ImageJ and assuming a spherical particle shape. Particle size distributions (PSDs) were obtained to compare the size of the copper particles after the different experiments. PSDs can appear visually distinct while others can appear similar. To provide a quantitative assessment of the similarity of PSDs that considers the statistical significance of the limited number of particles in the distributions, the ANOVA method was used to determine the probability that two different PSDs had the same mean particle size.<sup>11</sup> With this method, the PSDs were considered significantly different, if the probability was lower than 2.5% ( $p_{(\text{same mean size})} < 0.025$ ). To evaluate the progress of the particle formation, the size evolution of the particles should be combined with the evolution of the particle density. A simplistic measure, the "stage of particle evolution", quantifies the size and density evolution in a combined way by considering at each time the

average size of the same 20 or 25 copper particles, including the particle size of 0 nm for particles prior to their first appearance.

## Results & Discussion

### Copper phyllosilicate

The composition and structure of the as-prepared copper phyllosilicate was examined by several experimental techniques. X-ray diffraction shows that the as-prepared copper phyllosilicate mainly consisted of an amorphous phase (Figure 2.2A, blue), in agreement with earlier observations.<sup>8a</sup> Weak diffraction peaks reveal a minor crystalline phase corresponding to chrysocolla ( $\text{Cu}_2\text{Si}_2\text{O}_5(\text{OH})_2 \cdot n\text{H}_2\text{O}$ ), which is a form of copper phyllosilicate.<sup>8</sup> Diffraction peaks characteristic for silica or other copper species were absent. The reaction between copper and silica was furthermore confirmed by the BET surface area, which increased from 100  $\text{m}^2/\text{g}$  for colloidal silica to 550  $\text{m}^2/\text{g}$  for the as-prepared copper phyllosilicate, in agreement with a previous report.<sup>8b</sup> Moreover, TEM images as in Figure 2.2B reveal that the material consisted of platelets with a width and thickness in the range of 5 to 20 nm and a length of up to 100 nm. The anisotropic morphology was confirmed by a  $\text{N}_2$  physisorption profile that is typical for aggregates of platelets (Figure 2.2C).<sup>8b, 9</sup> The TEM images did not show any particles with a spherical morphology as the original colloidal silica spheres and therefore also indicate a complete reaction with copper. The chemical composition across the as-prepared copper phyllosilicate was addressed by EDX. Spot analysis of more than 20 regions of 100-500 nm in diameter revealed a Cu/Si atomic ratio of 0.59 with a standard deviation of 0.09, and 6 EDX line-scans of 100-500 nm in length crossing several single platelets revealed a Cu/Si ratio between 0.50 and 0.75 for all points. Thus, the copper loading was very homogeneous throughout the as-prepared copper phyllosilicate with a composition of Cu/Si that agrees with the nominal ratio of 0.66.

### Reduction of copper phyllosilicate

First, the reduction of copper phyllosilicate was addressed with TPR and TGA (Figure 2.2D). In TPR, the hydrogen consumption started at 220 °C, peaked at 255 °C and ceased above 270 °C. The amount of hydrogen consumed by this reduction was 140  $\text{cm}^3$  (STP)/g. The weight loss during the reduction up to 500 °C amounted to 15%, as determined by TGA. A minimum weight loss of 9% was expected based upon the loss of oxygen atoms acting as counter ions for the  $\text{Cu}^{2+}$ . The additional 6% is presumably due to crystal water in the copper phyllosilicate. Taking into account the weight loss during reduction, the amount of

H<sub>2</sub> consumed corresponded to the reduction of 40 wt% Cu<sup>2+</sup> to Cu<sup>0</sup>. Since the intended copper loading was ca. 41 wt%, it is concluded that copper phyllosilicate was fully reduced to metallic copper between 220 and 270 °C.<sup>7d, 9</sup> Consistently, XRD showed the presence of crystalline metallic Cu and silica after reduction at 250 °C in a plug-flow reactor with 20% H<sub>2</sub> in Ar for 2.5 hours (Figure 2.2A, red).

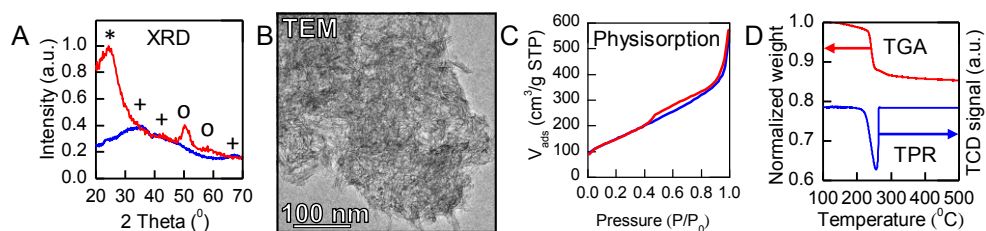


**Figure 2.2.** Characterization of the copper phyllosilicate. (A) X-ray diffractograms of the material before (blue) and after (red) reduction in the plug-flow reactor. The peak positions correspond to chrysocolla (+), silica (\*) and metallic copper (o). (B) A TEM image of the as-prepared copper phyllosilicate. (C) N<sub>2</sub> physisorption of the as-prepared copper phyllosilicate (adsorption blue, desorption red). (D) TPR (blue) and TGA (red) of copper phyllosilicate in H<sub>2</sub>/Ar flow.

Next, the reduction was examined in the electron microscope by exposing the copper phyllosilicate to 1 mbar H<sub>2</sub> at different temperatures (experiment E1). Figure 2.3 shows TEM images of four different samples acquired after reduction for 4 hours at 150 °C (A), and for 30 minutes at 200 °C (B), 250 °C (C) and 280 °C (D). That is, the TEM images show sample regions that were unexposed to the electron beam prior to and during the reduction. Therefore, the images show the results of transformations of the copper phyllosilicate that were inherent to the reduction process in the electron microscope, excluding any electron beam-induced changes. The copper phyllosilicate appeared unchanged after reduction at 150 and 200 °C, in line with TGA and TPR. After 30 minutes at 250 °C, nanoparticles were clearly visible and the average size of the nanoparticles was about 5 nm. Reducing the sample for up to 2 hours resulted in the appearance of more nanoparticles and a further growth of the nanoparticles to an average size of 8 nm (not shown in Figure 2.3). At the higher temperature of 280 °C, the nanoparticles developed with an average size of 8 nm already after half an hour of reduction (Fig 3D). Extending the reduction treatment to longer reduction times and increasing the temperature to 310 °C (75 min at 280 °C and 30 min at 310 °C) did not lead to any further changes. Thus, the copper phyllosilicate was fully reduced to Cu/SiO<sub>2</sub> within 30 minutes at 280 °C in the electron microscope. Subsequently, the reduction in the electron microscope was compared to the reduction in a plug-flow reactor. For the two instruments, Figure 2.4 shows TEM images of the copper phyllosilicate

after reduction and corresponding particle size distributions. The distributions, average particle size and standard deviation are similar (Table S2.2). Therefore, the formation of copper nanoparticles during reduction by  $H_2$  in the microscope was representative for the formation process in a standard plug-flow reactor. Moreover, the comparison demonstrates that the particle formation was insensitive to the different  $H_2$  pressure and heating rate employed in the two instruments.

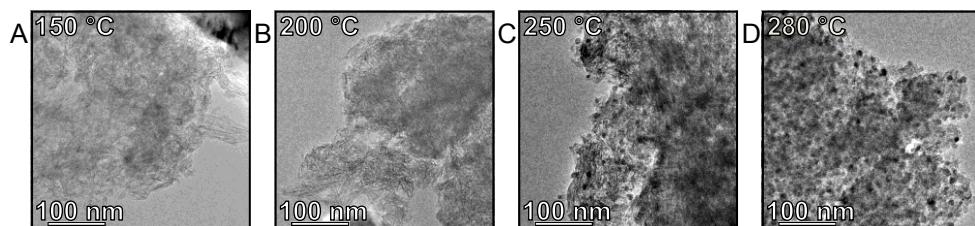


**Figure 2.3.** TEM images of copper phyllosilicate after exposure to 1 mbar  $H_2$  at different temperatures and reaction conditions in the electron microscope. Reduction conditions: (A) 150 °C, 4 hours (B) 200 °C, 30 min (C) 250 °C, 30 min and (D) 280 °C, 30 min. TEM image acquisition (A)-(B) in situ at 1 mbar  $H_2$  at 150 °C and (C)-(D) at vacuum at room temperature.

### Electron beam effects

For the in situ experiments, it is important to minimize the influence of the electron beam on the phenomena under investigation and to distinguish the thermally activated evolution of the sample from the electron beam-induced changes.<sup>5a, 12</sup> In this case, careful examination is particularly important given the ionic complex structure and constituent light elements of the copper phyllosilicate. In fact, electron beam alterations may even occur under high vacuum conditions.<sup>13</sup> It is therefore important to consider the electron beam illumination prior to as well as during the reduction treatment.

To address the impact of such pre-illumination, experiment E2 evaluates the reduction of copper phyllosilicate that was illuminated in vacuum at room temperature prior to the reduction. Specifically, five different regions were illuminated for 2 min. by electron dose-rates of 1, 5, 10, 20 and 100  $e^-/(\text{\AA}^2\text{s})$ , respectively. At these illumination conditions, the copper phyllosilicate remained visually unchanged at a dose-rate of 20  $e^-/(\text{\AA}^2\text{s})$  (Figure S2.1). The pre-illuminated sample was subsequently reduced in the microscope without electron illumination during reduction. After the reduction treatment, TEM images were acquired of reference sample regions, which had not been pre-illuminated, and of the five pre-illuminated regions. Figure 2.5 shows a TEM image representative of the reference regions,

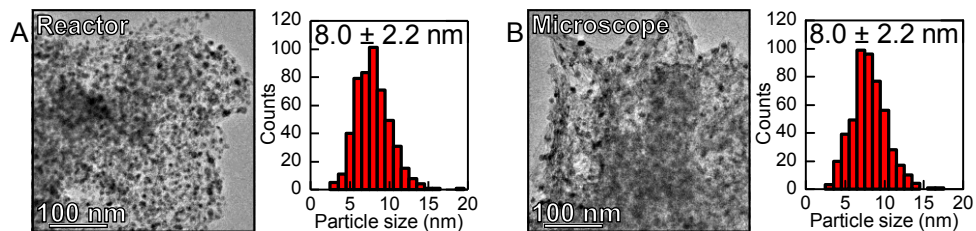


**Figure 2.4.** TEM images of copper phyllosilicate after reduction in a plug-flow reactor and in the electron microscope. (A) Copper phyllosilicate reduced in a plug-flow reactor (20% H<sub>2</sub> in Ar, 250 °C, 150 min) and re-reduced in the electron microscope (1 mbar H<sub>2</sub>, 250 °C, 45 min). The TEM image was acquired in situ at 1 mbar H<sub>2</sub> at 250 °C. The PSD is based on such TEM images of 17 different regions of the samples. (B) Copper phyllosilicate reduced in the electron microscope (1 mbar H<sub>2</sub>, 280 °C, 30 min). The TEM image was acquired in vacuum at room temperature. The PSD is based on such images of 17 different regions. Each PSD include the size of 500 copper nanoparticles and the number-averaged particle size and standard deviation of the distributions are included.

the particle size distribution (PSD) corresponding to the reference regions, and TEM images of the pre-illuminated regions with their corresponding PSDs. Compared to reference regions (Figure 2.5A), the PSDs tend to broaden toward larger sizes and the average copper nanoparticle size increases for the pre-illuminated regions (Figure 2.5B-F). Specifically, a significant number of nanoparticles larger than 14 nm formed after pre-illumination by the highest electron dose-rate of 100 e<sup>-</sup>/(Å<sup>2</sup>s) (Figure 2.5F). Even for pre-illumination with the lowest dose-rate of 1 e<sup>-</sup>/(Å<sup>2</sup>s), the PSD differs with statistical significance ( $p(\text{same mean size}) = 2.7 \cdot 10^{-5}$ , Table S2.3) from the PSD of the reference regions, even though the PSDs may appear close to identical. Thus, these experiments show that although the copper phyllosilicate remained visually unchanged after electron pre-illumination, the pre-illumination had a significant effect on the evolution of the copper particle sizes upon subsequent reduction. It is therefore important to log and control the electron illumination prior to and during reduction by H<sub>2</sub>. In the actual growth experiments, suitable sample areas were identified prior to reduction by employing a pre-illumination in 1 mbar H<sub>2</sub> at 200 °C, using a yet lower electron dose-rate of 0.05 e<sup>-</sup>/(Å<sup>2</sup>s). At this dose-rate, the image signal-to-noise ratio was just sufficient to localize regions of interest and the pre-illumination did not change the final PSD, as will be demonstrated by comparison to non-illuminated regions.

Next, the interaction of the electron beam with the combined gas-sample system is addressed in experiment E3. Specifically, different areas of copper phyllosilicate were illuminated continuously by electrons at rates of 1, 5, 10, 20 and 100 e<sup>-</sup>/(Å<sup>2</sup>s), respectively, in 1 mbar H<sub>2</sub> at 150 °C. This temperature is sufficiently low to suppress particle growth due to reduction by H<sub>2</sub> (Figure 2.3A). After 7 min of continuous illumination, TEM images reveal

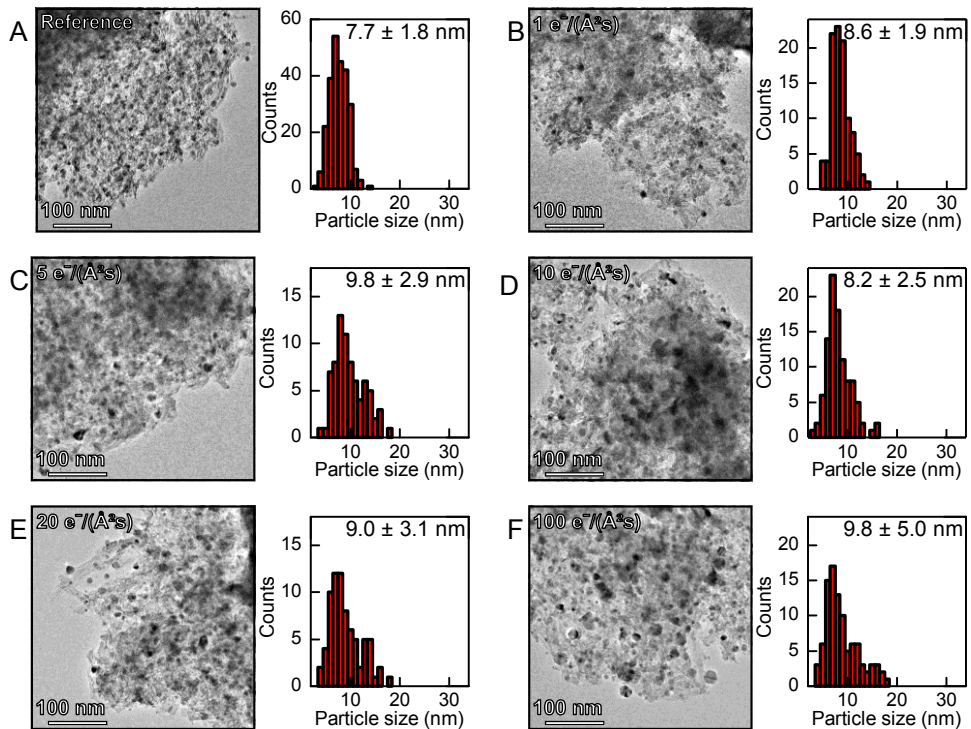


**Figure 2.5.** The effect of electron pre-illumination on the reduction of copper phyllosilicate (Experiment E2). (A) A TEM image of a reference region without pre-illumination and after reduction in 1 mbar  $\text{H}_2$  for 75 min at 280 °C and subsequently for 30 min at 310 °C. The PSD is evaluated from TEM images of 10 different reference regions (without pre-illumination and after reduction). (B-F) TEM images of copper phyllosilicate regions, which were pre-illuminated by the electron beam in base vacuum ( $2.3 \cdot 10^{-5}$  mbar) at room temperature and subsequently reduced in 1 mbar  $\text{H}_2$  for 75 min at 280 °C and 30 min at 310 °C. The pre-illumination comprised electron dose-rates of 1, 5, 10, 20 and 100  $e^-/(\text{\AA}^2\text{s})$ , respectively, for 2 min. All TEM images were acquired at base vacuum ( $2.3 \cdot 10^{-5}$  mbar) at room temperature after reduction. The pre-illuminated regions enabled acquisition of 1-3 independent TEM images, which were used to evaluate the PSD. For each PSD, its number-averaged particle size and standard deviation are included.

that particles had formed for all electron dose-rates. The particle density was significantly lower for the dose-rate of 1  $e^-/(\text{\AA}^2\text{s})$  than for higher dose-rates (Figure 2.6A-F). Extending the illumination at 1  $e^-/(\text{\AA}^2\text{s})$  up to 20 min led to an increased particle density, which by visual inspection appears to be similar to the particle density in regions illuminated for 7 min at higher dose-rates (Figure 2.6 and S2.2). Moreover, visual inspection of Figure 2.6D, F and S2.3 indicates that the particle density is significantly lower in the absence of  $\text{H}_2$  at 150 °C after similar electron illumination. The particle formation is thus not directly induced by the electron beam interaction with the sample but indirectly via the electron beam interaction with  $\text{H}_2$ , presumably via pre-dissociation of  $\text{H}_2$  to form more reactive H atoms.<sup>14</sup>

The stage of particle evolution was assessed quantitatively by simplistically convoluting the apparent particle density and the size of 20 or 25 particles over time (see Image analysis section). For regions illuminated at  $5 \text{ e}^-/(\text{\AA}^2\text{s})$  or higher, the majority of particles nucleated and grew larger than 5 nm within the first 10 minutes of reduction. Figure 2.6G shows that the stage of particle evolution developed similarly for these regions independent of applied electron dose-rate. In contrast, at an electron dose-rate of  $1 \text{ e}^-/(\text{\AA}^2\text{s})$ , the particle evolution was significantly slower and 15 minutes passed before the majority of nanoparticles had nucleated and grown larger than 5 nm. Thus, lowering the electron dose-rate and illumination time as much as possible is crucial to minimize the contribution from electron-induced reduction by  $\text{H}_2$ . In the present beam-insensitive experiments an electron dose-rate of  $1 \text{ e}^-/(\text{\AA}^2\text{s})$  was used and illumination times were limited to ensure that the formation of particles was dominated by the thermal reduction by  $\text{H}_2$ . This was demonstrated by comparing the particle formation in one region continuously illuminated to the formation in several regions illuminated intermittently during the reduction process.

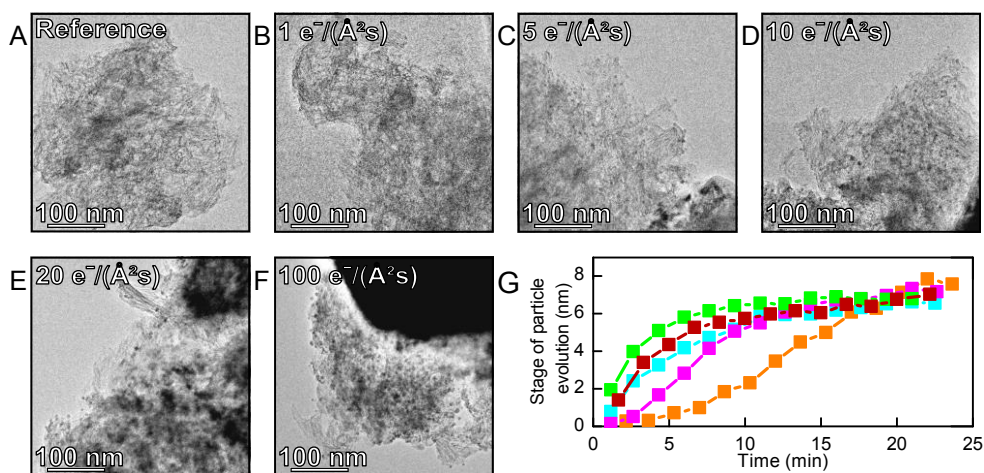


**Figure 2.6.** Formation of copper nanoparticles by reduction in 1 mbar  $\text{H}_2$  at  $150 \text{ }^\circ\text{C}$  under different electron illumination conditions. (A) TEM image of a reference area after 250 min in 1 mbar  $\text{H}_2$  at  $150 \text{ }^\circ\text{C}$ . (B-F) TEM images of the five different regions after 7 minutes of electron illumination at 1, 5, 10, 20 and  $100 \text{ e}^-/(\text{\AA}^2\text{s})$ , respectively. (G) The stage of particle evolution of 20 or 25 particles plotted as a function of time for regions exposed to electron dose-rates of 1 (orange), 5 (blue), 10 (pink), 20 (green) and  $100 \text{ e}^-/(\text{\AA}^2\text{s})$  (red).

### Monitoring nanoparticle formation by TEM

Guided by the investigation of the temperature and the electron beam-induced changes, the measurement scheme in Figure 2.1 was followed in monitoring the formation of copper

nanoparticles. This scheme excludes electron illumination of the sample in the microscope's base vacuum prior to the reduction process, uses a low electron dose-rate, limits the total illumination time by conducting reduction at 280 °C which increases the reaction rate, and acquires time-lapsed TEM image series at different intervals to fragmentize the effect of the accumulated electron dose. Two separate experiments were conducted to monitor the formation of copper nanoparticles in three distinct regions. In the first experiment, Region 1 was continuously illuminated during reduction. In the second experiment, Region 2 and Region 3 were intermittently illuminated with different time intervals (~2 and ~6 minutes) to address the effect of electron dose accumulation on the growth of copper nanoparticles. At the timed instants (Figure 2.1), TEM images were recorded enabling time-lapsed image series of the three regions during the reduction process. When such image series are played back as a movie, a vivid impression of the growth scenario is obtained. The movie of Region

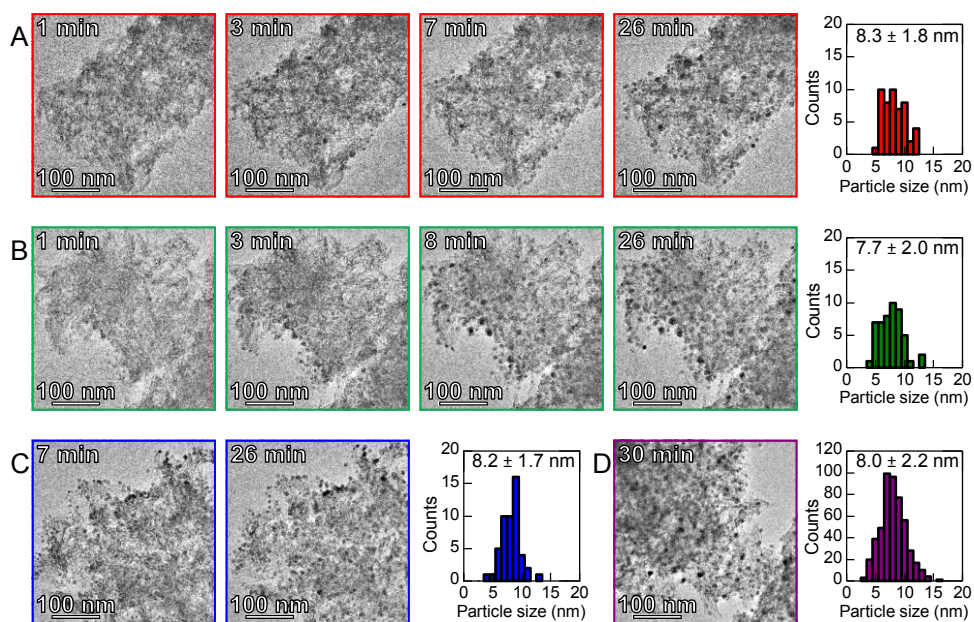


**Figure 2.7.** Time-resolved TEM images of copper phyllosilicate during exposure to 1 mbar H<sub>2</sub> at 280 °C. (A) Region 1 observed by continuous electron illumination at an electron dose-rate of  $1 \text{ e}^-/(\text{\AA}^2\text{s})$  (Supporting movie S2.1), and the corresponding PSD after reduction. (B) Region 2 observed with intermittent electron illumination at ca. 2 min intervals at an electron dose-rate of  $1 \text{ e}^-/(\text{\AA}^2\text{s})$  and the corresponding PSD after reduction. (C) Region 3 observed with intermittent electron illumination at ca. 6 min intervals at an electron dose-rate of  $1 \text{ e}^-/(\text{\AA}^2\text{s})$  and the corresponding PSD after reduction. (D) A TEM image of a reference region imaged after reduction and the PSD corresponding to 17 reference regions imaged after reduction. The PSDs include the number-averaged particle size and corresponding standard deviation.

1 is provided as supporting information (Movie S2.1). Figure 2.7 shows selected TEM images from the time-lapsed series of all three regions. After the reduction treatment, the sample was cooled to room temperature and the electron microscope evacuated to reestablish a base vacuum of  $1.9 \cdot 10^{-6}$  mbar. Under these conditions, TEM images were acquired of the three regions and of reference regions, which had not previously been illuminated by the electron beam.

The TEM images in Figure 2.7 reveal that the first appearance of copper nanoparticles occurred within the first few minutes at the reduction conditions. Due to the finite image SNR and resolution, it is possible that the particles had nucleated at earlier times and subsequently had grown beyond the size of 3 nm which is detectable in the TEM images. That is, the particle size at the first observation by TEM is likely larger than the critical size associated with the copper nanoparticle formation. Once formed, the nanoparticles remained immobile. This finding suggests that the continued growth (Figure 2.7) cannot be a result of particle migration and coalescence under the present conditions.<sup>15</sup> Instead, the observations suggest that the nanoparticles grew by the attachment of smaller copper species, which are formed during the reduction treatment and which are sufficiently mobile to reach a nanoparticle. As the copper nanoparticles appear to have formed homogeneously across the precursor material, this mobility was probably limited to diffusion distances on the order of the final spacing between the nanoparticles, which is roughly 10 nm. Moreover, a close-up inspection of particles near the precursor agglomerate edge did not indicate any marked preference for specific nucleation sites.<sup>7e</sup> Thus, these observations suggest that the copper nanoparticles tended to nucleate homogeneously and grew by attachment of copper species from their vicinity.

To develop a kinetic description of these dynamic observations, the role of the actual electron illumination, which is shown in Figure 2.1, is addressed. This assessment is done by comparison of the particle evolution and final PSD of the three regions (Region 1, 2 and 3) to each other and by comparison of the final PSDs of the three regions to the PSD of reference regions (Figure 2.7). The PSDs of the three regions (Region 1, 2 and 3) were visually similar and their deviations were within the statistical error ( $p_{(\text{same mean size})} > 0.025$ , Table S2.4). Thus the accumulated electron dose used in the present experiment did not affect the final nanoparticle size. The PSDs of the three regions (Region 1, 2 and 3) were also visually and statistically similar to the reference regions, (Figure 2.7D) indicating that the applied pre-illumination scheme and dose-rate were also of inferior importance for the final nanoparticle size. Moreover, the stage of particle evolution was evaluated by tracking 25 visually distinguishable particles per region. Figure 2.8 shows the stage of particle evolution as a function of time for the three regions. Since only particles that were clearly visible throughout the experiment were measured, this analysis was biased towards larger

particles resulting in a final average particle size close to 10 nm, instead of 8 nm (Figure 2.7). The progress of particle formation for the three regions (Region 1, 2 and 3) was close to identical, despite the different electron doses. Specifically, region 3 was imaged for the first time after 7 min at 1 mbar H<sub>2</sub> and 280 °C and the particle formation had progressed to the same extent as for Region 1, which had been continuously illuminated. This indicates that the electron illumination during reduction did not have a measurable influence on the evolution of the sample.

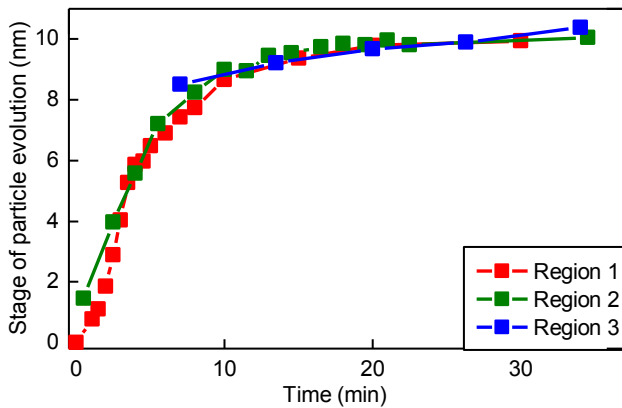


**Figure 2.8.** The stage of copper particle evolution versus time for reduction of copper phyllosilicate in 1 mbar H<sub>2</sub> at 280 °C. The stage of particle evolution is obtained from the time-resolved TEM images of Region 1-3 (Figure 2.7).

Quantitative information for the kinetic models is obtained from measuring the sizes of the 25 individual particles in region 1 at different stages of the reduction, as shown in Figure 2.9 (black dots, see Figure S2.5 for corresponding particles). At the time for first appearance, all particles were larger than 3.4 nm. Most particles were detected after 2 to 6 minutes and all particles had appeared within 15 minutes. After its appearance, a particle grew initially fast and later slower until it had reached its final size within the following 10 minutes.

### Kinetic models for the nanoparticle formation

The TEM observations made in situ of nanoparticle formation provide information about the time for the first observation of a nanoparticle and about its subsequent growth. This dynamic information is hereafter compared with two kinetic models that are consistent with the observed dynamic behavior of the nanoparticles. For both models, it is assumed that the reduction process starts as the temperature reached 280 °C, because particle formation did not occur below 250 °C in the experiments and because the heating rate is

fast (30 °C/min) (Figure 2.3). Furthermore, variations in temperature over time or over different locations are considered negligible because the particle size evolved similarly in different areas (Figure 2.7, 2.8).

### **Nucleation-and-growth model**

The first model considers the reduction of the phyllosilicate as a first order and irreversible reaction that feeds reduced mobile copper species to a reservoir, which leads to a classical nucleation-and-growth scenario (e.g. DeBenedetti,<sup>16</sup> LaMer and Dinegar,<sup>17</sup> see Supporting Information). That is, as the concentration of reduced species exceeds the saturation concentration, copper nuclei larger than a critical size are formed and subsequently grow by addition of diffusing reduced species. The concentration of these mobile reduced species is assumed to be uniform throughout the system, except for a diffusive boundary layer surrounding each particle (mean field approximation). As nucleation in this model is a statistical event, the model is consistent with a homogeneous distribution of nanoparticles. In the model, the size evolution of all particles was fitted with only two adjustable parameters, namely the kinetic constant of the reduction and the diffusion coefficient of the reduced species (see Supporting Information). The best fit of the model to the data in Figure 2.9 was obtained with a kinetic constant of  $0.64 \text{ min}^{-1}$  and a diffusion coefficient of  $\sim 5 \cdot 10^{-19} \text{ m}^2/\text{s}$ . With these parameters the model accounts reasonably for the observed nucleation times as well as for the growth of the nanoparticle size (See Figure 2.9, green lines and Figure S2.7).

However, the model has some implications that are physically improbable. Because nucleation does not occur until after a few minutes in the reduction treatment, a large fraction of the copper atoms must be present as mobile reduced copper species in the early phase (Figure S2.6). The peak amount of mobile reduced copper species exceeds 20% of all copper present, corresponding to a surface concentration of  $\sim 15 \text{ Cu atoms/nm}^2$  or about 100% of a monolayer. Such a high surface concentration is physically unrealistic. Another inconsistency of the model results from the mean-field approximation, which imposes that the chemical environment of all nanoparticles is the same at any given time. As a consequence the final size of the particles should depend only on the nucleation time, which is contradicted by the data since it exhibits a considerable scatter in the relation between nucleation time and final particle size (Figure 2.10). At last, it is expected that the reduction rate is sensitive to the  $\text{H}_2$  pressure while the diffusion of reduced copper species is not. Since in the nucleation-and-growth model the ratio between the reduction rate and the diffusion coefficient determines the final particle size and density, the model predicts a higher particle density and smaller particle sizes at higher  $\text{H}_2$  pressures. However, this prediction resulting from the nucleation-and-growth model is inconsistent with the

experimental observation that the final particle size is insensitive to the H<sub>2</sub> pressure at 1 mbar and 200 mbar.

**Nucleation-and-growth**

**Autocatalytic reduction: Diffusion-limited**

**Autocatalytic reduction: Reaction-limited**

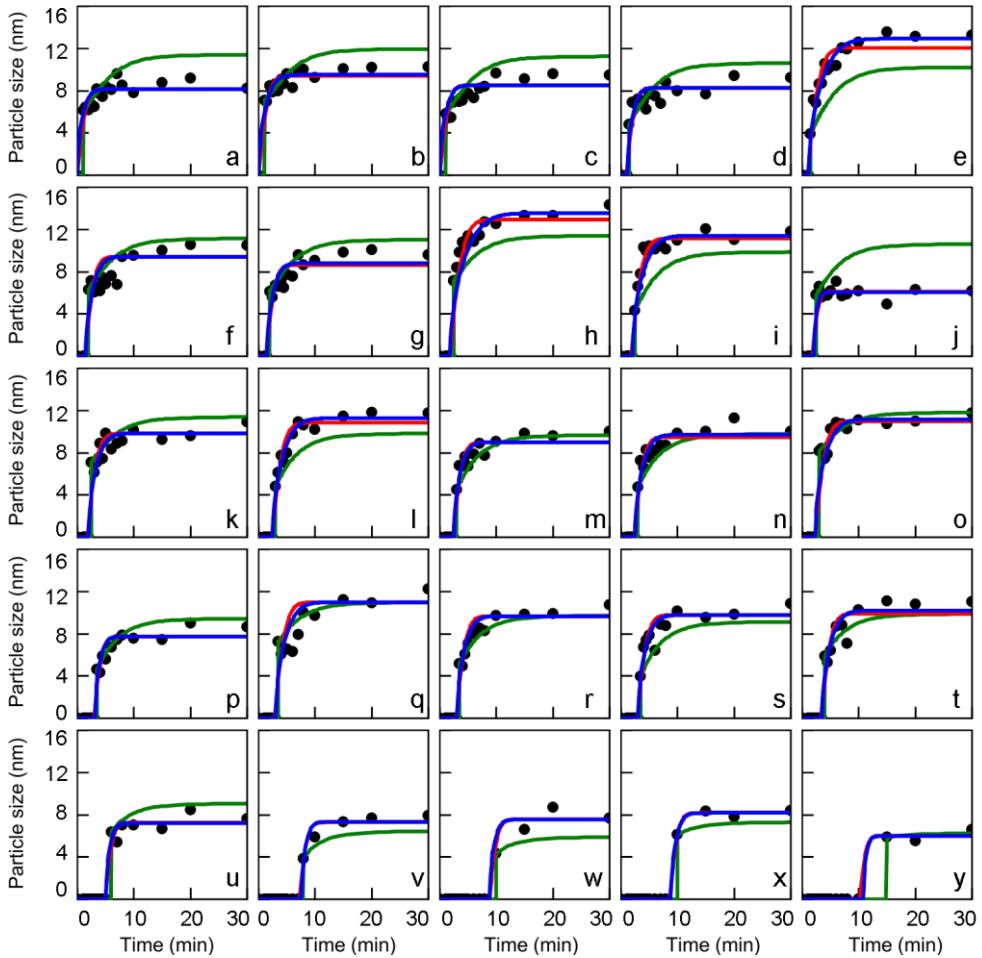


**Figure 2.9.** Size evolutions of the 25 copper particles selected in Region 1. The measured particle size is shown as black dots, the fitted nucleation-and-growth model is shown in green and the fitted autocatalytic model is shown in red (reaction-limited) and in blue (diffusion-limited).

### Autocatalytic model

In the light of the high and homogeneous particle density (Figure 2.7) and the inability of the mean field approximation proved unable to explain the scatter in the relation between nucleation time and final particle size, it seems inconsistent that a nanoparticle is able to grow from mobile species originating from a distance far away. Rather, a nanoparticle captures species from a limited spatial zone in its vicinity (< few (tens) of nanometer). Therefore the second model includes the additional assumption that the copper phyllosilicate is made up of regions, referred to as boxes, which do not exchange copper species. The structural characterization of the copper phyllosilicate shows that the material consists of agglomerations of platelets in the range of 5 - 20 nm in width and thickness and up to 100 nm in length (Figure 2.2). Logically, diffusion of copper species within a platelet is easier than from one platelet to another. It is thus probable that the copper particles effectively only grow from the copper phyllosilicate present in a certain volume. The final size of a particle is therefore related to the size of its surrounding copper phyllosilicate box. For example, an 8 nm copper particle would contain as many copper atoms as a copper phyllosilicate cubic box of size 17 nm. Depending on the exact dimensions of a copper phyllosilicate platelet this means that the phase transformation resulted into one or a few copper particles per platelet, which is also observed experimentally.<sup>7e</sup>

Since the appearance of particles seemed to be randomly occurring throughout the agglomerate and specific nucleation sites seemed to be absent, homogeneous nucleation was considered. In that light, every copper ion in a box is assumed to have a given probability of being reduced per unit of time resulting in a particle nucleus. As shown in the Supporting Information, such a nucleation phenomenon is governed by Poisson statistics. As a consequence, the probability of early nucleation is higher in larger boxes corresponding to larger final particle sizes, which is in qualitative agreement with Figure 2.9. The reduction probability obtained from a maximum-likelihood analysis of the data is  $5.42 \cdot 10^{-6} \text{ min}^{-1} \text{ ion}^{-1}$  (see supporting information). Based on that value, and using the final particle size to estimate the corresponding box volume, the overall nucleation probabilities were calculated as a function of time and they are shown in Figure 2.10. Most of the particles have a probability between 0.1 and 0.9 of having nucleated at the observed time. It has to be stressed that the Poisson model captures both the relation between the final size and the nucleation time, and the scatter in the data resulting from the inherently statistical nature of the process. The model assumes that only one particle nucleates in each box and that no secondary nucleation takes place. However, for large boxes corresponding to final particle sizes of about 13 nm, secondary nucleation should occur with a probability as large as 90% (see Supporting Information). Secondary nuclei are therefore assumed to coalesce with the primary particle. Although no mobility of particles larger than 3.4 nm was observed,

diffusion and coalescence of much smaller particles consisting of one or a few copper atoms can be expected to be fast.<sup>15</sup>

It is particularly interesting to observe that the statistical reduction rate of each ion before nucleation ( $5.42 \times 10^{-6} \text{ min}^{-1}$ ) is orders of magnitude lower than the overall reduction rate, which is of the order of  $0.64 \text{ min}^{-1}$  according to the kinetic constant of the nucleation-and-growth model. This difference suggests that an autocatalytic process may be at play, by which the reduction is catalyzed by the newly formed copper particles. Autocatalytic reduction is often observed in the synthesis of supported metal catalysts<sup>2, 18</sup> and it has been shown that the reduction of CuO is autocatalytic.<sup>19</sup>

To model the growth of the nucleated particles, it is therefore assumed that the autocatalytic process starts as soon as a particle nucleus has been formed. In principle, particle growth during autocatalytic reduction could be either diffusion-limited or reaction-limited.<sup>20</sup> Both limiting cases were therefore considered in models fitted to the data. In the reaction-limited model (Red lines in Figure 2.9, autocatalytic model<sub>reaction-limited</sub>) the reduction and hence growth of the particles is assumed to be catalyzed by the copper surface and therefore proportional to the average  $\text{Cu}^{2+}$  concentration in the box.<sup>18</sup> The best fit of the model was obtained with a kinetic constant of  $\sim 0.45 \text{ nm/min}$ , which corresponds to about 2 atomic layers per min. In the diffusion-limited model (Blue lines in Figure 2.9, autocatalytic model<sub>diffusion-limited</sub>) the reduction rate is high and all of the copper ions are

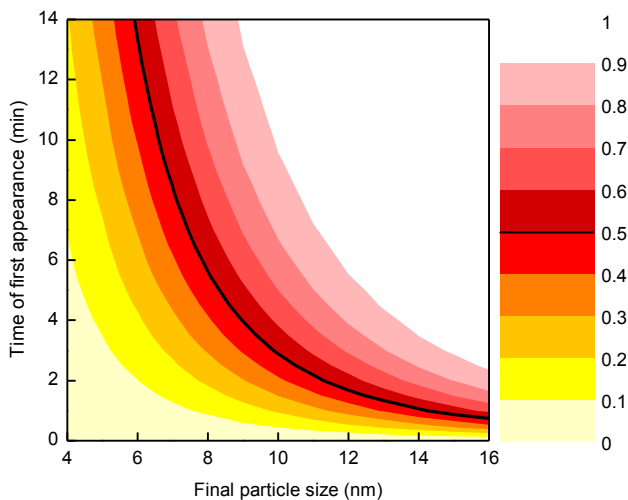


**Figure 2.10.** Observed time of first appearance of a particle against the observed final particle size (black dots). The colored regions indicate the cumulative probability according to Poisson statistics for nucleation to occur at a specific time for a given box size. Box sizes are expressed as the corresponding final particle sizes to aid the comparison with the observed experimental data.

considered to have the same mobility. The diffusion coefficient derived from fitting the model to the experimental data is  $4.5 * 10^{-19} \text{ m}^2/\text{s}$ , which is typical for solid state diffusion.<sup>21</sup> Extrapolated to 280 °C, coefficients around  $1 * 10^{-16} \text{ m}^2/\text{s}$  have been found for the diffusion of  $\text{Cu}^+$  ions in sodium enriched silica.<sup>22</sup> Gonella et al. have reported that the diffusion of  $\text{Cu}^{2+}$  is about two orders of magnitude slower than that of  $\text{Cu}^+$ .<sup>23</sup>

The experimental results are well described by both the diffusion-limited and the reaction-limited model and do not allow to distinguish between the two. In conclusion, the autocatalytic model seems to slightly better describe all of the observations in Figure 2.7 compared to the nucleation-and-growth model. Therefore the autocatalytic model seems to be a more attractive model for describing the reduction mechanism. It is plausible that initial particle growth is reaction-limited since the surrounding area is not yet depleted of copper. Analogous to this, the final stage of particle growth is more likely to be diffusion-limited since at that time the surrounding area is depleted of copper. Thus, a combination of the two limiting autocatalytic models could be possible for describing the observations.

## Conclusion

In situ TEM was used to follow the phase transformation of copper phyllosilicate to silica-supported copper particles during reduction with 1 mbar  $\text{H}_2$  at 280 °C. Similar particle size distributions after reduction in the TEM and in a plug-flow reactor were obtained, validating that the phase transformation inside the microscope was representative for the phase transformation in a plug-flow reactor. Based on an assessment of the electron beam illumination prior to and during reduction, a procedure was developed for time-resolved imaging of the dynamical changes of the copper phyllosilicate that are inherent to the reduction process. After an induction time of a few minutes, particles with a size larger than 3.4 nm were detected throughout the sample and grew in about 10 minutes to their final size of about 8 nm. Particle mobility was not observed indicating that growth of particles larger than 3.4 nm occurred via the diffusion of mobile copper species (likely  $\text{Cu}^{2+}$  ions) and their attachment to the copper particles. The size evolution of the particles was measured and was well described by a two-step reduction mechanism with either diffusion-limited or reaction-limited particle growth. It is concluded that reduction of copper phyllosilicate in  $\text{H}_2$  to silica supported copper particles is autocatalytic and occurs via the diffusion of copper species over a limited distance of a few (tens) of nanometers to the copper particles. Thus, with careful optimization of the imaging strategy, time-resolved TEM provided unique mechanistic and kinetic information about the nucleation and growth of nanoparticles that is representative for large scale nanomaterial synthesis.

## Supporting Movie

Movie S2.1 can be found in the online version of the article: van den Berg, R.; Elkjær, C. F.; Gommès, C. J.; Chorkendorff, I.; Sehested, J.; de Jongh, P. E.; de Jong, K. P.; Helveg, S. *J. Am. Chem. Soc.*, **2016**, *138*, 3433-3442

## Acknowledgments

The project was supported financially by Haldor Topsøe A/S. The authors also acknowledge Haldor Topsøe A/S for access to its in situ TEM facility. CJG is a research associate at the Funds for Scientific Research (F.R.S.-FNRS, Belgium). KPdj acknowledges the European Research Council, EU FP7 ERC Advanced Grant no. 338846. PEJ acknowledges The Netherlands Organization for Scientific Research NWO-Vici program. CFE and IC gratefully acknowledge The Danish National Research Foundation's Center for Individual Nanoparticle Functionality, supported by the Danish National Research Foundation (DNRF54).

## References

- (1) (a) Schüth, F.; Hesse, M.; Unger, K. K. *Precipitation and coprecipitation*. In *Handbook of Heterogeneous Catalysis*, Ertl, G.; Knözinger, H.; Schüth, F.; Weitkamp, J., Eds. Wiley-VCH Verlag GmbH & Co. KGaA: Weinheim, 2008; (b) Behrens, M. *Catal. Today* **2015**, *246*, 46-54; (c) de Jong, K. P.; (Ed.). *Synthesis of solid catalysts*. Wiley-VCH: Weinheim, **2009**; (d) Yin, Y.; Alivisatos, A. P. *Nature* **2005**, *437*, 664-670; (e) Peng, Z.; Kisielowski, C.; Bell, A. T. *Chem. Commun.* **2012**, *48*, 1854-1856.
- (2) Mondloch, J. E.; Bayram, E.; Finke, R. G. *J. Mol. Catal. A: Chem.* **2012**, *355*, 1-38.
- (3) (a) Gontard, L. C.; Chang, L. Y.; Hetherington, C. J.; Kirkland, A. I.; Ozkaya, D.; Dunin-Borkowski, R. E. *Angew. Chem. Int. Ed.* **2007**, *46*, 3683-3685; (b) Zhu, Y.; Ramasse, Q. M.; Brorson, M.; Moses, P. G.; Hansen, L. P.; Kisielowski, C. F.; Helveg, S. *Angew. Chem. Int. Ed.* **2014**, *53*, 10723-10727.
- (4) (a) Boyes, E. D.; Gai, P. L. *Ultramicroscopy* **1997**, *67*, 219-232; (b) Sharma, R.; Crozier, P. A. Environmental transmission electron microscopy in nanotechnology. In *Handbook of microscopy for nanotechnology*, Yao, N.; Wang, Z. L., Eds. Kluwer Academic Publishers: New York, 2005; pp 531-565; (c) Hansen, P. L.; Helveg, S.; Datye, A. K. *Adv. Catal.* **2006**, *50*, 77-95; (d) Creemer, J. F.; Helveg, S.; Hoveling, G. H.; Ullmann, S.; Molenbroek, A. M.; Sarro, P. M.; Zandbergen, H. W. *Ultramicroscopy* **2008**, *108*, 993-8; (e) de Jonge, N.; Ross, F. M. *Nature Nanotech.* **2011**, *6*, 695-704.
- (5) (a) Woehl, T. J.; Evans, J. E.; Arslan, I.; Ristenpart, W. D.; Browning, N. D. *ACS nano* **2012**, *6*, 8599-8610; (b) Liao, H. G.; Zheng, H. *J. Am. Chem. Soc.* **2013**, *135*, 5038-5043; (c) Williamson, M. J.; Tromp, R. M.; Vereecken, P. M.; Hull, R.; Ross, F. M. *Nat. Mater.* **2013**, *2*, 532-536.
- (6) (a) Banerjee, R.; Crozier, P. A. *J. Phys. Chem. C* **2012**, *116*, 11486-11495; (b) Li, P.; Liu, J.; Nag, N.; Crozier, P. *Appl. Catal., A* **2006**, *307*, 212-221; (c) Li, P.; Liu, J.; Nag, N.; Crozier, P. A. *Surf. Sci.* **2006**, *600*, 693-702; (d) Hayden, T. F.; Dumesic, J. A.; Sherwood, R. D.; Baker, R. T. K. *J. Catal.* **1987**, *105*, 299-318; (e) Li, P.; Liu, J.; Nag, N.; Crozier, P. A. *J. Catal.* **2009**, *262*, 73-82; (f) Hansen, L. P.; Johnson, E.; Brorson, M.; Helveg, S. *J. Phys. Chem. C* **2014**, *118*, 22768-22773; (g) Li, P.; Liu, J.; Nag, N.; Crozier, P. A. *J. Phys. Chem. B* **2005**, *109*, 13883-13890.
- (7) (a) Zhu, S.; Gao, X.; Zhu, Y.; Fan, W.; Wang, J.; Li, Y. *Catal. Sci. Technol.* **2015**, *5*, 1169-1180; (b) Simonov, M. N.; Zaikin, P. A.; Simakova, I. L. *Appl. Catal., B* **2012**, *119-120*, 340-347; (c) Gong, J.; Yue, H.; Zhao, Y.; Zhao, S.; Zhao, L.; Lv, J.; Wang, S.; Ma, X. *J. Am. Chem. Soc.* **2012**, *134*, 13922-13925; (d) Chen, L.; Guo, P.; Qiao, M.; Yan, S.; Li, H.;

- Shen, W.; Xu, H.; Fan, K. *J. Catal.* **2008**, *257*, 172-180; (e) van den Berg, R.; Zečević, J.; Sehested, J.; Helveg, S.; de Jongh, P. E.; de Jong, K. P. *Catal. Today* **2015**, doi:10.1016/j.cattod.2015.08.052; (f) Behrens, M.; Studt, F.; Kasatkin, I.; Kühl, S.; Hävecker, M.; Abild-Pedersen, F.; Zander, S.; Girgsdies, F.; Kurr, P.; Kniep, B. L.; Tovar, M.; Fischer, R. W.; Nørskov, J. K.; Schlögl, R. *Science* **2012**, *336*, 893-897; (g) Hansen, J. B.; Højlund Nielsen, P. E. Methanol Synthesis. In *Handbook of Heterogeneous Catalysis*, Ertl, G.; Knözinger, H.; Schüth, F.; Weltkamp, J., Eds. Wiley-VCH: 2008; pp 2920-2949.
- (8) (a) Toupance, T.; Kermarec, M.; Lambert, J.-F.; Louis, C. *J. Phys. Chem. B* **2002**, *106*, 2277-2286; (b) van der Grift, C. J. G.; Elberse, P. A.; Mulder, A.; Geus, J. W. *Appl. Catal.* **1990**, *59*, 275-289.
- (9) Huang, Z.; Cui, F.; Xue, J.; Zuo, J.; Chen, J.; Xia, C. *J. Phys. Chem. C* **2010**, *114*, 16104-16113.
- (10) Jinschek, J. R.; Helveg, S. *Micron* **2012**, *43*, 1156-1168.
- (11) ANOVA analysis performed using Analysis ToolPak in Excel 2010.
- (12) (a) Egerton, R. F. *Ultramicroscopy* **2013**, *127*, 100-108; (b) Kuwauchi, Y.; Yoshida, H.; Akita, T.; Haruta, M.; Takeda, S. *Angew. Chem. Int. Ed.* **2012**, *51*, 7729-7733; (c) Holve, C.; Elkjær, C. F.; Nierhoff, A.; Sehested, J.; Chorkendorff, I.; Helveg, S.; Nielsen, J. H. *J. Phys. Chem. C* **2015**, *119*, 2804-2812.
- (13) Kisielowski, C.; Wang, L.-W.; Specht, P.; Calderon, H. A.; Barton, B.; Jiang, B.; Kang, J. H.; Cieslinski, R. *Phys. Rev. B* **2013**, *88*, 024305.
- (14) Helveg, S.; Lauritsen, J. V.; Lægsgaard, E.; Stensgaard, I.; Nørskov, J. K.; Clausen, B. S.; Topsøe, H.; Besenbacher, F. *Phys. Rev. Lett.* **2000**, *84*, 951-954.
- (15) Wynblatt, P.; Gjostein, N. A. *Prog. Solid State Chem.* **1976**, *9*, 21-58.
- (16) Debenedetti, P. G. *Metastable liquids: concepts and principles*. Princeton University Press: New Jersey, 1996.
- (17) LaMer, V. K.; Dinegar, R. H. *J. Am. Chem. Soc.* **1950**, *72*, 4847-4854.
- (18) Watzky, M. A.; Finke, R. G. *J. Am. Chem. Soc.* **1997**, *119*, 10382-10400.
- (19) (a) Tiernan, M. J.; Barnes, P. A.; Parkes, G. M. *J. Phys. Chem. B* **1999**, *103*, 338-345; (b) Pease, R. N.; Taylor, H. S. *J. Am. Chem. Soc.* **1921**, *43*, 2179-2188.
- (20) Aiken, J. D.; Finke, R. G. *J. Am. Chem. Soc.* **1998**, *120*, 9545-9554.
- (21) Heitjans, P.; Kärger, J. *Diffusion in condensed matter*. Springer-Verlag: Berlin-Heidelberg, 2005.
- (22) Kaufmann, J.; Rüssel, C. *J. Non-Cryst. Solids* **2010**, *356*, 1158-1162.
- (23) Gonella, F.; Quaranta, A.; Padovani, S.; Sada, C.; D'Acapito, F.; Maurizio, C.; Battaglin, G.; Cattaruzza, E. *Appl. Phys. A* **2004**, *81*, 1065-1071.

## Supporting Information

### Supplementary experimental results

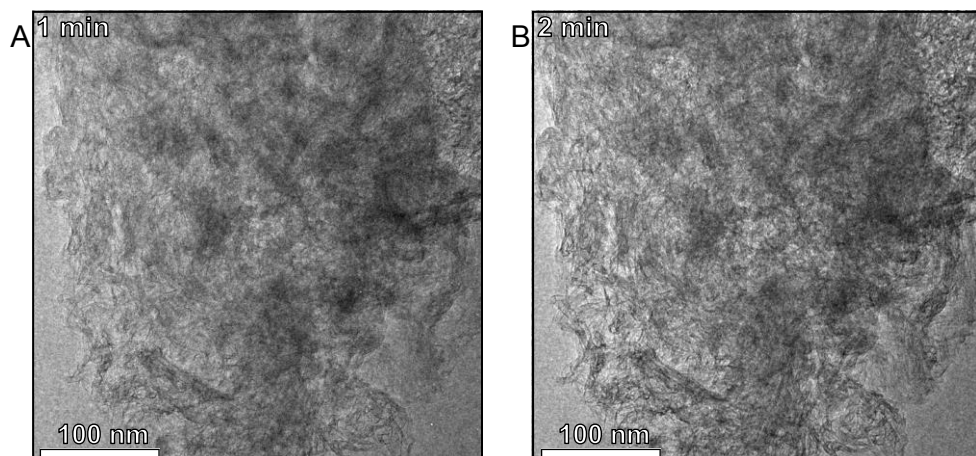


**Figure S2.1.** Effect of the electron beam on the copper phyllosilicate at room temperature at vacuum ( $7.5 \cdot 10^{-7}$  mbar): TEM images of copper phyllosilicate acquired after electron illumination at  $20 \text{ e}^-/(\text{\AA}^2\text{s})$  for 1 min (A) and for 2 min. The images reveal no visible changes of the copper phyllosilicate for electron illumination for 2 min at  $20 \text{ e}^-/(\text{\AA}^2\text{s})$ .

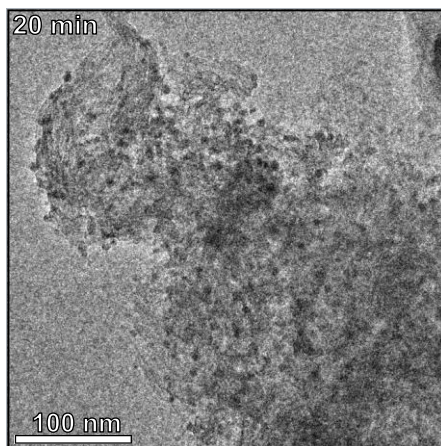


**Figure S2.2.** Effect of the electron beam during reduction: TEM image of copper phyllosilicate during exposure to 1 mbar  $\text{H}_2$  at  $150 \text{ }^\circ\text{C}$  after electron illumination for 20 minutes at  $1 \text{ e}^-/(\text{\AA}^2\text{s})$ . The image reveals a large number of particles.

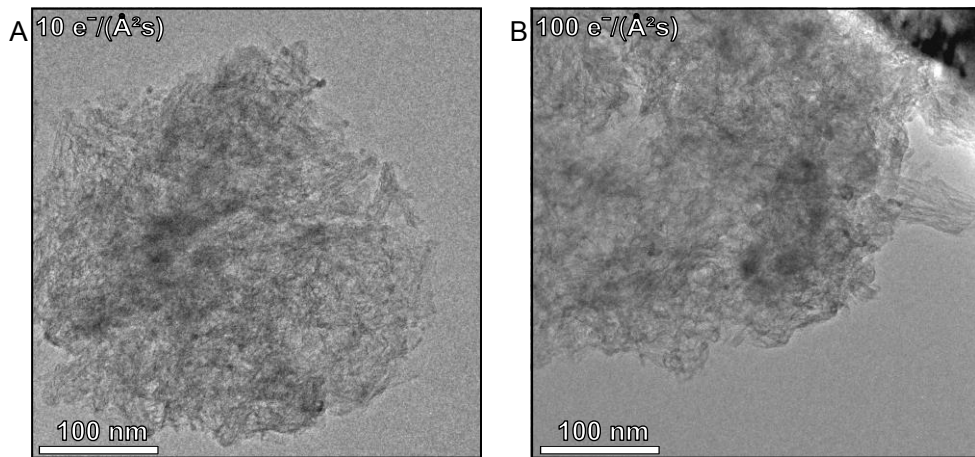


**Figure S2.3.** Effect of the electron beam and H<sub>2</sub> gas: TEM images of copper phyllosilicate acquired with the sample in vacuum ( $1.4 \cdot 10^{-6}$  mbar) at 150 °C, after electron illumination for 20 minutes at either 10 e<sup>-</sup>/(Å<sup>2</sup>s) (A) or 100 e<sup>-</sup>/(Å<sup>2</sup>s) (B). The TEM images reveal a density of particles that is lower compared to the sample similarly illuminated in the presence of H<sub>2</sub> (Figure 2.6).

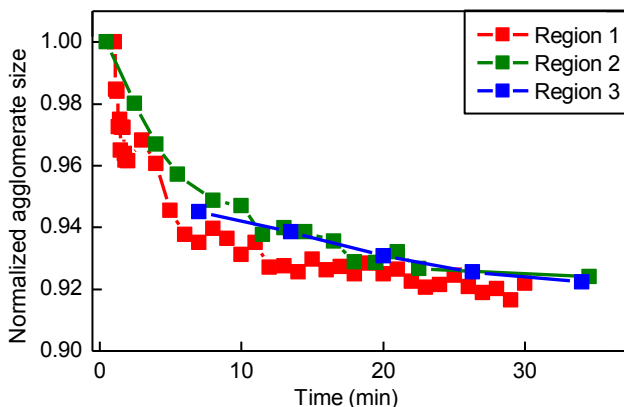


**Figure S2.4.** Evolution of agglomerate size during reduction (Figure 2.7). The size of the agglomerates corresponding to Region 1 (red), Region 2 (green), Region 3 (blue) in Figure 2.7. Agglomerate sizes were measured, using ImageJ, as the distance from one side of the agglomerate to the other side and normalized to the initial size. For Region 3, TEM commenced after 7 minutes of reduction and the normalized size is arbitrarily chosen as 0.945 for comparison with Region 1 and 2. The total decrease in agglomerate size of Regions 1 and 2 is about 8%, similar to the shrinkage observed for reference locations that were illuminated prior to reduction with an electron dose rate of  $20 \text{ e}^-/(\text{\AA}^2\text{s})$  for ca. 2 min and that were not illuminated during reduction. Moreover, TGA showed a weight loss of 15% upon reduction and  $\text{N}_2$ -physisorption showed a decrease in pore volume of 29%. As a result, the total volume loss during reduction is about 35% (see Table S2.1), corresponding to a linear agglomerate shrinkage of about 13%. Figure S2.4 indicates an inverse relationship between agglomerate size and particle evolution (Figure 2.8).

**Table S2.1.** Total volume before and after reduction for an agglomerate with an initial weight of 1 g.

Agglomerate before reduction	Agglomerate after reduction
1 g	0.85 g
$0.22 \text{ cm}^3$ material volume <sup>a</sup>	$0.18 \text{ cm}^3$ material volume <sup>b</sup>
$0.82 \text{ cm}^3$ pore volume <sup>c</sup>	$0.50 \text{ cm}^3$ pore volume <sup>d</sup>
$1.04 \text{ cm}^3$ total volume	$0.68 \text{ cm}^3$ total volume

<sup>a</sup>Based on a copper phyllosilicate density of  $4.5 \text{ kg/dm}^3$ , <sup>b</sup>based on the weight-averaged density ( $4.85 \text{ kg/dm}^3$ ) of the final  $\text{Cu/SiO}_2$  catalyst. <sup>c</sup>based on  $\text{N}_2$ -physisorption of copper phyllosilicate, <sup>d</sup>based on  $\text{N}_2$ -physisorption of the reduced  $\text{Cu/SiO}_2$  catalyst.

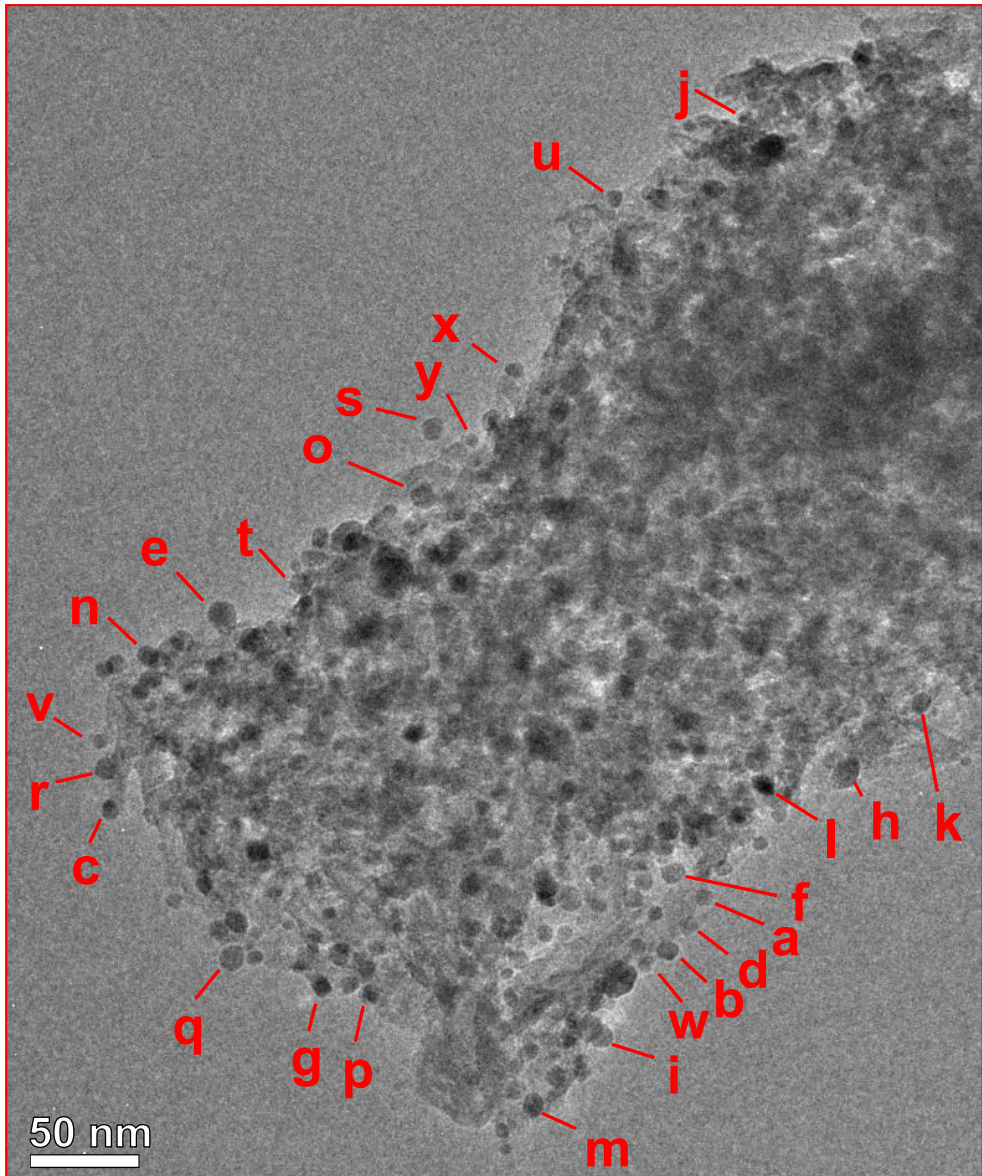


**Figure S2.5.** TEM image of Region 1 (Figure 2.7) after reduction in the microscope (at vacuum and room temperature) indicating the particles that were tracked back in time for measuring the evolution of their size. The letters correspond to the size evolutions shown in Figure 2.9.

**Table S2.2.** Results of analysis of the variance (ANOVA) in the particle size distributions shown in Figure 2.4.

Region	Count	Average	Variance	P-value
TEM	500	8.05	4.79	-
Reactor	500	7.98	4.83	$5.9 \cdot 10^{-1}$

For both samples the table shows the number of particles counted, the average particle size and the variance in the particle size distribution. The P-value shows the probability that the particle size distribution obtained for the sample reduced in a plug flow reactor has the same mean particle size as that of the sample reduced in the TEM.

**Table S2.3.** Results of analysis of the variance (ANOVA) in the particle size distributions shown in Figure 2.5.

Region	Count	Average	Variance	P-value
Reference	250	7.66	3.19	-
$1 \text{ e}^-/(\text{\AA}^2\text{s})$	100	8.57	3.45	$2.7 \cdot 10^{-5}$
$5 \text{ e}^-/(\text{\AA}^2\text{s})$	75	9.85	8.69	$5.6 \cdot 10^{-14}$
$10 \text{ e}^-/(\text{\AA}^2\text{s})$	100	8.20	6.08	$2.4 \cdot 10^{-2}$
$20 \text{ e}^-/(\text{\AA}^2\text{s})$	75	9.04	9.91	$2.3 \cdot 10^{-6}$
$100 \text{ e}^-/(\text{\AA}^2\text{s})$	100	9.76	25.38	$1.9 \cdot 10^{-8}$

For each region the table shows the number of particles counted, the average particle size and the variance in the particle size distribution. The P-value shows the probability that the particle size distribution obtained for a certain illuminated region has the same mean particle size as that of the reference locations.

**Table S2.4.** Results of analysis of the variance (ANOVA) in the particle size distributions shown in Figure 2.7.

Region	Count	Average	Variance	P-value
Reference	500	8.05	4.79	-
Region 1	50	8.26	3.28	$5.1 \cdot 10^{-1}$
Region 2	50	7.70	3.86	$2.7 \cdot 10^{-1}$
Region 3	50	8.15	2.74	$7.5 \cdot 10^{-1}$

For each region the table shows the number of particles counted, the average particle size and the variance in the particle size distribution. The P-value shows the probability that the particle size distribution obtained for Region 1, 2 or 3 has the same mean particle size as that of the reference locations.

## Modelling of the size evolutions

### Nucleation-and-growth model

We assume that copper is present in three different forms in the system: as ions in the copper phyllosilicate, as mobile reduced copper species, and in the form of nanoparticles. Let us consider a volume  $V$ , in which there are  $N_i(t)$  copper ions at time  $t$  and  $N_m(t)$  mobile reduced copper species. Assuming that reduction of copper ions is a first order and irreversible reaction,  $N_i$  undergoes an exponential decay as:

$$N_i(t) = N_i(0) \exp[-kt] \quad \text{Eq. 2.1}$$

where  $k$  is a reduction kinetic constant, and  $N_i(0)$  is the total number of copper ions in a volume  $V$  of copper phyllosilicate.

At the very end of the reduction, the copper is entirely in the form of nanoparticles supported on silica with an overall copper loading of 41 wt%. Using the densities of copper (8.96 kg/dm<sup>3</sup>) and silica (~2 kg/dm<sup>3</sup>), and correcting for the observed 8 % linear shrinkage of the silicate at the end of the reduction (Figure S2.4), the initial metal loading corresponds to  $N_i(0)/V = 8.6$  atoms per nm<sup>3</sup> (corresponding to a copper phyllosilicate density of ~4.5 kg/dm<sup>3</sup>). Assuming spherical particles, the total number of copper atoms in the 25 particles followed *in situ* by TEM is  $1.22 \cdot 10^6$ . Taking into account the initial metal loading, we assume in the rest of the analysis that the effective volume of the material is  $V = 1.4 \cdot 10^5$  nm<sup>3</sup>.

The time evolution of the number  $N_m(t)$  of mobile reduced copper species depends on the rate at which reduction proceeds, i.e. the decay of  $N_i(t)$  and at which they condense into nanoparticles. To calculate that rate, we shall assume that the concentration is uniform throughout the system, with value  $N_m(t)/V$ , except for a diffusive boundary layer surrounding each nanoparticle. Using Fick's classical law of diffusion, and assuming a Sherwood number of 2 as usual for mass transfer towards a sphere (R.B. Bird, W.E. Stewart, E.N. Lightfoot, Transport Phenomena, 2<sup>nd</sup> ed. Wiley, 2006), the time evolution of the number of atoms in, say, the  $p^{\text{th}}$  nanoparticle can eventually be written as

$$\frac{dn_p}{dt} = (4\pi)^{2/3} 3^{1/3} D \Omega^{1/3} \frac{N_m}{V} n_p^{1/3} \quad \text{Eq. 2.2}$$

where  $D$  is the diffusion coefficient of reduced copper species and  $\Omega$  is the volume of a copper atom in the nanoparticle, i.e.  $\Omega = 1.18 \cdot 10^{-2}$  nm<sup>3</sup>/atom. When writing Eq. 2.2, we assumed that the particles are spherical so that their radius is proportional to the cubic root of the number of atoms they contain. With that law governing the growth of

individual nanoparticles, the evolution of the number of mobile reduced copper species can then be written as follows

$$\frac{dN_m}{dt} = -\frac{dN_i}{dt} - \sum_p \frac{dn_p}{dt} = Ni(0)k \exp[-kt] - \sum_p \frac{dn_p}{dt} \quad \text{Eq. 2.3}$$

where the sum is over all the existing particles.

For the purpose of data analysis, it is convenient to normalize the number of atoms in each form by the total number  $N_i(0)$  and define  $\bar{N}_i(t) = N_i(t)/N_i(0)$  and  $\bar{N}_m(t) = N_m(t)/N_i(0)$ . With these variables, the governing equations can be put as

$$\begin{aligned} \frac{d}{dt} \bar{N}_m(t) &= k \exp[-kt] - \frac{\bar{D}}{N_i(0)} \bar{N}_m \sum_p n_p^{1/3} \\ \frac{d}{dt} n_p(t) &= \bar{D} \bar{N}_m n_p^{1/3} \end{aligned} \quad \text{Eq. 2.4}$$

where the parameter  $\bar{D}$  is defined as

$$\bar{D} = 3^{1/3} (4\pi)^{2/3} D \Omega^{1/3} \frac{N_i(0)}{V} \quad \text{Eq. 2.5}$$

Note that in the definition of  $\bar{D}$ , all quantities are known except the diffusion coefficient  $D$ .

The *in situ* TEM data provide information about the nucleation and growth of copper particles in the following ways: First the growth of the particles is analyzed using the times the particles first appeared and the initial particle sizes as input for the calculation. For this analysis the time a particle is first observed is assumed to be equal to the time it nucleated. In a second step the rate of particle appearance is compared to the nucleation rate predicted by the classical theory of homogeneous nucleation. For the analysis of the particle growth, let the nucleation time and the number of atoms in the  $i^{\text{th}}$  nucleus be  $t_{nuc}(i)$  and  $n_{nuc}(i)$ . The indices  $i$  of the nuclei (particles) are arranged in order of increasing nucleation times:  $t_{nuc}(1) \leq t_{nuc}(2) \leq \dots$ . For any given value of the parameters  $k$  and  $D$ , the following steps are followed.

1. From  $t = 0$  to  $t_{nuc}(1)$ , the number of mobile reduced copper species satisfies

$$\bar{N}_m(t) = 1 - \exp[-kt] \quad \text{Eq. 2.6}$$

because no metal nanoparticle has nucleated yet.

2. At time  $t = t_{nuc}(1)$ , the number of mobile copper is reduced by a quantity corresponding to the first nucleus formed:  $\bar{N}_m \rightarrow \bar{N}_m - n_{nuc}(1) / N_i(0)$  and the following two coupled equations are solved numerically from  $t = t_{nuc}(1)$  to  $t_{nuc}(2)$

$$\begin{aligned} \frac{d}{dt} \bar{N}_m(t) &= k \exp[-kt] - \frac{\bar{D}}{N_i(0)} \bar{N}_m n_1^{1/3} \\ \frac{d}{dt} n_1(t) &= \bar{D} \bar{N}_m n_1^{1/3} \end{aligned} \quad \text{Eq. 2.7}$$

3. At time  $t = t_{nuc}(2)$ , the number of mobile atoms is reduced by a quantity corresponding to the second nucleus formed:  $\bar{N}_m \rightarrow \bar{N}_m - n_{nuc}(2)/N_i(0)$  and the following three coupled equations are solved numerically from  $t = t_{nuc}(2)$  to  $t_{nuc}(3)$

$$\begin{aligned} \frac{d}{dt} \bar{N}_m(t) &= k \exp[-kt] - \frac{\bar{D}}{N_i(0)} \bar{N}_m (n_1^{1/3} + n_2^{1/3}) \\ \frac{d}{dt} n_1(t) &= \bar{D} \bar{N}_m n_1^{1/3} \\ \frac{d}{dt} n_2(t) &= \bar{D} \bar{N}_m n_2^{1/3} \end{aligned} \quad \text{Eq. 2.8}$$

4. Etc. This is continued until the last observed nucleus is accounted for.

With this procedure the radii of all the particles at all observation times are described by only two parameters:  $k$  and  $D$ . The concentration of ionic copper is assumed to be inversely proportional to the shrinkage of the copper phyllosilicate agglomerate (Figure S2.4). The entire dataset, comprising the time-dependent radii of all nanoparticles and the estimated time-dependent ionic copper concentration was fitted at once by least square with the kinetic constant  $k$  and diffusion coefficient  $D$  as only adjustable parameters. The best fits are shown in Figure S2.6 and Figure 2.9 of the main text. The values  $\Omega = 1.18 \cdot 10^{-2} \text{ nm}^3/\text{atom}$  and  $N_i(0)/V = 8.6 \text{ atoms}/\text{nm}^3$  were used for the fitting. The obtained diffusion coefficient was  $D \simeq 5 \cdot 10^{-19} \text{ m}^2/\text{s}$ , which is typical of solid-state diffusion, and the kinetic constant was  $k = 0.64 \text{ min}^{-1}$ .

As a byproduct of the modelling, the time-dependence of the number of copper atoms in the three states - ionic, mobile, and in the nanoparticles – is obtained. The curves are shown in Figure S2.6. The value of  $N_m(t)$  is particularly interesting because it is proportional to the supersaturation, which is the very driving force of the nucleation process.

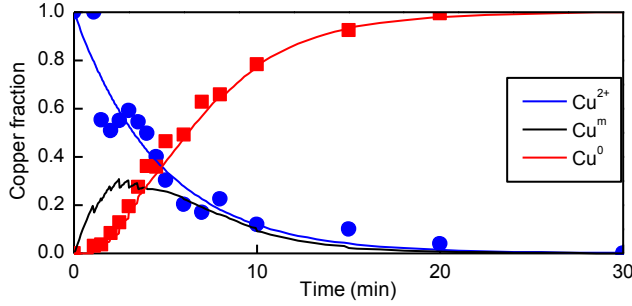


**Figure S2.6.** Fraction of copper atoms in the three states; ionic (blue), mobile reduced copper species (black) and in nanoparticles (red). The curves are obtained from the modelling. The red squares show the fraction of copper present in the observed nanoparticles over time, compared to the final amount. The blue dots indicate the fraction of copper in ionic state based on the assumption that the ionic concentration is inversely proportional to agglomerate shrinkage (Figure S2.4).

According to the classical theory of homogeneous nucleation (Debenedetti, *Metastable Liquids*, Princeton University Press, 1997), the nucleation rate  $\dot{I}$  corresponding to the number of nuclei formed per unit volume and per unit time is calculated as

$$\dot{I} \simeq D\Omega^{-5/3} \exp \left[ -\frac{16\pi}{3} \frac{\lambda^3/\Omega}{[\ln(S)]^2} \right] \quad \text{Eq. 2.9}$$

where  $S$  is the supersaturation ratio, and  $\lambda$  is a characteristic length of the phase being nucleated, defined as

$$\lambda = \frac{\gamma\Omega}{k_B T} \quad \text{Eq. 2.10}$$

where  $\gamma$  is the surface energy and  $k_B$  is Boltzmann's constant. In the case of copper with  $1.65 \text{ J/m}^2$  at  $T = 280 \text{ }^\circ\text{C}$ , the value is  $\lambda \simeq 2.5 \text{ nm}$ , leading to  $\lambda^3/\Omega \simeq 1300$ . In Eq. 2.9 there is a missing numerical prefactor, which is expected to be of order 1. Because the concentration of mobile species changes with time, Eq. 2.9 predicts a time-dependent nucleation rate. From the nucleation rate the total number of nuclei formed in a volume  $V$  at time  $t$  is obtained by integrating Eq. 2.9 with supersaturation expressed as  $S(t) = \bar{N}_m(t)/\bar{N}_m(\text{sat})$ . That is,

$$N_{\text{nuclei}}(t) \simeq D\Omega^{-5/3} V \int_0^t \exp \left[ -\frac{16\pi}{3} \frac{\lambda^3/\Omega}{[\ln(\bar{N}_m(t)/\bar{N}_m(\text{sat}))]^2} \right] \quad \text{Eq. 2.11}$$

according to nucleation theory, where  $\bar{N}_m(\text{sat})$  is the saturating value of  $\bar{N}_m$  corresponding to thermodynamic equilibrium.

The value of the prefactor in Eq. 2.11 is  $D\Omega^{-5/3}V \simeq 3.3 \cdot 10^7 \text{ s}^{-1}$ , and the value of  $\bar{N}_m(t)$  has been obtained from the particle growth model (Figure S2.6). The only unknown quantity to predict the nucleation rate from Eq. 2.11 is therefore  $\bar{N}_m(\text{sat})$ . The predicted value of  $N_{\text{nuclei}}(t)$  with the particular value  $\bar{N}_m(\text{sat}) = 1 \cdot 10^{-7}$  is shown in Figure S2.7. This figure shows that the predicted number of nucleated particles coincides qualitatively with the observed number of nanoparticles indicating that the nucleation time in the model agrees reasonably well with the time for the first observation of a particle in the experiment.

In passing, it is interesting to evaluate the size of the critical nuclei. The latter size is calculated as

$$R^* = \frac{2\lambda}{\ln(\bar{N}_m(t) / \bar{N}_m(\text{sat}))} \quad \text{Eq. 2.12}$$

which is equivalent to Kelvin's law. Assuming  $\bar{N}_m \simeq 0.2$  and  $\bar{N}_m = 1 \cdot 10^{-7}$  leads to  $R^* = 3.4 \text{ \AA}$ , which is consistent with the much larger particle sizes, observed by TEM.

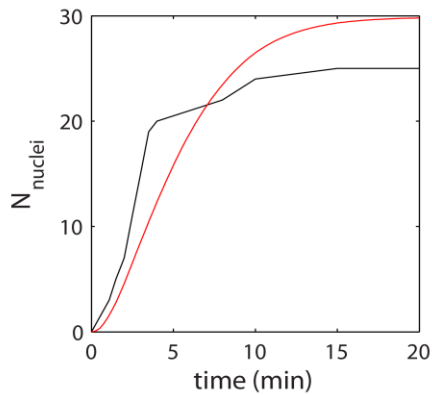


**Figure S2.7.** Number of particles nucleated as a function of time (black line) and prediction of the classical theory of homogeneous nucleation with  $\bar{N}_m(\text{sat}) = 1 \cdot 10^{-7}$ .

**Autocatalytic model**

**Poisson nucleation model**

In the following, the copper phyllosilicate is assumed to be made up of regions, boxes, that cannot exchange copper. During the reduction process, all the copper atoms remain in their respective boxes and are assumed to end up in a single particle per box. The copper concentration of the phyllosilicate is approximately  $c_i = 8.6 \text{ atoms/nm}^3$ . The volume of a copper atom in the metal is  $\Omega = 1.18 \cdot 10^{-2} \text{ nm}^3$ . Therefore, the volume of the box is a factor  $1 / (c_i \Omega) \simeq 10$  larger than the final volume of the nanoparticle. The typical particle diameter being 8 nm, the typical box is approximately 17 nm across.

The model we consider in this section is not strictly a nucleation model. Because the temperature and partial pressure of hydrogen are constant with time, each copper ion in a box is assumed to have a constant probability of being reduced per unit time, and the reduction is therefore described by a Poisson statistics. As soon as one ion has been reduced, autocatalytic reduction is assumed to occur and is described with the growth models that are described later. Before any copper particle is present, let  $\lambda dt$  be the probability for one copper ion to be reduced in a time interval  $dt$ . The probability for any copper ion in the box to be reduced during the same interval is therefore

$$\lambda dt \frac{4/3\pi R_f^3}{\Omega} A = \Lambda R_f^3 dt \tag{Eq. 2.13}$$

where the additional factor is the number of copper ions in the box, expressed as a function of the final particle radius  $R_f$ . The number of reduction events in the box at time  $t$  is a Poisson random variable with parameter  $\Lambda R_f^3 t$ . In particular, the probability for not observing any reduction yet at time  $t$  is

$$P [\text{No Ion Reduced}] = \exp(-\Lambda R_f^3 t) \tag{Eq. 2.14}$$

and the probability for observing at least one reduction is therefore

$$P [\text{At Least One Reduced}] = 1 - \exp(-\Lambda R_f^3 t) \tag{Eq. 2.15}$$

Equations 2.14 and 2.15 can be used to analyze the experimental nucleation data via a maximum likelihood method. Suppose that the  $i^{\text{th}}$  particle (with final radius  $R_f(i)$ ) appears in the interval between  $t_1(i)$  and  $t_2(i)$ . The likelihood of that particular event is

$$\exp(-\Lambda R_f(i)^3 t_1(i)) [1 - \exp(-\Lambda R_f(i)^3 t_2(i))] \tag{Eq. 2.16}$$

where the first factor is the probability that it was not there at time  $t_1(i)$  and the second factor is the probability that it was there at time  $t_2(i)$ . Because each box is independent from the others, the overall likelihood of the entire dataset is therefore

$$L = \prod_{i=1}^N \exp(-\Lambda R_f(i)^3 t_1(i)) [1 - \exp(-\Lambda R_f(i)^3 t_2(i))] \quad \text{Eq. 2.17}$$

where the product is over all  $N$  nanoparticles/boxes. Using the experimental values of  $t_1$ ,  $t_2$  and  $R_f$  for all the particles, the value of  $\Lambda$  that maximises  $L$  is found to be  $\lambda = 5.42 \cdot 10^6 \text{ min}^{-1} \text{ ion}^{-1}$ . The predictions of the Poisson reduction model are compared to the actual data in Figure 2.10 of the main text. The Poisson model captures both the effect of the box size on the nucleation time, and the scatter of the data.

The model assumes that only one particle nucleates in each box. The number of copper ions  $n_{\text{Cu}^{2+}}(t)$  remaining in a box at time  $t$  is calculated from the known time-dependent radius of the particle (Figure S2.8, top row) and from this the probability of secondary nucleation in a box is calculated. Because the number of copper ions is not a constant, the secondary nucleation is a non-stationary Poisson process. In particular the number of secondary nucleation events in a given time interval after the first nucleation is a Poisson random variable with parameter

$$\int_{t_{\text{nuc}}}^t n_{\text{Cu}^{2+}}(t) \lambda dt \quad \text{Eq. 2.18}$$

The corresponding probabilities are shown in the second row of Figure S2.8, using the value of  $\lambda$  determined previously. In the case of small particles created relatively late (e.g. particle u, Figure 2.9), the probability of not observing any secondary nucleation is 0.9. By contrast, for large particle created early (particle e, Figure 2.9), the probability of no secondary nucleation is 0.1, and the probability of observing as many as two secondary nucleation events is larger than 0.2.

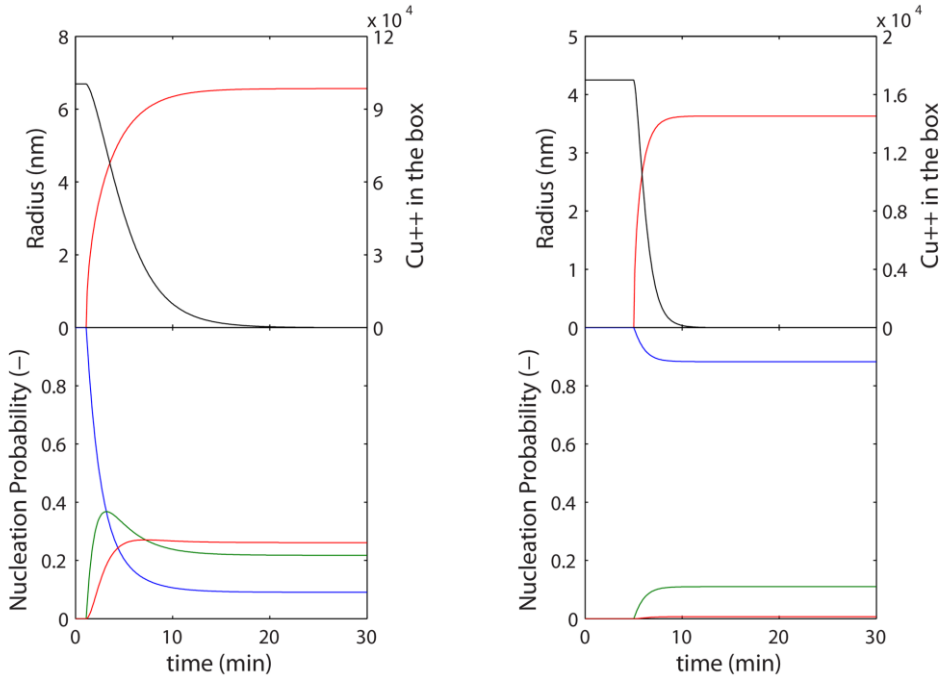


**Figure S2.8.** Expected secondary nucleation events within one box. The top row shows the time-dependent radius of the first particle created as fitted by the diffusion-limited particle growth model (red, see page 23), and the remaining number of Cu ions in the box (black). In the bottom row, the probabilities of secondary nucleation are plotted: no secondary nucleation (blue), one secondary nucleation event (green) and two secondary nucleation events (red). On the left is particle u, and on the right is particle e (see Figure S2.5 and 2.9).

### Reaction-limited particle growth

Once a metal nanoparticle has been created, its further growth can be either reaction-limited or diffusion-limited. Both possibilities are considered in the present and the following sections using the box hypothesis.

For the reaction-limited growth, the overall reduction rate is proportional to the surface area of the particle. The rate of growth of any particle therefore obeys

$$\frac{4\pi R^2}{\Omega} \frac{dR}{dt} = k4\pi R^2 c \quad \text{Eq. 2.19}$$

## Chapter 2

---

In this equation,  $\Omega$  is the volume of a copper atom in the particles,  $k$  is the rate constant per unit area, and  $c$  is the concentration of the unreduced copper in the box. Copper conservation therefore leads to

$$Vc(t) + \frac{4\pi R^3(t)}{3} \frac{1}{\Omega} = \frac{4\pi R_f^3}{3} \frac{1}{\Omega} \quad \text{Eq. 2.20}$$

where  $V$  is the volume of the box, and  $R_f$  is the final particle size. These two equations together leads to the following growth-rate equation

$$\frac{dR}{dt} = K_r \left[ 1 - \left( \frac{R}{R_f} \right)^3 \right] \quad \text{Eq. 2.21}$$

where  $K_r = k4/3\pi R_f^3/V$  is proportional to the kinetic constant. Note that the quantity  $4/3\pi R_f^3/V$  is the copper concentration in the box, which we shall assume is the same for all particles. Therefore, there is just one value of the constant  $K_r$ , which is the same for all particles. In order to find a solution to Eq. 2.21, a dimensionless form is useful and obtained by defining  $r = R/R_f$  and  $\tau = K_r t/R_f$ . Hereby

$$\frac{dr}{d\tau} = 1 - r^3 \quad \text{Eq. 2.22}$$

The numerical solution of Eq. 2.22 is plotted in Figure S2.9.

Because numerical solutions are not practical for data analysis, an approximate solution is developed by considering the following asymptotic relations are obtained from Eq. 2.22:

$$r \simeq \tau \text{ for } r \ll 1 \quad \text{Eq. 2.23}$$

$$r \simeq 1 - \text{constant} \times e^{-3\tau} \text{ for } r \simeq 1 \quad \text{Eq. 2.24}$$

where the constant is unknown. The following analytical expression satisfies those two asymptotic behaviours

$$r[\tau] = 1 - \frac{(1+A)e^{-\tau}}{A+e^{2\tau}} \quad \text{Eq. 2.25}$$

This particular approximation is plotted in Figure S2.9 as a solid red line, for the particular value  $A = 5$ . Due to the good match with the numerical solution (Figure S2.9), this semi-analytical expression is used to fit the *in situ* TEM data in Figure 2.9.

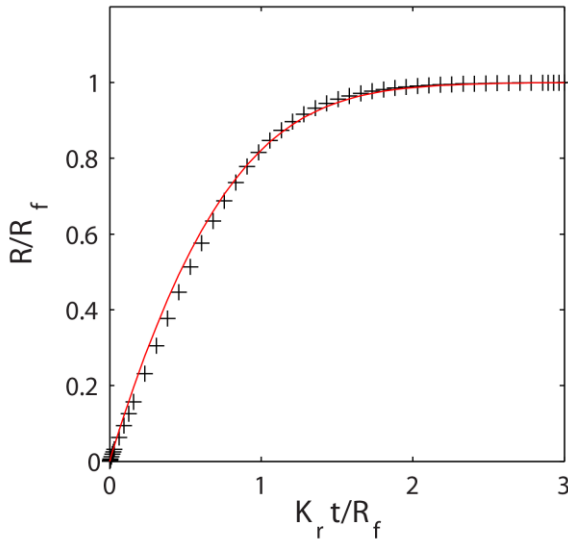


**Figure S2.9.** Exact numerical solution to Eq. 2.22 (+ black) and approximate analytical solution (solid red line) obtained from Eq. 2.25 with  $A = 5$ .

The time-dependent radii of the particles are fitted with the following equation

$$R(t) = \begin{cases} R_f \times r [K_r(t - t_{nuc})/R_f] & \text{for } t \geq t_{nuc} \\ 0 & \text{otherwise} \end{cases} \quad \text{Eq. 2.26}$$

where the function  $r[\tau]$  is given by Eq. 2.25,  $K_r$  is the kinetic constant,  $R_f$  is the final radius of that specific particle and  $t_{nuc}$  is its nucleation time. The least-square fitting of the data is shown in Figure 2.9 of the main text. The data was fitted with a total of 51 adjustable parameters, namely the values of  $R_f$  and  $t_{nuc}$  for each of the 25 particles, plus the kinetic constant  $K_r$ . For the adjustment, the nucleation time  $t_{nuc}$  was bounded to remain within a 10% interval of the first observation time of the particle. The final radius  $R_f$  was also bound to a 10% interval around the radius of the particle at the last observation time. The fitted value of the kinetic constant is  $K_r \approx 0.45$  nm/min.

**Diffusion-limited particle growth**

Here diffusion-limited growth is considered with the autocatalytic model. That is, mobile copper species with concentration  $c$  diffuse in the box with a diffusion constant  $D$  and as they reach the surface attach infinitely rapidly to a particle. For simplicity, the box is described as a sphere with radius  $R_b$ , and the particle is described as a sphere too with time-dependent radius  $R(t)$  located at the center of the box. The partial differential equation governing the diffusion of the copper species in the box is Fick's second law. Assuming spherical coordinates it takes the form

$$\partial_t c(r, t) = \frac{D}{r^2} \partial_r (r^2 \partial_r c(r, t)) \tag{Eq. 2.27}$$

where  $D$  is the diffusion coefficient. The boundary conditions on the concentration are

$$c = 0 \text{ for } r = R(t) \quad \forall t \tag{Eq. 2.28}$$

and

$$\partial_r c = 0 \text{ for } r = R_b(t) \quad \forall t \tag{Eq. 2.29}$$

The former condition expresses that the reaction is infinitely fast at the surface of the growing nanoparticle, and the latter expresses that the copper species cannot diffuse out of the box. The radius of the particle  $R(t)$  is a time-dependent quantity described by

$$\frac{4\pi R^2}{\Omega} \frac{dR}{dt} = D4\pi R^2 (\partial_r c)_{r=R(t)} \tag{Eq. 2.30}$$

where  $\Omega$  is the volume occupied by a copper atom in the particle. This equation expresses that the growth of the particle is fed (and limited by) by the diffusion of the copper species towards its surface. Because the boundary condition Eq. 2.28 is applied on a geometric surface that is moving according to the concentration profile (via Eq. 2.30), the diffusion-in-a-box model is a so-called Stefan mathematical problem. This is a notoriously difficult type of problem without a simple solution. It therefore has to be solved numerically.

For the numerical solution, Eq. 2.30 is first put in dimensionless form. The radius of the box  $R_b$  is used as a distance unit. The natural time unit is  $R_b^2/D$ , which is the approximate time required to diffuse over a distance  $R_b$ . The initial concentration  $c_i$  of copper species is

used as a concentration unit. Fick's second law takes the following dimensionless form

$$\partial_{\bar{t}} \bar{c} = \frac{1}{\bar{r}^2} \partial_{\bar{r}} (\bar{r}^2 d_{\bar{r}} \bar{c}) \quad \text{Eq. 2.31}$$

with boundary conditions

$$\bar{c} = 0 \text{ for } \bar{r} = \bar{R}(\bar{t}) \quad \text{Eq. 2.32}$$

$$\partial_{\bar{r}} \bar{c} = 0 \text{ for } \bar{r} = 1 \quad \text{Eq. 2.33}$$

and the equation governing the growth of the particle take the form

$$\frac{d\bar{R}}{d\bar{t}} = \Gamma (\partial_{\bar{r}} \bar{c})_{\bar{r}=\bar{R}(\bar{t})} \quad \text{Eq. 2.34}$$

where

$$\Gamma = \frac{4\pi}{3} \Omega c_i \quad \text{Eq. 2.35}$$

is the only dimensionless number of our problem. The copper concentration of the phyllosilicate is approximately  $c_i = 8.6 \text{ atoms/nm}^3$ . The volume of a copper atom in the metal is  $1.18 \cdot 10^{-2} \text{ nm}^3$ . The relevant value of  $\Gamma$  is therefore  $\Gamma \simeq 0.4$ . The numerical solution is shown in Figure S2.10. This was obtained via a finite-volume method with an adaptive mesh. The corresponding time-dependent radius of the particle is shown in Figure S2.11 as crosses.

In order to make the results in Figure S2.11 usable for data analysis, it is convenient to find an empirical analytical expression that approximates the numerical solution. By similarity with Eq. 2.25, the following expression was adopted

$$\frac{R(\bar{t})}{R_f} = 1 - (1 + A) \frac{\exp[-(B\bar{t} + \bar{t}^{1/2})]}{A + \exp[2(B\bar{t} + \bar{t}^{1/2})]} \quad \text{Eq. 2.36}$$

with  $A = 26.4$  and  $B = 1.19$ .

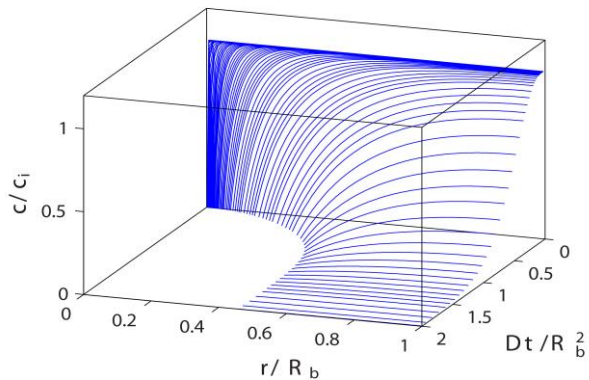


**Figure S2.10.** Time-dependent concentration profile around the growing nanoparticle, for  $\Gamma = 0.4$ .

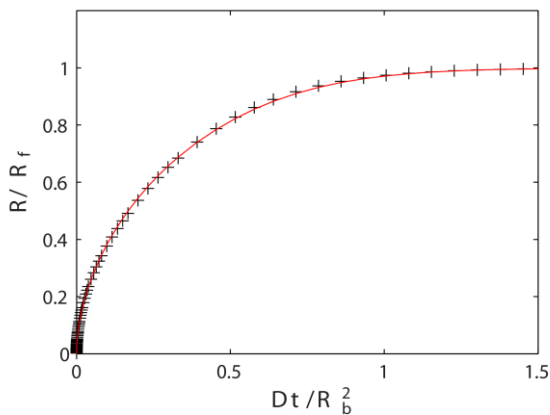


**Figure S2.11.** Time-dependent radius of the nanoparticle for  $\Gamma = 0.4$ . The crosses are obtained from the numerical solution, and the solid line is the empirical expression Eq. 2.36.

The least-square fit of the growth data is shown in Figure 2.11 of the main text. The diffusion coefficient is found to be  $4.5 \cdot 10^{-19} \text{ m}^2/\text{s}$ .



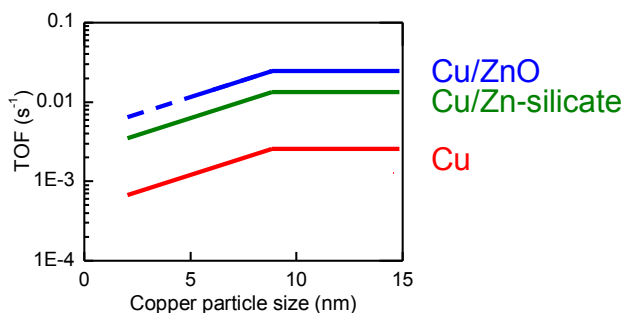


# Effect of Particle Size on the Activity of Supported Cu and CuZn catalysts in the Methanol Synthesis

Based on: van den Berg, R.; Prieto, G.; Korpershoek, G.; van der Wal, L. I.; van Bunningen, A. J.; Lægsgaard-Jørgensen, S.; Sehested, J.; Helveg, S.; de Jongh, P. E.; de Jong, K. P. *Nat. Commun.*, submitted

## Abstract

For decades, it has been debated whether the conversion of syngas to methanol by copper catalysts is sensitive or insensitive to the structure of the copper surface. We have for the first time systematically investigated the effect of the copper particle size in the range where changes in surface structure occur, i.e. < 10 nm. The effect of the copper particle size on the methanol synthesis activity is studied using catalysts based on supports without zinc, on supports containing zinc silicate and on supports containing zinc oxide. Catalysts containing zinc oxide were about ten times more active, and catalysts containing zinc silicate were about five times more active in the methanol synthesis reaction than catalysts without zinc. The differences in activity are ascribed to the promoting effect of zinc and to the thermodynamic stability of the zinc phase. The turnover frequency decreased significantly for copper particles smaller than 7 nm for all three types of catalysts thus revealing structure sensitivity. We propose that the methanol synthesis reaction either takes place at surface sites with a unique configuration of several copper atoms which smaller particles cannot accommodate, or that more unsaturated surface sites are poisoned by formate and that the reaction predominantly takes place at the more densely-packed copper surfaces which are not poisoned by formate.



## Introduction

Supported metal catalysts play a pivotal role in the production of fuels and chemicals, in the purification of exhaust gases and in electrochemical energy conversion systems.<sup>1</sup> Surface science and computational chemistry have shown that the performance of these materials depends in many cases on the surface structure of the metal nanoparticles.<sup>2</sup> Nanosizing metal particles to a size below 10 nm typically alters the surface structure by changing the fraction of different surface atoms and thereby the fraction of different surface sites.<sup>3</sup> As a result, an effect of the metal particle size on the activity and selectivity has been found for many reactions,<sup>2a, 2b, 4</sup> including the conversion of syngas to lower olefins by iron catalysts and to higher alkanes by cobalt catalysts.<sup>1d, 5</sup>

For decades, it has been debated whether the conversion of syngas to methanol by copper catalysts is sensitive or insensitive to the structure of the copper surface.<sup>6</sup> Several studies found a linear relationship between the exposed copper surface area and the activity, suggesting a structure-insensitive reaction.<sup>7</sup> Based on the measured copper surface areas reported in these studies, the particles were estimated to be larger than 10 nm. In contrast, recent studies proposed that the methanol synthesis reaction is in fact sensitive to the copper surface structure.<sup>8</sup> Furthermore, it has been shown that the activity also depends on the presence of zinc, be it in the form of zinc oxide or zinc hydroxy(phylo)silicate.<sup>7b-d, 8-9</sup> Thus, these findings suggest that the methanol synthesis reaction may display structure-sensitivity for catalysts with copper particle sizes below 10 nm.

To address the structure-sensitivity of the methanol synthesis reaction for supported copper catalysts, we examined the catalytic performance of catalysts with different copper particle sizes and with or without a zinc component. Specifically, we have synthesized 42 catalysts with copper particle sizes in the range from 2 to 15 nm on Zn-free supports (silica and carbon), on supports incorporating zinc as Zn silicate, and on supports incorporating zinc oxide. Furthermore we have synthesized series of catalysts with similar copper particle sizes and various zinc loadings, to determine the minimum amount of zinc required to achieve optimum activity. The performance of all catalysts in the methanol synthesis reaction was investigated under industrially relevant reaction conditions: 260 °C and 40 bar, using a synthesis gas feedstock containing 23% CO, 7% CO<sub>2</sub>, 60% H<sub>2</sub> and 10% Ar.

### Experimental Section

#### Cu(Zn)/SiO<sub>2</sub>

Copper/(Zinc) catalyst were prepared using different silica supports, including silica gels, (aminopropyl-functionalized) Stöber silica, SBA15, SBA16, FDU; see supporting information for synthesis details and N<sub>2</sub>-physisorption data. The supports were first dried at 150 °C under vacuum for 1 h to remove adsorbed water. Thereafter, the supports were incipient wetness impregnated with an aqueous solution of 0.25 to 4.35 M copper nitrate (Cu(NO<sub>3</sub>)<sub>2</sub>•3 H<sub>2</sub>O, Acros Organics) or copper and zinc nitrate with a total metal concentration between 1.0 and 5.0 M (Zn(NO<sub>3</sub>)<sub>2</sub>•6H<sub>2</sub>O, Sigma Aldrich) in a 65/35 atomic Cu/Zn ratio in 0.1 M HNO<sub>3</sub>. The samples (~2 g) were subsequently dried under vacuum at room temperature overnight and heat treated at 350 °C (2 °C/min) in a plug-flow reactor with either a flow of 750 mL/min N<sub>2</sub> or 375 mL/min 2% NO/N<sub>2</sub>. The nominal copper loading in the samples heat treated in N<sub>2</sub> was kept below 2 Cu atoms per nm<sup>2</sup> of support to avoid the formation of copper particles larger than 5 nm.<sup>10</sup> Cu/SiO<sub>2</sub> was also prepared via homogeneous deposition precipitation of copper on colloidal silica followed by a hydrothermal treatment and reduction as described by van den Berg et al.<sup>11</sup> Part of the as-prepared samples was used for catalysis following *in-situ* reduction as described below, and part (~1 g) was used for characterization. Characterization was done on as-prepared samples and on samples after reduction and passivation, mimicking the activation procedure used prior to catalysis. The reduction was performed in a flow of 100 ml/min of 20% H<sub>2</sub> in Ar at 250 °C (2 °C/min) for 2½ h. After reduction, samples were passivated for 15 min by slowly exposing them at room temperature to air diluted with N<sub>2</sub>. The samples were stored in a glove box under argon atmosphere. Table S3.1 shows a list of the samples, synthesis details, their main physicochemical characteristics (notably metal loading and dispersion) and at which catalyst synthesis stage these characteristics were determined, i.e. at the oxidized or reduced state.

#### Cu(Zn)/C

Copper/(Zinc) catalyst were prepared using different carbon supports, including carbon xerogels and high surface area graphite (HSAG); see supporting information for synthesis details and N<sub>2</sub>-physisorption data. The supports were first dried at 150 °C under vacuum for 1 h to remove adsorbed water. Thereafter, the carbon xerogels were incipient wetness impregnated with an aqueous solution of copper and zinc nitrate in a 65/35 atomic Cu/Zn ratio in 0.1 M HNO<sub>3</sub> with a total metal concentration between 1.15 and 3.0 M, and HSAG was incipient wetness co-impregnated with aqueous solutions of 2 M copper nitrate and 0 to 2 M zinc nitrate in 0.1 M HNO<sub>3</sub>. The samples (~2 g) were subsequently dried under

vacuum at room temperature overnight and reduced at 230 °C (2 °C/min) in a plug-flow reactor with 100 mL/min 20% H<sub>2</sub>/N<sub>2</sub>. After the reduction treatment the samples were passivated for 15 minutes by slowly exposing the sample to diluted air/N<sub>2</sub> at room temperature. The samples were subsequently characterized. Furthermore, the samples were loaded in a reactor, rereduced, and tested for their performance in the methanol synthesis reaction. Table S3.2 shows a list of the samples and their physicochemical characteristics.

### **Cu/ZnO(/Al<sub>2</sub>O<sub>3</sub>)**

Cu/ZnO(/Al<sub>2</sub>O<sub>3</sub>) catalysts were prepared by co-precipitation. Aqueous solutions of Cu, Zn and Al nitrates in varying atomic ratios with a total metal concentration of 2 M were added simultaneously with a 1.6 M Na<sub>2</sub>CO<sub>3</sub> solution to deionized water at 65 °C at a controlled rate of 20 ml/min in order to keep the pH constant around 8. The obtained precipitates were aged for 1 h at 70 °C in the mother liquor under stirring. The samples were extensively washed with water, dried at 80 °C and calcined in a muffle oven at 325 °C. Part of the as-prepared samples was used for catalysis following *in-situ* reduction as described below, and part (~1 g), intended for characterization, was reduced in a flow of 100 ml/min of 20% H<sub>2</sub> in Ar at 250 °C (2 °C/min) for 2½ h. After reduction the samples were passivated for 15 min by slowly exposing the samples at room temperature to air diluted with N<sub>2</sub>. The samples were stored in a glove box under argon atmosphere and subsequently characterized. Table S3.3 shows a list of the prepared samples and their physicochemical characteristics.

### **Characterization**

N<sub>2</sub> physisorption measurements on the supports were performed at -196 °C using a Micromeritics Tristar 3000 V6.08 apparatus. Prior to the measurements, the samples were outgassed at 130 °C in a nitrogen flow for 14 h. The Brunauer-Emmet-Teller (BET) method was used to calculate the specific surface areas.<sup>12</sup> The pore volumes were determined at p/p<sub>0</sub> = 0.9975. Barrett-Joyner-Halenda (BJH) method analysis (4V/A) of the adsorption branch was used to obtain the average pore size.<sup>13</sup>

X-ray diffraction was performed with a Bruker-Nonius D8 Advance X-ray diffractometer using Co-Kα12 (λ = 1.79026 Å) radiation. For impregnated Cu(Zn)/SiO<sub>2</sub> samples, diffractograms were taken after heat treatment in N<sub>2</sub> or 2% NO/N<sub>2</sub>. For precipitated Cu/ZnO(/Al<sub>2</sub>O<sub>3</sub>), impregnated Cu(Zn)/C and some of the Cu/SiO<sub>2</sub> samples, diffractograms were (also) taken after reduction and passivation. For these reduced and passivated catalysts, the specimen holder was loaded in the glove box and subsequently sealed. Diffractograms were collected at room temperature from 20° to 70° (2θ). Copper

and zinc oxide crystallite sizes were estimated by applying the Scherrer equation to the (111) diffraction of Cu ( $2\theta = 50.5^\circ$ ,  $k = 0.9$ ) or the (-111/002) diffraction of CuO ( $2\theta = 41.5^\circ$ ,  $k = 0.9$ ), and the (100) diffraction of ZnO ( $2\theta = 37.0^\circ$ ,  $k = 0.9$ ), respectively.<sup>14</sup> Temperature programmed reduction (TPR) measurements of the Cu(Zn)/SiO<sub>2</sub> samples after heat treatment in N<sub>2</sub> or 2% NO/N<sub>2</sub> were either done with a Micromeritics Autochem II ASAP 2920 (TPR-TCD) or in a fixed-bed flow setup with online gas analysis performed by a quadrupole mass spectrometer (Balzers GAM 445, TPR-MS). Prior to TPR-TCD measurements, the samples were dried at 80 °C for 1 h (CuZn/SiO<sub>2</sub> samples) or at 120 °C for 0.5 h (Cu/SiO<sub>2</sub> samples). Subsequently the temperature was increased to 500 °C (10 °C/min, CuZn/SiO<sub>2</sub> samples) or 300 °C (5 °C/min, Cu/SiO<sub>2</sub> samples) under a flow of 5% H<sub>2</sub>/Ar. During this treatment the H<sub>2</sub> concentration was determined with a thermal conductivity detector (TCD). TPR-MS measurements were performed by reduction at 220 °C (2 °C/min) in a 100 ml/min flow of 1% H<sub>2</sub>/He for 7 hours. The copper loading was estimated from the H<sub>2</sub> consumption by assuming the reduction stoichiometry:  $\text{CuO} + \text{H}_2 \rightarrow \text{Cu} + \text{H}_2\text{O}$ .

Transmission electron microscopy (TEM) images were acquired with a Tecnai 12 (FEI) microscope operated at 120 kV. The Cu(Zn)/C, Cu/ZnO/(Al<sub>2</sub>O<sub>3</sub>) after reduction and passivation and Cu/(functionalized)Stöber silica, Cu/FDU and Cu/SBA-16 after heat treatment in N<sub>2</sub> or 2% NO/N<sub>2</sub> were prepared by grinding followed by sonication in ethanol. A droplet of the resulting ethanol suspensions was deposited on carbon coated copper TEM grids (Agar S162 200 Mesh Cu). Other Cu(Zn)/SiO<sub>2</sub> samples after reduction and passivation were ground, embedded in a two-component epoxy resin (Epofix, EMS), cured at 60 °C overnight, and cut into thin sections (50-100 nm) using a Diatome Ultra 35° diamond knife mounted on an Ultracut E microtome (Reichert-Jung). Sections were deposited on a copper TEM grid. High-angle annular dark-field scanning-transmission electron microscopy (HAADF-STEM) and Energy dispersive X-ray (EDX) spectroscopy was performed using either a Tecnai 20FEG (FEI) electron microscope equipped with a field emission gun, a Fischione HAADF detector and an EDAX Super Ultra Thin Window EDX detector, or a TALOS F200x (FEI) electron microscope equipped with a field emission gun (XFEG), a Fischione HAADF detector and a SuperX EDX system. For these measurements, samples or microtomed sections were placed onto a carbon coated Ni TEM grid (Agar 162 200 Mesh Ni) and mounted either on a low-background sample holder (Philips) with a 0.1 mm thick Be specimen support film and a Be ring to clamp the grid, and inserted in the Tecnai 20FEG or on a high visibility low-background double-tilt sample holder (FEI) with a Be clamp, and inserted in the TALOS F200x. The signal and resolution in the different electron microscope systems was in general sufficient to detect copper particles larger than 2 nm on any of the supports. For each sample, at least 150 particles were analyzed

with respect to their size by measuring the diameter of a spherical approximation of the projected particle area. Processing of the EDX data is described in the supporting information at the respective figures.

### Catalytic testing

The performance of the catalysts in the methanol synthesis reaction was investigated in a fixed-bed stainless steel reactor with an inner diameter of 0.9 cm (Autoclave Engineers). The calcined Cu(Zn)/SiO<sub>2</sub> and Cu/ZnO/(Al<sub>2</sub>O<sub>3</sub>) samples, and the reduced and passivated Cu(Zn)/C samples were pressed, ground and sieved to obtain a granulate size of 0.42 to 0.63 mm. 0.03–0.9 g catalyst was diluted with 0–3 mL SiC granules (sieve fraction of granulate size 0.25–0.42 mm) and loaded into the reactor (catalyst bed height of 3–7 cm). Subsequently, the samples were (re)reduced in-situ at 250 °C (2 °C/min) for 2.5 h with a flow of 110 mL/min 20% H<sub>2</sub>/Ar. After that, the temperature was lowered to 100 °C to prevent premature production of methanol when switching to syngas. The reactor was flushed with syngas (10% Ar, 7% CO<sub>2</sub>, 23% CO, 60% H<sub>2</sub>, Linde), which was purified with a metal carbonyl trap<sup>15</sup> (4.0 g of 0.5–1.5 mm H-USY zeolite, CVB-780 from Zeolyst Int., and 5 g activated carbon, Norit R3B). The argon in the syngas feed acted as an internal standard for the gas chromatograph (GC). After 30 minutes of flushing the pressure was increased to 40 bar. Subsequently, the exit gas composition was analyzed every 110 minutes with a GC (Varian 450). The lines from the reactor to the GC were heated to 150 °C to avoid any methanol or water condensation. The first GC channel consisted of a HAYESEP Q (0.5 m x 1/8 in.) column followed by a MOLSIEVE 13x (15 m x 1/8 in.) column that led to a thermal conductivity detector (TCD). The second GC channel consisted of a CP-SIL 8CB FS capillary column that led to a flame ionization detector (FID). At least three chromatograms were recorded of the syngas feed. The temperature was then increased to 260 °C (2 °C/min) to initiate methanol production. The amount of catalyst and the syngas flow (10–30 mL/min) were chosen such that CO + CO<sub>2</sub> conversion levels below 20% were obtained. The initial (maximum) activity of the catalysts was determined by the maximum conversion of CO and CO<sub>2</sub> after about 2 to 10 hours on stream. The standard deviation in between different tests in the activity is ± 35%. Turnover frequencies (TOF) were calculated per surface metal atom. The dispersion was based upon (S)TEM particle size distributions assuming fully accessible spherical copper particles and calculated with the formula:  $dispersion = \frac{6V_m}{A_m * PS} = \frac{1.04}{PS}$ , where V<sub>m</sub> is the molar volume of copper, A<sub>m</sub> the molar area of copper and PS the surface-average particle size in nanometer. The selectivity was determined from the FID chromatograms and was in all cases more than 98.5% towards methanol, with trace amounts of dimethyl ether, methane, ethanol, ethane and propane. After catalysis, the

samples were passivated for 15 min by exposing the sample to air diluted with Ar at room temperature. The samples were stored in a glove box under argon atmosphere.

## Results & Discussion

### Copper particle size

The Cu(Zn)/SiO<sub>2</sub> catalysts were synthesized on different silica supports via a heat treatment of impregnated copper nitrate in N<sub>2</sub> or 2% NO/N<sub>2</sub> resulting in copper oxide and subsequent a reduction in H<sub>2</sub> resulting in metallic copper. The Cu and CuO phases are for the different catalysts associated with a particle size in the range from 2 to 15 nm based on XRD and (S)TEM measurements (Table S3.1, see supporting information for the identification of the particles containing copper in (S)TEM images). Similar crystallite sizes were found for the copper oxide phases after heat treatment and for metallic copper phases after reduction and passivation, as the change in particle size upon reduction is less than 15% based upon the difference in bulk density for the two phases (see Table S3.1 for the actual Cu and CuO sizes as determined with XRD and (S)TEM). Particle size distributions determined with (S)TEM after heat treatment are therefore representative for the size distribution of the copper particles after reduction. In the case of heat treatment in N<sub>2</sub> and reduction in H<sub>2</sub>, the copper particles obtained a size of about 2-3 nm, irrespective of the support porosity and the presence or absence of zinc (Table S3.1).<sup>9a, 10b, 16</sup> For these catalysts, the particle size measurement is based only on (S)TEM since the crystallite sizes were below the detection limit of XRD. In the case of heat treatment in 2% NO/N<sub>2</sub> and subsequent reduction in H<sub>2</sub>, the size of the copper particles, as determined by (S)TEM and XRD, ranged from 3 to 15 nm and depended on the support porosity and copper loading (Table S3.1).<sup>10a, 17</sup>

The Cu(Zn)/C were synthesized on HSAG and carbon xerogels with different pore sizes via a drying step and a reduction in H<sub>2</sub> (Table S3.2). The size of the copper particles as determined with TEM was between 5 to 11 nm and correlated to the average pore size of the support. For the series of catalysts on HSAG with varying Zn, the copper particle size as determined with TEM varied from 5-6 nm for the sample without zinc to about 9 nm for the sample impregnated with the solution containing up to 2 M zinc nitrate (Table S3.2).

The Cu/ZnO/(Al<sub>2</sub>O<sub>3</sub>) catalysts were synthesized via co-precipitation, followed by drying, calcination and reduction. The size of the resulting copper particles, as determined with TEM, increased from 5-6 nm for the samples with a low copper loading (<10 wt%) to more than 30 nm for the samples with high copper loadings (>85 wt%, Table S3.3). The Cu/ZnO samples with a copper loading close to the one of commercial methanol synthesis

catalysts (~ 55 wt%) had a copper particle size of about 12 nm. For the sample containing, in addition to copper and zinc, 11.6 wt% alumina the copper particle size lowered to around 7 nm, which is the typical size of the copper particles in commercial methanol synthesis catalysts.<sup>6, 18</sup> Metallic copper crystallite sizes determined with XRD were similar to the particle sizes determined with TEM indicating that the particles were mono-crystalline.

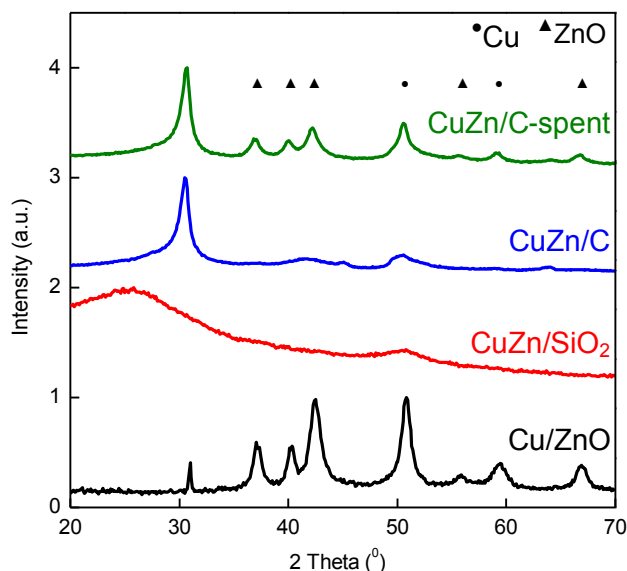


**Figure 3.1.** X-ray diffractograms of Cu/ZnO ( $\text{Cu}_{54}\text{Zn}$  after reduction, black), CuZn/SiO<sub>2</sub> ( $\text{Cu}_8\text{Zn}_{8.0}\text{HSAG}$  after reduction, red), and CuZn/C before ( $\text{Cu}_8\text{Zn}_{8.0}\text{HSAG}$  after reduction, blue) and after methanol synthesis ( $\text{Cu}_8\text{Zn}_{8.0}\text{HSAG}$  after catalysis, green). The broad peak at  $2\theta = 25^\circ$  for the CuZn/SiO<sub>2</sub> sample is due to the silica support and the peaks at  $31^\circ$  for the CuZn/C samples are due to the carbon support.

### Zinc species

Depending on the catalyst formulation and the synthesis procedure, different zinc species can exist after reduction prior to catalysis. X-ray diffraction on CuZn/SiO<sub>2</sub> after reduction revealed the absence of crystalline ZnO in the sample (Figure 3.1, red). This is in agreement with previous results from X-ray absorption that co-impregnation of copper and zinc led to the incorporation of zinc in the silica support resulting in zinc hydroxy(phylo)silicate,<sup>9a</sup> which is more stable than ZnO and SiO<sub>2</sub> separately.<sup>19</sup> For the CuZn/SiO<sub>2</sub> samples after heat treatment in N<sub>2</sub> or 2% NO/N<sub>2</sub>, zinc was thus most likely present in the form of zinc hydroxy(phylo)silicate. Similarly, X-ray diffraction of the CuZn/C samples after reduction did not show the presence of any crystalline zinc species

(Figure 3.1, blue). However, after 10 days of methanol synthesis, X-ray diffractions corresponding to ZnO were detected for samples with a Zn/(Cu+Zn) atomic ratio higher than 0.1 (Figure 3.1, green). Hence, for carbon-supported catalysts, the Zn promoter was present as highly-dispersed, amorphous ZnO prior to catalysis, and crystallized after prolonged exposure to reaction conditions. X-ray diffraction of Cu/ZnO/(Al<sub>2</sub>O<sub>3</sub>) samples after reduction showed the presence of crystalline ZnO with crystallite sizes around 12 nm (Figure 3.1, black).

### Element distribution

To determine the spatial distribution of copper and zinc in the different types of catalysts, STEM-EDX was employed. In the case of CuZn/SiO<sub>2</sub> after heat treatment in 2% NO/N<sub>2</sub> and reduction in H<sub>2</sub>, zinc was located throughout the support with an increased loading near high-density domains of copper particles (Figure S3.9).<sup>9a</sup> In the case of reduced and passivated CuZn/C, both copper nanoparticles and zinc species were found in close intimacy, showing local Cu/Zn ratios close to the bulk Cu/Zn ratios (Figure S3.10 and S3.11). For reduced and passivated Cu/ZnO/(Al<sub>2</sub>O<sub>3</sub>) samples, STEM-EDX showed that particles with a high copper content were located next to particles with a high zinc content (Figure S3.12). For all three different types of catalysts, zinc was thus detected in close proximity to the copper particles.

### Effect of zinc on activity

The activity and selectivity in the methanol synthesis reaction of the different catalysts were investigated at 40 bar (23% CO, 7% CO<sub>2</sub>, 60% H<sub>2</sub>, 10% Ar), 260 °C and CO + CO<sub>2</sub> conversions below 20%, i.e. below the thermodynamic per-pass conversion limit. The selectivity towards methanol was above 98.5% for all catalysts. The methanol synthesis productivity was calculated from the conversion of CO + CO<sub>2</sub> (see supporting information). Turnover frequencies (TOFs) were calculated per surface metal atom and the dispersion was based upon (S)TEM particle size distributions assuming fully accessible spherical copper particles. No correlation between silica support pore size and TOF was observed for samples with similar copper particle sizes, indicating that the copper particles were similarly accessible for methanol synthesis irrespective of the support porosity (Figure S3.15).

Copper catalysts without Zn and a copper particle size larger than 7 nm had a maximum TOF after 2 – 10 h on stream of about  $2.0 \cdot 10^{-3} \text{ s}^{-1}$ , in close accordance with previously reported values for copper on silica under similar conditions (Table S3.1, see Figure S3.13 for typical activity plots as a function of time on stream).<sup>7b, 7d, 7e</sup> Catalysts containing Cu particles and zinc hydroxy(phylo)silicate (Cu/Zn-silicate) were about 5 times

more active while catalysts containing Cu/ZnO were about 10 times more active than Cu catalysts (Table S3.2, S3.3). The TOF for copper particles larger than 7 nm promoted by ZnO was about  $2 \cdot 10^{-2} \text{ s}^{-1}$ , in reasonable agreement to values previously reported in literature.<sup>7d, 7e, 8a, 20</sup>

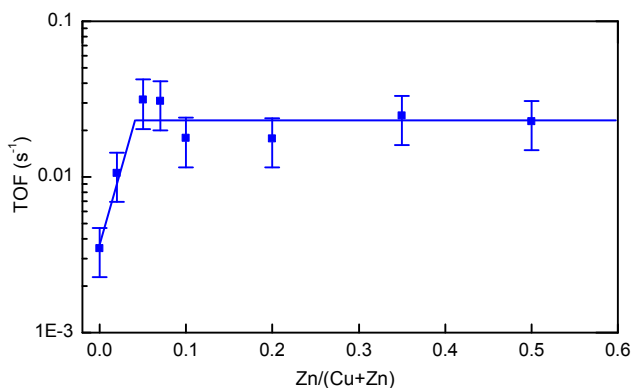


**Figure 3.2.** TOF for methanol synthesis after 2-10 h on stream at 260 °C and 40 bar as a function of zinc loading for CuZn/HSAG catalysts.

The catalytic performance of the CuZn/HSAG catalysts with similar copper particle sizes but varying amounts of ZnO is shown in Figure 3.2. The activity increased upon increasing zinc loading until the maximum activity was reached at a Zn/(Cu+Zn) atomic ratio of 0.05. A further increase in zinc loading did not change the activity significantly. For Cu/ZnO samples the amount of zinc oxide required to obtain maximum site-specific activity corresponds to a Zn/(Cu+Zn) atomic ratio of about 0.1 (Figure S3.14), similar to previous reports.<sup>21</sup> Since the zinc-containing catalysts used to study the effect of the copper particle size all have a zinc loading substantially higher and STEM-EDX showed for the different types of catalysts that zinc was located in close proximity to the copper particles, it is concluded that the promotion by zinc was not limited by the zinc loading for those catalysts. The observed promotion effect for zinc-containing catalysts thus seems to be inherent to the nature and hence thermodynamic stability of the zinc phase, i.e. the thermodynamically less stable ZnO has a stronger promoting effect than the more stable zinc hydroxy(phylo)silicate.<sup>19</sup>

Many mechanistic models have been proposed in literature to explain the role of zinc, including hydrogen spillover from zinc oxide to copper,<sup>22</sup> the facilitation of either Cu<sup>+</sup> or Cu<sup>-</sup> species,<sup>23</sup> shape changes of the Cu nanoparticles on zinc oxide supports,<sup>24</sup> and zinc-induced defects in the copper structure.<sup>8a, 21a</sup> Recent work indicates that the increase in TOF for zinc-containing catalysts is mainly due to the formation of (partially) reduced zinc

species from zinc oxide or zinc hydroxy(phylo)silicate and subsequent migration to the copper surface, increasing the surface specific activity.<sup>8, 25</sup> Since this process is affected by the thermodynamic stability of the zinc phases involved, we expect that for the catalysts containing Zn-silicate the equilibrium amount of zinc species migrated on the surface of the Cu nanoparticles is lower than for samples containing ZnO, and therefore results in a stronger zinc promotion effect for the latter samples.

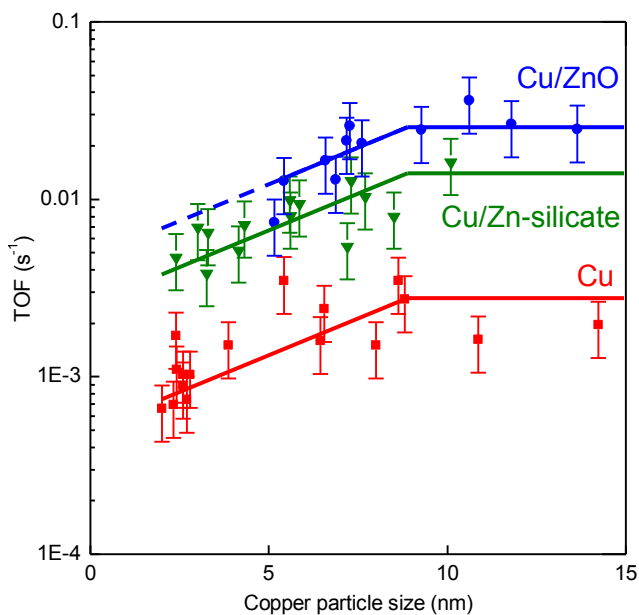


**Figure 3.3.** TOF for methanol synthesis after 2-10 h on stream at 260 °C and 40 bar as a function of number-averaged copper particle size for catalysts containing copper, i.e. Cu/SiO<sub>2</sub>, Cu/(functionalized)SiO<sub>2</sub>, and Cu/C (red), containing Cu/Zn-silicate, i.e. CuZn/SiO<sub>2</sub> (green), and containing Cu/ZnO, i.e. Cu/ZnO/(Al<sub>2</sub>O<sub>3</sub>) and CuZn/C (blue). Error bars indicate the standard deviation in the methanol synthesis activity (35%). For the standard deviation in the particle size, see Figures S3.5-S3.7. Trendlines were added to guide the eye.

### Effect of copper particle size on activity

For all three types of catalysts the TOF decreased with decreasing copper particle size below a size of about 7 nm (Figure 3.3). Within the uncertainty, similar trends seem to apply for catalysts containing Cu, Cu/Zn-silicate and Cu/ZnO although the data for the latter do not allow a conclusion concerning the effect of the particle size below 5 nm. This similarity suggests that the presence and speciation of zinc do not have a significant influence on the relative effect of the copper particle size.

The TOF per surface atom depends on the ratio between active sites and surface atoms, the activation energy of the rate-determining step and the active site coverages of the reactants in that step. Nanosized metallic particles have surface structures with a size-dependent fraction of different surface sites.<sup>3</sup> Every surface site provides an atomic arrangement with its own bond-making and bond-breaking capabilities resulting in a specific activation energy and reactant coverage. For particles larger than ca. 2-3 nm and with a significant d-valence electron density at the Fermi level, the local density of states for a specific surface site is considered to be size-insensitive.<sup>2a</sup> Particle size effects in these systems are therefore mostly due to changes in the fractions of sites with different activities.

The fraction of active sites normalized per surface atom depends on the configuration of metal atoms required and on the size-dependent geometry of the metal surface. Reactions that involve the cleavage or formation of molecular  $\pi$ -bonds, such as the cobalt catalysed Fischer-Tropsch reaction and ruthenium or iron catalysed ammonia synthesis, have been proposed to require a reaction centre with a unique configuration of several metal atoms which smaller particles cannot accommodate, e.g. B5 and C7 sites.<sup>2a, 2c, 3b, 5, 26</sup> Reactions involving the formation and breaking of  $\sigma$ -bonds, such as hydrogenation reactions and C-H bond cleavage, typically do not require a unique configuration of several metal atoms. Reactants, intermediates, transition states and products of these reactions, however, often show stronger adsorption on more unsaturated surface sites.<sup>2a</sup> In the case of the methanol synthesis reaction, density functional theory calculations were performed for a higher Miller-index copper surface Cu(211) which contains step sites, such as B5 and B6 sites, and copper step atoms with lower coordination numbers compared to atoms at the most densely-packed copper surface Cu(111). The DFT calculations predict that the energies of both the intermediates as well as the transition states are lower at the Cu(211) surface.<sup>8a</sup> As a result, the adsorption of (intermediate) surface species at this surface is stronger and the energy barriers for the formation of methanol lower. As shown by Janse van Rensburg et al. and Studt et al., in the case of a syngas feed comprising both CO and CO<sub>2</sub>, the strong adsorption of formate at the higher Miller-index facet results in a high formate surface coverage which can have a poisoning effect on the hydrogenation of CO and at high coverages also on the hydrogenation of CO<sub>2</sub> due to the unavailability of the metal surface to other reaction intermediates.<sup>20, 27</sup>

Considering these aspects, the observed decrease in activity for particles smaller than 7 nm points can be rationalized along two lines. The first possibility is that the active site consists of a unique configuration of copper atoms, in line with the suggestion by Behrens et al. that step sites are the active sites since they exhibit lower energy barriers.<sup>8a</sup> Van Helden et al. have calculated for cobalt fcc particles, that the site fraction of step sites

increases with increasing particle size.<sup>3b</sup> The fraction of so-called B5A and B6 sites stabilizes above 4 nm and the fraction of B5B sites above 8 nm. Although the equilibrium shapes under reaction conditions for copper particles might be slightly different, these calculations show that the observed particle size effect up to 7 nm might be due to changes in the fraction of specific step sites.

Another possibility is that more unsaturated surface sites are poisoned by formate and that the reaction predominantly takes place on sites at more densely-packed copper surfaces which are not poisoned by formate. In this case the copper particle size effect is due to the increase in the fraction of atoms with lower coordination numbers below 7 nm.<sup>3a</sup> Which of these possibilities contributes most to the observed particle size effect depends on whether for more unsaturated surface sites the poisoning effect or the lower energy barrier dominates the activity.

### Conclusion

Methanol synthesis catalysts with copper particle sizes in the range from 2 to 15 nm on supports without zinc, on supports containing zinc hydroxy(phylo)silicate and on supports containing zinc oxide were synthesized. Catalysts containing zinc oxide were about ten times and catalysts containing zinc hydroxy(phylo)silicate were about 5 times more active in the methanol synthesis reaction than catalysts without zinc. The differences in activity are ascribed to the promoting effect of zinc, which is affected by the thermodynamic stability of the zinc phase. The turnover frequency decreased significantly for copper particles smaller than 7 nm for all three types of catalysts. This suggests that the methanol synthesis reaction either takes place at surface sites with a unique configuration of several copper atoms which smaller particles cannot accommodate, or that more unsaturated surface sites are poisoned by formate and that the reaction predominantly takes place at the more densely-packed copper surfaces which are not poisoned by formate.

### Acknowledgments

The project was supported financially by Haldor Topsøe A/S. KPdJ acknowledges the European Research Council, EU FP7 ERC Advanced Grant no. 338846. PEdJ acknowledges The Netherlands Organization for Scientific Research NWO-Vici program. Sebastian Kuld is acknowledged for TPR-MS measurements. Hans Meeldijk is acknowledged for STEM-HAADF and EDX measurements. Ceri Zwart, Elian Griffioen, Jochem Blum and Luc Smulders are acknowledged for the synthesis of CuZnHSAG samples. The authors are grateful to Grace, in particular to Robert Goedvree, for providing the silica gel supports.

## References

- (1) (a) Galeano, C.; Meier, J. C.; Peinecke, V.; Bongard, H.; Katsounaros, I.; Topalov, A. A.; Lu, A.; Mayrhofer, K. J.; Schüth, F. *J. Am. Chem. Soc.* **2012**, *134*, 20457-20465; (b) Bell, A. T. *Science* **2003**, *299*, 1688-1691; (c) Zečević, J.; Vanbutsele, G.; de Jong, K. P.; Martens, J. A. *Nature* **2015**, *528*, 245-248; (d) Torres Galvis, H. M.; Bitter, J. H.; Davidian, T.; Ruitenbeek, M.; Dugulan, A. I.; de Jong, K. P. *J. Am. Chem. Soc.* **2012**, *134*, 16207-16215; (e) Munnik, P.; de Jongh, P. E.; de Jong, K. P. *Chem. Rev.* **2015**, *115*, 6687-6718.
- (2) (a) van Santen, R. A. *Acc. Chem. Res.* **2009**, *42*, 57-66; (b) Henry, C. R. *Surf. Sci. Rep.* **1998**, *31*, 231-325; (c) Hammer, B.; Nørskov, J. K. *Adv. Catal.* **2000**, *45*, 71-129; (d) Andersson, M. P.; Abild-Pedersen, F.; Remediakis, I. N.; Bligaard, T.; Jones, G.; Engbæk, J.; Lytken, O.; Horch, S.; Nielsen, J. H.; Sehested, J. *J. Catal.* **2008**, *255*, 6-19; (e) Somorjai, G. A.; Carrazza, J. *Ind. Eng. Chem. Fundam.* **1986**, *25*, 63-69.
- (3) (a) van Hardeveld, R.; Hartog, F. *Surf. Sci.* **1969**, *15*, 189-230; (b) van Helden, P.; Ciobîcă, I. M.; Coetzer, R. L. *J. Catal. Today* **2016**, *261*, 48-59.
- (4) Haruta, M. *Catal. Today* **1997**, *36*, 153-166.
- (5) Bezemer, G. L.; Bitter, J. H.; Kuipers, H. P.; Oosterbeek, H.; Holeywijn, J. E.; Xu, X.; Kapteijn, F.; van Dillen, A. J.; de Jong, K. P. *J. Am. Chem. Soc.* **2006**, *128*, 3956-3964.
- (6) Hansen, J. B.; Højlund Nielsen, P. E. Methanol Synthesis. In *Handbook of Heterogeneous Catalysis*, Ertl, G.; Knözinger, H.; Schüth, F.; Weltkamp, J., Eds. Wiley-VCH: 2008; pp 2920-2949.
- (7) (a) Chinchin, G. C.; Waugh, K. C.; Whan, D. A. *Appl. Catal.* **1986**, *25*, 101-107; (b) Robbins, J. L.; Iglesia, E.; Kelkar, C. P.; DeRites, B. *Catal. Lett.* **1991**, *10*, 1-10; (c) Kurtz, M.; Wilmer, H.; Genger, T.; Hinrichsen, O.; Muhler, M. *Catal. Lett.* **2003**, *86*, 77-80; (d) Burch, R.; Chappell, R. J. *Appl. Catal.* **1988**, *45*, 131-150; (e) Pan, W. X.; Cao, R.; Roberts, D. L.; Griffin, G. L. *J. Catal.* **1988**, *114*, 440-446.
- (8) (a) Behrens, M.; Studt, F.; Kasatkin, I.; Kühn, S.; Hävecker, M.; Abild-Pedersen, F.; Zander, S.; Girgsdies, F.; Kurr, P.; Knief, B. L.; Tovar, M.; Fischer, R. W.; Nørskov, J. K.; Schlögl, R. *Science* **2012**, *336*, 893-897; (b) Nakamura, J.; Choi, Y.; Fujitani, T. *Top. Catal.* **2003**, *22*, 277-285.
- (9) (a) Prieto, G.; Zečević, J.; Friedrich, H.; de Jong, K. P.; de Jongh, P. E. *Nat. Mater.* **2013**, *12*, 34-39; (b) Vesborg, P. C. K.; Chorkendorff, I.; Knudsen, I.; Balmes, O.; Nerlov, J.; Molenbroek, A. M.; Clausen, B. S.; Helveg, S. *J. Catal.* **2009**, *262*, 65-72.
- (10) (a) Prieto, G.; Meeldijk, J. D.; de Jong, K. P.; de Jongh, P. E. *J. Catal.* **2013**, *303*, 31-40; (b) van den Berg, R.; Parmentier, T. E.; Elkjær, C. F.; Gommès, C. J.; Sehested, J.; Helveg, S.; de Jongh, P. E.; de Jong, K. P. *ACS Catal.* **2015**, *5*, 4439-4448.
- (11) van den Berg, R.; Zečević, J.; Sehested, J.; Helveg, S.; de Jongh, P. E.; de Jong, K. P. *Catal. Today* **2015**, <http://dx.doi.org/10.1016/j.cattod.2015.08.052>.
- (12) Brunauer, S.; Emmett, P. H.; Teller, E. *J. Am. Chem. Soc.* **1938**, *60*, 309-319.
- (13) Barret, E. P.; Joyner, L. G.; Halenda, P. P. *J. Am. Chem. Soc.* **1951**, *73*, 373-380.
- (14) Patterson, A. L. *Phys. Rev.* **1939**, *56*, 978-982.
- (15) Smit, C. J.; Eijkhoudt, R.; Geus, J. W.; Van Dillen, A. J. *Prepr. Pap. -Am. Chem. Soc., Div Fuel Chem.* **1999**, *44*, 119-123.
- (16) Munnik, P.; Wolters, M.; Gabriëlsson, a.; Pollington, S. D.; Headdock, G.; Bitter, J. H.; de Jongh, P. E.; de Jong, K. P. *J. Phys. Chem. C* **2011**, *115*, 14698-14706.
- (17) Wolters, M.; van Grotel, L. J. W.; Eggenhuisen, T. M.; Sietsma, J. R. A.; de Jong, K. P.; de Jongh, P. E. *Catal. Today* **2011**, *163*, 27-32.
- (18) Baltes, C.; Vukojevic, S.; Schüth, F. *J. Catal.* **2008**, *258*, 334-344.
- (19) Barin, I. *Thermochemical Data of Pure Substances*. 3 ed.; VCH Wiley: Weinheim, 1995; Vol. 1.
- (20) Studt, F.; Behrens, M.; Kunkes, E. L.; Thomas, N.; Zander, S.; Tarasov, A.; Schumann, J.; Frei, E.; Varley, J. B.; Abild-Pedersen, F.; Nørskov, J. K.; Schlögl, R. *ChemCatChem* **2015**, *7*, 1105-1111.

## Chapter 3

---

- (21) (a) Günter, M. M.; Ressler, T.; Bems, B.; Büscher, C.; Genger, T.; Hinrichsen, O.; Muhler, M.; Schlögl, R. *Catal. Lett.* **2001**, *71*, 37-44; (b) Fujitani, T.; Nakamura, J. *Catal. Lett.* **1998**, *56*, 119-124.
- (22) Burch, R.; Golunski, S. E.; Spencer, M. S. *J. Chem. Soc. Faraday Trans.* **1990**, *86*, 2683-2691.
- (23) (a) Klier, K. *Adv. Catal.* **1982**, *31*, 243-313; (b) Frost, J. C. *Nature* **1988**, *334*, 577-580.
- (24) Hansen, P. L.; Wagner, J. B.; Helveg, S.; Rostrup-Nielsen, J. R.; Clausen, B. S.; Topsøe, H. *Science* **2002**, *295*, 2053-2055.
- (25) (a) Kuld, S.; Conradsen, C.; Moses, P. G.; Chorkendorff, I.; Sehested, J. *Angew. Chem. Int. Ed.* **2014**, *53*, 5941-5945; (b) Grunwaldt, J. D.; Molenbroek, A. M.; Topsøe, N. Y.; Topsøe, H.; Clausen, B. S. *J. Catal.* **2000**, *194*, 452-460; (c) Naumann d'Alnoncourt, R.; Xia, X.; Strunk, J.; Löffler, E.; Hinrichsen, O.; Muhler, M. *Phys. Chem. Chem. Phys.* **2006**, *8*, 1525-38; (d) Batyrev, E.; van den Heuvel, J.; Beckers, J.; Jansen, W.; Castricum, H. *J. Catal.* **2005**, *229*, 136-143; (e) Jansen, W.; Beckers, J.; v. d. Heuvel, J. C.; Denier v. d. Gon, A. W.; Blik, A.; Brongersma, H. H. *J. Catal.* **2002**, *210*, 229-236.
- (26) (a) Honkala, K.; Hellman, A.; Remediakis, I. N.; Logadottir, A.; Carlsson, A.; Dahl, S.; Christensen, C. H.; Nørskov, J. K. *Science* **2005**, *307*, 555-558; (b) Spencer, N. D.; Schoonmaker, R. C.; Somorjai, G. A. *J. Catal.* **1982**, *74*, 129-135.
- (27) Janse van Rensburg, W.; Petersen, M. A.; Datt, M. S.; van den Berg, J.-A.; van Helden, P. *Catal. Lett.* **2014**, *145*, 559-568.

## Supporting Information

### Supports

**Silica gels** (SG) were obtained from Merck (SG(5)) and Grace-Davison (SG(3), SG(6), SG(11), SG(15), SG(25)). The numbers in the brackets indicate the average pore size as determined from by BJH analysis (4V/A) of the adsorption branch of the N<sub>2</sub> physisorption isotherms.

**High surface area graphite 500** (HSAG) was obtained from Timcal Ltd., Switzerland.

**Stöber silica** (S) and **functionalized Stöber silica** (SN) were synthesized as described in Van den Berg et al. [van den Berg, R., Parmentier, T.E., Elkjær, C.F., Gommes, C.J., Sehested, J., Helveg, S., de Jongh, P.E., de Jong, K.P., *ACS Catal.* 2015, 5, 4439-4448].

**SBA15** was synthesized as described in Prieto et al. [Prieto, G., Zečević, J., Friedrich, H., de Jong, K.P., de Jongh, P.E., *Nat. Mater.*, 2013, 12, 34-39].

**SBA16** silica mesostructures were synthesized with varying porosity. Block-copolymers Pluronic F127 (EO<sub>106</sub>PO<sub>70</sub>EO<sub>106</sub>) and Pluronic P123 (EO<sub>20</sub>PO<sub>70</sub>EO<sub>20</sub>) from Sigma-Aldrich, 1-butanol (p.a., Acros), and tetraethyl ortosilicate (TEOS, 99%, Sigma-Aldrich) were used as received. SBA16c was synthesized following the procedure reported by Kim et al. [Kim, T.-W., Ryoo, R., Kruk, M., Gierszal, K. P., Jaroniec, M., Kamiya, S., Terasaki, O., *J. Phys. Chem. B*, 2004, 108, 11480-11489] using a synthesis gel with the following molar composition: 0.0016 P123/0.0037 F127/1.0 TEOS/4.4 HCl/140 H<sub>2</sub>O. The copolymers were dissolved at room temperature in HCl/H<sub>2</sub>O. TEOS was subsequently added dropwise while using a magnetic stirrer and the gel was aged in an oven at 35 °C for 20 h under static conditions. The mixture was hydrothermally treated at 60 °C for 24 h. SBA16a, SBA16b, SBA16d and SBA16e were prepared using 1-butanol (BuOH) as a swelling agent at low acid concentrations as described by Kleitz et al. [Kleitz, F., Solovyov, L. A., Anilkumar, G. M., Choi, S. H., Ryoo, R., *Chem. Commun.* 2004, 1536-1537]. A synthesis gel with the following molar ratios was used: 0.0035 F127 / 1.79 BuOH / 1.0 TEOS / 0.91 HCl / 120 H<sub>2</sub>O. After the block-copolymer was dissolved in HCl/H<sub>2</sub>O, 1-butanol was added and the mixture was stirred at 40 °C for ½ h (SBA16a and SBA16b) or 1 h (SBA16d and SBA16e). Then, TEOS was added dropwise under stirring and the gel was aged in an oven at 40 °C for 20 h under static conditions. SBA16b was stirred for 5 min prior to the aging. The mixtures were further treated for 48 h at 90 °C (SBA16b and SBA16d), 72 h at 100 °C (SBA16a) or 24 h at 120 °C (SBA16e). In all cases, after the hydrothermal treatment, the resulting solids were filtered, extensively washed with deionized water, and dried at 60 °C (SBA16a and SBA16b) or 120 °C for 10 h (SBA16d and SBA16e). Finally, the products were calcined at 350 °C (SBA16b), 500 °C (SBA16a) or 540 °C (SBA16c, SBA16d and SBA16e) in a muffle oven to remove the copolymer template.

**FDU12** silica materials were synthesized employing 1,3,5-trimethylbenzene (TMB) as a micelle swelling agent and tetraethyl ortosilicate (TEOS) as the silica source. Pluronic F127 (Sigma-Aldrich) and KCl (p.a., Acros) were dissolved in HCl/H<sub>2</sub>O at room temperature. TMB (99%, Acros) was subsequently added and the mixture stirred in a polyethylene bottle at 14 °C for 24 hours. Then TEOS (99%, Sigma-Aldrich) was added drop-wise under stirring and the mixture further stirred at 14 °C for 20 hours. The final synthesis gel molar composition was: 0.004 F127 : 1.7 KCl : 0.93 TMB : 1.0 TEOS : 6.1 HCl : 157 H<sub>2</sub>O. Subsequently, the mixture was divided into two aliquots, transferred to Teflon-lined autoclaves and treated hydrothermally for 48 hours in an oven. The temperature of this hydrothermal treatment was 60 °C (FDU(5)) and 130 °C (FDU(7)). The resulting solids were recovered by filtration and dried at 60 °C for 10 hours. Next, an additional hydrothermal treatment was carried out in order to remove the Na residues that might remain in the silica product. The silica solid was re-dispersed in a 2M HCl aqueous solution (70 mL/g solid) and the resulting suspension was transferred to a polypropylene bottle and hydrothermally treated at 70 °C for 72 hours. Next, the solid was recovered by filtration, washed extensively with 2M HCl and then water until the pH of the washing waters was 6. The solid was dried at 120 °C for 10 hours and then calcined in a muffle oven at 540 °C for 5 hours.

**Carbon Xerogels (CX)** were synthesized through resorcinol condensation catalyzed by sodium carbonate followed by pyrolysis. An amount of 12.89 g formaldehyde (37%, 12% methanol, Fisher chemical) and 8.65 g of resorcinol (99%, Sigma Aldrich) were successively added to 0.017g sodium carbonate (>99%, Acros Chemicals) dissolved in 3.08 g (CX4), 5.14 g (CX5), 8.55 (CX8) or 12.00 g (CX12) water. The mixtures were kept at room temperature for one day, heated to 60 °C for one day and heated to 90 °C for three days. The solid materials were crushed (< 3 mm) and washed twice with acetone for 1 h followed by drying at room temperature for 1 h and one time with acetone for 8 h followed by drying at room temperature for 72 h. Subsequently, the carbon xerogels were pyrolysed in a tubular oven in a 100 ml/min argon flow at 800 °C (5 °C/min) for 10 h and reduced at 600 °C (10 °C/min) for 5h in a 100 ml/min flow of 50% H<sub>2</sub>/Ar.

## Samples

 Table S3.1. Cu(Zn)/SiO<sub>2</sub> Sample list

Sample name <sup>a</sup>	[Cu <sup>2+</sup> ] (M) <sup>b</sup>	[Zn <sup>2+</sup> ] (M) <sup>c</sup>	HT <sup>d</sup>	Cu (%) <sup>e</sup>	Zn (%) <sup>f</sup>	d(Cu) <sub>XRD</sub> (nm) <sup>g</sup>	d(Cu) <sub>TEM</sub> (nm) <sup>h</sup>	X <sub>CO+CO<sub>2</sub></sub> (%) <sup>i</sup>	Activity (mol h <sup>-1</sup> kg <sup>-1</sup> cat) <sup>j</sup>	TOF (s <sup>-1</sup> ) <sup>k</sup>
Cu <sub>1</sub> SN-NO	0.25	-	NO	0.8 <sup>l</sup>	-	n.d.	2.6 <sup>o</sup>	0.6	0.14	8.9*10 <sup>-4</sup>
Cu <sub>1</sub> S-N <sub>2</sub>	0.25	-	N <sub>2</sub>	0.9 <sup>m</sup>	-	n.d.	2.3 <sup>o</sup>	0.9	0.13	7.0*10 <sup>-4</sup>
Cu <sub>2</sub> S-N <sub>2</sub>	0.50	-	N <sub>2</sub>	1.7 <sup>m</sup>	-	n.d.	2.4 <sup>o</sup>	2.7	0.38	1.1*10 <sup>-3</sup>
Cu <sub>2</sub> S-NO	0.50	-	NO	1.9 <sup>m</sup>	-	8.5 <sup>o</sup>	6.5 <sup>o</sup>	1.7	0.22	1.6*10 <sup>-3</sup>
Cu <sub>3</sub> S-NO	1.00	-	NO	3.4	-	10.6 <sup>o</sup>	6.6 <sup>o</sup>	2.9	0.44	2.4*10 <sup>-3</sup>
Cu <sub>14</sub> SBA16a-N <sub>2</sub>	2.86	-	N <sub>2</sub>	14.0	-	-	2.7 <sup>o</sup>	13.5	4.8	1.7*10 <sup>-3</sup>
Cu <sub>15</sub> SBA16b-N <sub>2</sub>	3.50	-	N <sub>2</sub>	15.0	-	-	2.4 <sup>o</sup>	3.8	2.4	7.4*10 <sup>-4</sup>
Cu <sub>7</sub> FDU(5)-N <sub>2</sub>	2.00	-	N <sub>2</sub>	7.1	-	-	2.8 <sup>o</sup>	4.1	1.3	1.0*10 <sup>-3</sup>
Cu <sub>5</sub> FDU(7)-N <sub>2</sub>	1.05	-	N <sub>2</sub>	5.1	-	-	2.6 <sup>o</sup>	4.1	1.1	1.0*10 <sup>-3</sup>
Cu <sub>8</sub> SG(3)-N <sub>2</sub>	4.35	-	N <sub>2</sub>	7.7 <sup>j</sup>	-	n.d.	2.0 <sup>n</sup>	2.2	1.3	6.6*10 <sup>-4</sup>
Cu <sub>16</sub> SG(3)-NO	4.35	-	NO	10.0 <sup>m</sup>	-	5.2 <sup>n</sup> , 3.2 <sup>o</sup>	3.9 <sup>n</sup>	5.1	1.5	1.2*10 <sup>-3</sup>
Cu <sub>9</sub> SG(5)-NO	2.86	-	NO	9.1 <sup>m</sup>	-	6.7 <sup>n</sup> , 7.3 <sup>o</sup>	8.8 <sup>n</sup>	7.3	1.4	2.7*10 <sup>-3</sup>
Cu <sub>9</sub> SG(6)-NO	2.00	-	NO	8.6 <sup>m</sup>	-	7.1 <sup>n</sup> , 7.6 <sup>o</sup>	8.6 <sup>n</sup>	12.9	1.8	3.5*10 <sup>-3</sup>
Cu <sub>7</sub> SG(11)-NO	1.05	-	NO	6.7 <sup>m</sup>	-	8.2 <sup>n</sup> , 10.2 <sup>o</sup>	10.9 <sup>n</sup>	3.2	0.5	1.6*10 <sup>-3</sup>
Cu <sub>6</sub> SG(15)-NO	0.86	-	NO	6.1 <sup>m</sup>	-	9.3 <sup>n</sup> , 14.6 <sup>o</sup>	14.2 <sup>n</sup>	3.2	0.4	2.0*10 <sup>-3</sup>
Cu <sub>40</sub> SiO <sub>2</sub> <sup>p</sup>	-	-	-	40.1 <sup>l</sup>	-	5.2 <sup>n</sup>	8.0 <sup>n</sup>	10.5	3.9	1.5*10 <sup>-3</sup>
Cu <sub>12</sub> ZnSBA15-N <sub>2</sub>	2.60	1.40	N <sub>2</sub>	11.5 <sup>l</sup>	5.9	2.4 <sup>n</sup>	3.3 <sup>n</sup>	10.3	6.5	3.9*10 <sup>-3</sup>
Cu <sub>12</sub> ZnSBA15-NO	2.60	1.40	NO	12.2 <sup>j</sup>	5.9	3.5 <sup>n</sup>	4.3 <sup>n</sup>	17.3	9.1	7.2*10 <sup>-3</sup>
Cu <sub>4</sub> ZnSBA16c-NO	2.60	1.40	NO	4.3 <sup>l</sup>	2.8	n.d.	2.4 <sup>n</sup>	7.8	3.6	4.7*10 <sup>-3</sup>
Cu <sub>10</sub> ZnSBA16d-NO	2.60	1.40	NO	9.9 <sup>l</sup>	6.1	7.9 <sup>o</sup>	3.3 <sup>n</sup>	12.1	7.9	6.5*10 <sup>-3</sup>
Cu <sub>12</sub> ZnSBA16e-NO	2.60	1.40	NO	11.9 <sup>l</sup>	7.2	7.3 <sup>o</sup>	4.8 <sup>n</sup>	16.0	10.2	7.0*10 <sup>-3</sup>
Cu <sub>11</sub> ZnSG(5)-NO	3.25	1.75	NO	10.8 <sup>l</sup>	5.9	2.4 <sup>o</sup>	4.2 <sup>n</sup>	15.8	7.2	5.2*10 <sup>-3</sup>
Cu <sub>10</sub> ZnSG(6)-NO	2.21	1.19	NO	10.0 <sup>l</sup>	5.3	3.2 <sup>o</sup>	5.6 <sup>n</sup>	14.7	9.2	1.0*10 <sup>-2</sup>
Cu <sub>12</sub> ZnSG(6)-NO	2.60	1.40	NO	11.8 <sup>l</sup>	6.1	4.8 <sup>o</sup>	5.6 <sup>n</sup>	13.1	8.3	8.1*10 <sup>-3</sup>
Cu <sub>8</sub> ZnSG(11)-NO	1.30	0.70	NO	7.6 <sup>l</sup>	4.1	5.4 <sup>o</sup>	5.9 <sup>n</sup>	13.1	5.4	9.5*10 <sup>-3</sup>
Cu <sub>12</sub> ZnSG(11)-NO	2.60	1.40	NO	11.8 <sup>l</sup>	7.3	6.4 <sup>o</sup>	7.7 <sup>n</sup>	12.0	7.5	1.0*10 <sup>-2</sup>
Cu <sub>7</sub> ZnSG(15)-NO	1.04	0.56	NO	6.9 <sup>l</sup>	3.9	6.8 <sup>o</sup>	7.2 <sup>n</sup>	5.7	2.6	5.4*10 <sup>-3</sup>
Cu <sub>16</sub> ZnSG(15)-NO	2.60	1.40	NO	16.0 <sup>l</sup>	8.2	9.5 <sup>o</sup>	7.3 <sup>n</sup>	18.0	11.5	1.3*10 <sup>-2</sup>
Cu <sub>5</sub> ZnSG(25)-NO	0.65	0.35	NO	5.2 <sup>m</sup>	2.9	6.7 <sup>o</sup>	8.5 <sup>n</sup>	8.3	2.2	8.1*10 <sup>-3</sup>
Cu <sub>17</sub> ZnSG(25)-NO	2.60	1.40	NO	17.0	9.4	9.9 <sup>o</sup>	10.1 <sup>n</sup>	12.9	12.4	1.6*10 <sup>-2</sup>

<sup>a</sup>Cu<sub>x</sub> stands for the copper weight loading, Zn indicates the presence of zinc (in a 65/35 Cu/Zn molar ratio), and the metal contents are followed by the abbreviation of the support. "N<sub>2</sub>" or "NO" indicates the gas atmosphere at which the sample is heat treated at 350 °C after incipient wetness impregnation and drying, i.e. with either 750 mL/min N<sub>2</sub> (N<sub>2</sub>) or 375 mL/min 2% NO/N<sub>2</sub> (NO). <sup>b</sup>Cu<sup>2+</sup> is the copper ion concentration in the aqueous impregnation solution, <sup>c</sup>Zn<sup>2+</sup> is the zinc ion concentration in the aqueous impregnation solution. <sup>d</sup>Heat treatment (HT) at 350 °C of sample after incipient wetness impregnation with either 750 mL/min N<sub>2</sub> (N<sub>2</sub>) or 375 mL/min 2% NO/N<sub>2</sub> (NO). <sup>e</sup>Nominal copper weight loading in the final catalyst (assuming copper is metallic and zinc oxidic).

<sup>f</sup>Nominal zinc weight loading in the final catalyst. <sup>g</sup>Cu or CuO crystallite size as determined by XRD with the Scherrer equation. <sup>h</sup>Number-averaged particle size as determined with TEM. <sup>i</sup>CO+CO<sub>2</sub> conversion, <sup>j</sup>Peak methanol productivity after 2 to 10 h on stream normalized per kg of catalyst per hour. <sup>k</sup>Turnover Frequency for methanol synthesis normalized per surface copper atom after 2 to 10 h on stream. <sup>l</sup>Copper loading determined with TPR-TCD. <sup>m</sup>Copper loading determined with TPR-MS. <sup>n</sup>Cu crystal or particle size. <sup>o</sup>CuO crystal or particle size. <sup>p</sup>Cu/SiO<sub>2</sub> prepared via precipitation followed by reduction.

**Table S3.2.** Cu(Zn)/C sample list

Sample name <sup>a</sup>	[Cu <sup>2+</sup> ] <sup>b</sup>	[Zn <sup>2+</sup> ] <sup>c</sup>	Cu (%) <sup>d</sup>	Zn (%) <sup>e</sup>	d(Cu) <sub>XRD</sub> (nm) <sup>f</sup>	d(Cu) <sub>TEM</sub> (nm) <sup>g</sup>	X <sub>CO+CO<sub>2</sub></sub> (%) <sup>h</sup>	Activity (mol h <sup>-1</sup> kg <sup>-1</sup> cat <sup>-1</sup> ) <sup>i</sup>	TOF (s <sup>-1</sup> ) <sup>j</sup>
Cu <sub>9</sub> HSAG	2.00	-	8.6	-	3.9	5.4	12.1	2.5	3.5*10 <sup>-3</sup>
Cu <sub>9</sub> Zn <sub>0.2</sub> HSAG	2.00	0.04	8.6	0.2	3.2	6.3	7.1	7.1	1.1*10 <sup>-2</sup>
Cu <sub>9</sub> Zn <sub>0.5</sub> HSAG	2.00	0.11	8.5	0.5	3.3	8.0	11.4	13.7	3.1*10 <sup>-2</sup>
Cu <sub>9</sub> Zn <sub>0.7</sub> HSAG	2.00	0.15	8.6	0.7	4.9	5.7	9.6	20.3	3.1*10 <sup>-2</sup>
Cu <sub>9</sub> Zn <sub>1.0</sub> HSAG	2.00	0.22	8.5	1.0	3.2	8.9	8.4	7.7	1.8*10 <sup>-2</sup>
Cu <sub>9</sub> Zn <sub>2.2</sub> HSAG	2.00	0.50	8.4	2.2	10.2	8.7	7.9	7.5	1.8*10 <sup>-2</sup>
Cu <sub>8</sub> Zn <sub>4.5</sub> HSAG	2.00	1.08	8.1	4.5	4.0	9.3	5.4	8.8	2.5*10 <sup>-2</sup>
Cu <sub>8</sub> Zn <sub>8.0</sub> HSAG	2.00	2.00	7.7	8.0	3.5	8.7	10.3	9.6	2.3*10 <sup>-2</sup>
CuZnCX(4)	1.95	1.05	4.4	2.4	11.6	5.4	7.2	5.1	1.3*10 <sup>-2</sup>
CuZnCX(5)	1.32	0.71	4.4	2.4	9.9	7.3	7.0	6.5	2.6*10 <sup>-2</sup>
CuZnCX(8)	0.75	0.40	3.9	2.1	7.1	7.6	5.1	4.8	2.1*10 <sup>-2</sup>
CuZnCX(12)	0.75	0.40	4.8	2.7	8.1	10.6	12.3	6.6	3.6*10 <sup>-2</sup>

<sup>a</sup>Cu<sub>x</sub> stands for the copper weight loading, Zn<sub>x</sub> stands for the zinc weight loading, and the metal contents are followed by the abbreviation of the support. <sup>b</sup>Cu<sup>2+</sup> is the copper ion concentration in the aqueous impregnation solution. <sup>c</sup>Zn<sup>2+</sup> is the zinc ion concentration in the aqueous impregnation solution. <sup>d</sup>Nominal copper weight loading in the final catalyst (assuming copper is metallic and zinc oxidic). <sup>e</sup>Nominal zinc weight loading in the final catalyst. <sup>f</sup>Cu crystallite size as determined by XRD with the Scherrer equation. <sup>g</sup>Number-averaged particle size as determined with TEM. <sup>h</sup>CO+CO<sub>2</sub> conversion, <sup>i</sup>Peak methanol productivity after 2 to 10 h on stream normalized per kg of catalyst per hour. <sup>j</sup>Turnover Frequency for methanol synthesis normalized per surface copper atom after 2 to 10 h on stream.

**Table S3.3.** Cu/ZnO(/Al<sub>2</sub>O<sub>3</sub>) sample list

Sample name <sup>a</sup>	[Cu <sup>2+</sup> ] (M) <sup>b</sup>	[Zn <sup>2+</sup> ] (M) <sup>c</sup>	[Al <sup>3+</sup> ] (M) <sup>d</sup>	Cu (%) <sup>e</sup>	ZnO (%) <sup>f</sup>	Al <sub>2</sub> O <sub>3</sub> (%) <sup>g</sup>	d(ZnO) <sub>xrd</sub> (nm) <sup>h</sup>	d(Cu) <sub>xrd</sub> (nm) <sup>i</sup>	d(Cu) <sub>TEM</sub> (nm) <sup>j</sup>	X <sub>CO+CO<sub>2</sub></sub> (%) <sup>k</sup>	Activity (mol h <sup>-1</sup> kg <sup>-1</sup> ) <sup>l</sup>	TOF (s <sup>-1</sup> ) <sup>m</sup>
Cu <sub>4</sub> Zn	0.1	1.9	-	4.2	95.8	-	11.8	7.9	6.6	11.3	4.4	1.7*10 <sup>-2</sup>
Cu <sub>21</sub> Zn	0.5	1.5	-	20.7	79.3	-	12.3	5.9	5.2	21.1	13.3	7.4*10 <sup>-3</sup>
Cu <sub>34</sub> Zn	0.8	1.2	-	34.2	65.8	-	12.9	5.5	6.9	9.0	30.1	1.3*10 <sup>-2</sup>
Cu <sub>54</sub> Zn	1.2	0.8	-	53.9	46.1	-	12.3	11.9	11.8	11.7	46.9	2.7*10 <sup>-2</sup>
Cu <sub>65</sub> Zn	1.4	0.6	-	64.6	35.4	-	13.9	13.5	13.6	11.7	55.2	2.5*10 <sup>-2</sup>
Cu <sub>88</sub> Zn	1.8	0.2	-	87.5	12.5	-	14.3	24.4	30.4	9.4	21.6	1.9*10 <sup>-2</sup>
Cu <sub>94</sub> Zn	1.9	0.1	-	93.7	6.3	-	16.3	31.6	33.7	0.3	0.79	1.2*10 <sup>-3</sup>
Cu <sub>58</sub> ZnAl	1.2	0.5	0.3	57.7	30.8	11.6	8.9	8.2	7.2	17.8	80.7	2.1*10 <sup>-2</sup>

<sup>a</sup>Cu<sub>x</sub> stands for the copper weight loading, Zn indicates the presence of zinc oxide, Al indicates the presence of alumina. <sup>b</sup>Cu<sup>2+</sup> is the copper ion concentration in the aqueous impregnation solution. <sup>c</sup>Zn<sup>2+</sup> is the zinc ion concentration in the aqueous impregnation solution. <sup>d</sup>Al<sup>3+</sup> is the aluminum ion concentration in the aqueous impregnation solution. <sup>e</sup>Nominal copper weight loading in the final catalyst (assuming catalyst compositions of metallic copper, zinc oxide and alumina). <sup>f</sup>Nominal zinc oxide weight loading in the final catalyst. <sup>g</sup>Nominal alumina weight loading in the final catalyst. <sup>h</sup>ZnO crystallite size as determined by XRD with the Scherrer equation. <sup>i</sup>Cu crystallite size as determined by XRD with the Scherrer equation. <sup>j</sup>Number-averaged particle size as determined with TEM, <sup>k</sup>CO+CO<sub>2</sub> conversion, <sup>l</sup>Peak methanol productivity after 2 to 10 h on stream normalized per kg of catalyst per hour. <sup>m</sup>Turnover Frequency for methanol synthesis normalized per surface copper atom after 2 to 10 h on stream.

**N<sub>2</sub>-physorption**

The N<sub>2</sub>-physorption data of all the supports and precipitated catalysts after reduction and passivation are shown below.

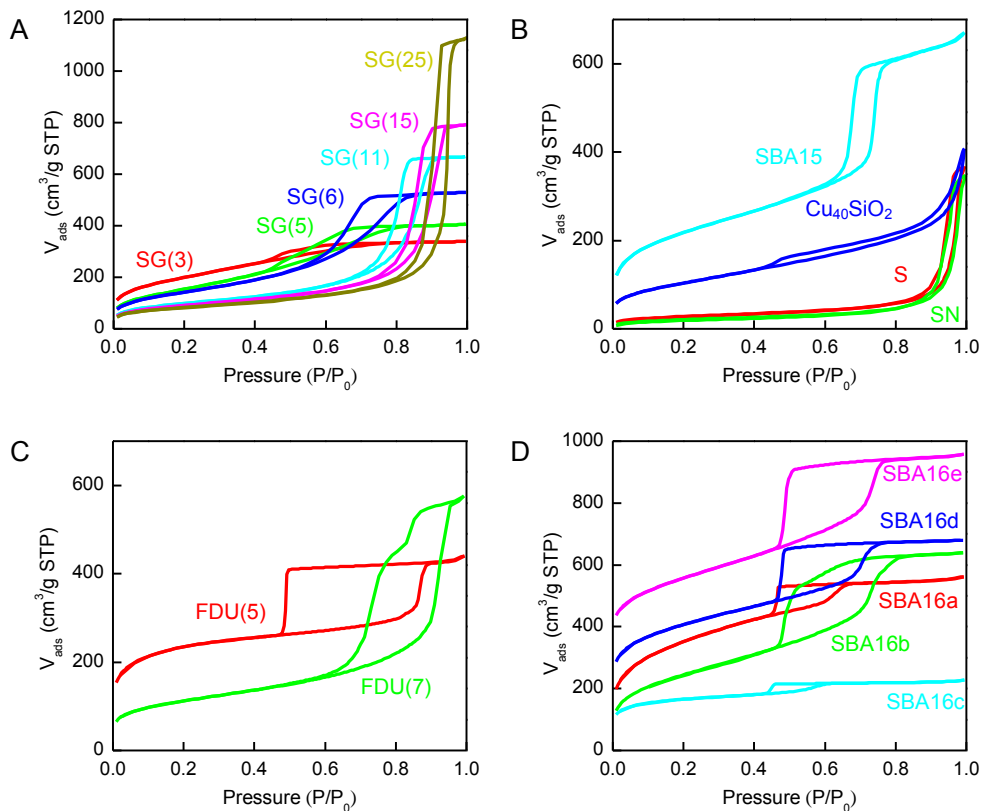


**Figure S3.1.** N<sub>2</sub>-physorption isotherms of the silica supports. (A) six different silica gels, (B) Stöber silica (S), functionalized Stöber silica (SN),  $\text{Cu}/\text{SiO}_2$  prepared via precipitation followed by reduction and SBA15, (C) two FDU supports and (D) SBA16 supports.

**Table S3.4.** Data derived from N<sub>2</sub>-physorption isotherms on the carbon supports shown in Figure S3.1; Pore Volume (PV) determined at  $p/p_0=0.9975$ ; average pore size from BJH analysis (4V/A) of the adsorption isotherm.

Support	BET (m <sup>2</sup> /g)	PV (cm <sup>3</sup> /g)	Average pore size (nm)
SG(3)	720	0.52	3.4
SG(5)	520	0.82	4.5
SG(6)	575	0.63	6.1
SG(11)	355	1.03	10.6
SG(15)	330	1.20	15.0
SG(25)	300	1.43	24.8
S	100	0.58	20.3
SN	75	0.53	23.0
SBA-15	775	1.00	4.3
Cu <sub>40</sub> SiO <sub>2</sub>	375	0.59	5.6
FDU(5)	815	0.66	4.8
FDU(7)	390	0.90	7.3
SBA-16a	1255	0.86	3.2
SBA-16b	885	0.98	4.8
SBA-16c	570	0.34	3.0
SBA-16d	925	0.82	4.3
SBA-16e	930	1.00	4.5

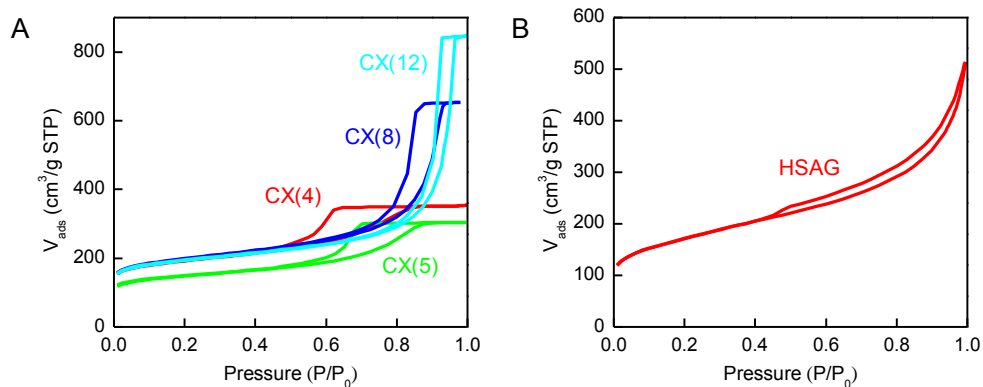


**Figure S3.2.** N<sub>2</sub>-physorption isotherms of the carbon supports. (A) four different carbon xerogels and (B) high surface area graphite.

## Chapter 3

**Table S3.5.** Data derived from N<sub>2</sub>-physorption isotherms on the carbon supports shown in Figure S3.2; Pore Volume (PV) determined at  $p/p_0=0.9975$ ; average pore size from BJH analysis (4V/A) of the adsorption isotherm.

Support	BET (m <sup>2</sup> /g)	PV (cm <sup>3</sup> /g)	Average pore size (nm)
HSAG	592	0.79	5.5
CX(4)	637	0.39	4.1
CX(5)	491	0.47	4.6
CX(8)	655	0.86	8.4
CX(12)	639	1.15	12.0

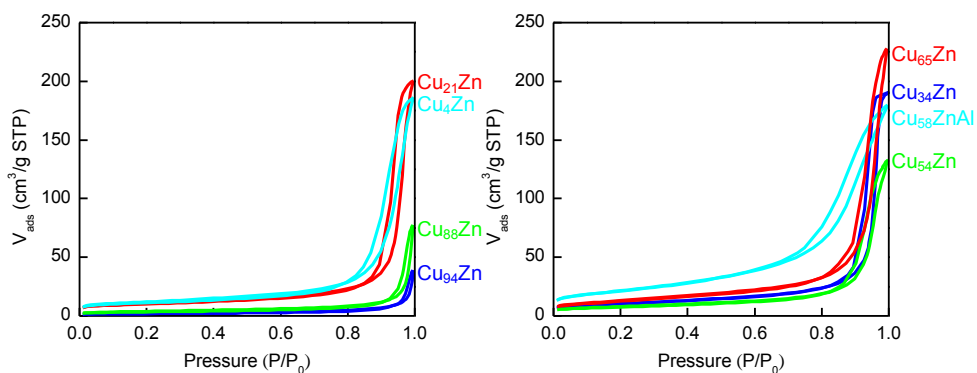


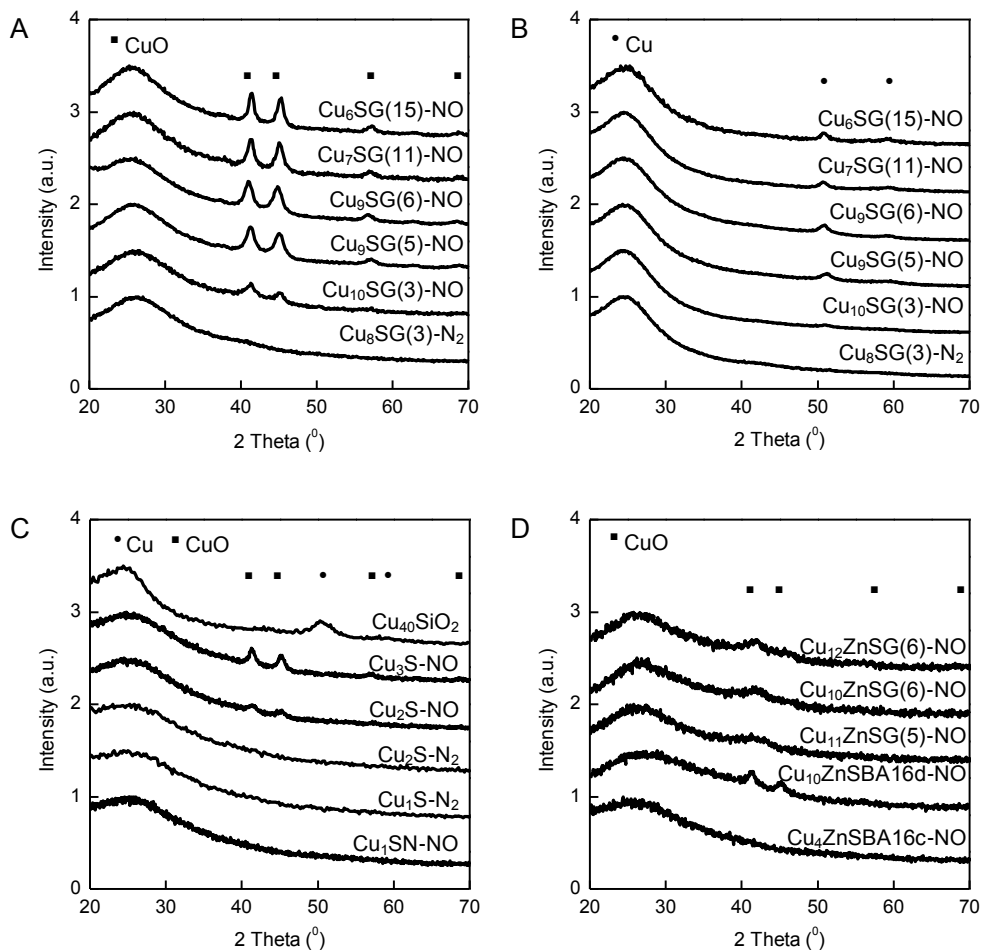
**Figure S3.3.** N<sub>2</sub>-physorption isotherms of the precipitated Cu/ZnO/(Al<sub>2</sub>O<sub>3</sub>) samples after reduction and passivation.

**Table S3.6.** Data derived from N<sub>2</sub>-physorption isotherms on the precipitated Cu/ZnO/(Al<sub>2</sub>O<sub>3</sub>) samples shown in Figure S3.3; Pore Volume (PV) determined at  $p/p_0=0.9975$ ; average pore size from BJH analysis (4V/A) of the adsorption isotherm.

Sample	BET (m <sup>2</sup> /g)	PV (cm <sup>3</sup> /g)	Average pore size (nm)
Cu <sub>4</sub> Zn	42	0.29	28.0
Cu <sub>21</sub> Zn	37	0.31	37.0
Cu <sub>34</sub> Zn	36	0.30	33.9
Cu <sub>54</sub> Zn	28	0.21	30.3
Cu <sub>58</sub> ZnAl	77	0.28	12.7
Cu <sub>65</sub> Zn	47	0.35	27.9
Cu <sub>88</sub> Zn	14	0.12	37.4
Cu <sub>94</sub> Zn	9	0.06	28.8

## XRD

For impregnated Cu(Zn)/SiO<sub>2</sub> samples diffractograms are taken after heat treatment. For precipitated Cu/ZnO(Al<sub>2</sub>O<sub>3</sub>), precipitated Cu/SiO<sub>2</sub>, and impregnated Cu(Zn)/C samples, diffractograms are taken after reduction and passivation.



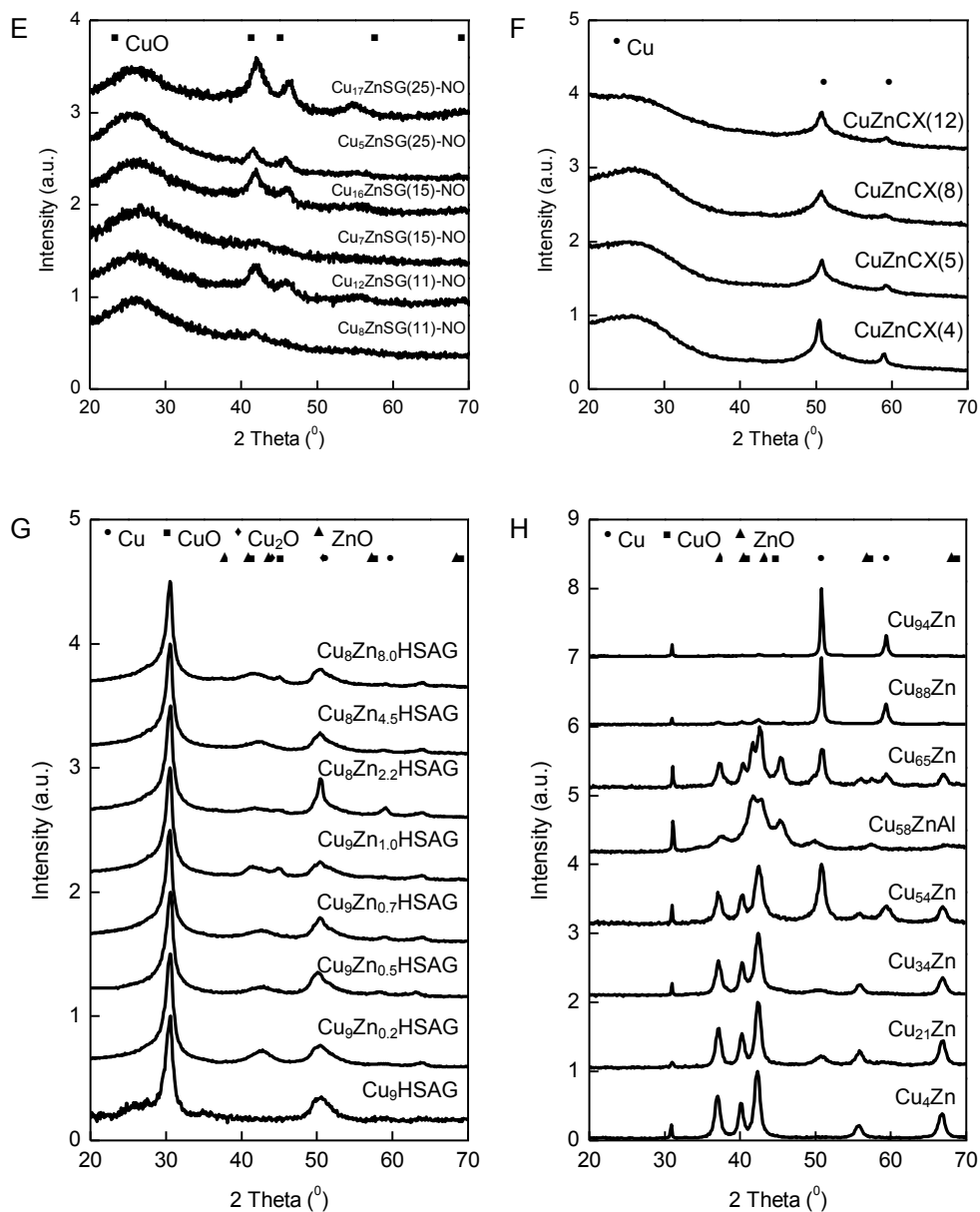


**Figure S3.4.** X-ray diffractograms of the different samples. (A) Cu/silica gel after heat treatment in N<sub>2</sub> or 2% NO/N<sub>2</sub>, (B) Cu/silica gel after reduction and passivation, (C) Cu/SiO<sub>2</sub>, (D and E) CuZn/SiO<sub>2</sub>, (F) CuZn/CX, (G) CuZn/HSAG and (H) Cu/ZnO/(Al<sub>2</sub>O<sub>3</sub>).

### (S)TEM

TEM micrographs and corresponding particle size distributions are shown in Figures S3.5, S3.6 and S3.7. Cu/SBA16 samples were imaged in dark-field mode with a Tecnai 12 electron microscope (FEI). CuZn/SG and CuZn/SBA16 samples were imaged in HAADF-STEM mode with a Tecnai 20FEG microscope (FEI). All other samples were imaged in bright-field mode with a Tecnai 12 electron microscope (FEI).

Cu/S, Cu/SN, Cu/SBA16 and Cu/FDU samples are imaged after heat treatment in N<sub>2</sub> or 2% NO/N<sub>2</sub>. All the other samples are imaged after reduction and passivation.

In the case of CuZn/SiO<sub>2</sub> and CuZn/C samples crystalline zinc species were not detected prior to catalysis (Figure 3.1 and Figure S3.4). High-contrast spherical particles were with STEM-EDX identified to consist mainly of copper (Figure S3.9-S3.11). The size of high-contrast spherical particles in (S)TEM was therefore used to determine the copper particle size distribution.

In the case of Cu/ZnO/(Al<sub>2</sub>O<sub>3</sub>) samples XRD showed the presence of ZnO crystallites with an average size varying from 9 to 16, and Cu crystallites with an average size varying from 6 to 32 (Table S3.3 and Figure S3.4). STEM-EDX showed that high-contrast spherical particles consisted mainly of copper while lower-contrast anisotropic particles consisted mainly of ZnO (Figure S3.12). For the different samples the estimated ratio between high-contrast spherical particles and lower-contrast anisotropic particles seemed to correspond to the Cu/ZnO weight ratio. The projected area of the high-contrast spherical particles in TEM was therefore used to determine the copper particle size distribution. The number-average particle size of the as-determined distributions was similar to the average crystallite sizes determined with XRD, evidencing the validity of the criteria used to identify the copper particles.

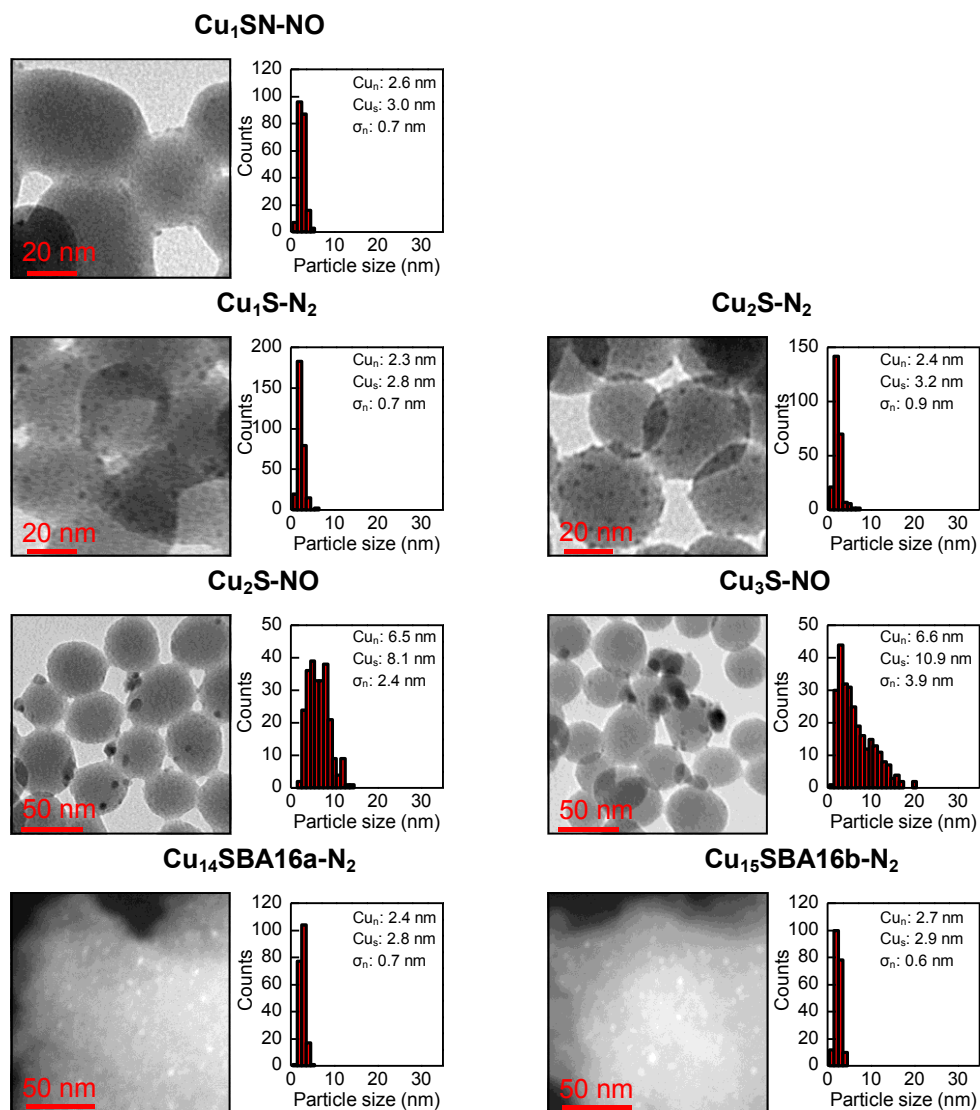


**Figure S3.5a.** TEM images of Cu(Zn)/SiO<sub>2</sub> samples and corresponding particle size distributions, number-averaged particle size ( $Cu_n$ ), surface-averaged particle size ( $Cu_s$ ), and standard deviation of the particle size distribution ( $\sigma_n$ ).

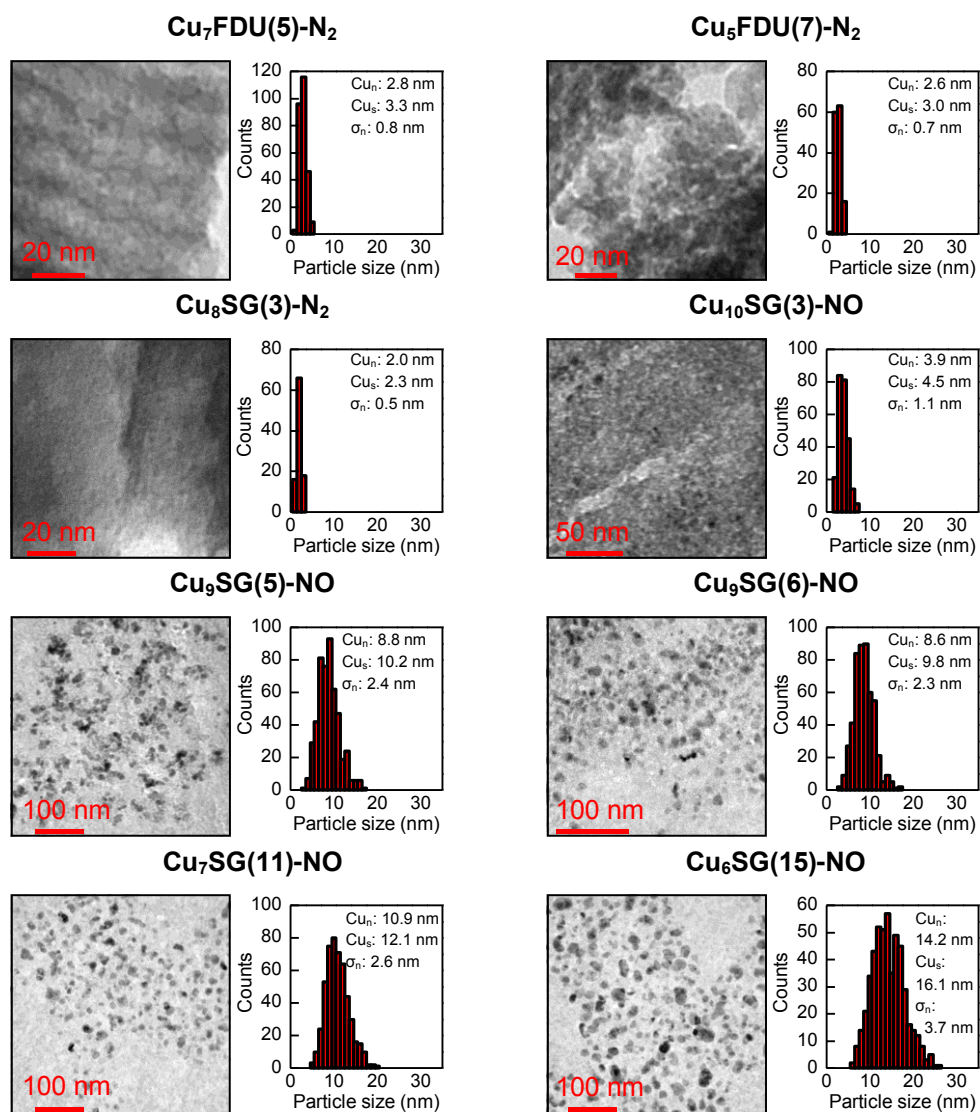


**Figure S3.5b.** TEM images of Cu(Zn)/SiO<sub>2</sub> samples and corresponding particle size distributions, number-averaged particle size ( $Cu_n$ ), surface-averaged particle size ( $Cu_s$ ), and standard deviation of the particle size distribution ( $\sigma_n$ ).

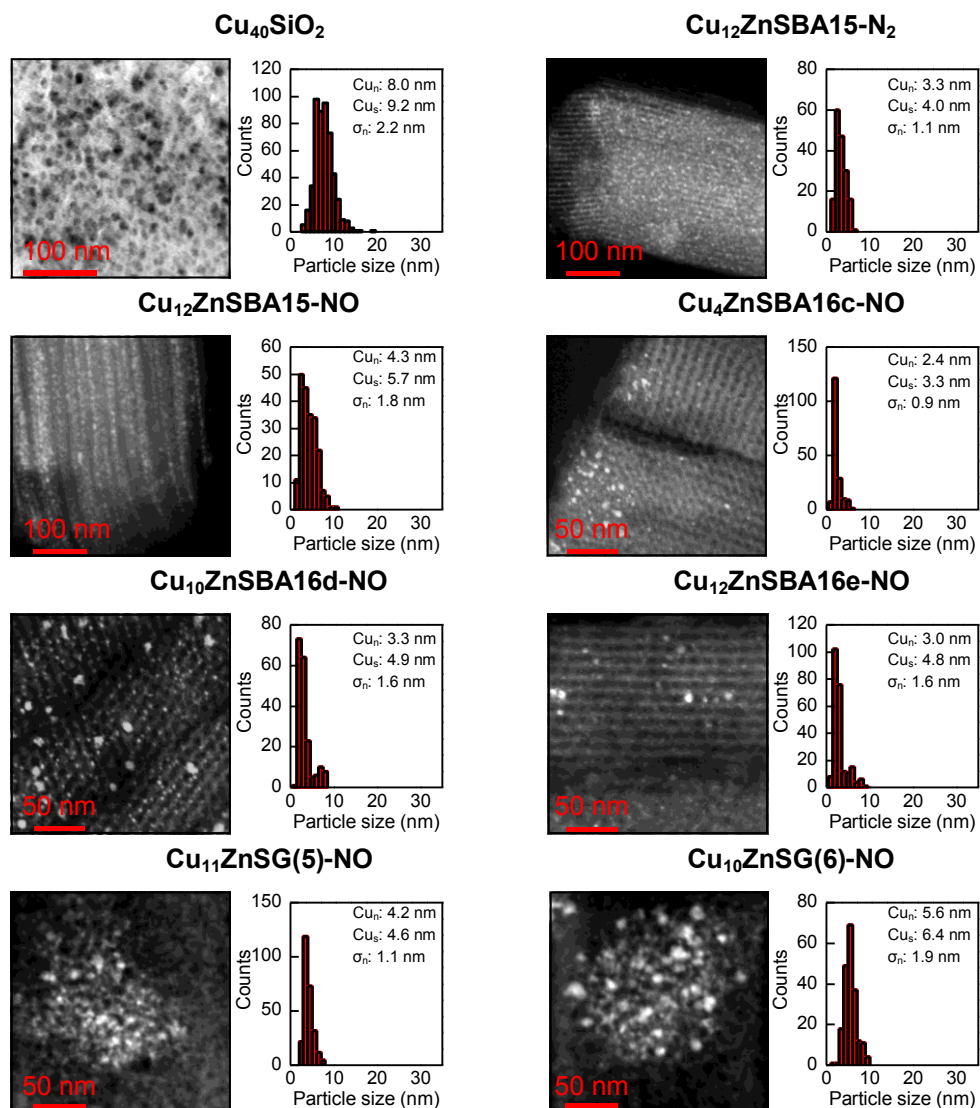


**Figure S3.5c.** TEM images of Cu(Zn)/SiO<sub>2</sub> samples and corresponding particle size distributions, number-averaged particle size (Cu<sub>n</sub>), surface-averaged particle size (Cu<sub>s</sub>), and standard deviation of the particle size distribution (σ<sub>n</sub>).

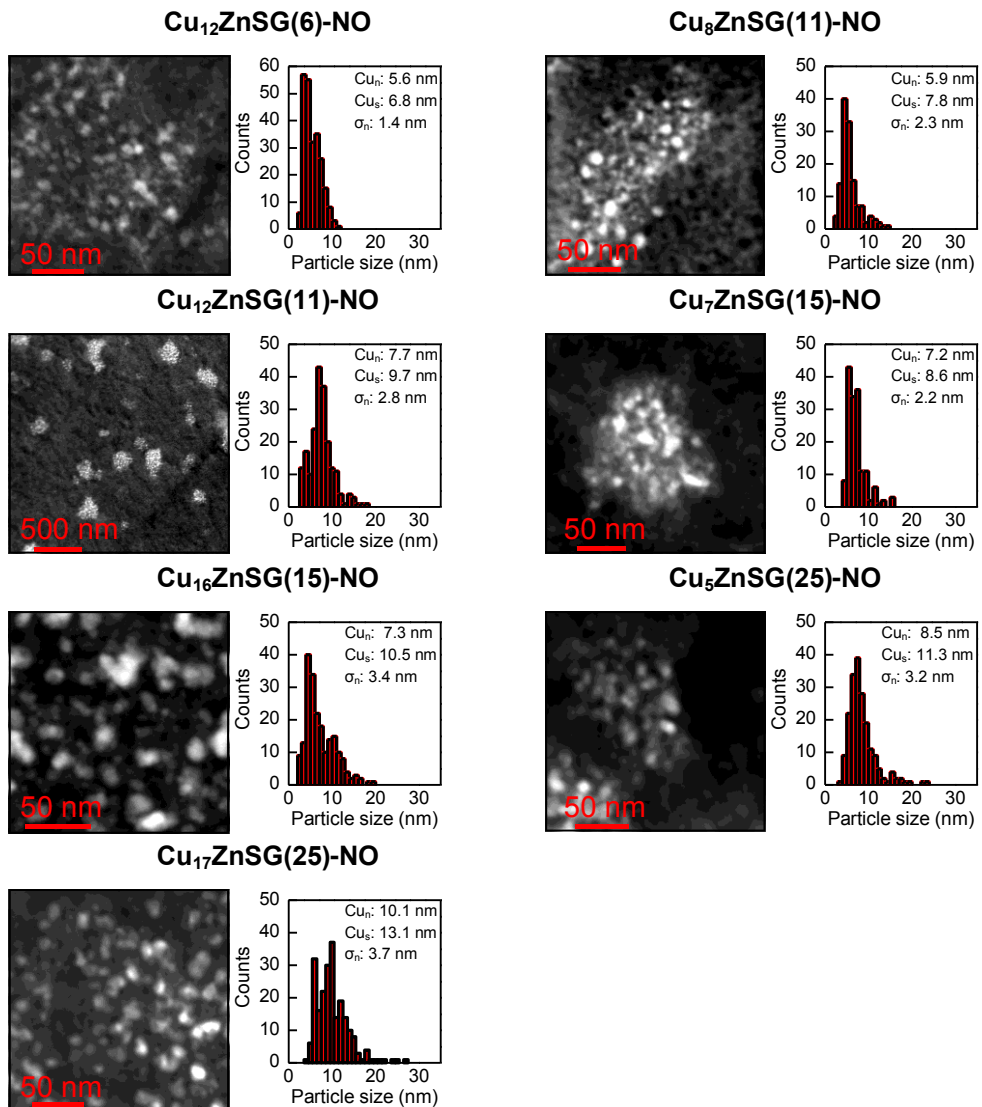


**Figure S3.5d.** TEM images of Cu(Zn)/SiO<sub>2</sub> samples and corresponding particle size distributions, number-averaged particle size ( $Cu_n$ ), surface-averaged particle size ( $Cu_s$ ), and standard deviation of the particle size distribution ( $\sigma_n$ ).

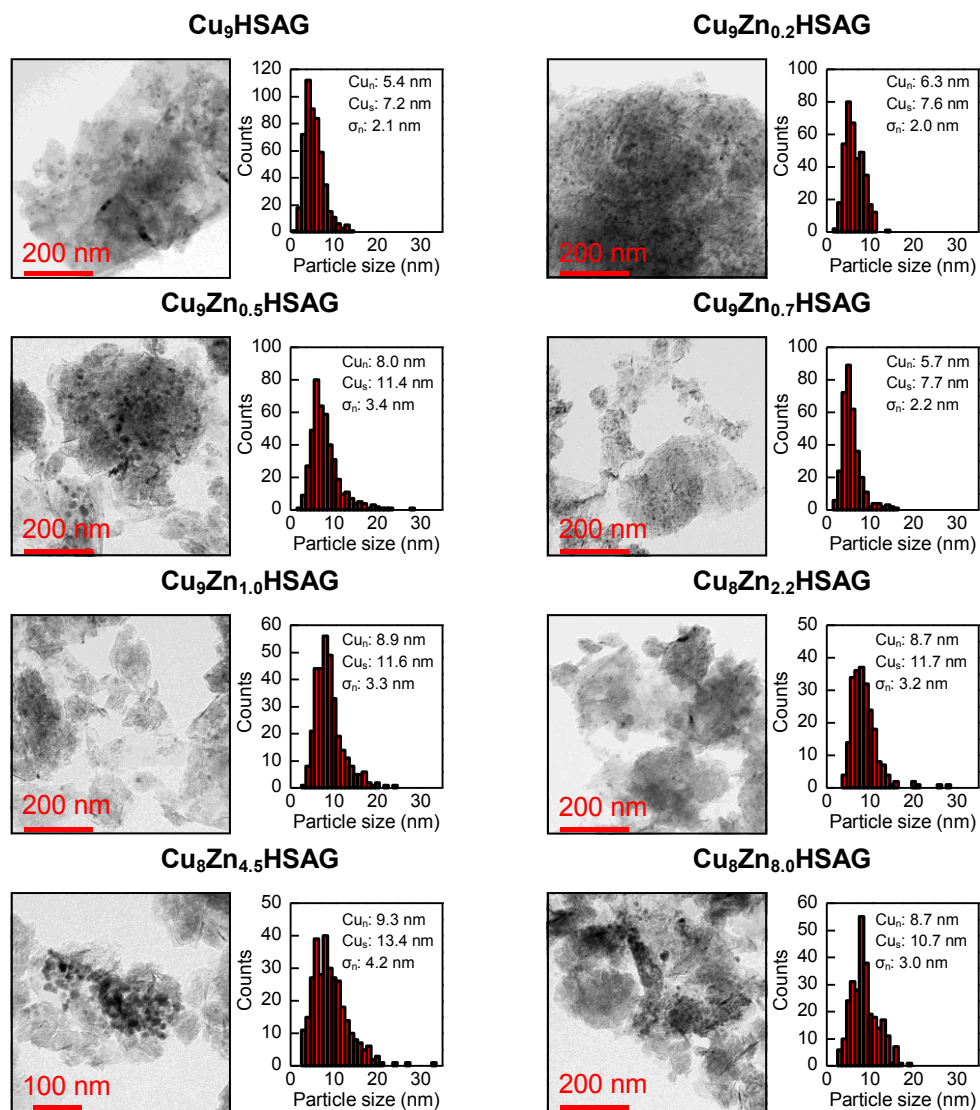


**Figure S3.6a.** TEM images of Cu(Zn)/C samples and corresponding particle size distributions, number-averaged particle size ( $Cu_n$ ), surface-averaged particle size ( $Cu_s$ ), and standard deviation of the particle size distribution ( $\sigma_n$ ).

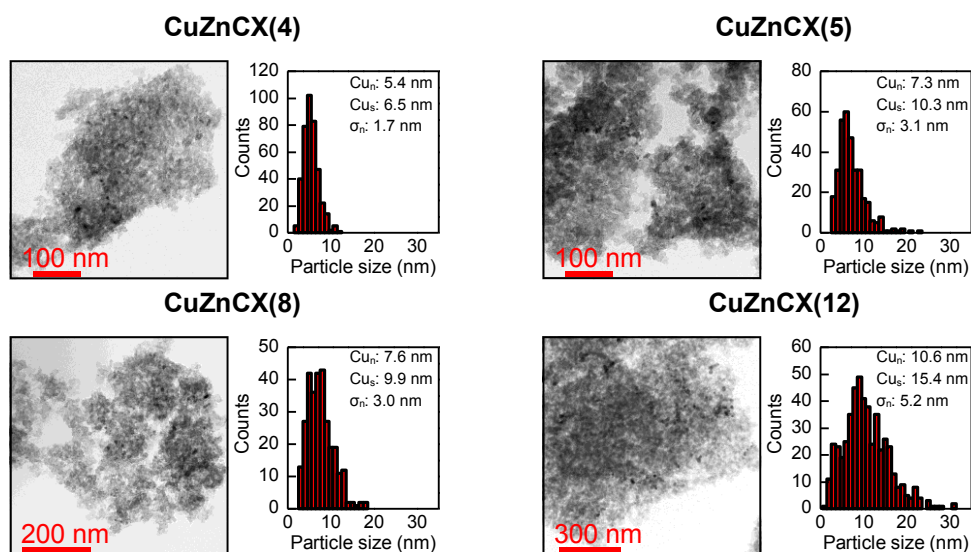


**Figure S3.6b.** TEM images of Cu(Zn)/C samples and corresponding particle size distributions, number-averaged particle size ( $Cu_n$ ), surface-averaged particle size ( $Cu_s$ ), and standard deviation of the particle size distribution ( $\sigma_n$ ).

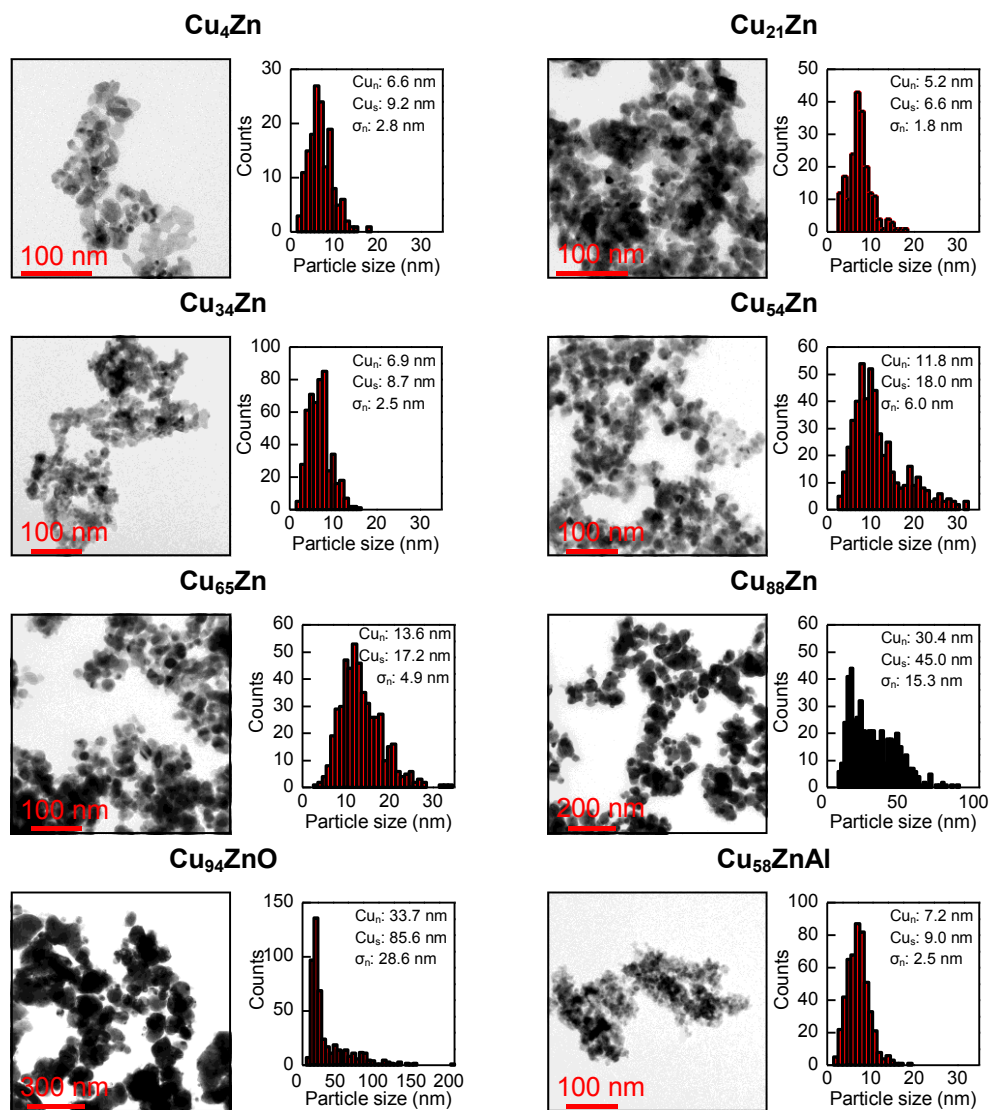


**Figure S3.7.** TEM images of Cu/ZnO/Al<sub>2</sub>O<sub>3</sub> samples and corresponding particle size distributions, number-averaged particle size ( $Cu_n$ ), surface-averaged particle size ( $Cu_s$ ), and standard deviation of the particle size distribution ( $\sigma_n$ ).

TEM number-averaged copper particle size as a function of the copper loading in Cu/ZnO(/Al<sub>2</sub>O<sub>3</sub>) samples

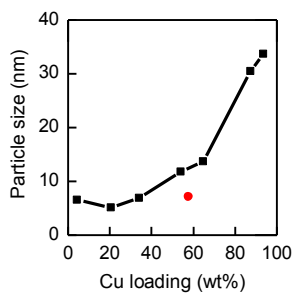


**Figure S3.8.** TEM number-averaged copper particle size as a function of the copper loading for Cu/ZnO (black) and Cu/ZnO/Al<sub>2</sub>O<sub>3</sub> (red). Cu/ZnO/Al<sub>2</sub>O<sub>3</sub> had a lower copper particle size than Cu/ZnO with comparable copper loadings.

STEM-EDX

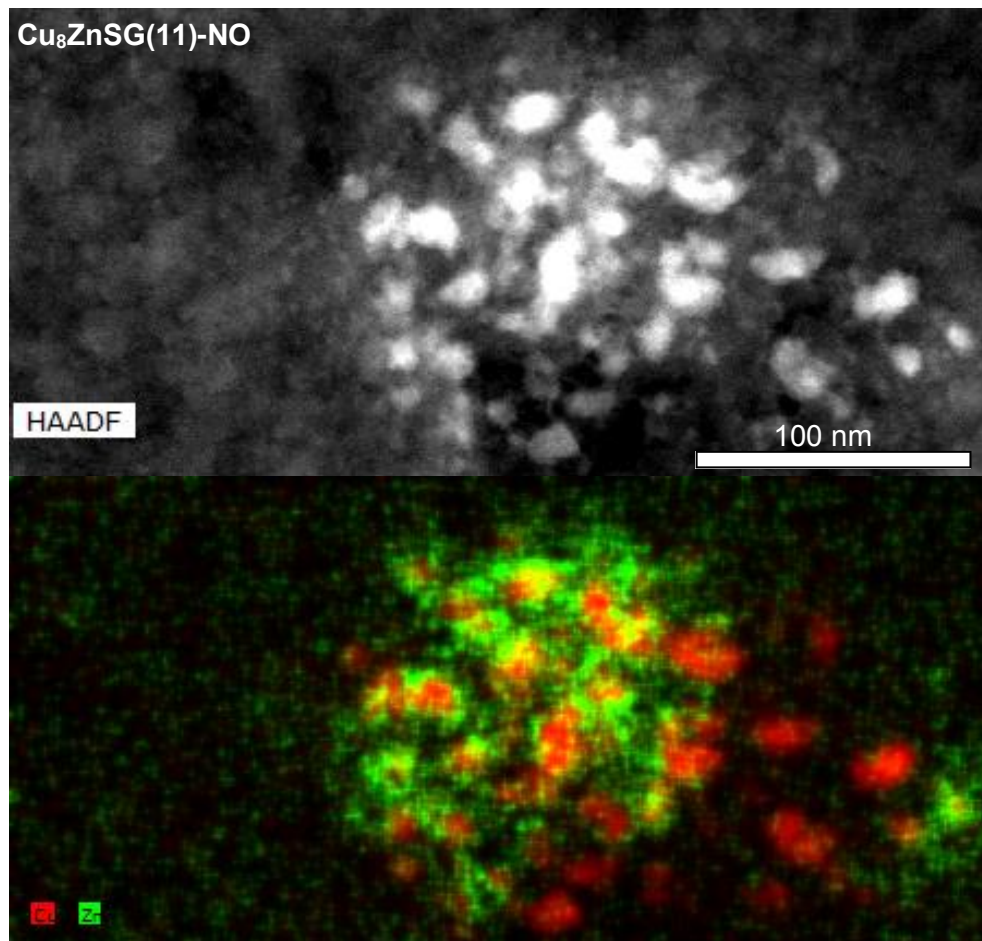


**Figure S3.9.** STEM-HAADF image and corresponding EDX map with a pixel size of 0.62 nm of Cu<sub>8</sub>ZnSG(11)-NO using the TALOS F200x microscope. EDX spectra were processed using the Esprit software (Bruker AXS). Color intensities correspond to the integrated intensities of the Cu-K and Zn-K signal after background correction and are normalized per element. A smooth (3) map filter is used. The average Cu:Zn atomic ratio in the region is 90:10, as determined by using a k-factor of 1.820 and 1.948 for Cu and Zn, respectively.

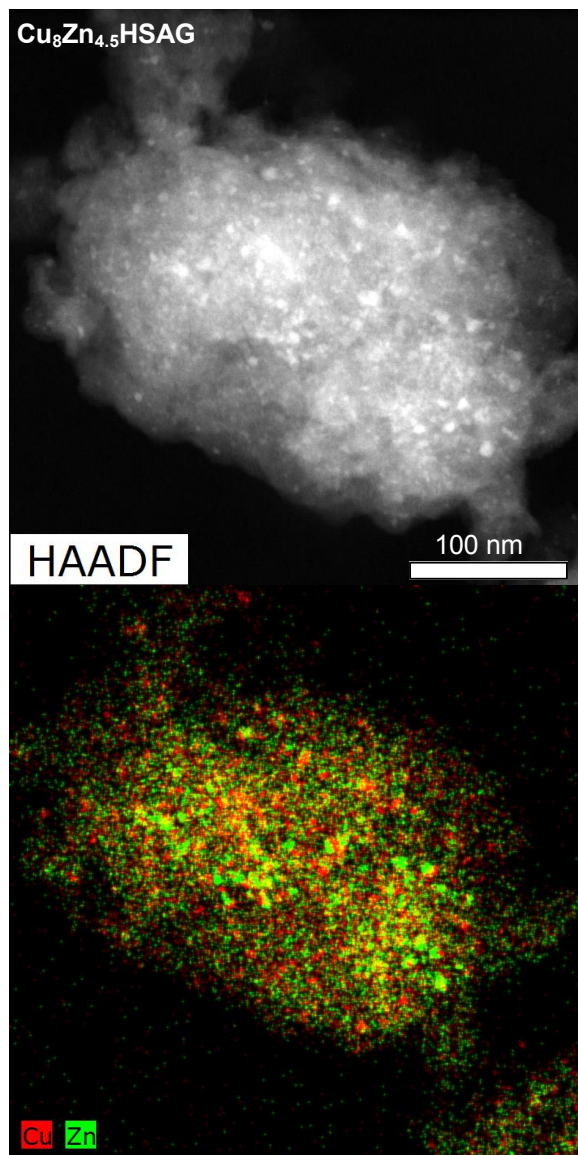


**Figure S3.10.** STEM-HAADF image and corresponding EDX map with a pixel size of 0.51 nm of  $\text{Cu}_8\text{Zn}_{4.5}\text{HSAG}$  using the TALOS F200x microscope. EDX spectra were processed using the Esprit software (Bruker AXS). Color intensities correspond to the integrated intensities of the Cu-K and Zn-K signal after background correction and are normalized per element. The average Cu:Zn atomic ratio in the region is 63:37, as determined by using a k-factor of 1.820 and 1.948 for Cu and Zn, respectively.

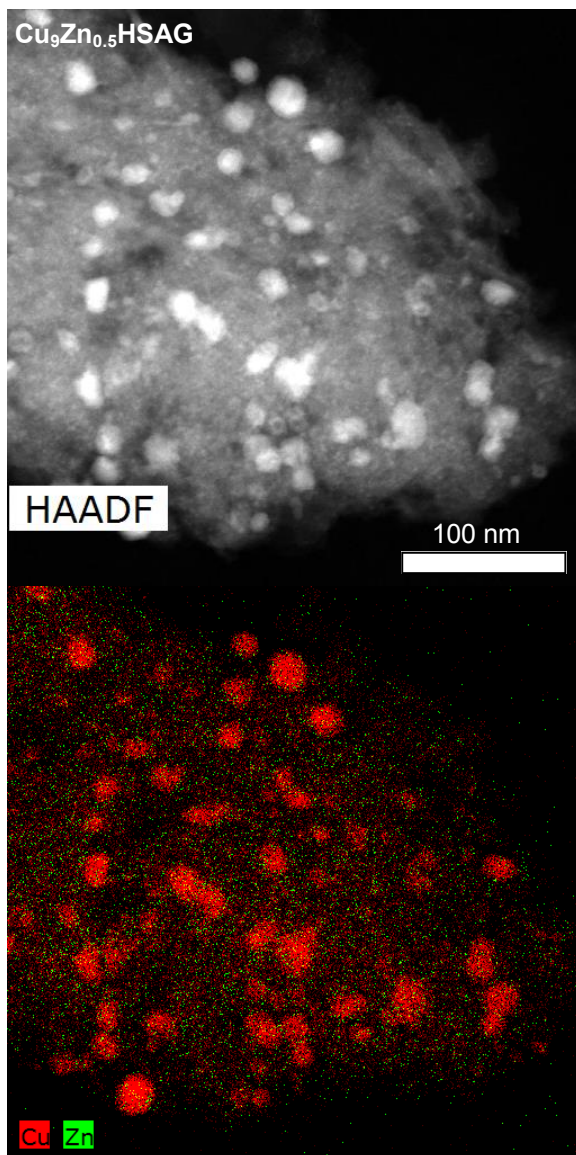


**Figure S3.11.** STEM-HAADF image and corresponding EDX map with a pixel size of 0.68 nm of  $\text{Cu}_9\text{Zn}_{0.5}\text{HSAG}$  using the TALOS F200x microscope. EDX spectra were processed using the Esprit software (Bruker AXS). Color intensities correspond to the integrated intensities of the Cu-K and Zn-K signal after background correction and are normalized per element. The average Cu:Zn atomic ratio in the region is 96:4, as determined by using a k-factor of 1.820 and 1.948 for Cu and Zn, respectively.

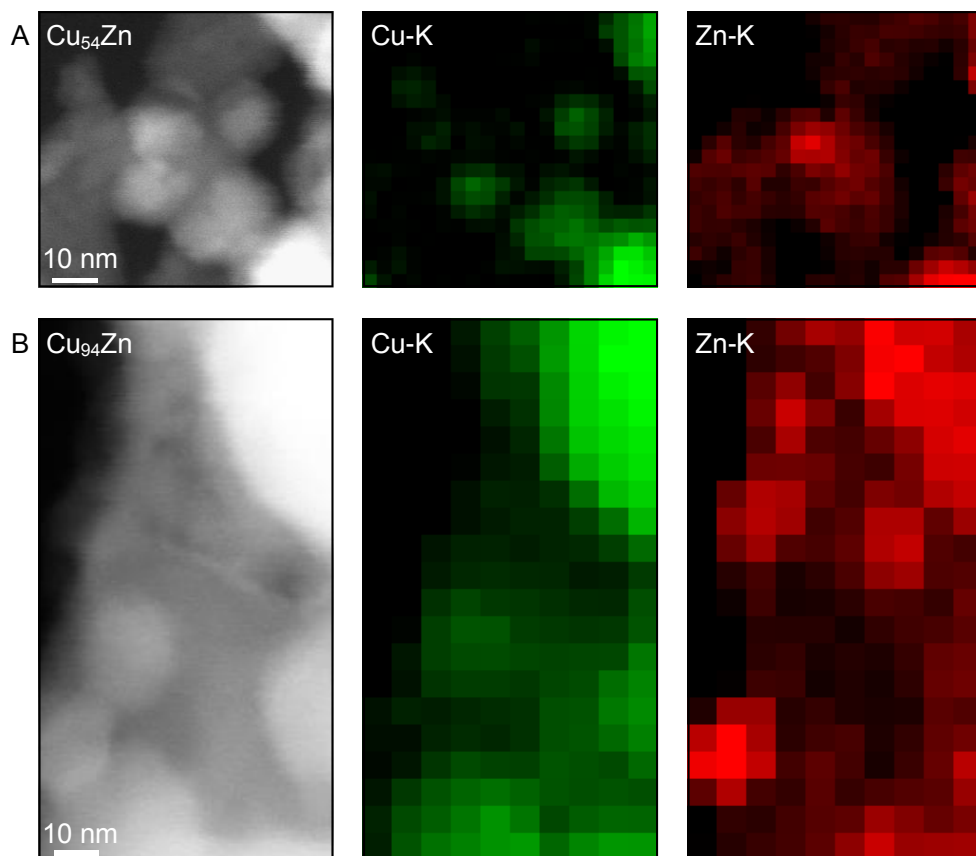


**Figure S3.12.** STEM-HAADF images and corresponding EDX maps of (A)  $\text{Cu}_{44}\text{Zn}$  and (B)  $\text{Cu}_{94}\text{Zn}$  using the Tecnai 20FEG microscope. EDX spectra were processed using the Tecnai Imaging and Analysis software. Color intensities correspond to the integrated peak intensities of the Cu-K and Zn-K signal after background correction and are normalized per element. The average Cu:Zn atomic ratio per region, as determined by using a detector correction of 0.997 and 0.997 and a k-factor of 1.757 and 1.851 for Cu and Zn, respectively, is 52:48 for  $\text{Cu}_{54}\text{Zn}$  and 82:18 for  $\text{Cu}_{94}\text{Zn}$ .

### Catalytic activity calculation

The methanol productivity is based upon the CO + CO<sub>2</sub> conversion. The conversion of CO or CO<sub>2</sub> is calculated by the difference in CO/Ar or CO<sub>2</sub>/Ar ratio between chromatograms taken during reaction and chromatograms taken of the gas feed before reaction (eq. 3.1 and 3.2).

$$X_{CO} = \frac{\frac{CO_{feed}}{Ar_{feed}} - \frac{CO_{reaction}}{Ar_{reaction}}}{\frac{CO_{feed}}{Ar_{feed}}} \quad \text{Eq. 3.1}$$

$$X_{CO_2} = \frac{\frac{CO_2_{feed}}{Ar_{feed}} - \frac{CO_2_{reaction}}{Ar_{reaction}}}{\frac{CO_2_{feed}}{Ar_{feed}}} \quad \text{Eq. 3.2}$$

X<sub>CO</sub> and X<sub>CO<sub>2</sub></sub> are the conversion of CO and CO<sub>2</sub>, respectively. CO<sub>feed</sub>, CO<sub>2feed</sub> and Ar<sub>feed</sub> are the peak areas of the corresponding gases in the TCD chromatograms of the syngas feed before catalysis. CO<sub>reaction</sub>, CO<sub>2reaction</sub> and Ar<sub>reaction</sub> are the peak areas of the exit gas composition during catalysis. The methanol productivity is calculated by the CO + CO<sub>2</sub> conversion (eq. 3.3).

$$n_{MeOH} = X_{CO} * n_{CO} + X_{CO_2} * n_{CO_2} \quad \text{Eq. 3.3}$$

n<sub>MeOH</sub> is the rate of methanol production. n<sub>CO</sub> or n<sub>CO<sub>2</sub></sub> is the molar flow rate of CO or CO<sub>2</sub>, respectively, into the reactor, calculated via equation 3.4 and 3.5.

$$n_{CO} = \frac{Q_{CO} * P_{ref}}{RT_{ref}} * \phi \quad \text{Eq. 3.4}$$

$$n_{CO_2} = \frac{Q_{CO_2} * P_{ref}}{RT_{ref}} * \phi \quad \text{Eq. 3.5}$$

Q<sub>CO</sub> or Q<sub>CO<sub>2</sub></sub> are the molar fractions of CO and CO<sub>2</sub> in the syngas feed, P<sub>ref</sub> is the pressure and T<sub>ref</sub> the temperature at which the mass flow controller has been calibrated and R is the gas constant. φ is the syngas flow into the reactor as measured by the mass flow controller. To obtain catalyst mass-based productivities (P) The calculated rate of methanol production was divided by the mass of the catalyst (m<sub>cat</sub>) according to Eq. 3.6. The catalyst mass is corrected for the loss of mass during reduction prior to catalysis.

$$P = \frac{n_{MeOH}}{m_{cat}} \quad \text{Eq. 3.6}$$

Turnover frequencies (TOF) were calculated per surface metal atom. The number of surface atoms was based on the TEM copper particle size distributions assuming fully accessible spherical particles. First, the surface averaged particle size (PS) was calculated via Eq. 3.7.

$$PS = \frac{\sum_1^n D_i^3}{\sum_1^n D_i^2} \quad \text{Eq. 3.7}$$

$D_i$  is the diameter of the  $i$ th particle. The dispersion (ratio between copper surface atoms and total copper atoms) was calculated according to Eq. 3.8.

$$dispersion = \frac{6V_m}{A_m * PS} \quad \text{Eq. 3.8}$$

$V_m$  is the molar volume and  $A_m$  the molar area of the particles. In the case of copper  $V_m$  is  $7.09 * 10^{21} \text{ nm}^3$  and  $A_m$  is  $4.10 * 10^{22} \text{ nm}^2$ . The dispersion of copper ( $dispersion_{cu}$ ) is therefore given by Eq. 3.9 with PS in nm.

$$dispersion_{cu} = \frac{1.04}{PS} \quad \text{Eq. 3.9}$$

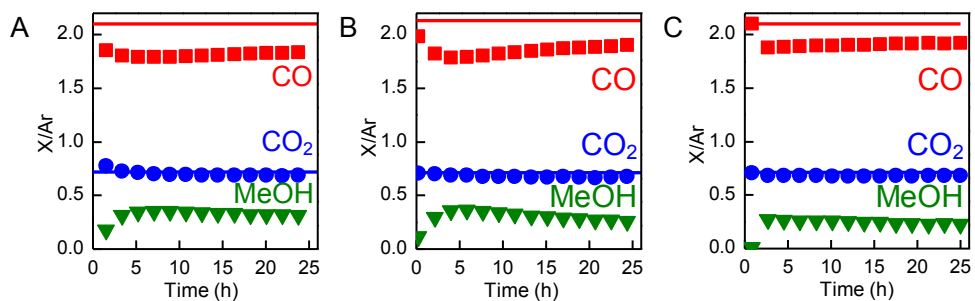
The molar amount of copper surface atoms in the catalyst ( $Cu_{surf}$ ) was calculated by Eq. 3.10

$$Cu_{surf} = dispersion_{cu} * \frac{Wt_{cu}}{M_{cu}} * m_{cat} \quad \text{Eq. 3.10}$$

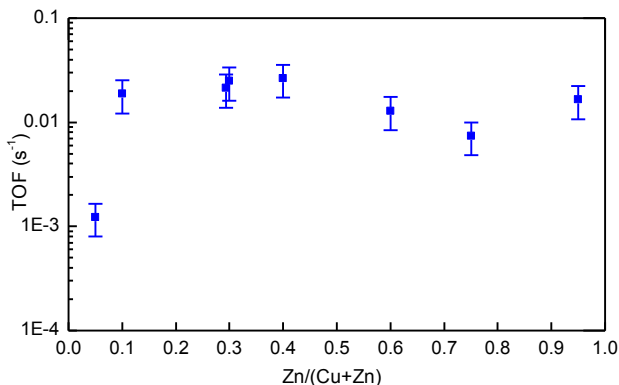
Where  $Wt_{cu}$  is the weight fraction of copper in the catalyst and  $M_{cu}$  the molar mass of copper. TOFs were calculated according to Eq. 3.11

$$TOF = \frac{n_{MeOH}}{Cu_{surf}} \quad \text{Eq. 3.11}$$

## Catalytic performance over time



**Figure S3.13.** Exit CO/Ar, CO<sub>2</sub>/Ar and MeOH/Ar ratios of the integrated peak intensities in the GC chromatograms during the first 25 hours on stream for three different catalysts; A) Cu<sub>9</sub>HSAG, B) Cu<sub>8</sub>ZnSG(11)-NO, C) Cu<sub>34</sub>Zn. Solid lines indicate the ratios in the feed composition. At t=0 the temperature is increased from 100 °C to 260 °C with a heating rate of 2 °C/min. The peak CO+CO<sub>2</sub> conversion after 2 to 10 h on stream is used to calculate the TOF.

TOF for methanol synthesis as a function of zinc loading for Cu/ZnO/(Al<sub>2</sub>O<sub>3</sub>) samples

**Figure S3.14.** Turnover frequency of the eight Cu/ZnO/(Al<sub>2</sub>O<sub>3</sub>) samples plotted against the zinc loading. The maximum activity was reached at Zn/(Cu+Zn) loading of about 0.1. A further increase did not change the activity significantly.

**Support confinement**

Heat treatment in N<sub>2</sub> of non-functionalized SiO<sub>2</sub> impregnated with copper nitrate resulted in the formation of 2-3 nm sized copper particles, irrespective of the support porosity. Figure S3.15 shows the TOFs of the six Cu/SiO<sub>2</sub>-N<sub>2</sub> (red) samples plotted against the corresponding support pore size. There is no clear correlation between the support pore size and TOF indicating that the copper particles were similarly accessible for methanol synthesis irrespective of the support porosity.

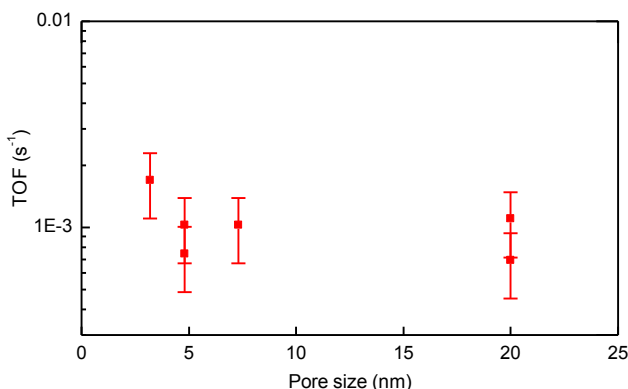
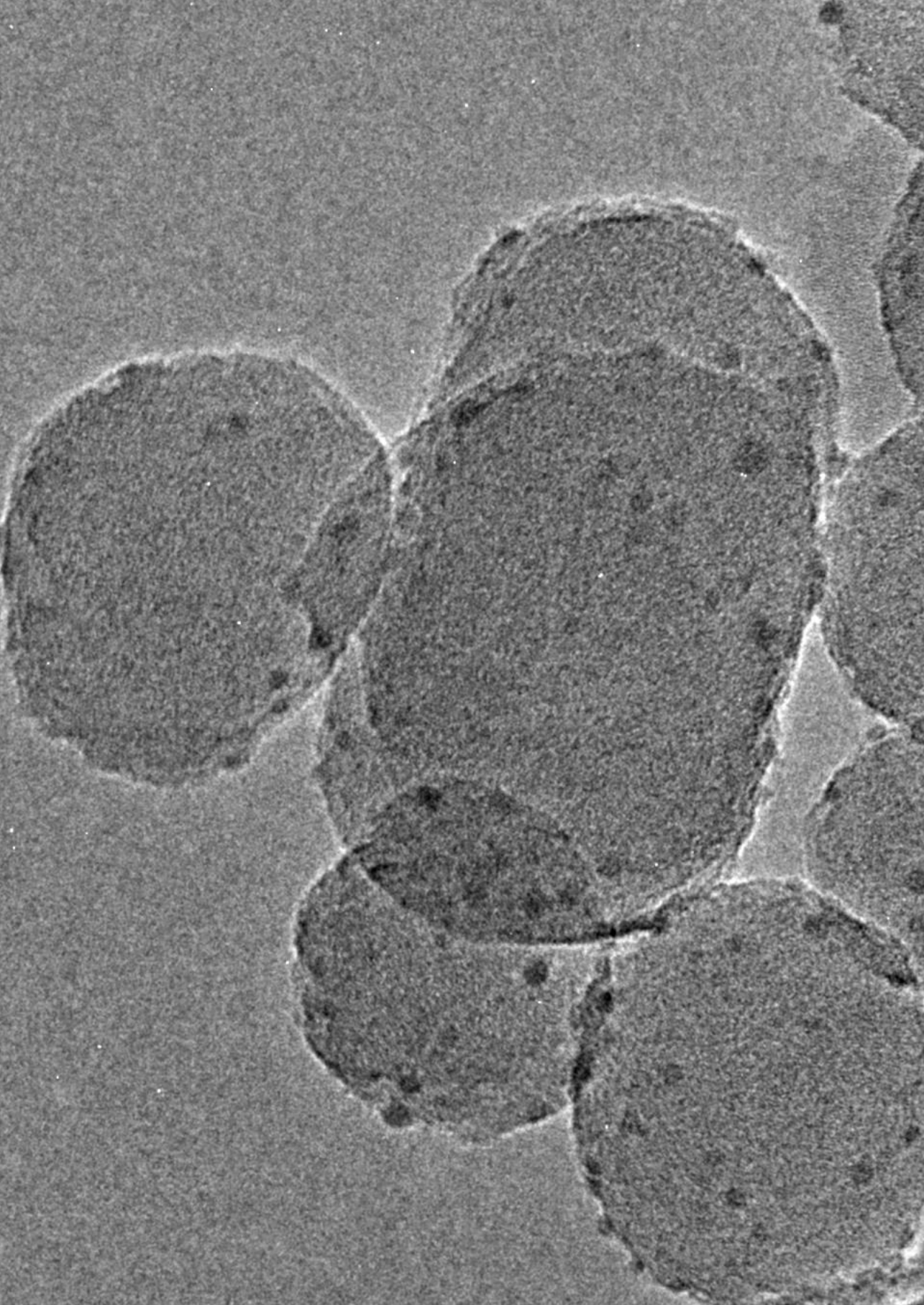


**Figure S3.15.** Turnover frequency for methanol synthesis of the six Cu/SiO<sub>2</sub>-N<sub>2</sub> samples plotted against the support pore size.

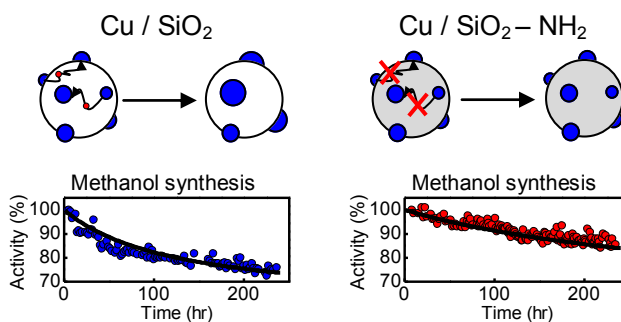


# Support Functionalization to Retard Ostwald Ripening in Copper Methanol Synthesis Catalysts

Based on: van den Berg, R.; Parmentier, T. E.; Elkjær, C. F.; Gommès, C. J.; Sehested, J.; Helveg, S.; de Jongh, P. E.; de Jong, K. P. *ACS Catal.* **2015**, *5*, 4439-4448

## Abstract

A main reason for catalyst deactivation in supported catalysts for methanol synthesis is copper particle growth. We have functionalized the support surface in order to suppress the formation and/or transport of mobile copper species and thereby catalyst deactivation. A Stöber silica support was functionalized by treatment with aminopropyltriethoxysilane that introduces aminopropyl groups on the surface. Copper was deposited on both unfunctionalized and functionalized Stöber silica via incipient wetness impregnation with aqueous copper nitrate solutions followed by drying and calcination. Similar particle size distributions (1-5 nm) were obtained for both supports by changing the flow of  $N_2$  to a flow of 2%  $NO/N_2$  during calcination of the unfunctionalized and amine-functionalized silica, respectively. The effect of support functionalization with aminopropyl groups was an increased stability in the methanol synthesis reaction (40 bar, 260 °C, 23%  $CO$  / 7%  $CO_2$  / 60%  $H_2$  / 10% Ar, 3%  $CO_x$  conversion) due to more limited copper particle growth as determined by transmission electron microscopy (TEM). Changing the interparticle distance did not have an influence on the deactivation rate while the addition of few very large copper particles did, indicating that Ostwald ripening was most probably the dominant particle growth mechanism for these samples. *In-situ* TEM images showed the contact angle between the reduced copper particles and the support. As shape and size was similar on silica as on amine-functionalized silica, the thermodynamic stability of the copper particles was unaltered. The driving force for copper particle growth was thus unchanged upon functionalization. We therefore suggest that Ostwald ripening in methanol synthesis catalysts was retarded by inhibiting the transport of copper species over the support surface. Diffuse reflectance infrared Fourier transform spectroscopy (DRIFTS) revealed a decrease in the number of surface groups (hydroxyl, methoxy and aminopropyl) upon functionalization since aminopropyltriethoxysilane reacted with multiple hydroxyl groups. Because of that, the distance between neighboring functional groups was increased, suppressing the mobility of Ostwald ripening species from one copper particle to another.



## Introduction

Metal particle growth is one of the main causes for catalyst deactivation.<sup>1</sup> Cobalt and iron catalysts in the Fischer-Tropsch reaction,<sup>2</sup> platinum and palladium in the three-way catalyst,<sup>3</sup> nickel catalysts in the methanation reaction<sup>4</sup> and copper catalysts in the water-gas shift and methanol synthesis reaction<sup>5</sup> all deactivate due to particle growth. The coarsening of particles leads to a decrease in metallic specific surface area and hence activity, and can also change the selectivity for structure-sensitive reactions.<sup>6</sup>

Two main particle growth mechanisms have been postulated in literature.<sup>7</sup> One mechanism is the migration of entire particles across the support followed by their coalescence.<sup>8</sup> The other mechanism involves the detachment of metal species from one particle followed by transport across the support or in the vapor phase and by subsequent attachment to another particle.<sup>9</sup> The concentration of metal species around a certain particle depends on the thermodynamic stability of the particle in comparison to the stability of the metal species in such a way that smaller particles are less stable and have a higher concentration of metal species in their vicinity, as compared to larger particles. As a result, a concentration gradient of metal species is established between particles with different sizes leading to a net flux of metal species from smaller to larger particles and hence growth of larger particles at the expense of smaller particles; a process often referred to as Ostwald ripening. Irrespective of the mechanism, particle growth is generally considered to depend on catalyst characteristics such as the particle size (distribution),<sup>3b, 10</sup> interparticle spacing,<sup>11</sup> support geometry<sup>12</sup> and metal-support interaction.<sup>12b, 13</sup>

Catalysts based upon copper, such as Cu/ZnO/Al<sub>2</sub>O<sub>3</sub>, are used in industry in the water-gas shift and the methanol synthesis reaction. The worldwide production of methanol is about 65 million metric tons a year. The produced methanol is used as a building block for other products like methyl tert-butyl ether (MTBE), acetic acid and formaldehyde.<sup>14</sup> Furthermore, methanol can be converted into olefins via the methanol to olefins (MTO) process or can be used in the future to store renewable energy.<sup>15</sup> In the Cu/ZnO/Al<sub>2</sub>O<sub>3</sub> catalyst, copper acts as the catalytically active metal, zinc oxide as a chemical promoter and alumina as a structural promoter.<sup>14, 16</sup> Typically, one third of the initial activity of the catalyst is lost during the first 1000 hours of operation, with copper particle growth being the main reason for deactivation.<sup>5, 14</sup> The reaction temperature (480 K – 580 K) is well below the Tammann temperature of copper (680 K), indicating that thermal migration of atoms in the absence of a reactive adsorbate is unlikely.<sup>14</sup> This is further illustrated by the strong dependence of the deactivation on the composition of the synthesis gas.<sup>17</sup> Copper particle growth in the methanol synthesis reaction is therefore probably mediated by mobile copper species either on the copper surface (effectively changing the center of

mass resulting in particle migration) or on the support surface (resulting in Ostwald ripening).<sup>5, 11a, 18</sup> Suppressing the formation and/or transport of these mobile species is therefore of paramount importance to retard deactivation. In the case of Ostwald ripening, the rate of formation of these species depends on the thermodynamic stability of the metallic particles and of the metal species, which both depend on the chemical nature of the support surface.<sup>19</sup> Moreover, the transport of mobile metal species over a support also depends upon the chemical nature of the support surface. In this contribution we report on our efforts to determine the effect of functionalizing the surface of a support on particle growth during the methanol synthesis reaction.

Support functionalization was performed by introducing aminopropyl groups onto the surface of Stöber silica.<sup>20</sup> The synthesized Stöber silica consisted of non-porous spheres of around 40 nm in diameter, enabling the functionalization of its surface without significantly changing its porosity or geometry.<sup>21</sup> Functionalization was carried out before copper deposition to avoid blocking the active metal sites (see supporting information). Incipient wetness impregnation with aqueous copper nitrate solutions was performed to deposit copper on the (un)functionalized silica support. Heat treatment was performed in either N<sub>2</sub> or in 2% NO/N<sub>2</sub>, resulting in different decomposition pathways of the copper nitrate.<sup>22</sup> The performance of the synthesized catalysts in the methanol synthesis reaction was determined at 40 bar of 7% CO<sub>2</sub>, 23% CO, 60% H<sub>2</sub> and 10% Ar at 260 °C for 10 days. The catalysts were retrieved after the reaction to determine the extent of copper particle growth.

## Experimental Section

### Stöber silica support

Non-porous silica spheres of 30-50 nm in diameter were synthesized via a procedure adapted from Stöber et al.<sup>21b</sup> 230 ml ethanol and 11.25 ml ammonia (NH<sub>3</sub>, Merck, 25% solution for analysis) in a PET bottle were heated to 35 °C and stirred at 230 rpm. Subsequently, 17.3 gram of tetraethyl orthosilicate (TEOS, Aldrich, 98%) was instantaneously added. The solution was left for 15 hours at 35 °C at 230 rpm to ensure full conversion of TEOS into silica. After this time the solution was neutralized with 8.5-9 ml nitric acid (HNO<sub>3</sub>, Merck, 65% for analysis) and the liquid was removed using a rotary evaporator. The silica was then dried overnight at 120 °C and calcined in air according to the following 3-step schedule: 2 hours at 200 °C (100 °C/h) to remove all remaining water, 1 hour at 400 °C (100 °C/h) to decompose unreacted ethoxy silicates and 3 hours at 600 °C

(100 °C/h) to decrease the microporosity within the silica spheres. The yield of the synthesis was 4.8 gram silica (96 wt%).

### Functionalization

Functionalization of the Stöber silica with aminopropyl groups was performed according to a procedure from Jacinto et al.<sup>20e</sup> and Oliveira et al.<sup>20d</sup> Aminopropyl groups were introduced on the silica surface via a reaction between aminopropyltriethoxysilane (APTES, Aldrich, 99%) and hydroxyl groups. To avoid self-hydrolysis of APTES due to the presence of water, the functionalization was carried out under inert N<sub>2</sub> atmosphere using standard Schlenk techniques and dry organic solvents. First, 0.8 gram silica was dried overnight at 120 °C under vacuum. Then, 50 ml of 1 vol% APTES in toluene (Interchemica, > 99.99%, dried with an mBraun MB SPS-800 column) was added dropwise under vigorous stirring. The suspension was stirred for 2 hours at room temperature. After that, the mixture was centrifuged for 5 minutes at 5000 rpm. The solvent was decanted and the silica was washed twice with dry toluene and once with ethanol (Interchemica, 100%) using centrifugation. The obtained functionalized silica was dried overnight at 60 °C in air.

### Copper deposition

Copper was deposited via incipient wetness impregnation followed by drying and calcination. Before impregnation the supports were dried at 150 °C under vacuum for 1 hour to remove adsorbed water. After that, the supports were impregnated with 0.25 M to 1 M of aqueous copper nitrate (Cu(NO<sub>3</sub>)<sub>2</sub>\*3H<sub>2</sub>O, Acros Organics) in 0.1M HNO<sub>3</sub>, followed by drying overnight under vacuum at room temperature. Subsequently, the samples (~ 2 g) were heated at 350 °C (2 °C/min) in a plug flow reactor with either 750 ml/min N<sub>2</sub> or 375 ml/min of 2% NO/N<sub>2</sub>.<sup>22</sup> Table 4.1 shows a list of the prepared samples.

### Catalytic testing

The performance of the catalysts in the methanol synthesis reaction was investigated in a continuous fixed-bed stainless steel reactor with an inner diameter of 0.9 cm (Autoclave Engineers). The calcined catalysts were pressed, crushed and sieved to obtain a sieve fraction of 425 to 630 μm. 0.6-0.9 g (bed height of 3-5 cm) of the catalysts was loaded into the reactor and reduced in-situ at 250 °C (2 °C/min) for 2.5 h with a flow of 110 ml/min 20% H<sub>2</sub>/Ar. After that, the temperature was lowered to 100 °C to prevent premature production of methanol when switching to syngas. The reactor was flushed with syngas (10% Ar, 7% CO<sub>2</sub>, 23% CO, 60% H<sub>2</sub>, Linde), which was purified with a metal carbonyl trap<sup>24</sup> (4.0 g of H-USY zeolite, CVB-780 from Zeolyst Int., 0.5-1.5 mm and 5 g activated carbon, Norit R3B). The argon was added to the syngas feed as an internal standard for the gas

Table 4.1. Sample list

Sample name	Density surface groups (nm <sup>-2</sup> )	[Cu <sup>2+</sup> ] (M)	Cu (wt%)	Surface density copper atoms (nm <sup>2</sup> )	Molar ratio OH or NH <sub>2</sub> to Cu	Heat treatment
S	4.6 OH	-	-	-	-	-
CS_1a	4.6 OH	0.25	0.9	0.9	5	N <sub>2</sub>
CS_1b	4.6 OH	0.25	0.9	0.9	5	NO/N <sub>2</sub>
CS_2a	4.6 OH	0.50	1.8	1.8	2.5	N <sub>2</sub>
CS_4a	4.6 OH	1	3.5	3.5	1.3	N <sub>2</sub>
SN	2.6 NH <sub>2</sub>	-	-	-	-	-
CSN_1a	2.6 NH <sub>2</sub>	0.25	0.8	1.2	2.2	N <sub>2</sub>
CSN_1b	2.6 NH <sub>2</sub>	0.25	0.8	1.2	2.2	NO/N <sub>2</sub>

The sample designations are as follows: S stands for Stöber silica, C for copper and N for NH<sub>2</sub> surface groups. 1, 2 and 4 refer to the copper concentration used during incipient wetness impregnation: 1 is 0.25 M, 2 is 0.5 M and 4 is 1 M of copper nitrate. a or b correspond to the heat treatment used after impregnation and drying: a is heat treatment in N<sub>2</sub> at 350 °C. b is heat treatment in 2% NO/N<sub>2</sub> at 350 °C. The nominal amount of copper atoms per nm<sup>2</sup> support is calculated using the experimental BET surface areas of the supports. The nominal amount of OH groups per nm<sup>2</sup> support is based upon work from Zhuravlev et al.<sup>23</sup> The nominal amount of NH<sub>2</sub> groups per nm<sub>2</sub> support is based upon the amount of aminopropyl groups introduced on Stober silica (~1.8 wt%, ICP and TGA) and the BET surface area of SN.

chromatograph (GC). After 30 minutes of flushing the pressure was increased to 40 bar. From this time on the exit gas composition was measured every 110 minutes with a GC (Varian 450). The lines from the reactor to the GC were heated to 150 °C to avoid any methanol or water condensation. The first GC channel consisted of a HAYESEP Q (0.5Mx1.8") column followed by a MOLSIEVE 13x (15x1/8") column that led to a thermal conductivity detector (TCD). The second GC channel consisted of a CP-SIL 8CB FS capillary column that led to a flame ionization detector (FID). After reaching 40 bar, the temperature was increased to 260 °C (2 °C/min) to produce methanol. The amount of catalyst and the syngas flow (10-30 ml/min) were chosen such that CO<sub>x</sub> conversion levels near 3% were obtained. The activity of the catalysts was calculated from the conversion of CO plus CO<sub>2</sub> during reaction (see supporting information). Turn over frequencies (TOF) were calculated with the assumption that each copper surface atom was an active site. The copper dispersion was based upon TEM particle size distributions assuming spherical particles and calculated with the formula:  $dispersion = \frac{6V_m}{A_m * PS} = \frac{1.04}{PS}$ , where V<sub>m</sub> is the molar volume, A<sub>m</sub> the molar area and PS the surface averaged particle size in nanometer. For CS\_4a the copper dispersion was calculated assuming that 2.1 wt% (EDX) of the copper was present in 2-3 nm particles and that the remaining 1.4 wt% was present in particles larger than 100 nm, resulting in a negligible contribution of these large particles to the total copper surface area. The selectivity was determined from the FID

chromatograms and was in all cases more than 95% towards methanol, with dimethyl ether as the main side product. The stability of the methanol productivity over time was based upon the methanol signal from the TCD detector. Second order deactivation curves were fitted according to the formula:  $(a - a_s)^{-1} = k_{d,2} \times t + \frac{1}{(1 - a_s)}$ ,<sup>1</sup> in which  $a$  is the activity. " $a_s$ " is the normalized activity at  $t = \infty$  (for all catalysts 60% of the initial activity),  $k_{d,2}$  is the second-order deactivation constant, and  $t$  is the time.

### Characterization

N<sub>2</sub>-physisorption measurements were done with a Micromeritics Tristar 3000 V6.08 at liquid nitrogen temperature. Prior to the measurements the samples were outgassed at 130 °C in a nitrogen flow for 14h. The Brunauer-Emmett-Teller (BET) method was used to determine the specific surface area.<sup>25</sup> The pore volume was determined at  $p/p_0 = 0.9975$ . BJH method analysis of the desorption branch was used to obtain the average pore size. The t-plot method was used to determine the micropore volume. X-ray diffraction was performed with a Bruker-Nonius D8 Advance X-ray diffractometer using Co-K<sub>α12</sub> ( $\lambda = 1.79026 \text{ \AA}$ ) radiation. Diffractograms were obtained at room temperature from 20 ° to 70 ° (2 $\theta$ ). Diffuse reflectance infrared Fourier transform spectroscopy (DRIFTS) spectra were recorded with a Bruker Tensor 27 using a HVC-DRP-3 diffuse reflectance reaction chamber with CaF<sub>2</sub> windows and a mercury-cadmium-telluride (MCT) detector. The sample cup holder was filled for 2/3 with silicon carbide, covered by a grid on which ~ 15 mg of sample was placed. The sample was dried in-situ prior to the measurement at 200 °C (2 °C/min) with a N<sub>2</sub> flow of 10 ml/min. Spectra were recorded after cooling down to room temperature and normalized to the SiO<sub>2</sub> peak at 1860 cm<sup>-1</sup>.<sup>26</sup> The chemical composition of the catalysts was determined with inductively coupled plasma (ICP) analysis at the Mikroanalytisches Laboratorium Kolbe (Mülheim an der Ruhr, Germany) using optical emission spectra (OES), recorded with a Perkin Elmer spectrometer. Thermogravimetric analysis (TGA) of the samples was measured with a Perkin Elmer Pyris 1 TGA device. After drying for 20 minutes at 30 °C, 10 mg of sample was heated to 600 °C (5 °C/min) in a flow of 10 ml/min O<sub>2</sub>. Temperature programmed reduction (TPR) measurements were done with a Micromeritic Autochem II ASAP 2920. Prior to the measurements the samples were dried at 120 °C for 30 minutes. After cooling down, the temperature was increased to 800 °C (5 °C/min) under a flow of 5% H<sub>2</sub>/Ar. During this treatment the H<sub>2</sub> concentration was determined with a thermal conductivity detector (TCD).

### Transmission Electron Microscopy

Samples for Transmission Electron Microscopy (TEM) were prepared by crushing them followed by sonication in ethanol. A droplet of this suspension was deposited onto a

carbon coated copper TEM grid (Agar S162 200 Mesh Cu, Van Loenen instruments). TEM images were acquired with a Tecnai 12 (FEI) electron microscope operated with a primary electron energy of 120 kV. For each sample at least 200 particles were analyzed with respect to their size by measuring the apparent diameter (see supporting information for the relation between the apparent diameter and the radius of curvature). Before reaction, the images were taken of the samples after calcination. After reaction, the samples were passivated for 15 minutes by exposing the samples at room temperature to a diluted air/argon flow by creating a small leak in the flow supply system. Before taking TEM images the samples were furthermore exposed for a limited time (< 2 h) to air. In general, this treatment results into a (partial) oxidation of the copper particles as evidenced by the appearance of CuO and/or Cu<sub>2</sub>O peaks in XRD and CuO and/or Cu<sub>2</sub>O lattice fringes in high-resolution TEM. Taking into account the densities of Cu and CuO, the increase in particle size upon full oxidation is around 15%. The Kirkendall effect, which results in hollow particles after oxidation, was never observed for particles smaller than 8 nm. The effect of the oxidation state on the particle size distribution was therefore minor and within the statistical error of the measurements. Energy dispersive X-ray (EDX) spectroscopy was performed on a Tecnai 20FEG (FEI) electron microscope equipped with a field emission gun with an EDAX Super Ultra Thin Window (SUTW) EDS detector and processed with Tecnai Imaging and Analysis software (TIA). For this, CS\_4a was placed on a carbon coated Ni TEM grid (Agar 162 200 Mesh Ni, Van Loenen instruments). Several regions (1 x 1 μm) without very large (> 100 nm) particles were analysed.

In-situ TEM was performed using an image aberration corrected Titan 80-300 SuperTwin ETEM (FEI Company) operated at a primary electron energy of 300 keV. Prior to the experiment, the image aberration corrector was tuned using an Au/C cross-grating (Agar S106) and the spherical aberration coefficient was set in the range of -10 to -20 μm. TEM samples of CSN\_1a, CSN\_1b and CS\_1a were prepared by grinding and dispersing the resulting powder on stainless steel grids. The samples were inserted in the microscope using a Gatan heating holder (model 628). CSN\_1a was reduced at 250 °C at 1 mbar H<sub>2</sub> for 0.5 h and TEM images were subsequently acquired under similar conditions with a bottom-mounted 2k × 2k charged-coupled device (Gatan US1000). Initial images were taken at a low dose rate of 20 e<sup>-</sup>/Å<sup>2</sup>s. Subsequently, the electron dose was increased to 100 e<sup>-</sup>/Å<sup>2</sup>s and images were acquired after 20 minutes exposure. CSN\_1b and CS\_1a were reduced at 300 °C at 1 mbar H<sub>2</sub> for 0.5 h and TEM images were subsequently acquired at these conditions. To assess the effect of the electron beam on the apparent contact angle of the copper particles, first an overview image was taken at a low dose rate of 5 e<sup>-</sup>/Å<sup>2</sup>s. Subsequently, the dose rate was increased to 100 e<sup>-</sup>/Å<sup>2</sup>s to obtain higher magnification images. Lastly, the electron dose was decreased to 5 e<sup>-</sup>/Å<sup>2</sup>s to assess the changes in the

sample upon exposure to  $100 \text{ e}^-/\text{\AA}^2\text{s}$ . An effect of the electron exposure upon the apparent contact angle was not observed.

## Results

### Supports

TEM showed that the synthesized Stöber silica (S) consisted of 30-50 nm silica primary spheres (Figure 4.1). These spheres were partly fused together forming larger aggregates as shown by electron tomography (see supporting information). The TEM images further showed a uniform contrast across the Stöber spheres suggesting the absence of micropores, which agrees with  $\text{N}_2$ -physisorption results (Table 4.2, caption).

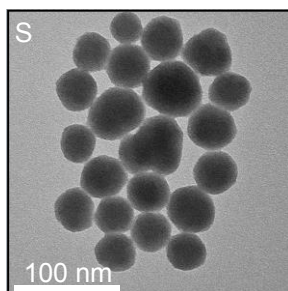


Figure 4.1. TEM image of Stöber silica (S).

Upon functionalization, the three ethoxy groups of aminopropyltriethoxysilane (APTES) can react with a maximum of three hydroxyl groups at the surface of the silica (Figure 4.2A). Assuming  $4.6 \text{ OH groups per nm}^2$  of silica surface<sup>23</sup> and taking into account the specific surface area of the Stöber silica, the theoretical amount of introduced functional groups is 1.4 wt% (0.9 wt% carbon, 0.3 wt% nitrogen and 0.2 wt% hydrogen). Elemental analysis with inductively coupled plasma (ICP) showed a carbon content of 1.36 wt% and a nitrogen content of 0.36 wt% after functionalization (SN). Thermal gravimetric analysis (TGA) in an oxygen flow up to  $600 \text{ }^\circ\text{C}$  showed a weight loss of 1.8 wt% for sample SN, whereas no weight loss was observed for the parent Stöber silica sample (S). The weight loss for sample SN was thus ascribed to the decomposition of aminopropyl groups. Both techniques suggested a slightly higher amount of aminopropyl groups in the sample than theoretically expected. The small excess might be due to self-hydrolysis of one or more of the APTES ethoxy groups, effectively lowering the number of hydroxyl groups that bind APTES. After functionalization of the Stöber silica, both the specific surface area and pore volume had decreased due to the addition of aminopropyl groups (Table 4.2).

**Table 4.2.** N<sub>2</sub>-physorption

Sample	SA (m <sup>2</sup> /g)	PV (cm <sup>3</sup> /g)	Pore size (nm)
S	100	0.58	20
SN	75	0.53	26

N<sub>2</sub>-physorption data of Stöber silica (S) and Stöber silica functionalized with NH<sub>2</sub> groups (SN). The BET surface area (SA), pore volume (PV) and average pore size of the supports are given in the table. For both materials the micropore volume was < 0.01 cm<sup>3</sup>/g.

Figure 4.2B shows DRIFTS spectra of Stöber silica before and after functionalization. The peaks below 2200 cm<sup>-1</sup> are assigned to the stretching modes of Si-O-Si and dangling modes of Si-O.<sup>26</sup> This part of the spectrum is similar for both supports since they both consisted mainly of silica. On the functionalized support peaks originating from C-H and N-H vibrations appeared. The peaks at 2875 cm<sup>-1</sup> and 2940 cm<sup>-1</sup> are assigned to C-H vibrations originating from the propyl chain of the functional groups.<sup>27</sup> The peak at 3320 cm<sup>-1</sup> is attributed to the asymmetric N-H stretch vibration and the peak at 3380 cm<sup>-1</sup> to the symmetric N-H stretch vibration in aminopropyl groups.<sup>27-28</sup> The broad peak of the O-H stretch vibration at 3615 cm<sup>-1</sup>, ascribed to hydrogen bonded hydroxyl groups, remained present after functionalization.<sup>28</sup> The O-H stretch vibration at 3745 cm<sup>-1</sup> is attributed to

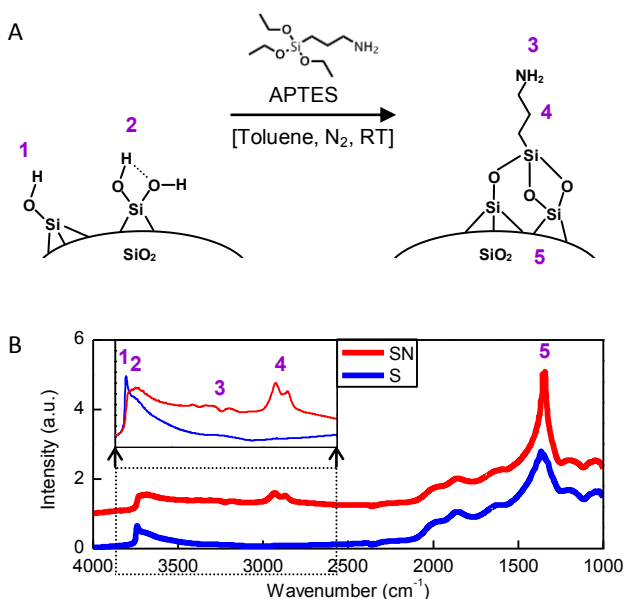


**Figure 4.2.** (A) Schematic representation of one possible reaction between hydroxyl groups and APTES. (B) DRIFTS spectra of Stöber silica (S) and amine-functionalized Stöber silica (SN). The different peaks are numbered and correspond to the groups numbered in (A). The inset on the top left of the image is a blow-up of the spectrum from 3800 to 2600 cm<sup>-1</sup>. No vertical offset is used herein.

isolated hydroxyl groups and was largely reduced upon functionalization due to the reaction with APTES.<sup>28</sup> The functionality of the surface was thus successfully altered by the addition of aminopropyl groups at the expense of isolated hydroxyl groups.

### Copper

Six different catalysts were made via incipient wetness impregnation of the (functionalized) silica supports with aqueous copper nitrate followed by drying and heat treatment in N<sub>2</sub> or 2% NO/N<sub>2</sub> (table 4.1). The first set was prepared by impregnating non-functionalized Stöber silica with 0.25 M, 0.5 M and 1 M of copper nitrate followed by calcination in N<sub>2</sub> flow. Representative TEM images of the samples after calcination are shown in Figure 4.3A-D. The resolution of the microscope and the structure of the catalysts allowed us to detect copper oxide particles down to ca. 1.5 nm.

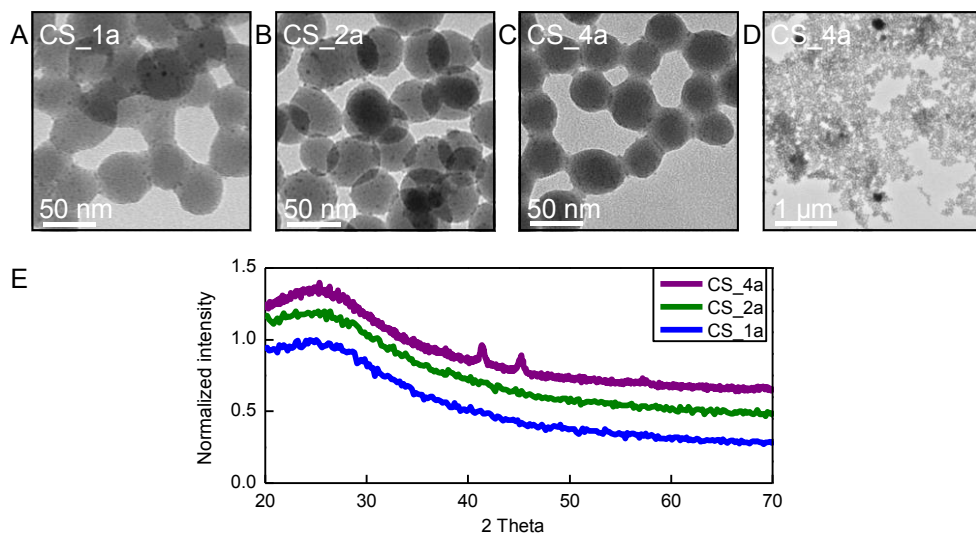


**Figure 4.3.** TEM images of (A) CS\_1a, (B) CS\_2a and (C-D) CS\_4a. (E) X-ray diffractograms of the samples; designated peaks (\*) correspond to CuO. All samples contain 2-3 nm sized copper oxide particles, as visualized with TEM. For CS\_4a, however, additionally also the presence of large (> 100 nm) particles was detected with TEM. For this sample XRD confirmed the presence of CuO crystallites larger than 20 nm.

In the case of CS\_1a and CS\_2a, heat treatment in a flow of N<sub>2</sub> resulted in 2-3 nm sized copper oxide particles (darker image features) homogeneously distributed over the support, in agreement with earlier observations.<sup>11a, 29</sup> TEM images of CS\_4a revealed additionally to the 2-3 nm sized particles some large (> 100 nm) particles (Figure 4.3C, D). XRD confirmed the presence of large CuO crystallites for this sample (Figure 4.3E). Energy

dispersive x-ray spectroscopy in regions with only 2-3 nm particles showed a local copper loading of around  $2.1 \pm 0.5$  wt%. Since the total copper loading was 3.5 wt%, the remaining 1.4 wt% was present in the large ( $> 100$  nm) particles. According to Munnik et al., anhydrous copper nitrate is formed during  $N_2$  calcination.<sup>22</sup> This species is volatile and very mobile and gives rise to copper redispersion over the silica surface. Assuming two surface hydroxyl groups as anchoring site for one molecule copper nitrate and 4.6 OH groups per  $nm^2$  silica,<sup>23</sup> the maximum amount of anchored anhydrous copper nitrate amounts to 2.3 copper complexes per  $nm^2$ ,<sup>29</sup> which corresponds to a copper loading of 2.3 wt% for Stöber silica. For CS\_1a and CS\_2a the copper loading was lower, so all anhydrous copper nitrate was able to anchor to the support. Upon decomposition of the copper nitrate, 2-3 nm copper oxide particles were formed as a result. The copper loading for CS\_4a was, however, higher than 2.3 wt% resulting in the aggregation of excess copper nitrate and hence the formation of very large copper oxide particles.

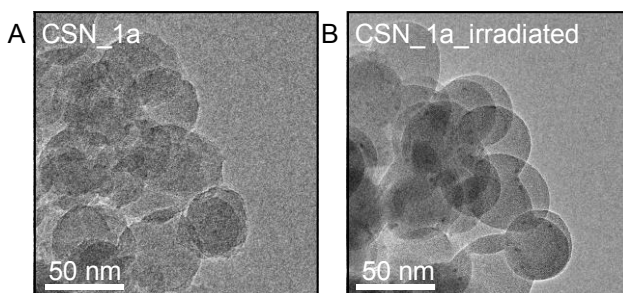


**Figure 4.4.** (A) TEM image of CSN\_1a at 250 °C at 1 mbar of  $H_2$ . No copper particles were detected. (B) The same area as (A) after intense prolonged electron beam exposure ( $\sim 20$  minutes at  $100 e^-/\text{\AA}^2s$ ). 1-2 nm particles were detected.

In contrast to copper on silica (CS\_1a), TEM images of 0.8 wt% of copper on amine-functionalized silica (CSN\_1a) did not show the presence of 2-3 nm particles, not even after in-situ TEM reduction at 250 °C at 1 mbar  $H_2$  for 0.5 h (Figure 4.4A). In fact, no particles were detected at all at low electron dose rates ( $20 e^-/\text{\AA}^2s$ ). The usage of a higher electron dose rate ( $100 e^-/\text{\AA}^2s$ ) yields a better image signal to noise ratio. The higher dose rate in conjunction with longer exposure times ( $\sim 20$  minutes) resulted in a smoother silica surface and the appearance of 1-2 nm wide particles which are presumably of copper (Figure 4.4B). Initially the copper is distributed as atomic species or as particles smaller than 1-2 nm representing the critical size for unambiguous distinction of features on the silica support. Adsorption of copper nitrate during synthesis was in this case probably via aminopropyl groups. The ratio of aminopropyl groups to copper was for this sample

higher than 2 (see table 4.1). Increasing the copper loading further might lead to an oversaturation of these groups with copper nitrate which might result in larger particles similarly to copper on unfunctionalized silica. Sintering of copper species during drying and calcination at the current loading was very limited as evidenced by the absence of particles larger than 1-2 nm after calcination. This indicates that anhydrous copper nitrate, similar to copper ions,<sup>30</sup> was more strongly adsorbed by the aminopropyl groups than by hydroxyl groups, limiting its mobility.

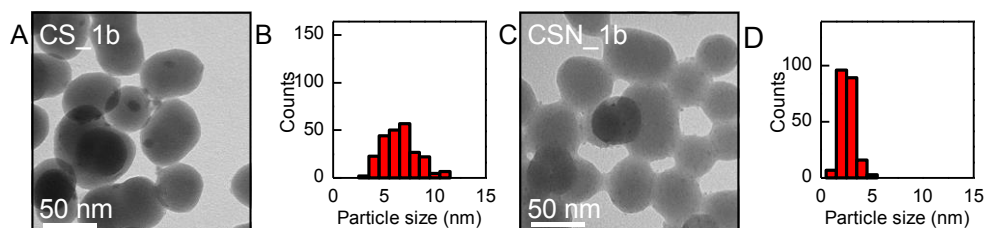


**Figure 4.5.** (A) TEM image of CS\_1b. (B) Copper oxide particle size distribution of CS\_1b determined with TEM. (C) TEM image of CSN\_1b. (D) Copper oxide particle size distribution of CSN\_1b determined with TEM.

Representative TEM images and particle size distributions of copper on functionalized and non-functionalized silica after 2% NO/N<sub>2</sub> calcination (CS\_1b and CSN\_1b) are shown in Figure 4.5A-D. For both supports, the size of the copper oxide particles was larger after 2% NO/N<sub>2</sub> calcination than after N<sub>2</sub> calcination (Figure 4.5A and C vs. Figure 4.3A and 4.4A, respectively). For copper on non-functionalized silica (CS\_1b) the heat treatment in 2% NO resulted in particles with sizes ranging from 4 to 15 nm, while for copper on functionalized silica (CSN\_1b) this resulted in 2-3 nm particles. The distribution of the particles in CSN\_1b seemed to be homogeneous across the support surface. The difference with the N<sub>2</sub> heat treated samples was due to a different decomposition route of copper nitrate to copper oxide in the case of heat treatment in NO. According to Munnik et al., a non-volatile and non-mobile copper species, Cu<sub>2</sub>NO<sub>3</sub>(OH)<sub>3</sub>, is formed upon heating to 110 °C in NO.<sup>22</sup> During the formation of this phase it can grow from mobile copper nitrate, Cu(NO<sub>3</sub>)<sub>2</sub>\*3H<sub>2</sub>O. The smaller particles for CSN\_1b compared to CS\_1b indicate that different mobility of such species could explain the observations and that mobility is higher on silica than on amine-functionalized silica. This suggests that aminopropyl groups adsorb not only copper ions and anhydrous copper nitrate but also copper nitrate trihydrate stronger than hydroxyl groups do.

The temperature required to reduce the copper precursors of the heat treated samples to metallic copper was determined with temperature programmed reduction

(TPR). Figure 4.6 shows the H<sub>2</sub> consumption as a function of temperature up to 350 °C. Above 350 °C no further hydrogen consumption was observed for any of the samples.

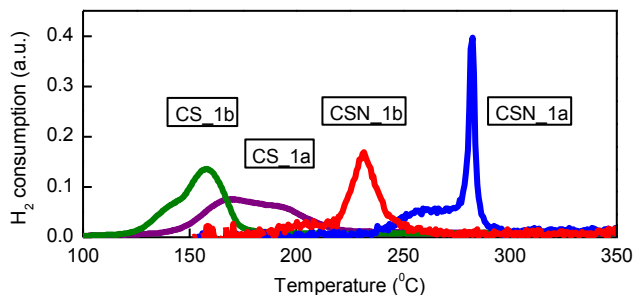


**Figure 4.6.** H<sub>2</sub> consumption as a function of temperature determined with TPR. For all samples, the amount of consumed hydrogen corresponds to the complete reduction of Cu<sup>2+</sup> species to metallic copper.

The hydrogen consumption corresponds for all samples to the complete reduction of Cu<sup>2+</sup> species to metallic copper. For CS\_1a the reduction occurred between 150 °C and 210 °C and for CS\_1b between 130 °C and 170 °C. In both cases, two overlapping peaks were visible, which might be due to a stepwise reduction from CuO through monovalent Cu<sub>2</sub>O to metallic copper. CS\_1b consisted of 4-8 nm and CS\_1a of 2-3 nm copper oxide particles on unfunctionalized Stöber silica. Smaller CuO particles thus required a higher temperature during reduction, consistent with literature for other metal oxides.<sup>31</sup> For both functionalized samples, the temperature required to reduce the copper species was higher, i.e. 230 °C and 260-280 °C, even though the particle size distribution was similar for CSN\_1b compared to CS\_1a. The retarded reduction for these samples is therefore not

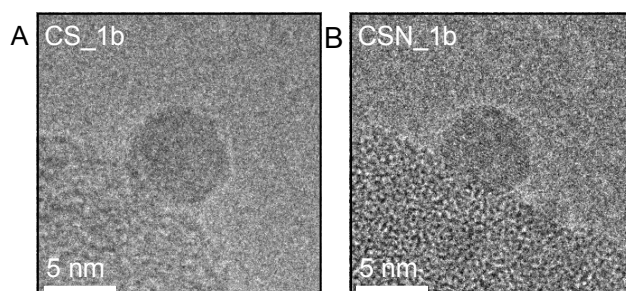


**Figure 4.7.** (A) In-situ TEM image of CS\_1b and (B) CSN\_1b at 1 mbar of H<sub>2</sub> at 300 °C. For clarity, images of relatively large copper particles (~ 5 nm) are shown in this figure. No dependence of the contact angle upon the particle size (2–5 nm) was found. The contact angle between the metallic copper and the support is similar for both supports (Table S4.1).

only ascribed to small copper oxide particles but also to a stabilization of copper oxide by aminopropyl groups.

TEM images of copper particles on non-functionalized and amine-functionalized Stöber silica after reduction are shown in Figure 4.7A, B. The samples were re-reduced in the electron microscope at 1 mbar H<sub>2</sub> at 300 °C for half an hour to ensure that the particles were fully metallic, as evidenced by the lattice fringe spacing of 0.208 nm corresponding to the distance of the (111) planes in metallic copper (Figure 4.7B). Based on the densities of copper oxide and metallic copper the change in particle size upon reduction is less than 15%. The copper oxide particle size distributions after calcination were therefore assumed to be similar to the size distribution of the copper particles after reduction. The contact angle between the metallic copper particles and the support was similar for both samples, i.e. 135 ° ± 20 ° vs. 125 ° ± 20 °, respectively (see supporting information). According to the Young-Duprez relation the contact angle is determined by the surface energies of the metal and the support, and the adhesion energy between the two. A lower contact angle after functionalization therefore indicates either a lower support surface energy or a stronger adhesion energy between copper and functionalized silica. The chemical potential of a copper particle is related to the curvature of the copper surface and hence to the contact angle. Since the observed difference in contact angle is minor the change in copper surface curvature for a given particle volume upon functionalization is also minor (see supporting information). Amine-functionalization has thus a limited effect, if any, on the thermodynamic potential of the copper particles.

### Catalytic performance

To study the effect of the support functionalization on the stability of the copper particles during methanol synthesis, the two catalysts with similar characteristics were selected: CS\_1a and CSN\_1b (Figure 4.8A-F). The initial size of the copper particles (2-3 nm, Figure 4.8A, B), the copper loading and the particle distribution were similar for these two catalysts. The performance of these catalysts was tested in the methanol synthesis reaction (260 °C, 40 bar, 23% CO / 7% CO<sub>2</sub> / 60% H<sub>2</sub> / 10% Ar, 5% CO conversion). The selectivity towards methanol was above 95% with dimethyl ether as the main side product. The methanol synthesis productivity was therefore calculated by the CO + CO<sub>2</sub> conversion (Figure 4.8F). In literature it has been reported that for Cu/SiO<sub>2</sub> catalysts the rate of methanol formation from a mixture of CO and CO<sub>2</sub> is proportional to the exposed metallic copper surface area.<sup>32</sup> Turn over frequencies were therefore calculated with the assumption that each copper surface atom was an active site. The number of copper surface atoms was based on the TEM particle size distributions assuming fully accessible

spherical particles. The TOF was similar for both catalysts indicating that the functionalization did not change the activity of copper, and was slightly lower compared to values reported in literature for Cu/SiO<sub>2</sub> methanol synthesis catalysts, possibly due to the small size of the copper particles.<sup>16b, 29, 32a</sup> The TOFs were about 1 order of magnitude lower compared to an industrial-type Cu/ZnO/Al<sub>2</sub>O<sub>3</sub> reference catalyst tested at the same conditions (TOF of  $8.0 \cdot 10^{-3} \text{ s}^{-1}$ , see supporting information). This difference in activity is generally attributed to the promoting effect of ZnO.<sup>14, 16</sup> The loss in activity with increasing time on stream was 3 times faster for the non-functionalized catalyst. This difference in deactivation is in line with the increase in particle size during reaction (Figure 4.8A-D). For CSN\_1b the particle growth was limited, whereas for CS\_1a, a significant amount of larger (> 3 nm) copper particles was detected after reaction. Copper particle growth was clearly more extensive for copper on silica than for copper on amine-functionalized silica.

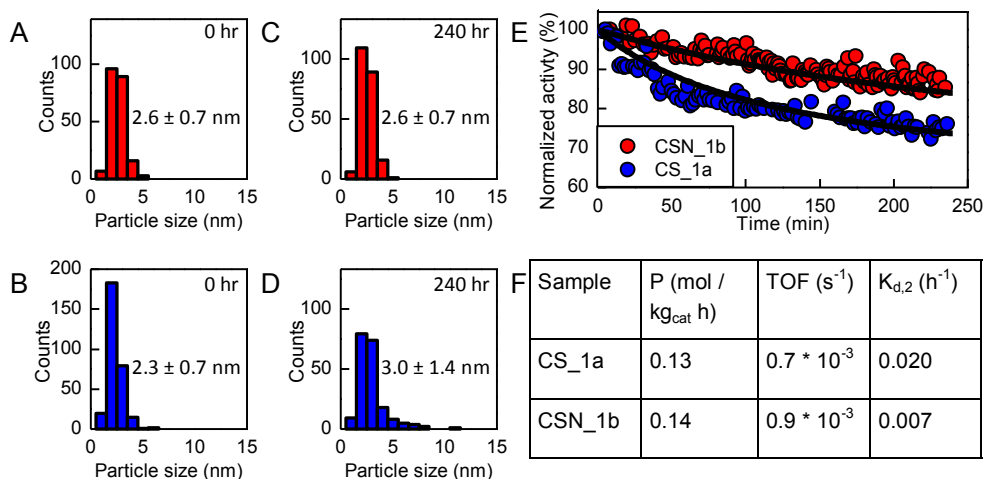


**Figure 4.8.** (A-B) Copper oxide particle size distributions of CSN\_1b (A) and CS\_1a (B) before reaction. (C-D) Copper (oxide) particle size distributions of CNS\_1b (C) and CS\_1a (D) after reaction. (E) Normalized methanol synthesis activity over time for CSN\_1b (red) and CS\_1a (blue). Second order deactivation curves were fitted for both samples (black). (F) The initial productivity (P), initial turn over frequency (TOF) and deactivation constant (K<sub>d,2</sub>) for CSN\_1b and CS\_1a. Deactivation due to particle growth was faster in the case of CS\_1a.

The stability of the aminopropyl groups during copper deposition and methanol synthesis reaction was assessed with ICP (Table 4.3) and DRIFTS (Figure 4.9). The carbon and nitrogen content in the sample decreased upon copper deposition, most likely due to the relatively high calcination temperature (350 °C), resulting in the partial decomposition of aminopropyl groups. After methanol synthesis reaction for 10 days, the carbon and

nitrogen content had not changed, indicating that the aminopropyl groups were stable under these conditions.

**Table 4.3.** Elemental analysis

Element	SN	CSN_1b	CSN_1b_rxn
C (wt%)	1.36	0.84	0.89
N (wt%)	0.36	0.17	0.24

Carbon and nitrogen content of SN, CSN\_1b and CSN\_1b after reaction (CSN\_1b\_rxn) determined with ICP.

DRIFTS spectra were recorded to verify whether N-H or C-H vibrations of the aminopropyl groups were still present after calcination and after reaction. The intensity of the N-H vibrations was already very low for SN (Figure 4.2B) and after calcination or reaction these peaks could no longer be detected. The main difference between the spectra of the samples at different stages was found in the region of C-H vibrations (Figure 4.9). C-H vibrations were absent for the Stöber silica support (S) and appeared after functionalization (SN). After copper deposition (CSN\_1b) the intensity in the C-H region decreased, in line with the loss of carbon determined with ICP, and the peak positions were changed. The peak at  $2860\text{ cm}^{-1}$  decreased and a new peak at  $2978\text{ cm}^{-1}$  appeared. After reaction (CSN\_1b\_rxn) two additional peaks were detected; one at  $2966\text{ cm}^{-1}$  and one at  $2855\text{ cm}^{-1}$ . These peaks were also detected after methanol synthesis reaction of an unfunctionalized copper on silica sample (CS\_2a\_rxn). These peaks correspond therefore not to the carbon chain of the aminopropyl groups. According to literature, alkoxylation of the silica surface is possible.<sup>33</sup> Methanol produced during reaction can open siloxane bridges, creating methoxy and hydroxyl groups. The peaks at  $2966\text{ cm}^{-1}$  and  $2855\text{ cm}^{-1}$  after methanol synthesis reaction are therefore ascribed to these methoxy groups. The intensity of the peaks at  $2966\text{ cm}^{-1}$  and  $2855\text{ cm}^{-1}$  was much lower for the amine-functionalized catalyst than for the unfunctionalized catalyst. This indicates that the presence of aminopropyl groups at the surface decreased the amount of available siloxane bridges for methoxylation. Also the total intensity of C-H vibrations was lower for CSN\_1b\_rxn than for CS\_2a\_rxn. Since the OH-stretch region was similar for both samples, this indicates that the total amount of surface functional groups (amino-propyl, methoxy and hydroxyl groups) was lower for the functionalized sample. The functionality of the support surface was thus markedly different during methanol synthesis reaction for copper on silica than for copper on amine-functionalized silica.

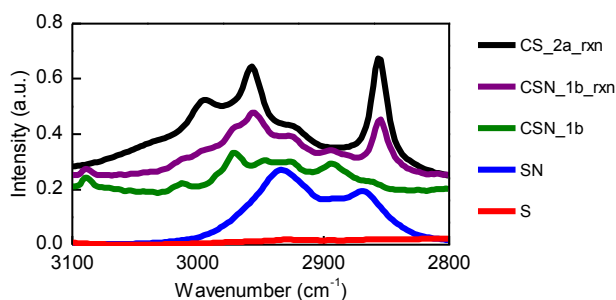


**Figure 4.9.** DRIFTS spectra between 3100  $\text{cm}^{-1}$  and 2800  $\text{cm}^{-1}$  of several samples at different catalyst life stages. The peaks correspond to C-H vibrations.<sup>27</sup> For clarity the y-axis of the samples with copper has been shifted 0.25 upwards. C-H vibrations of methoxy groups (2966 and 2855  $\text{cm}^{-1}$ ) were detected after methanol synthesis reaction for both copper on silica (CS\_2a\_rxn) and copper on amine-functionalized silica (CSN\_1b\_rxn).

### Copper particle growth mechanism

To understand better why copper particle growth was suppressed upon functionalization, it was necessary to obtain more information about the mechanisms involved for copper particles on silica. The effect of changing the loading on copper growth in the methanol synthesis reaction was therefore investigated (Figure 4.10A-F). CS\_1a and CS\_2a had a similar copper particle size distribution, but the loading was twice as high for CS\_2a. The main difference between the two samples was therefore the particle density. CS\_4a had a similar amount (2.1 wt%) of small (2-3 nm) particles as CS\_2a (Figure 4.10A, B), next to some large copper particles (> 100 nm). The catalytic performance of the three catalysts is displayed in Figure 4.10E, F. The turn over frequency was similar for all three catalysts. Despite the difference in particle density, the deactivation rate for CS\_1a and CS\_2a was also similar. Hence, the interparticle distance did not influence the rate of deactivation, although the observed increase in copper particle size was larger for CS\_2a than for CS\_1a (Figure 4.8D, 4.10B). The addition of very large, virtually inactive copper particles in the case of CS\_4a led, however, to a faster deactivation. The particle size distributions of CS\_2a and CS\_4a before and after reaction are shown in Figure 4.10A-D. For sample CS\_2a, a relatively high fraction of particles had grown larger to 4-15 nm. For sample CS\_4a just a few particles were detected with a size between 4 and 11 nm. Next to the particle size distributions shown in Figure 4.10B and D, also some large (> 100 nm) particles were observed. The number of very large particles was not enough to obtain a statistically relevant particle size distribution in that size range. These particles might, however, have grown larger at the expense of small 2-3 nm particles.

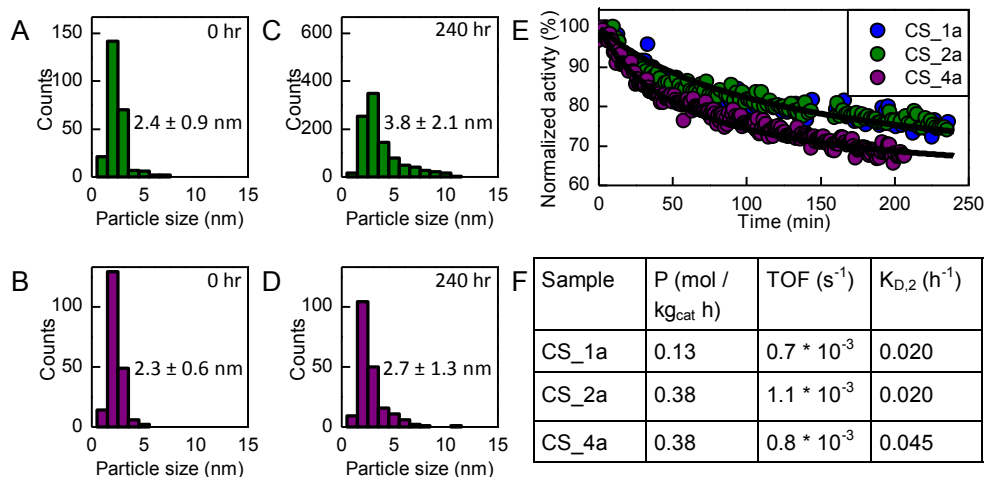


**Figure 4.10.** (A-B) Copper oxide particle size distributions of CS\_2a (A) and CS\_4a (B) before reaction. (C-D). Copper (oxide) particle size distributions of CS\_2a (C) and CS\_4a (D) after reaction. For CS\_4a a small number of very large (> 100 nm) particles were detected before and after reaction. For clarity, these particles are not included in the particle size distributions shown in (B) and (D). Particle size distributions of CS\_1a are shown in Figure 8B and D. (E) Normalized methanol synthesis activity over time for CS\_1a, CS\_2a and CS\_4a. Second order deactivation curves were fitted for the three samples. (F) The initial productivity (P), initial turn over frequency (TOF) and deactivation constant ( $K_{D,2}$ ) for CS\_1a, CS\_2a and CS\_3a.

In the case of copper particle growth due to particle migration and coalescence, a change in interparticle spacing has been shown to lead to a faster deactivation.<sup>11a, 12a</sup> Furthermore, the presence of a few, very large, catalytically inactive particles in the case of CS\_4a is not expected to have a significant influence on the migration and coalescence of catalytically active 2-3 nm particles. It is therefore improbable that particle migration and coalescence was the dominant particle growth mechanism for these copper on silica catalysts. Ostwald ripening can, however, explain the above-mentioned results. The calculated interparticle distance between the 2-3 nm particles was for all samples more than two times the particle size, i.e. > 5 nm. According to the mean field approximation there is a gradient in Ostwald ripening species just around a particle but beyond that the concentration can be considered to be independent of location.<sup>7</sup> Since the distances between the particles are relatively large compared to their size, they are considered to be isolated particles in a mean field of Ostwald ripening species. As a result, the deactivation did not increase upon decreasing the interparticle spacing. Also the effect of a few, very large copper particles can be explained by Ostwald ripening, since a bimodal particle size distribution increases the thermodynamic driving force for sintering. With Ostwald ripening, the largest particles grow at the expense of the smallest particles. In the

case of CS\_2a the larger 3 nm copper particles could grow at the expense of the smaller 2 nm particles to a size of 4 to 11 nm. In the case of CS\_4a very large (> 100 nm) particles could grow at the expense of the small 2 and 3 nm particles, explaining the lack of 4-11 nm particles after reaction for this sample. Ostwald ripening therefore seems the most probable mechanism accounting for the present growth of the copper nanoparticles.

### Discussion

Our results show that copper on amine-functionalized silica was more resistant against deactivation than copper on unfunctionalized silica and that the growth of the copper nanoparticles in our catalysts is best explained by the Ostwald ripening mechanism. The particle size distributions and the contact angles of copper particles on the support were similar for the non-functionalized (CS\_1a) and for the functionalized (CSN\_1b) samples, meaning that the surface energy of the copper particles and hence the driving force for Ostwald ripening, was similar (see supporting information).<sup>7</sup> We therefore conclude that the introduced aminopropyl groups suppressed the Ostwald ripening of copper by affecting the stability or mobility of the Ostwald ripening species.

The species that are held responsible for the Ostwald ripening are copper adsorbate species, such as  $\text{CuCO}_3$ .<sup>18</sup> Due to the relatively low reaction temperature, volatilization of copper species into the gas phase (eventually leading to a loss of copper after reaction) is unlikely. Diffusion of copper species from one particle to another therefore most likely occurred across the support surface. The increase in copper dispersion after catalyst synthesis indicated that  $\text{Cu}(\text{NO}_3)_2$  and  $\text{Cu}(\text{NO}_3)_2 \cdot 3\text{H}_2\text{O}$  either bind stronger to or diffuse slower on the amine-functionalized support. A strong bonding between copper species and an amine-functionalized silica is furthermore evidenced by the retarded reduction of copper oxide to metallic copper and is consistent with the finding that aminopropyl groups bind strongly to  $\text{Cu}^{2+}$  ions.<sup>30b</sup> Copper adsorbate species are therefore expected to bind stronger to an amine-functionalized support, increasing the activation barrier for the displacement across the support surface correspondingly.

DRIFTS showed that an amine-functionalized silica surface is rather complex with aminopropyl, hydroxyl and methoxy groups present during reaction. Due to the high occurrence of methoxy and hydroxyl groups it seems unlikely that the metal species can diffuse via the aminopropyl groups only. Since the copper adsorbate species are expected to bind strongly to an aminopropyl group, diffusion to another group is energetically less favorable. Secondly, due to the reaction of one APTES with multiple hydroxyl groups, the density of functional groups on the surface was lower for the functionalized sample (Figure 4.11). The distance between two neighboring functional groups became larger,

lowering the chance of migration from one group to another. Due to the increased bonding between the copper adsorbate species and aminopropyl groups and due to the increased distance between different surface functional groups, the transport of Ostwald ripening species is expected to be suppressed on an amine-functionalized sample.

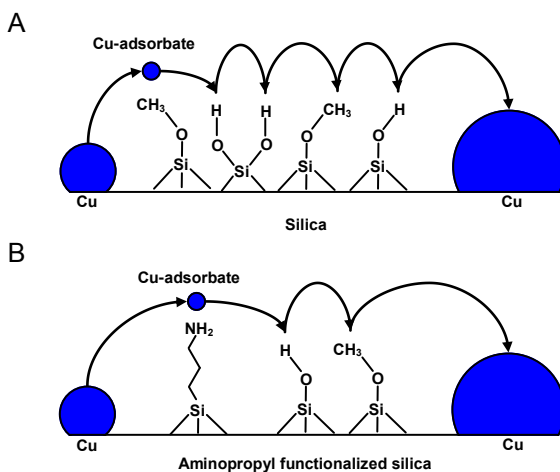


**Figure 4.11.** Schematic representation of Cu-adsorbate diffusion on silica (A) and on amine-functionalized silica (B). The effective distance between aminopropyl groups and neighboring groups is larger than between methoxy and/or hydroxyl groups. The increased distance, together with a stronger interaction between copper adsorbate species and aminopropyl groups, is expected to lead to slower diffusion of Cu-adsorbate species.

## Conclusion

Copper on silica and copper on aminopropyl-functionalized silica were synthesized using impregnation of copper nitrate followed by drying, calcination and reduction. Aminopropyl functionalization increased the dispersion of the copper due to a stronger interaction of the copper precursor with the support. Furthermore, aminopropyl functionalization retarded the reduction of the copper oxide to metallic copper, indicating a stronger interaction between copper oxide and the support. Similar particle size distributions were obtained for unfunctionalized silica and aminopropyl-functionalized silica when the N<sub>2</sub> flow during calcination of the former was changed to a 2% NO/N<sub>2</sub> flow for the latter catalyst. The support functionalization with aminopropyl groups resulted in an increased stability during methanol synthesis due to less copper particle growth. Changing the interparticle distance did not have an influence on the deactivation rate while the addition of few large particles did, indicating that Ostwald ripening is the most

probable dominant particle growth mechanism for these samples. In-situ TEM images showed that the contact angle between the copper particles and the support was similar for both samples. With similar size and shape, the driving force for Ostwald ripening of the copper nanoparticles was thus unchanged upon functionalization. Since the functionalization molecule, aminopropyltriethoxysilane, can react with three hydroxyl groups, the density of surface functional groups decreased upon functionalization, as was also evidenced by DRIFTS. Due to the larger distance between neighboring functional groups and due to the strong bonding of copper species with aminopropyl groups, the transport of Ostwald ripening species from one group to another is expected to be suppressed. In conclusion, these results point to Ostwald ripening in methanol synthesis catalysts being thus retarded by functionalization of the silica support with aminopropyl groups.

### Acknowledgments

The project was supported financially by Haldor Topsøe A/S. The authors also acknowledge Haldor Topsøe A/S for access to its in-situ TEM facility.

### References

- (1) Bartholomew, C. H. *Appl. Catal.* **1993**, *107*, 1-57.
- (2) van de Loosdrecht, J.; Botes, F. G.; Ciobica, I. M.; Ferreira, A.; Gibson, P.; Moodley, D. J.; Saib, A. M.; Visagie, J. L.; Weststrate, C. J.; Niemantsverdriet, J. W. *Fischer-Tropsch Synthesis: Catalysts and Chemistry*. In *Comprehensive Inorganic Chemistry II*, Reedijk, J.; Poepelmeier, K., Eds. Elsevier: Oxford, 2013; Vol. 7, pp 525-557.
- (3) (a) Moulijn, J. A.; Diepen, A. E. V.; Kapteijn, F. *Science* **2001**, *212*, 3-16; (b) Simonsen, S. B.; Chorkendorff, I.; Dahl, S.; Skoglundh, M.; Sehested, J.; Helveg, S. *J. Am. Chem. Soc.* **2010**, *132*, 7968-7975.
- (4) Munnik, P.; Velthoen, M. E. Z.; de Jongh, P. E.; de Jong, K. P.; Gommers, C. J. *Angew. Chem. Int. Ed.* **2014**, *126*, 9647-9651.
- (5) Twigg, M. V.; Spencer, M. S. *Appl. Catal., A* **2001**, *212*, 161-174.
- (6) van Santen, R. A. *Acc. Chem. Res.* **2009**, *42*, 57-66.
- (7) Wynblatt, P.; Gjostein, N. A. *Prog. Solid State Chem.* **1976**, *9*, 21-58.
- (8) (a) Pulvermacher, B. *J. Catal.* **1973**, *245*, 224-245; (b) Harris, P. J. F. *Int. Mater. Rev.* **1995**, *40*, 97-115; (c) Munnik, P.; de Jongh, P. E.; de Jong, K. P. *J. Am. Chem. Soc.* **2014**, *136*, 7333-7340.
- (9) Lifshitz, I. M.; Slyozov, V. V. *J. Phys. Chem. Solids* **1961**, *19*, 35-50.
- (10) (a) Campbell, C. T.; Parker, S. C.; Starr, D. E. *Science* **2002**, *298*, 811-814; (b) Datye, A. K.; Xu, Q.; Kharas, K. C.; McCarty, J. M. *Catal. Today* **2006**, *111*, 59-67.
- (11) (a) Prieto, G.; Zečević, J.; Friedrich, H.; de Jong, K. P.; de Jongh, P. E. *Nat. Mater.* **2013**, *12*, 34-39; (b) Simonsen, S. B.; Chorkendorff, I.; Dahl, S.; Skoglundh, M.; Sehested, J.; Helveg, S. *J. Catal.* **2011**, *281*, 147-155; (c) Morgenstern, K.; Rosenfeld, G.; Comsa, G. *Surf. Sci.* **1999**, *441*, 289-300.
- (12) (a) Prieto, G.; Shakeri, M.; de Jong, K. P.; de Jongh, P. E. *ACS Nano* **2014**, *8*, 2522-2531; (b) Cao, A.; Lu, R.; Vesper, G. *Phys. Chem. Chem. Phys.* **2010**, *12*, 13499-13510.

- (13) (a) Ouyang, R.; Liu, J.-X.; Li, W.-X. *J. Am. Chem. Soc.* **2013**, *135*, 1760-1771; (b) Wallace, W. T.; Min, B. K.; Goodman, D. W. *J. Mol. Catal. A: Chem.* **2005**, *228*, 3-10.
- (14) Hansen, J. B.; Højlund Nielsen, P. E. Methanol Synthesis. In *Handbook of Heterogeneous Catalysis*, Ertl, G.; Knözinger, H.; Schüth, F.; Weltkamp, J., Eds. Wiley-VCH: 2008; pp 2920-2949.
- (15) Olah, G. A. *Angew. Chem. Int. Ed.* **2005**, *44*, 2636-2639.
- (16) (a) Behrens, M.; Studt, F.; Kasatkin, I.; Kühl, S.; Hävecker, M.; Abild-Pedersen, F.; Zander, S.; Girgsdies, F.; Kurr, P.; Kniep, B.-L.; Tovar, M.; Fischer, R. W.; Nørskov, J. K.; Schlögl, R. *Science* **2012**, *336*, 893-897; (b) Nakamura, J.; Choi, Y.; Fujitani, T. *Top. Catal.* **2003**, *22*, 277-285.
- (17) (a) Wu, J.; Saito, M.; Takeuchi, M.; Watanabe, T. *Appl. Catal., A* **2001**, *218*, 235-240; (b) Kuechen, C.; Hoffman, U. *Chem. Eng. Sci.* **1993**, *48*, 3767-3776; (c) Sun, J. T.; Metcalfe, I. S.; Sahibzada, M. *Ind. Eng. Chem. Res.* **1999**, *38*, 3868-3872.
- (18) Rasmussen, D. B.; Janssens, T. V. W.; Temel, B.; Bligaard, T.; Hinnemann, B.; Helveg, S.; Sehested, J. *J. Catal.* **2012**, *293*, 205-214.
- (19) (a) Campbell, C. T. *Acc. Chem. Res.* **2013**, *46*, 1712-1719; (b) Campbell, C. T.; Sellers, J. R. V. *Faraday Discuss.* **2013**, *162*, 9.
- (20) (a) Brühwiler, D. *Nanoscale* **2010**, *2*, 887-892; (b) Hoffmann, F.; Cornelius, M.; Morell, J.; Fröba, M. *Angew. Chem. Int. Ed.* **2006**, *45*, 3216-3251; (c) Linares, N.; Serrano, E.; Rico, M.; Balu, A. M.; Losada, E.; Luque, R.; García-Martínez, J. *Chem. Commun.* **2011**, *47*, 9024-9035; (d) Oliveira, R. L.; Kiyohara, P. K.; Rossi, L. M. *Green Chem.* **2010**, *12*, 144-149; (e) Jacinto, M. J.; Kiyohara, P. K.; Masunaga, S. H.; Jardim, R. F.; Rossi, L. M. *Appl. Catal., A* **2008**, *338*, 52-57.
- (21) (a) Green, D. L.; Lin, J. S.; Lam, Y.-F.; Hu, M. Z.-C.; Schaefer, D. W.; Harris, M. T. *J. Colloid Interface Sci.* **2003**, *266*, 346-358; (b) Stober, W. *J. Colloid Interface Sci.* **1968**, *26*, 62-69.
- (22) Munnik, P.; Wolters, M.; Gabrielsson, a.; Pollington, S. D.; Headdock, G.; Bitter, J. H.; de Jongh, P. E.; de Jong, K. P. *J. Phys. Chem. C* **2011**, *115*, 14698-14706.
- (23) Zhuravlev, L. T. *Colloids Surf.* **2000**, *173*, 1-38.
- (24) Smit, C. J.; Eijkhoudt, R.; Geus, J. W.; Van Dillen, A. J. *Prepr. Pap. - Am. Chem. Soc., Div Fuel Chem.* **1999**, *44*, 119-123.
- (25) Brunauer, S.; Emmett, P. H.; Teller, E. *J. Am. Chem. Soc.* **1938**, *60*, 309-319.
- (26) Pires, J.; Pinto, M.; Estella, J.; Echeverría, J. C. *J. Colloid Interface Sci.* **2008**, *317*, 206-213.
- (27) Panchenko, V. N.; Pozimenco, V. A.; Paukshtis, E. A.; Zakharov, V. A. *Russ. J. Inorg. Chem.* **2009**, *54*, 1798-1803.
- (28) Kovalchuk, T.; Sfihi, H.; Kostenko, L.; Zaitsev, V.; Fraissard, J. *J. Colloid Interface Sci.* **2006**, *302*, 214-229.
- (29) Prieto, G.; Meeldijk, J. D.; de Jong, K. P.; de Jongh, P. E. *J. Catal.* **2013**, *303*, 31-40.
- (30) (a) Aguado, J.; Arsuaga, J. M.; Arencibia, A.; Lindo, M.; Gascón, V. *J. Hazard. Mater.* **2009**, *163*, 213-221; (b) Deng, S.; Bai, R.; Chen, J. P. *Langmuir* **2003**, *19*, 5058-5064.
- (31) Khodakov, A. Y.; Lynch, J.; Bazin, D.; Rebours, B.; Zanier, N.; Moisson, B.; Chaumette, P. *J. Catal.* **1997**, *25*, 16-25.
- (32) (a) Robbins, J. L.; Iglesias, E.; Kelkar, C. P.; DeRites, B. *Catal. Lett.* **1991**, *10*, 1-10; (b) Burch, R.; Chappell, R. J. *Appl. Catal.* **1988**, *45*, 131-150.
- (33) (a) Dumesic, J. A. *J. Catal.* **1998**, *268*, 252-268; (b) Luts, T.; Katz, A. *Top. Catal.* **2012**, *55*, 84-92; (c) Azrak, R. G.; Angeli, C. L. *J. Phys. Chem.* **1973**, *77*, 3048-3052.

## Supporting Information

## Amine functionalization after copper deposition

Copper on silica (CS\_2a) was functionalized with amine groups after copper deposition (CS\_2a\_N). The performance of both catalysts in the methanol synthesis reaction is shown in Figure S4.1. It can be seen that aminopropyl functionalization led to a stable performance over time. The activity of the catalyst had, however, decreased significantly. The loss in activity was probably due to blocking of the copper by the introduced amine groups.

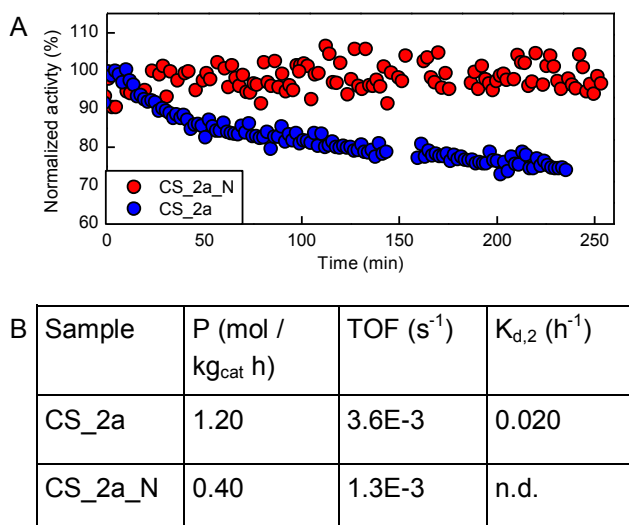


**Figure S4.1.** A) Normalized methanol synthesis activity over time for copper on silica (CS\_2a, blue) and for a copper on silica functionalized after copper deposition (CS\_2a\_N, red). B) The initial productivity (P), initial turn over frequency (TOF) and deactivation constant ( $K_{d,2}$ ) for CS\_2a and CS\_2a\_N.

## Effect of contact angle on Ostwald ripening

In the present section, we show that the observed changes in the deactivation rate are too large to be explained by the changes in the contact angles between the nanoparticles and the support. For that purpose, we assume that the overall rate of Ostwald ripening is proportional to the mass transfer between the smallest and the largest particles. We then calculate how that rate depends on the contact angle. Because our analysis overlooks screening and mean-field effects it provides an upper bound, which is sufficient for our present purpose. The typical shape of the nanoparticles is sketched in Figure S4.2: we

assume the particles to consist in a spherical cap having a radius of curvature  $R$ , and making an angle  $\theta$  with the surface.

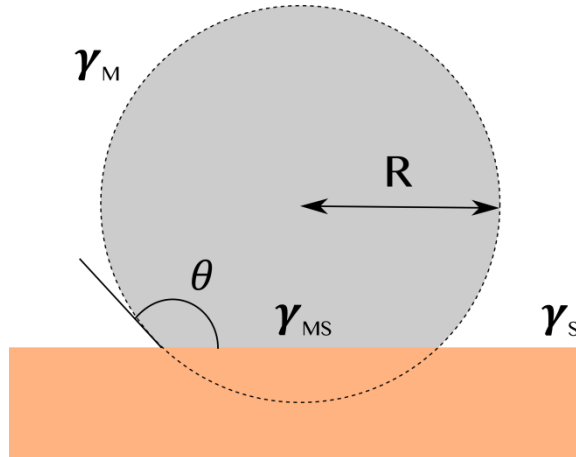


**Figure S4.2.** Sketch of a particle on a flat surface, with definition of the radius of curvature  $R$ , of the contact angle  $\theta$ , as well as of the surface energies  $\gamma$  of the metal (M), support (S), and metal-support (MS) interfaces.

Using the standard formulae for the area and volume of spherical caps, one may express the volume  $V$  and free surface area  $A$  of the particle as follows as a function of the radius of curvature and of the contact angle.

$$V = \frac{4}{3}\pi R^3 f_V(\theta) \quad \text{Eq. 4.1}$$

and

$$A = 4\pi R^2 f_A(\theta) \quad \text{Eq. 4.2}$$

The  $\theta$ -dependent factors  $f_V$  and  $f_A$  can be seen as corrections compared to the spherical shape. They are given explicitly by

$$f_V = \frac{1 - \cos(\theta)}{2} \left( 1 - \cos(\theta) \frac{1 + \cos(\theta)}{2} \right) \quad \text{Eq. 4.3}$$

and

$$f_A = \frac{1 - \cos(\theta)}{2} \quad \text{Eq. 4.4}$$

Both functions are equal to one for the particular value  $\theta = \pi$ , which corresponds to a complete sphere.

**Relation between a particle’s apparent diameter and its radius of curvature**

Analyzing TEM microscopy data with the geometrical model of Figure S4.2 is not straightforward because only the projections of the particles are measured. In particular, for a given radius of curvature R, the apparent diameter of the particle d depends on the value of  $\theta$ .

The relation between d and R can be analyzed rigorously using Cauchy’s relation between the surface area A of a 3D convex object and its average projected 2D area  $A_{\text{projected}}$ .

$$A_{\text{projected}} = \frac{A}{4} \quad \text{Eq. 4.5}$$

Where the average is calculated over all possible directions for the prognosis (Russ, J.C., Dehoff, R.T., “Practical stereology,” second ed. Kluwer Academic, New York (2010)).

Defining the apparent diameter as the equivalent diameter of the projected area,  $A_{\text{projected}} = \pi d^2/4$ , Cauchy’s formula can be particularized as

$$\pi \frac{d^2}{4} = \frac{1}{4} [4\pi R^2 f_A(\theta) + \pi R^2 \sin^2(\theta)] \quad \text{Eq. 4.6}$$

Where the first term in the brackets is the free area of the particle and the second term is the area in contact with the support. The relation can be written equivalently as

$$\frac{R}{d/2} = \left[ 1 - \left( \frac{1 + \cos(\theta)}{2} \right)^2 \right]^{-1/2} \quad \text{Eq. 4.7}$$

The relation between the apparent radius d/2 of the projected particles and their actual radius of curvature R is plotted in Figure S4.3. The figure shows that projection biases are

significant only for contact angles shallower than 90°. For contact angles larger than 135°, the effect is negligible, and we can therefore safely assume  $R = d/2$ .

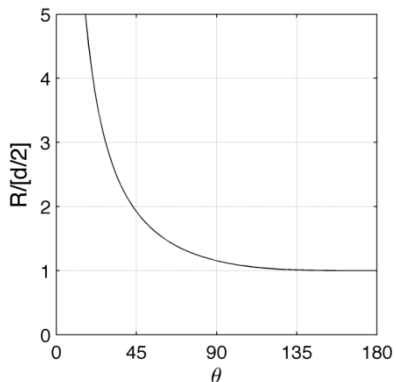


**Figure S4.3.** Relation between a particle's radius of curvature  $R$  and its apparent diameter  $d$  as a function of the contact angle  $\theta$ .

### Influence of the contact angle on Ostwald ripening

The main physicochemical characteristic of a nanoparticle for analyzing Ostwald ripening is its chemical potential  $\mu$ , which controls the propensity of an atom to leave it or to condense on it. The chemical potential is thermodynamically defined as  $\mu = (\partial G/\partial N)$  where  $G$  is the free energy of the nanoparticle and  $N$  is the number of atoms it contains.

Because of the surface contributions to the free energy, the chemical potential of a nanoparticle is generally size-dependent. In the case of a supported nanoparticle, as in Figure S4.2, Gibbs relation writes

$$dG = \mu_0 dN + \gamma_M dA + \gamma_S dA_S + \gamma_{MS} dA_{MS} \quad \text{Eq. 4.8}$$

where  $\mu_0$  is the chemical potential of the bulk (i.e. macroscopic) material,  $A$  is the area of the particle's free surface,  $A_S$  is the area of the support, and  $A_{MS}$  is the area of the metal-support interface. The latter area can be expressed as

$$A_{MS} = \pi R^2 \sin^2(\theta) \quad \text{Eq. 4.9}$$

and the change in area of the free surface of the support satisfies  $dA_S + dA_{MS} = 0$ . Taking also into account that the surface energies are related to the contact angle via the Young-Duprez relation

$$\gamma_M \cos(\theta) = \gamma_S - \gamma_{MS} \quad \text{Eq. 4.10}$$

one eventually finds the simple relation

$$\mu = \left( \frac{\partial G}{\partial N} \right) = \mu_0 + \frac{2\gamma_M \Omega}{R} \quad \text{Eq. 4.11}$$

where  $\Omega$  is the volume occupied by an atom in the nanoparticle.

Eq. 4.11 is identical to the case of a spherical nanoparticle, only  $R$  is here the radius of curvature, which for a given particle volume  $V$  depends on the contact angle  $\theta$  via Eq. 4.1. The solubility of a material or the partial pressure of a vapor in equilibrium with it scales with its chemical potential as

$$c_{eq} \propto \exp\left(\frac{\mu}{k_b T}\right) \quad \text{Eq. 4.12}$$

where  $k_b$  is Boltzmann's constant and  $T$  is the temperature. Assuming that Ostwald ripening is limited by the diffusion of species from small nanoparticles to larger ones, the overall rate of the process can therefore be estimated as the difference between Eq. 4.12 estimated for the smallest and for the largest values of  $R$ .

The contact-angle dependence of  $c_{eq}$  for two particles having the same volumes as spheres with diameter 4 nm and 2 nm are plotted in Figure S4.4a. These curves were obtained by combining Eq. 4.11 and 4.12 with  $\lambda = \gamma_M \Omega / k_b T = 5.28$  nm. The latter value corresponds to Cu at  $T = 260$  °C. The values of  $c_{eq}$  converge to the bulk equilibrium concentration for extremely shallow contact angles because the metal surface is almost flat in that limit.

When everything else is kept constant, the rate of diffusion between the small and the large nanoparticles considered in Figure S4.4a, scales like the difference of the two concentrations. The corresponding values are plotted in Figure S4.4b. This figure therefore shows that experimentally observed changes in contact angle (see Table S4.1) would result in changes of only about 10% of the rate of Ostwald ripening. The change in contact angle can thus not explain the 3-fold faster deactivation for the non-functionalized sample.

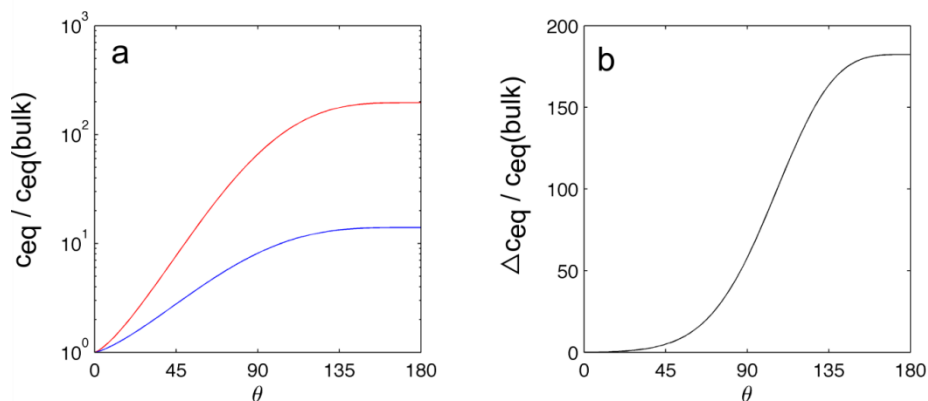


**Figure S4.4.** (a) Contact-angle dependence of the equilibrium vapor concentrations of two nanoparticles having the same volume as spheres with diameter 4 nm (blue) and 2 nm (red). (b) Difference of the two concentrations, proportional to the rate of diffusion between the two particles. In both graphs, the concentrations are normalized by the bulk value, corresponding to a flat interface (i.e.  $\theta = 0$ )

### Measured contact angle

The contact angle of copper on silica and on amine-functionalized silica, determined with *in-situ* TEM, was measured in two ways. If particles were imaged (almost) edge on, the contact angle was measured directly. The directly measured contact angles set the lower value of the real contact angle since the observed contact angle is lower if the particle is not perfectly imaged edge on. If particles were imaged close to edge on, the contact angle was also determined via the height ( $h$ ) / width ( $w$ ) ratio. The formula used to calculate the contact angle ( $\theta$ ) was:

$$\theta = 180 - \cos^{-1}\left(\frac{h - \frac{w}{2}}{\frac{w}{2}}\right) \quad \text{Eq. 4.13}$$

With this method the determined contact angle is larger than the real contact angle if the particle is not perfectly imaged edge on. The real contact angle was estimated by averaging the contact angles obtained via both methods (Table S4.1). No dependence of the contact angle upon the particle size (2-5 nm) was found.

**Table S4.1.** Contact angles determined via the direct and indirect method for both samples.

Sample	Direct $\theta$	Counts	Indirect $\theta$ (h/w)	Counts	Average $\theta$
CS_1a	$130 \pm 24$	23	$141 \pm 14$	33	135
CSN_1b	$116 \pm 18$	14	$135 \pm 16$	23	125

**Electron Tomography**

Electron tomography was performed on CS\_2a after reduction on a Tecnai 20 (FEI) transmission electron microscope at a primary electron energy of 200 kV in bright-field imaging mode. Copper grids with parallel bars and carbon films with thin areas of just 2 nm in thickness were used. These grids were wetted with a solution of 5 nm colloidal gold particles and subsequently dried. These gold particles acted as fiducial markers during the alignment. The catalyst sample was dispersed in ethanol and subsequently deposited on the copper grids. Tilt images were recorded from  $-70^\circ$  to  $+70^\circ$  with intervals of 2 degrees. The resulting images were aligned to a common origin and rotation axis by tracking the 5 nm Au fiducial markers. 3D reconstruction was performed on these tilt series using a weighted back-projection algorithm in IMOD (J.R. Kremer, D.N. Mastronarde, J.R. McIntosh, Journal of Structural Biology, 116 (1996) 71-76.).

In the electron tomogram section of CS\_2a after reduction in Figure S4.5 it can be seen that the silica primary particles were partly fused together forming larger aggregates. Moreover, a few 2-3 nm sized copper particles located on the silica (darker image features) are visible.

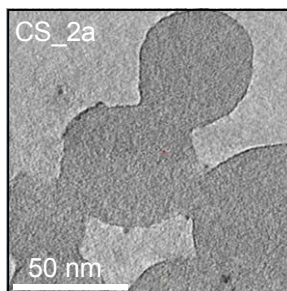


**Figure S4.5.** Electron tomogram section (0.52 nm in thickness) of CS\_2a after reduction.

### Catalyst activity calculation

The methanol productivity is based upon the CO + CO<sub>2</sub> conversion. The conversion of CO or CO<sub>2</sub> is calculated by the difference in CO/Ar or CO<sub>2</sub>/Ar ratio between chromatograms taken during reaction and chromatograms taken of the gas feed before reaction (eq. 4.14 and 4.15).

$$X_{CO} = \frac{\frac{CO_{feed}}{Ar_{feed}} - \frac{CO_{reaction}}{Ar_{reaction}}}{\frac{CO_{feed}}{Ar_{feed}}} \quad \text{Eq. 4.14}$$

$$X_{CO_2} = \frac{\frac{CO_2_{feed}}{Ar_{feed}} - \frac{CO_2_{reaction}}{Ar_{reaction}}}{\frac{CO_2_{feed}}{Ar_{feed}}} \quad \text{Eq. 4.15}$$

X<sub>CO</sub> and X<sub>CO<sub>2</sub></sub> are the conversion of CO and CO<sub>2</sub>, respectively. CO<sub>feed</sub>, CO<sub>2feed</sub> and Ar<sub>feed</sub> are the peak areas of the corresponding gases in the TCD chromatograms of the syngas feed before catalysis. CO<sub>reaction</sub>, CO<sub>2reaction</sub> and Ar<sub>reaction</sub> are the peak areas of the exit gas composition during catalysis. The methanol productivity is calculated by the CO + CO<sub>2</sub> conversion (eq. 4.16).

$$n_{MeOH} = X_{CO} * n_{CO} + X_{CO_2} * n_{CO_2} \quad \text{Eq. 4.16}$$

n<sub>MeOH</sub> is the rate of methanol production. n<sub>CO</sub> or n<sub>CO<sub>2</sub></sub> is the molar flow rate of CO or CO<sub>2</sub>, respectively, into the reactor, calculated via equation 4.17 and 4.18.

$$n_{CO} = \frac{Q_{CO} * P_{ref}}{RT_{ref}} * \phi \quad \text{Eq. 4.17}$$

$$n_{CO_2} = \frac{Q_{CO_2} * P_{ref}}{RT_{ref}} * \phi \quad \text{Eq. 4.18}$$

Q<sub>CO</sub> or Q<sub>CO<sub>2</sub></sub> are the molar fractions of CO and CO<sub>2</sub> in the syngas feed, P<sub>ref</sub> is the pressure and T<sub>ref</sub> the temperature at which the mass flow controller has been calibrated and R is the gas constant. φ is the syngas flow into the reactor as measured by the mass flow controller. To obtain catalyst mass-based productivities (P) The calculated rate of methanol production was divided by the mass of the catalyst (m<sub>cat</sub>) according to Eq. 4.19.

$$P = \frac{n_{MeOH}}{m_{cat}} \quad \text{Eq. 4.19}$$

Turn over frequencies (TOF) were calculated with the assumption that each copper surface atom was an active site. The number of copper surface atoms was based on the TEM particle size distributions assuming fully accessible spherical particles. First, the surface averaged particle size (PS) was calculated via Eq. 4.20.

$$PS = \frac{\sum_1^n D_i^3}{\sum_1^n D_i^2} \quad \text{Eq. 4.20}$$

$D_i$  is the diameter of the  $i$ th particle. The dispersion (ratio between copper surface atoms and total copper atoms) was calculated according to Eq. 4.21.

$$dispersion = \frac{6V_m}{A_m * PS} \quad \text{Eq. 4.21}$$

$V_m$  is the molar volume and  $A_m$  the molar area of the particles. In the case of copper  $V_m$  is  $7.09 * 10^{21} \text{ nm}^3$  and  $A_m$  is  $4.10 * 10^{22} \text{ nm}^2$ . The dispersion of copper ( $dispersion_{cu}$ ) is therefore given by Eq. 4.22 with PS in nm.

$$dispersion_{cu} = \frac{1.04}{PS} \quad \text{Eq. 4.22}$$

The molar amount of copper surface atoms in the catalyst ( $Cu_{surf}$ ) was calculated by Eq. 4.23

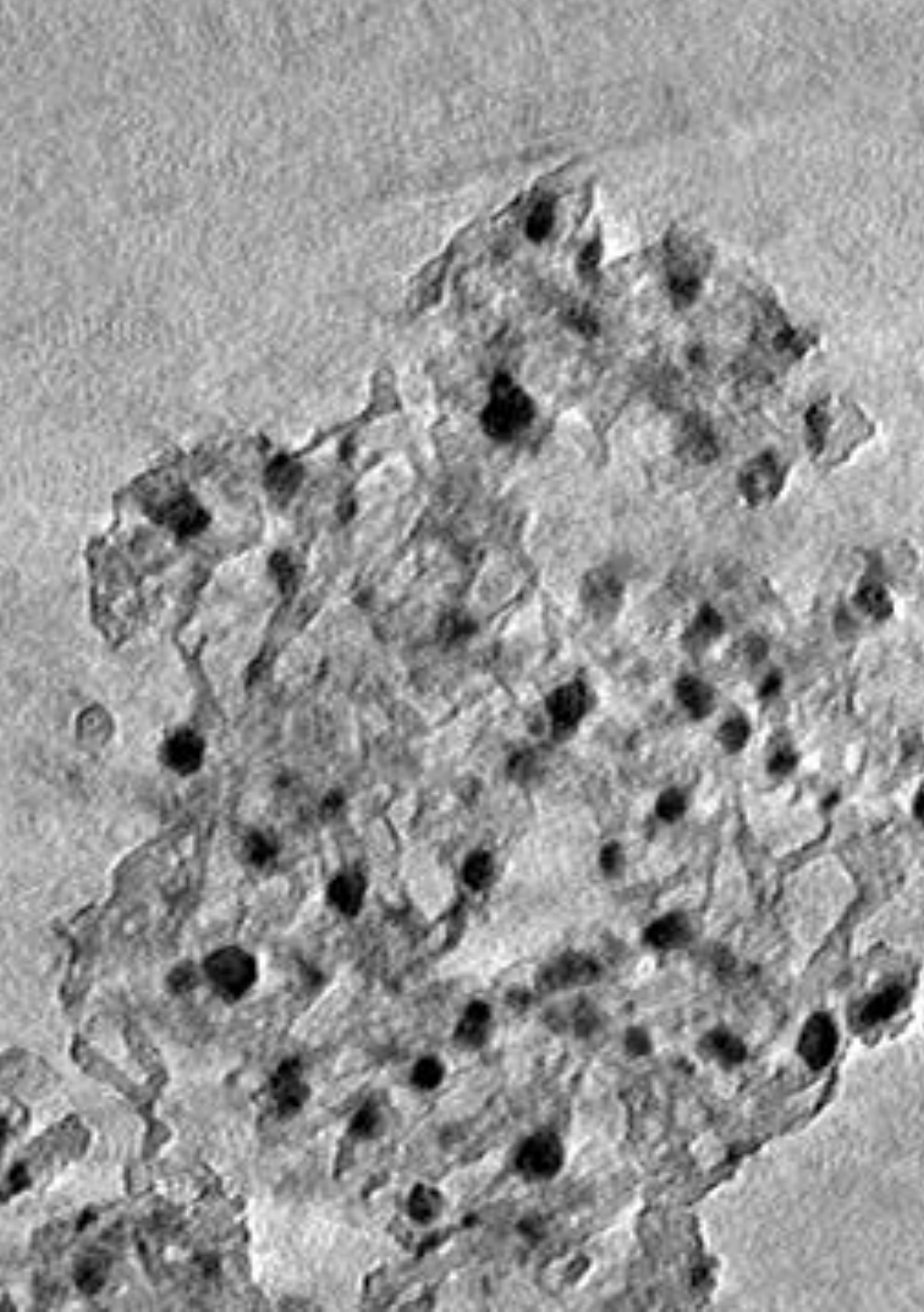
$$Cu_{surf} = dispersion_{cu} * \frac{Wt_{cu}}{M_{cu}} * m_{cat} \quad \text{Eq. 4.23}$$

where  $Wt_{cu}$  is the weight fraction of copper in the catalyst and  $M_{cu}$  the molar mass of copper. TOFs were calculated according to Eq. 4.24

$$TOF = \frac{n_{MeOH}}{Cu_{surf}} \quad \text{Eq. 4.24}$$

### **Cu/ZnO/Al<sub>2</sub>O<sub>3</sub>**

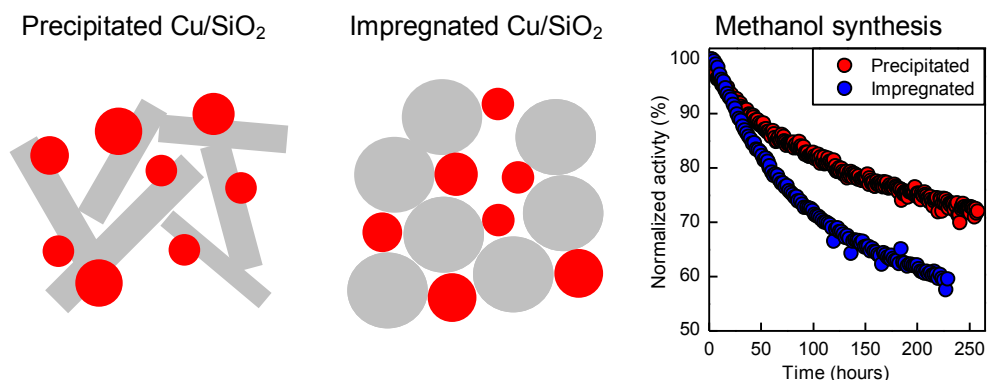
The reference Cu/ZnO/Al<sub>2</sub>O<sub>3</sub> catalyst was prepared by co-precipitation. 30 ml of a 1M aqueous solution of Cu and Zn and Al nitrates (55:30:15 atomic ratio) was added dropwise (2 ml min<sup>-1</sup>) to 50 ml of deionized water kept at 338 K for which the pH had been previously adjusted to 7.0 with Na<sub>2</sub>CO<sub>3</sub>. Simultaneously 1.5 M Na<sub>2</sub>CO<sub>3</sub> solution was added at a controlled rate over a period of 15 minutes in order to keep the pH at 7 ± 0.1. The obtained precipitate was aged for 2 h at 338 K in the mother liquor under vigorous stirring, filtrated, extensively washed with water, dried at 343 K and calcined at 673 K in a muffle oven. Catalytic testing was performed at the same conditions as the (functionalized) Cu/SiO<sub>2</sub> catalysts. For this, 0.06 g Cu/ZnO/Al<sub>2</sub>O<sub>3</sub> was diluted with SiC in a SiC:catalyst volume ratio of 4:1. The syngas flow was adjusted to obtain CO conversion levels near 20%.



# Impact of the synthesis route of supported copper catalysts on the performance in the methanol synthesis reaction

## Abstract

Two Cu/SiO<sub>2</sub> methanol synthesis catalysts were synthesized, one via precipitation and one via impregnation. The copper particle size distribution and local copper weight loading were similar for both catalysts. Electron tomography revealed for the precipitated catalyst a plate-like silica structure with copper particles partially entrapped, whereas for the impregnated catalyst the copper particles were located in the pores between the primary particles of a silica gel. The precipitated catalyst displayed a lower initial copper weight normalized activity and a higher stability in the methanol synthesis reaction (40 bar, 260 °C). Copper particle growth during reaction, as determined by transmission electron microscopy, was more limited for the precipitated catalyst, in line with the higher catalyst stability, possibly due to the partial entrapment of the copper particles. In addition to copper particle growth, deactivation of both catalysts was ascribed to restructuring of the silica resulting in partial coverage of the copper surface.



## Introduction

Supported metal catalysts are the workhorses of the chemical and petrochemical industry<sup>1</sup>. In general, catalysis takes place at the surface of the metal. Small particles and hence a high dispersion are therefore a prerequisite for a high activity. The role of the support is to facilitate the formation of small particles and to improve their thermal stability<sup>2</sup>. In some cases the support is also a chemical promoter, which increases the activity due to strong metal support interactions<sup>3</sup>. Despite the stabilizing effect of the support, metal particle growth is still one of the main causes for deactivation of cobalt and iron catalysts in the Fischer-Tropsch reaction<sup>4</sup>, platinum and palladium in three-way catalysts<sup>5</sup>, nickel catalysts in the methanation reaction<sup>6</sup>, and copper catalysts in the water-gas shift and methanol synthesis reactions<sup>7</sup>.

Particle growth can occur via particle diffusion and coalescence and via Ostwald ripening<sup>8</sup>. In the former mechanism, entire particles diffuse over the support surface until they meet each other and coalesce. In the latter, larger particles grow at the expense of smaller particles due to a net flux of metal-containing species from thermodynamically less stable smaller particles to more stable larger particles. Irrespective of the mechanism, particle growth is generally considered to depend on the reaction conditions<sup>9</sup>, the metal-support interaction<sup>10</sup>, the particle size (distribution)<sup>11</sup> and the interparticle spacing<sup>12</sup>, and also on the geometry of the support<sup>5b, 10a, 10b, 13</sup>. It has for instance been shown that particle migration can be restricted by encagement or entrapment<sup>13-14</sup>. The geometry of the support can also affect the thermodynamic stability of a supported nanoparticle since the chemical potential of a supported nanoparticle depends on the contribution of the metal-support interfacial energy<sup>2, 15</sup>. As a result, particles whose dimensions and volumes are commensurate with concavities in the support and hence have a large metal-support interface area tend to be more stable than particles on a flat support<sup>15</sup>. An increased metal-support interface area of the nanoparticle also leads to a decreased metal surface area accessible to the reactants and, hence, a lower activity. The optimal metal-support interface area is thus the one that provides a balance between nanoparticle activity and nanoparticle stability.

In industry two main routes are used to prepare supported metal catalysts, i.e. precipitation and impregnation<sup>16</sup>. In precipitation, a metal precursor is deposited on a preformed support (deposition-precipitation) or precipitated together with a support precursor (co-precipitation). Subsequent drying, calcination and reduction results in the formation of metallic particles and in the case of a co-precipitate also in the formation of the support<sup>17</sup>. In impregnation, a support is contacted with a metal solution and metallic particles are formed upon drying, calcination and reduction<sup>18</sup>. The interface area between the metal particles and the support is dependent on the preparation route<sup>19</sup>. It might be

larger in case of precipitation due to incomplete segregation<sup>20</sup>. During reaction the interface area might change due to a change in particle size, particle shape or support structure<sup>15,21</sup>.

To study the effect of the synthesis method on the metal-support interaction and hence on metal nanoparticle activity and stability, we selected Cu/SiO<sub>2</sub> methanol synthesis catalysts as a model system. In such catalysts, the activity for CO/CO<sub>2</sub> hydrogenation scales with the copper surface area, and the loss of activity during reaction is often mainly due to copper particle growth<sup>7,22</sup>. Moreover, recent developments in the synthesis of well-defined copper on silica catalysts allow careful tuning of the size and distribution of the copper particles<sup>23</sup>. In this work Cu/SiO<sub>2</sub> catalysts with similar copper particle sizes and local copper weight loadings were synthesized via impregnation and via precipitation. Electron tomography was used to characterize the SiO<sub>2</sub> support structure and the location of the Cu particles within the support. The performance in the methanol synthesis reaction of both catalysts was investigated at 40 bar at 260 °C for a period of 10 days. The catalysts were retrieved after reaction to determine the extent of copper particle growth and change in support structure.

## Experimental Section

### Synthesis Cu/SiO<sub>2</sub> via precipitation

Precipitated Cu/SiO<sub>2</sub> was synthesized via a modified method of van der Grift et al.<sup>24</sup>. 20.1 g LUDOX-AS 30 (Sigma-Aldrich, 30 wt% SiO<sub>2</sub>), 16.1 g Cu(NO<sub>3</sub>)<sub>2</sub>•3H<sub>2</sub>O (Acros Organics, 99% for analysis) and 12.1 g Urea (Acros Organics, 99.5% for analysis) were added to 1.7 l of demineralized water in a 2 l reaction vessel. The pH was adjusted to 2-3 with a few drops of HNO<sub>3</sub> (Merck, 65% for analysis) to prevent premature hydrolysis of copper nitrate. The suspension was then heated to 90 °C over 1 hour under stirring. At 90 °C the hydrolysis of urea led to an increase in pH resulting in precipitation of Cu<sub>2</sub>(NO<sub>3</sub>)(OH)<sub>3</sub>. The well-stirred reaction vessel was kept at 90 °C for 7 days to allow recrystallization of precipitated copper and silica, which resulted in the formation of copper phyllosilicate<sup>25</sup>. The precipitate was obtained by hot filtration of the suspension and washed three times with demineralized water, filtered and dried overnight at 60 °C. The yield was 10 g. Part of the as-prepared copper phyllosilicate was used for catalytic reaction (with in-situ reduction to obtain metallic Cu on SiO<sub>2</sub>) as described below. Another part (2 g) intended for characterization was reduced at 250 °C (2 °C/min) in a flow of 100 ml/min of 20% H<sub>2</sub> in Ar for 2½ h. After the reduction treatment the resulting Cu/SiO<sub>2</sub> was passivated for 15

minutes by slowly exposing the sample to diluted air/N<sub>2</sub> at room temperature. The sample was stored in a glove box under argon atmosphere.

### Synthesis Cu/SiO<sub>2</sub> via impregnation

Copper was deposited on a commercial silica gel (Davicat 1454, Grace-Davison, pore volume  $p/p_0 < 0.95 = 0.81 \text{ cm}^3/\text{g}$ , pore diameter 9 nm) via incipient wetness impregnation with an aqueous solution of 2 M Cu(NO<sub>3</sub>)<sub>2</sub>•3H<sub>2</sub>O (Acros Organics, 99% for analysis) and 0.1 M HNO<sub>3</sub> (Merck, 65% for analysis), followed by drying overnight under vacuum at room temperature and calcination in 375 ml/min (GHSV = 15000 h<sup>-1</sup>) of 2% NO/N<sub>2</sub> at 350°C (2°C/min) for 1 hour. Part of the as-prepared sample was used for catalytic reaction (with in-situ reduction to obtain metallic Cu on SiO<sub>2</sub>) as described below and a portion (2 g) intended for characterization that underwent reduction in a flow of 100 ml/min of 20% H<sub>2</sub> in Ar at 250°C (2 °C/min) for 2½ h. After the reduction treatment, the resulting Cu/SiO<sub>2</sub> was passivated for 15 minutes by slowly exposing the sample to diluted air/N<sub>2</sub> at room temperature. The sample was stored in a glove box under argon atmosphere.

### Characterization

N<sub>2</sub>-physisorption measurements were performed at -196°C using a Micromeritics Tristar 3000 apparatus. The BET method was used to calculate the specific surface areas. The pore volumes were determined at  $p/p_0 = 0.983$ . Pore size distributions were determined from the adsorption branch by the BJH method<sup>26</sup>. X-ray diffraction (XRD) was performed with a Bruker-Nonius D8 Advance X-ray diffractometer using Co-K<sub>α12</sub> ( $\lambda = 1.79026 \text{ \AA}$ ) radiation. Diffractograms were collected at room temperature from 20° to 70° (2θ). The specimen holder was loaded in the glove box with the catalysts either after reduction and passivation or catalysis and passivation and was subsequently sealed. Copper crystallite sizes were estimated by applying the Debye-Scherrer equation to the (111) diffraction of Cu (2θ = 50.5°,  $k = 0.9$ )<sup>27</sup>. H<sub>2</sub>-TPD was performed on the catalysts before and after methanol synthesis<sup>28</sup>. Measurements were carried out in a fixed-bed flow setup and online gas analysis was performed by a quadrupole mass spectrometer (Balzers GAM 445). The copper phyllosilicate was reduced in-situ at 250 °C (2 °C/min) in 100 ml/min of 1% H<sub>2</sub>/He. At 250 °C the gas flow was changed to 100 ml/min of 100% H<sub>2</sub> for 2½ h. The calcined copper on silicagel and the samples after catalysis and passivation were reduced in-situ at 220 °C (2 °C/min) in a flow 100 ml/min of 1% H<sub>2</sub>/He for 7 hours. Then the samples were flushed for ½ h in 100 ml/min of He to remove any adsorbed hydrogen and subsequently cooled down to 0 °C. At this temperature the reactor was pressurized to 1.6 MPa of H<sub>2</sub>, before it was cooled down further to -33 °C. After ½ h, the catalyst was rapidly cooled to -196 °C and depressurized. The gas flow was changed to 100 ml/min of He to

flush out the excessive hydrogen. After 1 hour the temperature was increased up to 210 °C (6 °C/min) and the H<sub>2</sub> desorption profile was recorded. Copper surface areas (SA<sub>Cu, H<sub>2</sub></sub>) were calculated from the amount of desorbed hydrogen assuming a H/Cu ratio of 0.5 and  $1.47 \cdot 10^{19}$  copper surface atoms per m<sup>2</sup>. Temperature programmed reduction (TPR) was performed using an Autochem II ASAP 2910 from micromeritics. The H<sub>2</sub> concentration during the experiment was measured with a thermal conductivity detector. About 0.05 g of sample was put on top of a quartz wool bed in a glass reactor tube and subsequently heated to 500 °C (5 °C/min) under a (50 ml/min) flow of 5% H<sub>2</sub>/Ar. The copper loading was estimated from the H<sub>2</sub> consumption by assuming the following reduction stoichiometry:  $\text{CuO} + \text{H}_2 \rightarrow \text{Cu} + \text{H}_2\text{O}$ . Transmission electron microscopy (TEM) images were acquired with a Tecnai 12 (FEI) microscope operated at 120 kV with a pixel size of 0.45 nm. Precipitated Cu/SiO<sub>2</sub> samples before and after catalytic tests were prepared by grinding followed by sonication in ethanol. A droplet of the ethanol suspension was deposited on a carbon coated copper TEM grid (Agar S162 200 Mesh Cu). The resolution and contrast were sufficient to detect particles larger than 2 nm (4x4 pixels). The impregnated Cu/SiO<sub>2</sub> was ground, embedded in a two component epoxy resin (Epofix, EMS) and cured at 60 °C overnight, and cut into thin sections (50-100 nm) using a Diatome Ultra 35° diamond knife mounted on an Ultracut E microtome (Reichert-Jung). Sections were deposited on a TEM grid. The resolution and contrast were sufficient to detect and measure particles larger than 3 nm (6x6 pixels). Copper surface areas (SA<sub>Cu, TEM</sub>) were calculated from the particle size distributions obtained via TEM, and assuming spherical particles. Energy dispersive X-ray (EDX) spectroscopy was performed on a Technai 20FEG (FEI) electron microscope equipped with a field emission gun and an EDAX Super Ultra Thin Window EDX detector and processed with Tecnai Imaging and Analysis software. Samples were placed onto a carbon coated Ni TEM grid (Agar 162 200 Mesh Ni) and mounted on a low-background sample holder (Philips) with a 0.1 mm thick Be specimen support film and a Be ring to clamp the grid. The Cu/Si atomic ratio was determined for areas with a diameter of 100 to 500 nm from the integrated intensity of the Si-K and Cu-K signal. From that the weight loading of copper on silica was calculated.

### Electron tomography

Electron tomography was performed on a Tecnai 20 (FEI) transmission electron microscope at 200 kV acceleration voltage in bright-field imaging mode. Quantifoil R2/1 Cu TEM grids with thin carbon film were used. The grids were wetted with a solution of 5 nm colloidal gold particles and subsequently dried. The gold particles acted as fiducial markers during the alignment. The catalyst samples were dispersed in ethanol and subsequently deposited on the grids. Tilt images were recorded from -70° to +70° with

intervals of 2°. The resulting images were aligned to a common origin and rotation axis by tracking the 5 nm Au fiducial markers. 3D reconstruction of aligned tilt series was performed using a weighted back-projection algorithm in IMOD<sup>29</sup>.

### Catalytic testing

The performance of the catalysts in the methanol synthesis reaction was investigated in a fixed-bed stainless steel reactor with an inner diameter of 0.9 cm (Autoclave Engineers). The precipitated and impregnated Cu/SiO<sub>2</sub> prior to reduction were ground and sieved to obtain a sieve fraction of 0.42 to 0.63 mm. 0.55 g of the precipitated sample was diluted with SiC granules (sieve fraction of 0.25-0.42 mm) in a SiC : sample volume ratio of 1:4 and loaded into the reactor (catalyst bed height of 7 cm). 0.81 g of the impregnated sample was loaded into the reactor (catalyst bed height of 5 cm) without dilution. Subsequently, both samples were reduced in-situ at 250 °C (2 °C/min) for 2.5 h with a flow of 110 ml/min 20% H<sub>2</sub>/Ar. After that, the temperature was lowered to 100 °C to prevent premature production of methanol when switching to syngas. The reactor was flushed with syngas (10% Ar, 7% CO<sub>2</sub>, 23% CO, 60% H<sub>2</sub>, Linde), which was purified with a metal carbonyl trap<sup>30</sup> (4.0 g of 0.5-1.5 mm H-USY zeolite, CVB-780 from Zeolyst Int. and 5 g activated carbon, Norit R3B). The argon in the syngas feed acted as an internal standard for the gas chromatograph (GC). After 30 minutes of flushing the pressure was increased to 40 bar. From this time on the exit gas composition was analysed every 110 minutes with a GC (Varian 450). The lines from the reactor to the GC were heated to 150 °C to avoid any methanol or water condensation. The first GC channel consisted of a HAYESEP Q (0.5Mx1.8") column followed by a MOLSIEVE 13x (15x1/8") column that led to a thermal conductivity detector (TCD). The second GC channel consisted of a CP-SIL 8CB FS capillary column that led to a flame ionization detector (FID). Three chromatograms were recorded of the syngas feed. The temperature was then increased to 260 °C (2 °C/min) to initiate methanol production. The amount of catalyst and the syngas flow (10-30 ml/min) were chosen such that CO conversion levels near 15% were obtained. The activity of the catalyst was determined by the conversion of CO and CO<sub>2</sub> during reaction. The deviation in between different tests in the initial activity is ± 35% and in the deactivation ± 3%. Turnover frequencies (TOF) were calculated with the assumption that one copper surface atom is an active site. The initial and final (at the end of the catalytic testing) amount of active sites was based upon H<sub>2</sub>-TPD before and after reaction, respectively. The selectivity was determined from the FID chromatograms and was in all cases more than 98.5% towards methanol, with trace amounts of dimethyl ether, methane, ethanol, ethane and propane. The stability of the methanol productivity over time was based upon the methanol signal from the TCD detector. Second order deactivation constants were

calculated according to the formula:  $\frac{1}{a} = 1 + k_{d,2} * t^2$ , in which  $a$  is the activity,  $k_{d,2}$  the second order deactivation constant and  $t$  time. After catalysis the samples were passivated for 15 min by slowly exposing the sample to air diluted with Ar at room temperature. The sample was stored in a glove box under argon atmosphere.

## Results & Discussion

### Characterization of Cu/SiO<sub>2</sub>

Cu/SiO<sub>2</sub> was prepared via either precipitation or incipient wetness impregnation (Figure 5.1A-D). For the precipitated catalyst, XRD of the reduced and passivated sample showed that reduction at 250 °C in a flow of 20% H<sub>2</sub> in Ar for 2½ hours resulted in the reduction of precipitated copper phyllosilicate to metallic copper with an average crystallite size of 5.2 nm and silica (Figure 5.1A), in line with literature<sup>25b, 31</sup>. TEM showed the presence of 8 nm sized copper particles homogeneously distributed over the silica support after reduction and passivation (Figure 5.1B). The copper loading as determined with TPR was 40.1 wt%, which corresponds well to the theoretical amount of 41 wt% based on quantitative deposition. The local copper loading measured with TEM-EDX was 38 ± 1 wt% (5 different locations), in agreement with the bulk copper loading.

Incipient wetness impregnation with a 2 M aqueous copper nitrate solution of commercially available silica gel with an average pore diameter of 9 nm, followed by drying, calcination in NO/N<sub>2</sub> flow, reduction and passivation, resulted in 8 nm sized copper particles, in high-density domains of a couple of hundred nanometers to even micrometers, as determined by TEM (Figure 5.1D). The bulk copper loading in this catalyst as determined with TPR was 8.6 wt%, which corresponds to the nominal loading of 9.0 wt%. EDX revealed a weight loading of 37 ± 6% (9 locations) copper on silica within the high-density domains of particles, while other parts of the silica support were almost empty (< 1 wt% Cu, 6 locations). These domains are a consequence of the drying and calcination process<sup>23a, 32</sup>. In a flow of 2% NO/N<sub>2</sub>, non-mobile Cu<sub>2</sub>NO<sub>3</sub>(OH)<sub>3</sub> is nucleated, which might grow larger from mobile Cu(NO<sub>3</sub>)<sub>2</sub>•3H<sub>2</sub>O. As a result, Cu<sub>2</sub>NO<sub>3</sub>(OH)<sub>3</sub> completely filled up the pores in some regions while the pores in other regions were left empty. The maximum amount of copper within a region, assuming a density of Cu<sub>2</sub>NO<sub>3</sub>(OH)<sub>3</sub> of 1.675 g/cm<sup>3</sup><sup>23b, 33</sup> and a silica pore volume of 0.81 ml/g, was calculated to be 41 wt%. This is in close accordance to the observed copper loading within the high-density domains. Upon further decomposition in NO/N<sub>2</sub> flow and reduction using H<sub>2</sub>, metallic copper particles with an average copper crystallite size of 8.7 nm were formed, as determined from XRD after reduction and passivation (Figure 5.1C). The final size of the copper particles (~8 nm)

was close to the size of the pores of the silica support ( $\sim 9$  nm) as found before<sup>23b, 34</sup>. Both Cu/SiO<sub>2</sub> prepared via impregnation and via precipitation thus consisted on a local scale of a similar loading of similarly sized copper particles.

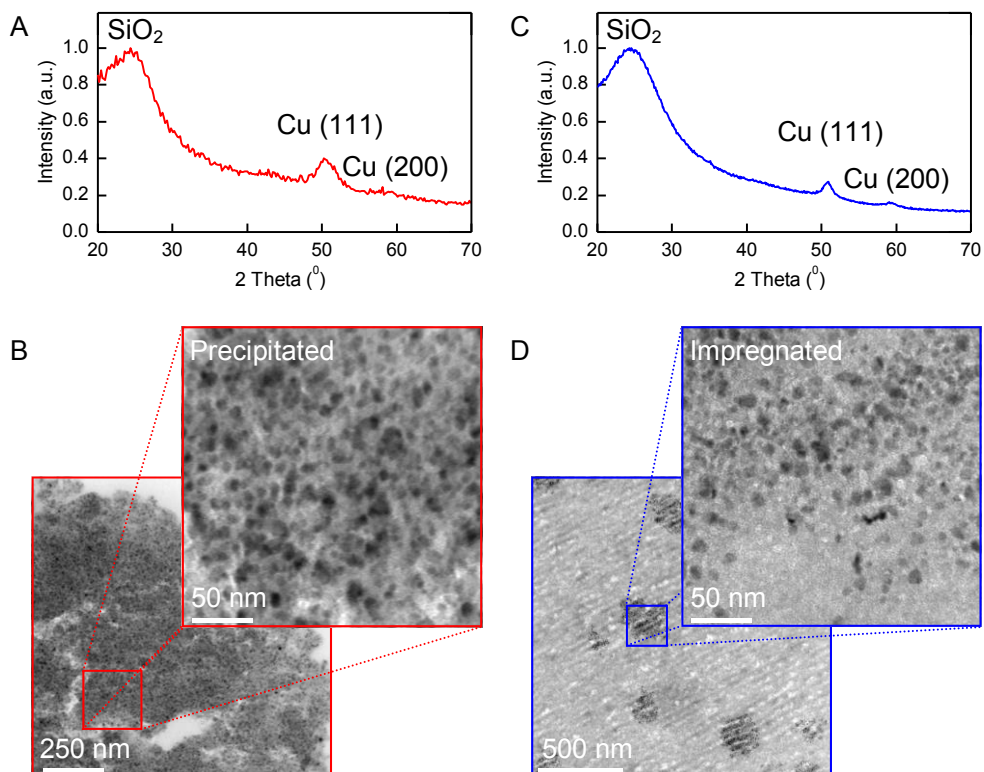


**Figure 5.1.** (A, C) X-ray diffractograms of Cu/SiO<sub>2</sub> after reduction and passivation prepared via either precipitation (A) or incipient wetness impregnation (C). (B, D) TEM images at lower (bottom left) and higher (top right) magnifications of Cu/SiO<sub>2</sub> after reduction and passivation prepared via either precipitation (B) or incipient wetness impregnation (D).

N<sub>2</sub>-physisorption was used to assess the porosity of the impregnated and precipitated Cu/SiO<sub>2</sub> after reduction and passivation (Figure 5.2A-D and Table 5.1). The physisorption isotherms were markedly different for both samples. The impregnated Cu/SiO<sub>2</sub> had a type H2 hysteresis loop which is generally obtained for porous materials consisting of agglomerates of approximately uniform spheres like silica gel<sup>35</sup>. The pore size distribution was relatively narrow with a maximum near 9 nm (Figure 5.2B). The precipitated Cu/SiO<sub>2</sub> displayed a type H4 hysteresis loop which is associated with slit-like pores and typical for

aggregates of plates<sup>24, 36</sup>. As a result, the pore size distribution was very broad with macropores (>50 nm) next to mesopores (2-50 nm)(Figure 5.2D).

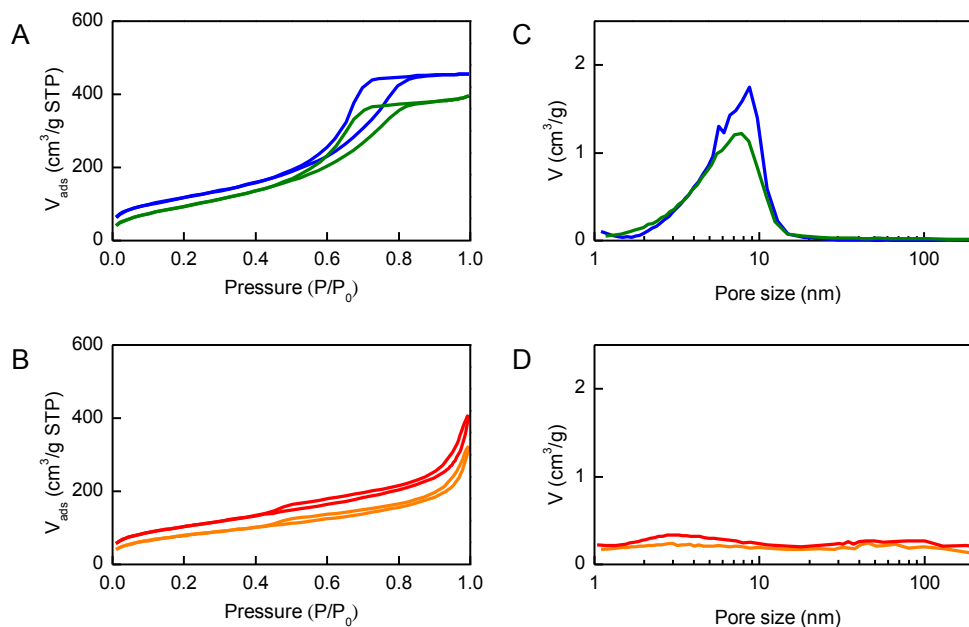


**Figure 5.2.** N<sub>2</sub>-physorption isotherms (A) and corresponding pore size distributions (B) after reduction and passivation (blue) and after catalysis and passivation (green) of Cu/SiO<sub>2</sub> prepared via impregnation. N<sub>2</sub>-physorption isotherms (C) and corresponding pore size distributions (D) after reduction and passivation (red) and after catalysis and passivation (orange) of Cu/SiO<sub>2</sub> prepared via precipitation.

**Table 5.1.** Data derived from N<sub>2</sub>-physorption for fresh and spent catalysts.

	After reduction and passivation		After catalysis and passivation	
	BET surface area (m <sup>2</sup> /g <sub>cat</sub> )	Pore volume (cm <sup>3</sup> /g <sub>cat</sub> )	BET surface area (m <sup>2</sup> /g <sub>cat</sub> )	Pore volume (m <sup>3</sup> /g <sub>cat</sub> )
Precipitated Cu/SiO <sub>2</sub>	375	0.59	290	0.46
Impregnated Cu/SiO <sub>2</sub>	430	0.70	365	0.61

Electron tomography was used to visualize the support structure and the 3D location of the copper particles within the silica support<sup>32, 37</sup>. Figure 5.3A and B show tomogram thin sections of the precipitated Cu/SiO<sub>2</sub> after reduction and passivation. In Figure 5.3A the silica support shows a plate-like structure with different pore sizes. This is in line with the broad pore size distribution found from N<sub>2</sub>-physorption. Careful analysis going through the material section by section at higher magnifications indicated that some copper particles (darker image features) were at least partially embedded within the silica,

as shown in Figure 5.3B and illustrated in the scheme at the bottom right of Figure 5.3B (See supporting information for a movie of the reconstructed volume). Figure 5.3C shows a tomogram section of the impregnated Cu/SiO<sub>2</sub> after reduction and passivation. In this case the copper particles were located in between the silica primary particles as illustrated in the scheme at the bottom right of the figure. The porosity in this sample was harder to resolve compared to the precipitated sample, due to the narrower pores located within more dense Cu/SiO<sub>2</sub> aggregates of several hundreds of nanometers. Despite the similar local weight loadings, the interparticle distances seem to be smaller for the impregnated catalyst. The higher volumetric copper loading might be due to the lower porosity in the impregnated silica gel (Figure 5.2).

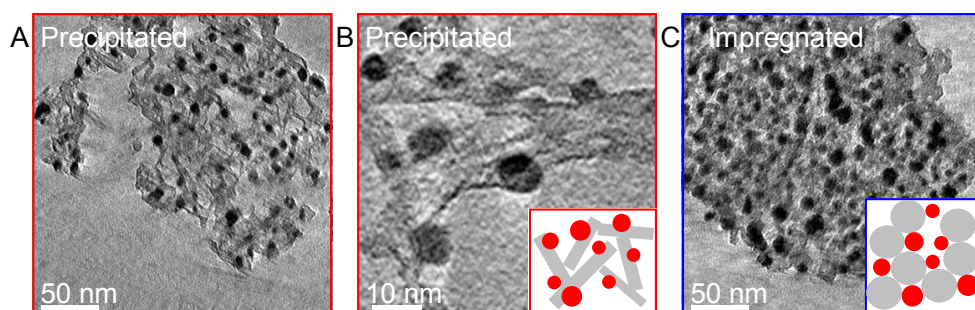


**Figure 5.3.** Electron tomogram sections of precipitated (A and B) and impregnated (C) Cu/SiO<sub>2</sub>. The thickness of numerical section A and C is 3.6 nm, the thickness of numerical section B is 0.56 nm. Schematic representations of the copper (red) and silica (grey) in both catalysts are depicted in the bottom right of Figure 5.3 B and C.

H<sub>2</sub>-TPD was used to determine the accessible copper surface area of the two catalysts (Table 5.2). For the precipitated catalyst the specific copper surface area measured with H<sub>2</sub>-TPD was about 33% lower than the one based on the TEM particle size distributions, probably due to partial entrapment of the copper particles as suggested by electron tomography. For the impregnated copper on silica the copper surface area inaccessible for H<sub>2</sub> adsorption was insignificant, indicating a less extensive metal-support interface area for this catalyst.

**Table 5.2.** Specific copper surface areas before and after reaction based on H<sub>2</sub>-TPD and TEM

	Before reaction		After reaction	
	SA <sub>Cu,TEM</sub> (m <sup>2</sup> <sub>Cu</sub> /g <sub>Cu</sub> )	SA <sub>Cu,H2</sub> (m <sup>2</sup> <sub>Cu</sub> /g <sub>Cu</sub> )	SA <sub>Cu,TEM</sub> (m <sup>2</sup> <sub>Cu</sub> /g <sub>Cu</sub> )	SA <sub>Cu,H2</sub> (m <sup>2</sup> <sub>Cu</sub> /g <sub>Cu</sub> )
Precipitated Cu/SiO <sub>2</sub>	73	48	65	39
Impregnated Cu/SiO <sub>2</sub>	68	67	62	38

### Catalytic performance

The performance of impregnated and precipitated Cu/SiO<sub>2</sub> was investigated in the methanol synthesis reaction at 40 bar, 260 °C at 15% CO conversion. The selectivity towards methanol was above 98.5%. The methanol synthesis productivity was calculated from the conversion of CO + CO<sub>2</sub> (Table 5.3). The TOFs of the catalysts were between 2.0 and 4.0\*10<sup>-3</sup> s<sup>-1</sup>, in close accordance with previously reported values for copper on silica<sup>22b, 23b, 38</sup>. The copper weight-based methanol productivity as well as the TOF based on the copper surface area measured with H<sub>2</sub>-TPD was lower for the precipitated catalyst (Table 5.3). Robbins et al. have reported that the activity for Cu/SiO<sub>2</sub> catalysts in the methanol synthesis reaction from a mixture of CO and CO<sub>2</sub>, scales linearly with the metallic copper surface area<sup>22b, 39</sup>. The lower TOF for the precipitated catalyst indicates that for this sample even less copper surface area had been available for methanol synthesis than was indicated by H<sub>2</sub>-TPD.

**Table 5.3.** Catalytic performance of Cu/SiO<sub>2</sub> in the methanol synthesis at 260 °C and 40 bar; TOF values based on H<sub>2</sub>-TPD.

	Initial MeOH productivity (mol MeOH kg <sub>Cu</sub> <sup>-1</sup> h <sup>-1</sup> )	Initial TOF (s <sup>-1</sup> )	Final TOF (s <sup>-1</sup> )	Deactivation constant (h <sup>-1</sup> )
Precipitated Cu/SiO <sub>2</sub>	8.8 ± 3.1	2.1 ± 0.7 * 10 <sup>-3</sup>	1.9 ± 0.7 * 10 <sup>-3</sup>	0.0023
Impregnated Cu/SiO <sub>2</sub>	20.5 ± 7.2	3.5 ± 1.2 * 10 <sup>-3</sup>	3.6 ± 1.3 * 10 <sup>-3</sup>	0.0033

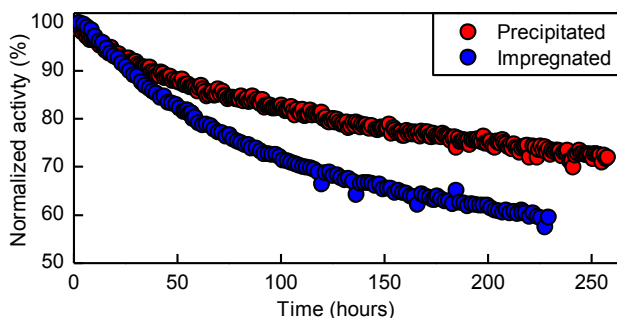


**Figure 5.4.** Normalized activity over time for Cu/SiO<sub>2</sub> prepared via precipitation (red) and via impregnation (blue).

The loss in activity over time was less for the precipitated catalyst than for the impregnated catalyst resulting in a lower second-order deactivation constant (Figure 5.4 and Table 5.3). For both catalysts the deactivation corresponded to the loss of accessible copper surface area upon reaction as determined by  $H_2$ -TPD (Table 5.2). To determine the loss of copper surface area due to copper particle growth, the particle size distributions after catalysis and passivation were determined with TEM (Figure 5.5). For the precipitated catalyst the particle size distribution had increased from  $8.0 \pm 2.2$  nm to  $8.6 \pm 2.6$  nm and for the impregnated catalyst from  $8.3 \pm 2.6$  nm to  $9.2 \pm 2.7$  nm. Analysis of the variance in the size distribution showed that the increase in particle size is statistically significant for both samples ( $p_{(\text{same mean size})} \ll 0.001$ ). The copper crystallite size as determined with XRD had increased from 5.2 to 5.8 nm for the precipitated catalyst and from 8.7 to 9.2 nm for the impregnated catalyst (Figure 5.6). For both catalysts, the increase in crystallite size had been similar to the increase in particle size. The precipitated catalyst had thus been more resistant against particle growth in line with the higher catalyst stability in the methanol synthesis reaction. The higher nanoparticle stability for the precipitated catalyst might have been due to a stronger metal-support interaction<sup>2,15</sup>. For the short interparticle distances ( $< 5$  nm), particle migration and coalescence has been identified to significantly contribute to particle growth<sup>8b, 32</sup>. Electron tomography indicated for the precipitated catalyst that the particles were partially entrapped in the silica support, possibly limiting their mobility due to the increased metal-support interface area<sup>2,15</sup>.

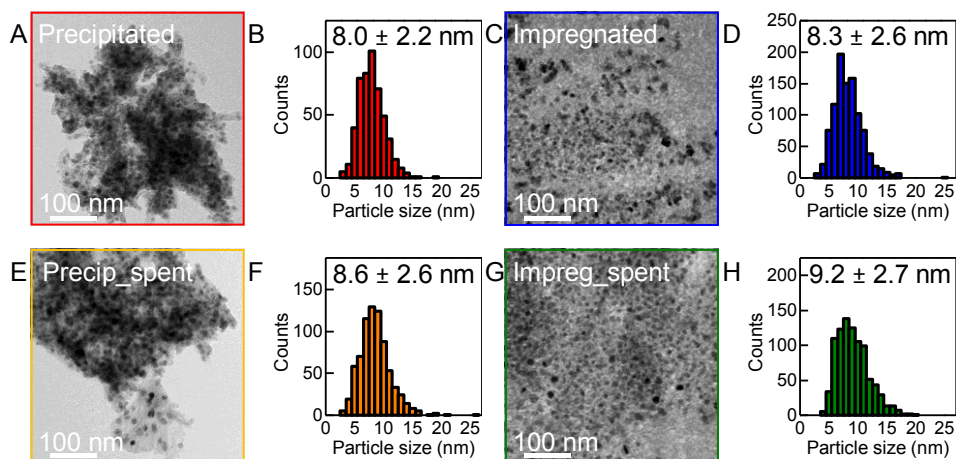


**Figure 5.5.** TEM images and corresponding particle size distributions of  $Cu/SiO_2$  prepared via precipitation before (A, B) and after reaction (E, F). TEM images and corresponding particle size distributions of  $Cu/SiO_2$  prepared via impregnation before (C, D) and after reaction (G, H).

Particle growth only explained part of the loss of copper surface area, especially in the case of the impregnated catalyst, indicating that secondary effects like copper surface blockage by silica also play a role.  $N_2$ -physisorption measurements after catalysis and passivation showed a significant decrease of pore volume and BET surface area for both catalysts (Figure 5.2 and Table 5.1). Silica restructuring during reaction had taken place and probably led to reduced gas accessibility of the copper surface by e.g. partial coverage. Since for the impregnated catalyst the size of the copper particles was close to the size of the pores, the metal-support interface area might furthermore have been increased during reaction due to growth of the copper particles or due to shrinkage of the pores<sup>15</sup>. Previously it has been reported that the support in CuZn/SiO<sub>2</sub> catalysts was stable during the methanol synthesis at similar conditions<sup>13a</sup>. During synthesis of these catalysts, co-impregnation of copper and zinc led to the incorporation of zinc in the silica support, resulting in a zinc-silicate, which is more stable than ZnO and SiO<sub>2</sub> separately<sup>40</sup>.

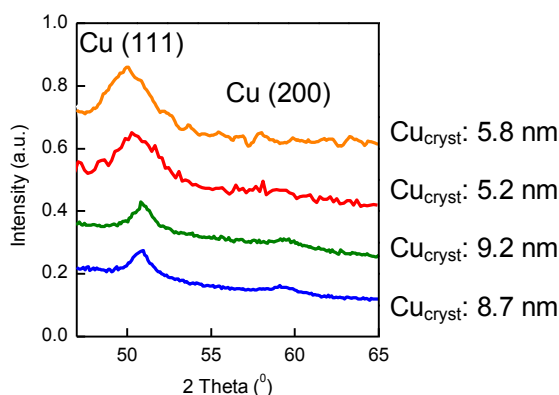


**Figure 5.6.** X-ray diffractograms of Cu/SiO<sub>2</sub> prepared via impregnation before (blue) and after reaction (green) and of Cu/SiO<sub>2</sub> prepared via precipitation before (red) and after reaction (orange). Corresponding crystallite sizes ( $Cu_{cryst}$ ) are displayed next to the respective diffractogram.

## Conclusion

Cu/SiO<sub>2</sub> catalysts with similar copper particle size and local copper loading were synthesized via either precipitation or incipient wetness impregnation. Electron tomography revealed for the precipitated catalyst a plate-like silica structure with copper particles partially entrapped, whereas for the impregnated catalyst the copper particles were located in the pores between the primary particles of the silica gel. For the precipitated catalyst, the initial copper-weight normalized activity in the methanol synthesis reaction was lower, but catalyst stability higher partly due to more limited

copper particle growth. Additionally, silica restructuring during reaction had occurred and resulted in catalyst deactivation attributed to partial coverage of the copper surface. Partial entrapment of the copper particles, achieved via precipitation and subsequent reduction, can hence lead to lower catalyst activity but at the same time to higher catalyst stability.

### Supporting Movie

Movie S5.1 can be found in the online version of the article: van den Berg, R.; Zečević, J.; Sehested, J.; Helveg, S.; de Jongh, P. E.; de Jong, K. P. *Catal. Today* **2015**, doi:10.1016/j.cattod.2015.08.052

### Acknowledgments

The project was supported financially by Haldor Topsøe A/S. The authors are grateful to Grace, in particular to Robert Goedvree, for providing the silica gel support. Sebastian Kuld is acknowledged for H<sub>2</sub>-TPD measurements. Hans Meeldijk is acknowledged for microtomy and TEM-EDX analysis.

### References

- (1) (a) Bell, A. T. *Science* **2003**, *299*, 1688-91; (b) Torres Galvis, H. M.; Bitter, J. H.; Khare, C. B.; Ruitenbeek, M.; Dugulan, A. I.; de Jong, K. P. *Science* **2012**, *335*, 835-838.
- (2) Bartholomew, C. H. *Appl. Catal., A* **1993**, *107*, 1-57.
- (3) (a) Lunkenbein, T.; Schumann, J.; Behrens, M.; Schlögl, R.; Willinger, M. G. *Angew. Chem. Int. Ed.* **2015**, *127*, 1-6; (b) Tauster, S. J.; Fung, S. C.; Baker, R. T. K.; Horsley, J. A. *Science* **1981**, *211*, 1121-1125.
- (4) (a) van de Loosdrecht, J.; Botes, F. G.; Ciobica, I. M.; Ferreira, A.; Gibson, P.; Moodley, D. J.; Saib, A. M.; Visagie, J. L.; Weststrate, C. J.; Niemantsverdriet, J. W. *Fischer-Tropsch Synthesis: Catalysts and Chemistry. In Comprehensive Inorganic Chemistry II*, Reedijk, J.; Poeppelmeier, K., Eds. Elsevier: Oxford, 2013; Vol. 7, pp 525-557; (b) Munnik, P.; de Jongh, P. E.; de Jong, K. P. *J. Am. Chem. Soc.* **2014**, *136*, 7333-40.
- (5) (a) Moullijn, J. A.; Diepen, A. E. V.; Kapteijn, F. *Science* **2001**, *212*, 3-16; (b) Simonsen, S. B.; Chorkendorff, I.; Dahl, S.; Skoglundh, M.; Sehested, J.; Helveg, S. *J. Am. Chem. Soc.* **2010**, *132*, 7968-7975.
- (6) Munnik, P.; Velthoen, M. E. Z.; de Jongh, P. E.; de Jong, K. P.; Gommers, C. J. *Angew. Chem. Int. Ed.* **2014**, *126*, 9647-9651.
- (7) Twigg, M. V.; Spencer, M. S. *Appl. Catal., A* **2001**, *212*, 161-174.
- (8) (a) Pulvermacher, B. *J. Catal.* **1973**, *245*, 224-245; (b) Lifshitz, I. M.; Slyozov, V. V. *J. Phys. Chem. Solids* **1961**, *19*, 35-50.
- (9) Rasmussen, D. B.; Janssens, T. V. W.; Temel, B.; Bligaard, T.; Hinnemann, B.; Helveg, S.; Sehested, J. *J. Catal.* **2012**, *293*, 205-214.
- (10) (a) Cao, A.; Lu, R.; Vesper, G. *Phys. Chem. Chem. Phys.* **2010**, *12*, 13499-510; (b) Ouyang, R.; Liu, J.-X.; Li, W.-X. *J. Am. Chem. Soc.* **2013**, *135*, 1760-1771; (c) Wallace, W. T.; Min, B. K.; Goodman, D. W. *J. Mol. Catal. A: Chem.* **2005**, *228*, 3-10.
- (11) (a) Campbell, C. T.; Parker, S. C.; Starr, D. E. *Science* **2002**, *298*, 811-814; (b) Datye, A. K.; Xu, Q.; Kharas, K. C.; McCarty, J. M. *Catal. Today* **2006**, *111*, 59-67.

- (12) (a) Morgenstern, K.; Rosenfeld, G.; Comsa, G. *Surf. Sci.* **1999**, *441*, 289-300; (b) Simonsen, S. B.; Chorkendorff, I.; Dahl, S.; Skoglundh, M.; Sehested, J.; Helveg, S. *J. Catal.* **2011**, *281*, 147-155; (c) Prieto, G.; Zečević, J.; Friedrich, H.; de Jong, K. P.; de Jongh, P. E. *Nat. Mater.* **2013**, *12*, 34-39.
- (13) (a) Prieto, G.; Shakeri, M.; de Jong, K. P.; de Jongh, P. E. *ACS Nano* **2014**, *8*, 2522-2531; (b) Arnal, P. M.; Comotti, M.; Schüth, F. *Angew. Chem. Int. Ed.* **2006**, *45*, 8224-8227.
- (14) (a) Joo, S. H.; Park, J. Y.; Tsung, C. K.; Yamada, Y.; Yang, P.; Somorjai, G. A. *Nat. Mater.* **2009**, *8*, 126-131; (b) Lu, J.; Fu, B.; Kung, M. C.; Xiao, G.; Elam, J. W.; Kung, H. H.; Stair, P. C. *Science* **2012**, *335*, 1205-1208; (c) Laursen, A. B.; Højholt, K. T.; Lundegaard, L. F.; Simonsen, S. B.; Helveg, S.; Schüth, F.; Paul, M.; Grunwaldt, J. D.; Kegnæs, S.; Christensen, C. H.; Egeblad, K. *Angew. Chem. Int. Ed.* **2010**, *49*, 3504-3507.
- (15) Wynblatt, P.; Gjostein, N. A. *Progr. Solid State Chem.* **1976**, *9*, 21-58.
- (16) de Jong, K. P.; (Ed.). *Synthesis of solid catalysts*. Wiley-VCH: Weinheim, 2009.
- (17) (a) Baltes, C.; Vukojevic, S.; Schüth, F. *J. Catal.* **2008**, *258*, 334-344; (b) Fujita, S.-I.; Moribe, S.; Kanamori, Y.; Kakudate, M.; Takezawa, N. *Appl. Catal., A* **2001**, *207*, 121-128.
- (18) Neimark, A. V.; Kheifez, L. I.; Fenelonov, V. B. *Ind. Eng. Chem. Prod. Rd.* **1981**, *20*, 439-450.
- (19) Montini, T.; Condo, A. M.; Hickey, N.; Lovey, F. C.; De Rogatis, L.; Fornasiero, P.; Graziani, M. *Appl. Catal., B* **2007**, *73*, 84-97.
- (20) (a) Behrens, M.; Furche, A.; Kasatkin, I.; Trunschke, A.; Busser, W.; Muhler, M.; Kniep, B.; Fischer, R.; Schlögl, R. *ChemCatChem* **2010**, *2*, 816-818; (b) Behrens, M.; Kasatkin, I.; Kühl, S.; Weinberg, G. *Chem. Mater.* **2010**, *22*, 386-397; (c) ü, S.; Tarasov, A.; Zander, S.; Kasatkin, I.; Behrens, M. *Chem. Eur. J.* **2014**, *20*, 3782-3792.
- (21) Hansen, P. L.; Wagner, J. B.; Helveg, S.; Rostrup-Nielsen, J. R.; Clausen, B. S.; Topsøe, H. *Science* **2002**, *295*, 2053-2055.
- (22) (a) Hansen, J. B.; Højlund Nielsen, P. E. Methanol Synthesis. In *Handbook of Heterogeneous Catalysis*, Ertl, G.; Knözinger, H.; Schüth, F.; Weltkamp, J., Eds. Wiley-VCH: 2008; pp 2920-2949; (b) Robbins, J. L.; Iglesia, E.; Kelkar, C. P.; DeRites, B. *Catal. Lett.* **1991**, *10*, 1-10.
- (23) (a) Munnik, P.; Wolters, M.; Gabriëlsson, a.; Pollington, S. D.; Headdock, G.; Bitter, J. H.; de Jong, P. E.; de Jong, K. P. *J. Phys. Chem. C* **2011**, *115*, 14698-14706; (b) Prieto, G.; Meeldijk, J. D.; de Jong, K. P.; de Jongh, P. E. *J. Catal.* **2013**, *303*, 31-40.
- (24) van der Grift, C. J. G.; Elberse, P. A.; Mulder, A.; Geus, J. W. *Appl. Catal.* **1990**, *59*, 275-289.
- (25) (a) Toupance, T.; Kermarec, M.; Lambert, J.-F.; Louis, C. *J. Phys. Chem. B* **2002**, *106*, 2277-2286; (b) Chen, L.; Guo, P.; Qiao, M.; Yan, S.; Li, H.; Shen, W.; Xu, H.; Fan, K. *J. Catal.* **2008**, *257*, 172-180.
- (26) Barret, E. P.; Joyner, L. G.; Halenda, P. P. *J. Am. Chem. Soc.* **1951**, *73*, 373-380.
- (27) Patterson, A. L. *Phys. Rev.* **1939**, *56*, 978-982.
- (28) (a) Muhler, M.; Nielsen, L. P.; Tornqvist, E.; Clausen, B. S.; Topsøe, H. *Catal. Lett.* **1992**, *14*, 241-249; (b) Genger, T.; Hinrichsen, O.; Muhler, M. *Catal. Lett.* **1999**, *59*, 137-141.
- (29) Kremer, J. R.; Mastronarde, D. N.; McIntosh, J. R. *J. Struct. Biol.* **1996**, *116*, 71-76.
- (30) Smit, C. J.; Eijkhoudt, R.; Geus, J. W.; Van Dillen, A. J. *Prepr. Pap. -Am. Chem. Soc., Div. Fuel Chem.* **1999**, *44*, 119-123.
- (31) Gong, J.; Yue, H.; Zhao, Y.; Zhao, S.; Zhao, L.; Lv, J.; Wang, S.; Ma, X. *J. Am. Chem. Soc.* **2012**, *134*, 13922-13925.
- (32) Prieto, G.; Zečević, J.; Friedrich, H.; de Jong, K. P.; de Jongh, P. E. *Nat. Mater.* **2013**, *12*, 34-39.
- (33) Guillou, N.; Louer, M.; Louer, D. *J. Solid State Chem.* **1994**, *109*, 307-314.
- (34) Khodakov, A. Y.; Griboval-Constant, A.; Bechara, R.; Villain, F. *J. Phys. Chem. B* **2001**, *105*, 9805-9811.
- (35) Sing, K. S. W. *Pure Appl. Chem.* **1982**, *54*, 2201-2218.
- (36) Huang, Z.; Cui, F.; Xue, J.; Zuo, J.; Chen, J.; Xia, C. *J. Phys. Chem. C* **2010**, *114*, 16104-16113.
- (37) Midgley, P. A.; Dunin-Borkowski, R. E. *Nat. Mater.* **2009**, *8*, 271-80.
- (38) Please note that these values are slightly lower than those reported in reference (23b), as we found the calculation in (23b) not to be fully correct. The correct calculation procedure can be found in the supporting

information of Chapter 3 and 4. (b) van den Berg, R.; Parmentier, T. E.; Elkjær, C. F.; Gommès, C. J.; Sehested, J.; Helveg, S.; de Jongh, P. E.; de Jong, K. P. *ACS Catal.* **2015**, *5*, 4439-4448.

(39) Waugh, K. C. *Catal. Lett.* **2012**, *142*, 1153-1166.

(40) Barin, I. *Thermochemical Data of Pure Substances*. 3 ed.; VCH Wiley: Weinheim, 1995; Vol. 1.



## Chapter 6a

### Summary, Concluding Remarks and Outlook

The methanol synthesis reaction is a large scale industrial process to convert  $H_2$ , CO and  $CO_2$ , a mixture also referred to as syngas, to methanol. Methanol is one of the essential building blocks in the petrochemical industry since it can be converted to almost everything. Methanol could, furthermore, potentially be used as a fuel or energy carrier in a more sustainable energy system. Syngas is nowadays primarily produced from oil, coal and natural gas, but can also be produced from biomass, waste, or even via artificial photosynthesis from  $CO_2$  and  $H_2O$ . Syngas conversion to methanol therefore presents an alternative, and potentially more sustainable, route for products, fuels, or energy carriers that are traditionally derived from oil. The attractiveness of the reaction for the (near) future is reflected in the expected increase in methanol production from 65 million tons in 2013 to 105 million tons in 2023.

The catalyst used in industry for this process is  $Cu/ZnO/Al_2O_3$  obtained via co-precipitation containing copper particles with an initial size of about 7 nm. As discussed in **Chapter 1**, although copper-based methanol synthesis catalysts have been intensively studied over the past decades, a number of pressing scientific and technological challenges remain. First of all, the fundamental understanding and control of the processes involved in the synthesis of supported copper catalysts is rather limited. Secondly, the sensitivity of the reaction to the copper surface structure and the role of the zinc promoter are under debate in literature and it is unclear which structural parameters are essential for maximum activity. Thirdly, growth of the copper particles results in a substantial loss in activity over time and thereby limits the lifetime of the catalyst. The influence of different catalyst characteristics on its performance at industrial conditions is still largely unexplored. A fundamental understanding of these aspects is highly relevant for the optimization of methanol synthesis catalysts, but also for the rational design of supported metal catalysts in general. To obtain more insight into these issues well-defined 3D model catalysts were synthesized, characterized with bulk and microscopy techniques, and their performance investigated at industrially relevant conditions.

In **chapter 2**, the formation of copper nanoparticles on a silica support during synthesis is examined by transmission electron microscopy. Specifically, time-lapsed TEM image series were acquired during the reduction in  $H_2$  atmosphere of a solid homogeneous precursor, namely copper phyllosilicate. Similar particle size distributions after reduction in the TEM and in a plug-flow reactor were obtained, validating that the phase transformation inside the microscope was representative for the phase transformation at larger scale. Based on an assessment of the electron beam illumination prior to and during reduction, a procedure was developed for time-resolved imaging of the dynamical changes of the copper phyllosilicate that are inherent to the reduction process. Hereby a generic approach for deriving insights into dynamical processes is

presented that should be applicable for a wide range of chemical reactions. After an induction time of a few minutes, particles with sizes larger than 3.4 nm were detected that grew in about 10 minutes to their final size of about 8 nm throughout the sample. Particle mobility was not observed indicating that growth of particles larger than 3.4 nm occurred via the diffusion of mobile copper species (likely  $\text{Cu}^{2+}$  ions) and their attachment to the copper particles. The size evolution of the individual particles was measured and was described by a two-step reduction mechanism with either diffusion-limited or reaction-limited particle growth. It is concluded that reduction of copper phyllosilicate in  $\text{H}_2$  to silica supported copper particles is likely autocatalytic and occurs via the diffusion of copper species over a limited distance of a few (tens) of nanometers to the copper particles.

The obtained kinetic and mechanistic information allows designing the (final) copper catalysts by controlling the process of nanoparticle formation. This can be achieved by either influencing the diffusion of copper species or by changing the kinetics of the reduction. The diffusion of copper is limited to a few (tens) of nanometers on a copper phyllosilicate sheet. Changing the size of the copper phyllosilicate sheets would thus result in a different particle size (distribution). Alternatively, the particle size distribution can be changed by influencing the mobility of the copper species. This might be achieved by changing the gas environment resulting in more mobile copper adsorbate species. Another way of controlling the properties of the catalyst is to change the kinetics of the reduction. Reduction by  $\text{H}_2$  involves the splitting of the molecule. Metallic copper can split  $\text{H}_2$  at increased temperatures, which might explain why the process is autocatalytic. The reduction rate during the nucleation phase when no copper particles are present yet, is orders of magnitude slower. Adding promoters to the precursor that are able to split  $\text{H}_2$  efficiently during the nucleation phase would speed up the reduction during nucleation and thereby alter the final catalyst. Another option to change the kinetics is by changing the reducing agent to for instance CO. As reduction by CO does not involve the splitting of the molecule, this process might be non-autocatalytic and therefore result in a different catalyst after reduction.

In **Chapter 3**, the sensitivity of the methanol synthesis reaction to the copper surface structure and the role of the zinc promoter are studied by investigating the effect of the copper particle size, the addition of zinc, and the thermodynamic stability of the zinc phase on catalyst activity. Catalysts containing zinc oxide were about ten times and catalysts containing zinc hydroxy(phyllo)silicate were about five times more active than catalysts without zinc. The differences in activity are ascribed to the promoting effect of zinc, which is affected by the thermodynamic stability of the zinc phase. The turnover frequency decreased significantly for copper particles smaller than 7 nm for all three types

of catalysts. This suggests that the methanol synthesis reaction either takes place at surface sites with a unique configuration of several copper atoms which smaller particles cannot accommodate, or that more unsaturated surface sites are poisoned by formate and that the reaction predominantly takes place at the more densely-packed copper surfaces which are not poisoned by formate.

Current methanol synthesis catalysts have an initial copper particle size of about 7 nm, close to the optimum particle size. Changing the shape or structure of the copper particles to increase the number of active sites might be possible, but as copper particle growth occurs under reaction conditions, the copper particles are likely to reconstruct to their equilibrium configuration. The zinc promoter, on the other hand, leaves more room for further optimization. Firstly, a Zn/(Cu+Zn) atomic ratio of 0.05 appeared to be sufficient for maximum site-specific activity, while in industry the ratio is typically about 0.3. With regard to activity the zinc content could thus be lowered substantially. However, zinc oxide also acts as a physical spacer for the copper particles and as a sulphur trap via the formation of ZnS from ZnO and thereby increases catalyst stability. For industrial purposes low zinc loadings might thus not be beneficial. For academic purposes catalysts with a low Zn/(Cu+Zn) atomic ratio and maximum activity might, however, be very interesting since a substantial percentage of the zinc is expected to be directly involved in the promotion of the copper particles. These catalysts thus allow investigating the zinc responsible for the promotion with a limited amount of non-promoting zinc oxide. Secondly, the promoting effect was larger for the catalysts containing ZnO, which is thermodynamically less stable than zinc hydroxy(phylo)silicate. Decreasing the thermodynamic stability of the zinc phase by using a different composition, adding promoters or nanosizing might thus increase the methanol synthesis activity further.

In **Chapter 4**, the effects of the chemical nature of the support surface, particle size distribution and interparticle spacing on copper particle growth in the methanol synthesis reaction are investigated independently from each other. Copper on silica and copper on aminopropyl-functionalized silica with copper loadings below 4 wt% were synthesized using impregnation of copper nitrate followed by drying, calcination, and reduction. Changing the interparticle distance for Cu/SiO<sub>2</sub> samples did not influence the deactivation rate while the addition of few large particles did, indicating that Ostwald ripening is the most probable dominant particle growth mechanism for these samples. The support functionalization with aminopropyl groups increased stability in the methanol synthesis reaction due to more limited copper particle growth. As shape and size of the copper particles was similar on silica as on aminopropyl-functionalized silica, the thermodynamic stability of the copper particles was unaltered. It is therefore suggested that Ostwald ripening was retarded by inhibiting the transport of copper species over the support

surface. Diffuse Reflectance Infrared Fourier Transform Spectroscopy (DRIFTS) revealed a decrease in the number of surface groups (hydroxyl, methoxy, and aminopropyl) upon functionalization because aminopropyltriethoxysilane reacted with multiple hydroxyl groups. Because of that, the distance between neighboring functional groups was increased, suppressing the transport of Ostwald ripening species from one copper particle to another.

The systematic approach used here for deriving mechanistic insights into metal particle growth at industrially relevant conditions is applicable for supported metal catalysts in general. The mechanistic information by which the copper particles in the investigated catalysts grow, enables to identify the importance of certain catalyst characteristics with respect to stability and provides new suggestions to improve catalyst stability further. Although for these methanol synthesis catalysts particle diffusion and coalescence has not been identified to play a significant role in the deactivation, this might be different for industrially applied catalysts which have a much higher copper loading. For Cu/SiO<sub>2</sub>, the interparticle distances did not influence the deactivation rate, indicating that the formation of Ostwald ripening species is rate-limiting for these catalysts. For copper on aminopropyl-functionalized silica the diffusion is proposed to be rate-limiting. This suggests that for these catalysts deactivation depends on the interparticle distances. Moreover, the results suggest that the diffusion coefficient of Ostwald ripening species over the support surface depends on the density, configurational freedom and interaction with Ostwald ripening species of the functional groups. Decreasing the density of functional groups, restricting the configurational freedom of functional groups, and increasing the interaction with Ostwald ripening species might thus lower the diffusion rate and hence retard catalyst deactivation.

In **chapter 5**, the impact of the synthesis route on the support structure, the location of the copper particles therein, and the performance in the methanol synthesis reaction are investigated. Cu/SiO<sub>2</sub> catalysts with similar copper particle size and local copper loading were synthesized via either precipitation or incipient wetness impregnation. Electron tomography revealed for the precipitated catalyst a plate-like silica structure with copper particles partially entrapped, whereas for the impregnated catalyst the copper particles were located in the pores between the primary particles of the silica gel. The precipitated catalyst displayed a lower initial copper weight normalized activity and a higher stability in the methanol synthesis reaction. Copper particle growth during reaction was more limited for the precipitated catalyst, possibly due to the partial entrapment of the copper particles. In addition to copper particle growth, deactivation of both catalysts was ascribed to restructuring of the silica resulting in partial coverage of the copper surface.

As indicated by this study, partial entrapment of the copper particles provides a tool to find the optimal balance between catalyst activity and stability. The increased nanoparticle stability in the precipitated sample is ascribed to a stronger metal-support interaction. Due to the entrapment the metal-support interface area is larger for the copper particles prepared via precipitation, but also the metal-support interfacial energy might be larger due to the different preparation route for both catalysts. To investigate the latter effect, similar catalyst structures should be made via both routes. One option to achieve this might be to leach the copper from the precipitated and reduced sample, deposit copper via incipient wetness impregnation on the thus obtained silica support, and compare its performance with the original precipitated sample. Next to instability of the copper phase resulting in particle growth, also restructuring of the silica supports had occurred during reaction and contributed to catalyst deactivation. Similarly, in the industrially applied catalyst, zinc oxide might restructure and form larger crystallites. This process can be retarded by stabilizing the support (surface) using additives.

In conclusion, the work described in this thesis presents new fundamental insights into the physicochemical processes involved in the synthesis and performance of copper-based methanol synthesis catalysts and the structural parameters influencing these processes. These insights provide new strategies for the rational design of copper-based methanol synthesis catalysts in particular and supported metal catalysts in general.

## Chapter 6b

### Nederlandse Samenvatting

Methanol wordt op industriële schaal geproduceerd vanuit een gasmengsel van waterstof, koolstofmonoxide en koolstofdioxide, dat ook wel synthegas of kortweg 'syngas' wordt genoemd. Methanol is één van de essentiële bouwstenen in de petrochemische industrie aangezien het in bijna alles omgezet kan worden. Daarnaast kan methanol eventueel gebruikt worden als brandstof of energiedrager voor een duurzamer energievoorziening. Syngas wordt momenteel voornamelijk geproduceerd uit olie, kolen en aardgas, maar kan ook geproduceerd worden uit biomassa, afval of in de toekomst mogelijk via kunstmatige fotosynthese uit CO<sub>2</sub> en H<sub>2</sub>O. De omzetting van syngas naar methanol is daarom een alternatieve en mogelijk duurzamere route om producten, brandstoffen en energiedragers die traditioneel uit olie worden gemaakt, te verkrijgen. De aantrekkelijkheid van deze route voor de ( nabije) toekomst is terug te zien in de verwachte toename in de methanolproductie van 65 miljoen ton in 2013 naar 105 miljoen ton in 2023.

De katalysator die in de industrie gebruikt wordt voor dit proces is een mengsel van koper, zinkoxide en alumina, waarbij de aanvankelijke grootte van de koperdeeltjes circa 7 nm is; deze katalysator wordt veelal verkregen via een gelijktijdige neerslagreactie. Zoals beschreven in **hoofdstuk 1** zijn katalysatoren gebaseerd op koper voor de methanolsynthese intensief bestudeerd in de afgelopen decennia, echter er resteren een aantal prangende wetenschappelijke en technologische uitdagingen. Allereerst, het fundamentele begrip van, en de controle over de processen die plaatsvinden tijdens de synthese van kopergedragen katalysatoren is beperkt. Ten tweede, de gevoeligheid van de reactie ten aanzien van de structuur van het koperoppervlak en de rol van zink als promotor zijn onderwerpen van discussie en het is onduidelijk welke structurele parameters essentieel zijn voor maximale activiteit. Ten derde, de groei van koperdeeltjes resulteert over tijd in een substantieel verlies van activiteit en verkort daarmee de levensduur van de katalysator. De invloed van verschillende katalysatorkarakteristieken op de werking onder industriële condities is grotendeels nog onbekend. Een fundamenteel begrip van deze aspecten is zeer relevant voor de optimalisatie van katalysatoren voor de methanolsynthese, maar ook voor de weldoordachte ontwikkeling van gedragen metaalkatalysatoren in het algemeen. Om meer inzicht te verkrijgen in deze zaken, werden goed gedefinieerde 3D model katalysatoren gesynthetiseerd, gekarakteriseerd met bulk- en microscopietechnieken, en werd hun werking onder industrieel relevante omstandigheden onderzocht.

In **hoofdstuk 2** is de vorming van koperdeeltjes op een silicadrager bestudeerd door middel van transmissie electronen microscopie (TEM). Specifiek zijn met TEM beeldintervalopnamen genomen tijdens de reductie onder een H<sub>2</sub>-atmosfeer van een vaste stof, namelijk koperphyllosilicaat. Er was geen verschil tussen de

deeltjesgrootteverdelingen na reductie in de TEM en in een propstroomreactor, wat aantoonde dat de omzetting in de microscoop representatief was voor de omzetting op grotere schaal. Gebaseerd op een analyse van de effecten van de blootstelling aan de electronenbundel voorafgaand en tijdens de reductie is een procedure ontwikkeld voor het met tijdsintervallen opnemen van TEM-beelden van de dynamische veranderingen van het koperphyllosilicaat die inherent zijn aan het reductieproces. Dit biedt een generieke aanpak voor het verkrijgen van inzichten in dynamische processen die toepasbaar is voor een grote variatie aan chemische reacties. Na een inductieperiode van een paar minuten werden door het hele monster heen deeltjes groter dan 3.4 nm gedetecteerd die in ongeveer 10 minuten groter groeiden tot uiteindelijk 8 nm. Mobiliteit van de deeltjes werd niet waargenomen, wat aangeeft dat de groei van deeltjes groter dan 3.4 nm plaatsvindt via diffusie van een mobiele kopersoort (waarschijnlijk  $\text{Cu}^{2+}$ -ionen) gevolgd door aangroei aan de koperdeeltjes. De ontwikkeling van de grootte van de koperdeeltjes werd opgemeten en beschreven door een tweestaps reductiemechanisme met ofwel diffusie-gelimiteerde, ofwel reactie-gelimiteerde deeltjesgroei. De conclusie is dat de reductie van koperphyllosilicaat door  $\text{H}_2$  tot silicagedragen koperdeeltjes waarschijnlijk autokatalytisch is en plaatsvindt via de diffusie van een mobiele koperverbinding over een beperkte afstand van enkele (tientallen) nanometers naar de koperdeeltjes toe.

De verkregen mechanistische en kinetische informatie maakt het mogelijk om de koperkatalysator te variëren door het vormingsproces van de nanodeeltjes te beheersen. Dit kan bereikt worden door ofwel de diffusie van de mobiele koperverbinding te beïnvloeden, ofwel door de kinetiek van de reductie te veranderen. De diffusie van koper is gelimiteerd tot enkele (tientallen) nanometers op een koperphyllosilicaatplaat. Het veranderen van de afmetingen van de koperphyllosilicaatplaten zal dus resulteren in een andere deeltjesgrootte. Als alternatief kan de deeltjesgrootteverdeling veranderd worden door de mobiliteit van de koperbindingen te beïnvloeden. Dit kan gedaan worden door de gasatmosfeer te veranderen wat zou kunnen leiden tot mobielere (gasgeadsorbeerde) koperbindingen. Een andere manier om de eigenschappen van de katalysator te beheersen is door de reductiekinetiek te veranderen. Reductie door  $\text{H}_2$  omvat de splitsing van een molecuul. Metallisch koper kan  $\text{H}_2$  splitsen bij verhoogde temperaturen wat kan verklaren waarom het onderzochte proces autokatalytisch is. De reductiesnelheid tijdens de nucleatiefase, wanneer er nog geen metallische koperdeeltjes aanwezig zijn, is ordes van grootte langzamer. Het toevoegen van promotoren aan de precursor die in staat zijn om effectief  $\text{H}_2$  te splitsen tijdens de nucleatiefase zou de reductie in die fase versnellen en daarmee de uiteindelijke katalysator veranderen. Een andere mogelijkheid om de kinetiek te veranderen is door een ander reductiemiddel te gebruiken, bijvoorbeeld

koolstofmonoxide. Aangezien de reductie door CO geen splitsing van een molecuul behelst, is dit proces wellicht niet autokatalytisch en kan daardoor tot een andere katalysator na reductie leiden.

In **hoofdstuk 3** zijn de gevoeligheid van de methanolsynthesereactie voor de structuur van het koperoppervlak en de rol van de zinkpromotor bestudeerd door het effect van de grootte van de koperdeeltjes, de toevoeging van zink, en de thermodynamische stabiliteit van de zinkfase op de activiteit van de katalysator te onderzoeken. Katalysatoren die zinkoxide bevatten waren tien keer actiever en katalysatoren die zinkhydroxy(phylo)silicaat bevatten waren vijf keer actiever dan katalysatoren zonder zink. De verschillen in activiteit zijn toe te schrijven aan het prestatieverhogende effect van zink, dat beïnvloed wordt door de thermodynamische stabiliteit van de zinkfase. De omzetsnelheid per koperatoom op het oppervlak daalde significant voor koperdeeltjes kleiner dan 7 nm voor alle drie type katalysatoren. Dit suggereert dat de methanolsynthesereactie ofwel plaatsvindt op oppervlakteplaatsen die een unieke configuratie van meerder koperatomen vereisen die op kleinere deeltjes niet voorkomt, ofwel dat meer onverzadigde adsorptieplekken vergiftigd zijn met formaat en dat de reactie voornamelijk plaatsvindt op de meer dichtgepakte koperoppervlakken die niet vergiftigd zijn met formaat.

De huidige methanolsynthesekatalysatoren hebben een aanvankelijke koperdeeltjesgrootte van ongeveer 7 nm, dichtbij de optimale deeltjesgrootte. De structuur of vorm van de koperdeeltjes veranderen zodat het aantal actieve locaties toeneemt is wellicht mogelijk, maar aangezien koperdeeltjesgroei plaatsvindt onder reactiecondities is het waarschijnlijk dat de koperdeeltjes zich herrangschikken tot hun evenwichtsconfiguratie. Anderzijds biedt de zinkpromotor meer ruimte voor verdere optimalisering. Allereerst, een  $Zn/(Cu+Zn)$  atomaire verhouding van 0.05 bleek genoeg te zijn voor maximale oppervlakteplaats-specifieke activiteit, terwijl in de industrie een ratio van ongeveer 0.3 wordt gebruikt. Wat betreft de activiteit zou de zinkbelading dus substantieel verlaagd kunnen worden. Echter, zinkoxide houdt ook de koperdeeltjes op afstand van elkaar en vangt zwavel af via de formatie van ZnS uit ZnO en verhoogt daarmee de stabiliteit van de katalysator. Voor industriële toepassingen zijn lage zinkbeladingen dus wellicht niet aantrekkelijk. Vanuit academisch oogpunt zijn lage zinkbeladingen met een maximale activiteit echter erg interessant aangezien een substantieel percentage van de zink direct betrokken is bij de promotie van de koperdeeltjes. Deze katalysatoren zijn dus uitermate geschikt om de zinkverbinding die verantwoordelijk is voor de promotie te onderzoeken omdat de hoeveelheid zink die niet promoterend werkt, laag is. Ten tweede, het promoterende effect was groter voor katalysatoren die zinkoxide bevatten, hetgeen thermodynamisch instabieler is dan

zinkhydroxy(phylo)silicaat. Het verlagen van de thermodynamische stabiliteit van de zinkfase door het gebruik van een andere samenstelling, toevoegen van andere promotoren of een kleinere deeltjesgrootte van de zinkfase, verhogen mogelijk de activiteit in de methanolsynthese verder.

In **hoofdstuk 4** zijn de effecten van de chemische eigenschappen van het drageroppervlak, de koperdeeltjesgrootteverdeling, en de afstanden tussen de deeltjes op de deeltjesgroei van koper in de methanolsynthesereactie, onafhankelijk van elkaar onderzocht. Koper op silica en koper op aminopropyl-gefunctionaliseerde silica met koperbeladingen onder de 4 wt% zijn gesynthetiseerd door middel van impregnatie met kopernitrat gevolgd door een droogstap, calcinatie en reductie. Een verandering in de afstanden tussen de deeltjes voor Cu/SiO<sub>2</sub> katalysatoren beïnvloedde de deactivatiesnelheid niet maar de toevoeging van een paar grote koperdeeltjes wel, hetgeen een aanwijzing is dat Ostwald rijping het waarschijnlijk meest dominante deeltjesgroeiemechanisme is voor deze materialen. De functionalisatie van het drageroppervlak met aminopropylgroepen verhoogde de stabiliteit in de methanolsynthese vanwege een afname van de deeltjesgroei. Aangezien de vorm en grootte van de koperdeeltjes vergelijkbaar was op silica en aminopropylgefunctionaliseerde silica is de thermodynamische stabiliteit van de koperdeeltjes onveranderd gebleven. Het is daarom gesuggereerd dat Ostwald rijping werd vertraagd door belemmering van het transport van koperverbindingen over het drageroppervlak. Infraroodspectroscopie liet een afname in het aantal oppervlaktegroepen (hydroxyl-, methoxy-, en aminopropylgroepen) na functionalisatie zien omdat aminopropyltriethoxysilica met meerdere hydroxylgroepen had gereageerd. Hierdoor nam de afstand toe tussen naburige functionele groepen hetgeen de verplaatsing van Ostwald-rijpingverbindingen van het ene naar het andere koperdeeltje vertraagde.

De systematische aanpak die gebruikt werd voor het afleiden van mechanistische inzichten in metaaldeeltjesgroei onder industrieel relevante condities is toepasbaar voor gedragen metaalkatalysatoren in het algemeen. De mechanistische informatie over hoe de koperdeeltjes in deze katalysatoren groeien, maakt het mogelijk om het belang van bepaalde katalysator karakteristieken voor de stabiliteit te bepalen en levert nieuwe suggesties op voor het verder verbeteren van de katalysatorstabiliteit. Alhoewel voor de onderzochte katalysatoren diffusie en coalescentie van koperdeeltjes niet aantoonbaar bijdroeg aan de deactivatie, ligt dit wellicht anders voor de industrieel toegepaste katalysatoren die een veel hogere kopergehalte hebben. Voor Cu/SiO<sub>2</sub> katalysatoren beïnvloedde de afstanden tussen de deeltjes de deactivatiesnelheid niet, wat aangeeft dat de vorming van Ostwald-rijpingverbindingen snelheidslimiterend is voor deze katalysatoren. Voor koper op aminopropylgefunctionaliseerde silica is voorgesteld dat de

diffusie snelheidslimiterend is. Dit suggereert dat voor deze katalysatoren de deactivatie wel afhangt van de afstanden tussen de deeltjes. Daarnaast is geopperd dat de diffusiecoëfficiënt van de Ostwald-rijpingverbindingen over het drageroppervlak afhangt van de dichtheid, configuratieve vrijheid en interactie tussen de Ostwald-rijpingverbindingen en de functionele groepen. Het verlagen van de dichtheid van functionele groepen, het beperken van de configuratieve vrijheid van de functionele groepen en het verhogen van de interactie met de Ostwald-rijpingverbindingen zou dus kunnen leiden tot een lagere diffusiesnelheid en daarmee tot een vertraagde deactivatie van de katalysator.

In **hoofdstuk 5** wordt de impact van de synthesroute op de structuur van de drager, de locatie van de koperdeeltjes daarin, en de werking van de katalysator in de methanolsynthese onderzocht. Cu/SiO<sub>2</sub>-katalysatoren met vergelijkbare koperdeeltjesgrootte en lokale koperbelading zijn bereid via ofwel een neerslagreactie ofwel impregnatie. Electronentomografie liet voor de neergeslagen katalysator een plaatstructuur zien waarin de koperdeeltjes gedeeltelijk ingebed zaten, terwijl voor de geïmpregneerde katalysator de koperdeeltjes gelocaliseerd waren in de poriën tussen de primaire deeltjes van de silicagel. De neergeslagen katalysator liet een lagere initiële activiteit genormaliseerd per gram koper en een hogere stabiliteit zien in de methanolsynthese. Koperdeeltjesgroei tijdens de reactie had minder plaatsgevonden in de neergeslagen katalysator, mogelijk vanwege de gedeeltelijke opsluiting van de koperdeeltjes. Naast deeltjesgroei is deactivatie voor beide katalysatoren toegeschreven aan de herstructurering van de silicadrager wat resulteerde in een gedeeltelijke bedekking van het koperoppervlak.

Dit onderzoek laat zien dat gedeeltelijke opsluiting van koperdeeltjes gebruikt kan worden om een optimale balans te vinden tussen activiteit en stabiliteit van de katalysator. De verhoogde stabiliteit van de nanodeeltjes is toe te schrijven aan een sterkere interactie tussen het metaal en de drager. Vanwege de gedeeltelijke opsluiting is het grensvlak tussen metaal en drager groter voor de neergeslagen katalysator, maar ook de interactie-energie tussen de twee kan verschillend zijn voor de verschillende preparatiemethodes. Om dit laatste effect te onderzoeken moeten vergelijkbare katalysatorstructuren gemaakt worden via beide preparatiemethodes. Een mogelijkheid om dit te bereiken is door het koper uit het neergeslagen materiaal te wassen, koper er weer op aan te brengen door middel van impregnatie, en vervolgens de werking van de katalysator te vergelijken met de originele neergeslagen katalysator. Behalve de instabiliteit van het koper wat resulteerde in deeltjesgroei, waren ook de silicadragers veranderlijk tijdens reactie wat bijdroeg aan de deactivatie van de katalysator. Op een vergelijkbare manier kan zinkoxide in de industrieel toegepaste katalysator zich ook

herrangschikken. Dit proces kan vertraagd worden door (het oppervlak van) de drager te stabiliseren door andere elementen toe te voegen.

Het werk beschreven in deze thesis presenteert nieuwe fundamentele inzichten in de fysisch-chemische processen die betrokken zijn bij de synthese en werking van katalysatoren gebaseerd op koper voor de methanolsynthese, en de structurele parameters die deze processen beïnvloeden. Deze inzichten leveren nieuwe strategieën op voor de rationele ontwikkeling van op kopergebaseerde methanolsynthesekatalysatoren in het bijzonder, en van gedragen metaalkatalysatoren in het algemeen.

### List of Publications

#### Scientific publications

R. van den Berg, G. Prieto, G. Korpershoek, L. I. van der Wal, A. J. van Bunningen, S. Lægsgaard-Jørgensen, J. Sehested, S. Helveg, P.E. de Jongh, K.P. de Jong, Structure Sensitivity of Cu and CuZn Catalysts Relevant to Industrial Methanol Synthesis, 2016, submitted to Nature Communications

G. Wang, R. van den Berg, C. De Mello Donega, K.P. de Jong, P.E. de Jongh, Silica-Supported Cu<sub>2</sub>O Nanoparticles with Tunable Size for Sustainable Hydrogen Generation, Applied Catalysis B: Environmental, 2016, 192, 199-207

R. van den Berg, C.F. Elkjær, C.J. Commes, I. Chorkendorff, J. Sehested, P.E. de Jongh, K.P. de Jong, S. Helveg, Revealing the formation of copper nanoparticles from a homogeneous solid precursor by electron microscopy, Journal of the American Chemical Society, 2016, 138, 3433-3442

R. van den Berg, J. Zečević, J. Sehested, S. Helveg, P.E. de Jongh, K.P. de Jong, Impact of the Synthesis Route of Supported Copper Catalysts on the Performance in the Methanol Synthesis Reaction, Catalysis Today, 2015, DOI: 10.1016/j.cattod.2015.08.052

R. van den Berg, T.E. Parmentier, C.F. Elkjær, C.J. Commes, J. Sehested, S. Helveg, P.E. de Jongh, K.P. de Jong, Support functionalization to retard Ostwald Ripening in Copper Methanol Synthesis Catalysts, ACS Catalysis, 2015, 5, 4439-4448

R.W. Gosselink, R. van den Berg, W. Xia, M. Muhler, K.P. de Jong, J.H. Bitter, Gas Phase Oxidation as a Tool to Introduce Support Oxygen Groups on Metal Loaded Carbon Based Materials, Carbon, 2012, 50, 4424-4431

P. Ngene, R. van den Berg, M.H.W. Verkuijlen, K.P. de Jong, P.E. de Jongh, Reversibility of the Hydrogen Desorption from NaBH<sub>4</sub> by Confinement in Nanoporous Carbon, Energy Environmental Science, 2011, 4, 4108-4115

### Oral Presentations

R. van den Berg, C.F. Elkjær, C.J. Commes, J.Sehested, S.Helveg, P.E. de Jongh, J. Zečević, K.P. de Jong, Revealing the mechanism of formation of copper particles and the effect of their location on catalyst stability, CHAINS 2015, November 30 - December 2 2015, Veldhoven, The Netherlands

R. van den Berg, T.E. Parmentier, C.F. Elkjær, C.J. Commes, J.Sehested, S.Helveg, P.E. de Jongh, K.P. de Jong, Support functionalization to retard copper particle growth in the methanol synthesis reaction, EuropaCat-XII, August 30 - September 4 2015, Kazan, Russia

R. van den Berg, T.E. Parmentier, C.F. Elkjær, C.J. Commes, J.Sehested, S.Helveg, P.E. de Jongh, K.P. de Jong, Support functionalization to retard copper particle growth in the methanol synthesis reaction, 24<sup>th</sup> North American Catalysis Society Meeting, June 14-19 2015, Pittsburgh, United States of America

R. van den Berg, T.E. Parmentier, C.F. Elkjær, C.J. Commes, J.Sehested, S.Helveg, P.E. de Jongh, K.P. de Jong, Support functionalization to retard copper particle growth in the methanol synthesis reaction, Netherlands Catalysis and Chemistry Conference XV, March 2-4 2015, Noordwijkerhout, The Netherlands

R. van den Berg, C.F. Elkjær, P.E. de Jongh, K.P. de Jong, J.Sehested, S.Helveg, *In-situ* TEM and electron tomography: revealing the mechanism of formation and location of copper particles, NVvM Materials Science Meeting, December 2 2014, Utrecht, The Netherlands

R. van den Berg, C.F. Elkjær, P.E. de Jongh, K.P. de Jong, J.Sehested, S.Helveg, The formation of copper nanoparticles during reduction of a copper silicate imaged in real time with *in-situ* TEM, Advanced Electron Microscopy for Catalysis III, September 3-6 2014, Seeon Monastery, Germany

R. van den Berg, C.F. Elkjær, P.E. de Jongh, K.P. de Jong, J.Sehested, S.Helveg, The formation of copper nanoparticles during reduction of a copper silicate imaged in real time with *in-situ* TEM, Scientific Bases for the Preparation of Heterogeneous Catalysts 11, July 6-10 2014, Louvain-la neuve, Belgium

### Poster presentations

R. van den Berg, C.F. Elkjær, C.J. Gommès, J. Sehested, P.E. de Jongh, K.P. de Jong, S.Helveg, The formation, location and stability of copper nanoparticles formed during the reduction of a copper silicate, EuropaCat-XII, August 30 - September 4 2015, Kazan, Russia

R. van den Berg, C.F. Elkjær, C.J. Gommès, J. Sehested, P.E. de Jongh, K.P. de Jong, S.Helveg, The formation, location and stability of copper nanoparticles formed during the reduction of a copper silicate, 24<sup>th</sup> North American Catalysis Society Meeting, June 14-19 2015, Pittsburgh, United States of America

R. van den Berg, C.F. Elkjær, P.E. de Jongh, K.P. de Jong, J.Sehested, S.Helveg, Partial entrapment of copper particles in a silica support to restrict particle growth in the methanol synthesis reaction, Netherlands Catalysis and Chemistry Conference XIV, March 10-12 2014, Noordwijkerhout, The Netherlands

R. van den Berg, C.F. Elkjær, P.E. de Jongh, K.P. de Jong, J.Sehested, S.Helveg, The formation of copper particles during reduction of a precipitated copper silicate visualized with in-situ TEM, Operando Research in Catalysis, June 24-28 2013, Leiden, The Netherlands

R. van den Berg, G. Korpershoek, S. Helveg, J.Sehested, P.E. de Jongh, K.P. de Jong, Particle size effect of copper in the methanol synthesis reaction, Netherlands Catalysis and Chemistry Conference XIII, March 11-13 2013, Noordwijkerhout, The Netherlands

R. van den Berg, R.W. Gosselink, W. Xia, M. Muhler, K.P. de Jong, J.H. Bitter, Selective decarboxylation of stearic acid: The influence of support oxygen groups, Netherlands Catalysis and Chemistry Conference XI, February 28 – March 2 2011, Noordwijkerhout, The Netherlands

### Acknowledgments

Many people have contributed to work described in this thesis, and made the time during my PhD very enjoyable. First of all, I like to thank my supervisors Krijn, Petra, Jens and Stig, and Haldor Topsøe A/S for financially supporting this project. Thank you for the opportunity to perform this research with you, the guidance throughout the project, and the freedom to pursue scientific questions that came up during the research in the field of nanomaterial synthesis, electron microscopy, catalysis or modelling. I would also like to thank you for the opportunity to collaborate with a lot of different people, such as technicians, students and colleagues at Utrecht University, Haldor Topsøe A/S, University of Liège and Technical University of Denmark. Furthermore, I would like to thank you for encouraging and supporting me to develop personally by the opportunity to attend schools, courses or symposia, present at (inter)national conferences, organize social events and company trips with the NIOK PhD Platform, and promote science as a 'Face of Science'.

Krijn, thank you for the general guidance of the project and the interesting (scientific) discussions. You were always able to surprise me with scientific questions I had not thought about and this resulted in the search to obtain an even more fundamental understanding of the investigated processes. Furthermore, I admire your philosophy that the most important 'output' as a professor is the people you have educated and I am grateful for the care you have taken not just for the project but also for me personally. It was a pleasure to work with you and I will especially cherish the memories from the trips to Denmark and Prepa11.

Petra, thank you for all the support you have given me, especially in the projects with the bachelor students. Your knowledge about inorganic nanomaterials and your critical eye with regard to science and language, has improved the quality of the research and this thesis a lot. Furthermore, thank you for nominating me as a 'Face of Science' and encouraging me to attend conferences and to visit companies. I am very grateful for the way how you promote your people at conferences and other events, and your enthusiasm is contagious.

Jens, thank you for the very pleasant collaboration. It was a pleasure to work together with someone who has so much experience with copper-based methanol synthesis catalysts. A specific 'thank you' for your inspiration and input for the study on particle size effects. Stig, thank you for your input and ideas on the electron microscopy experiments and for your critical eye on the results and papers in general. Your approval has become a

## Acknowledgments

---

certificate of quality to me and when assessing something I will try to apply the same standards.

Apart from my official supervisors, I have also had a few unofficial mentors. Gonzalo, I would like to thank you for introducing me to the synthesis and testing of copper-based methanol synthesis catalysts. Furthermore I would like to thank you for your contribution to chapter 3. Jovana, I would like to thank you for teaching me electron tomography, for your personal advice in general, and for your contributions to Chapter 5. Cedric, I would like to thank you for your contributions to Chapters 2 and 4 in particular with regard to the modelling. Furthermore, you inspired me to think out-of-the-box and question things that seem normal but might in fact be very special.

Christian, it was a great pleasure to work with you regarding the *in-situ* TEM experiments and subsequent writing. I think we can be proud of the results described in Chapter 2. Sebastian, thank you for the H<sub>2</sub>-TPR/TPD and N<sub>2</sub>O chemisorption measurements and subsequent analysis and discussion of the results. Hideto, thank you for your experiments involving electron microscopy. Gang, thank you for the collaboration involving the usage of supported copper materials for photocatalysis. Lisette, thank you for the collaboration regarding methanol synthesis catalysts and I hope you can use some of the implications from this work and bring it a step further.

Several BSc and MSc students have done their research project with me and I would like to acknowledge all of them for their contribution to this thesis. Tanja, thank you for the collaboration and chapter 4 is based on the work you carried out. Gerda, Lars, Naud, Luc, Elian, Jochem and Ceri, thank you for your contributions to chapter 3. Christa, I would like to thank you for the project with you. It did, unfortunately, not make it into this thesis, but it had a valuable contribution to the overall project. Rene, thank you for the literature thesis. Parts of your work found their way into chapters 1, 4 and 5.

I would like to thank staff members for helping me throughout my PhD. Hans and Chris, thank you for helping me with electron microscopy. The large number of electron microscopy images in this thesis highlights the importance of your support. Rien and Jan-Willem, thank you for the technical assistance with the catalytic testing set-up. Marjan, Fouad, Ad M, Ad E, Oscar, Herrick and Pascal thank you for your technical assistance. Iris, Dymph and Monique thank you for helping me out with non-scientific issues.

I would like to thank Bert, Pieter and Frank for the (scientific) discussions. Furthermore, I would like to thank Harry, Peter N, Rob, Arjen and Jaap for supervision and education during my bachelor and master thesis. Moreover, I would like to thank Peter M, Thomas, Arjan, Jesper, JX, Jeroen, Nazila, Carlo, Peter B, Rafael, Fernando, Martin and the rest of the inorganic chemistry and catalysis group for their scientific discussions and the input to my research.

Apart from the science I would also like to thank the people that made my PhD study very enjoyable. First of all, I would like to thank my office mates. Thank you Yuen, Jesper, Sophie, Peter M, Hendrik, Clare, Gonzalo, Jovana, Mozaffar, Cedric, Christoph, Fiona, Gareth, Jan, Mathijs W, Bo Feng, Leila, Mahnaz, Abhishek and Joel. Secondly, I would like to thank the people for the great time I had, whether it was skiing in Winterberg, partying at the Oktoberfest in München or the Gentse feesten, visiting Iceland, Luxemburg, Istanbul, Italy or companies abroad, or travelling to or after conferences in Belgium, Germany, Unites States and Russia. Thank you Nynke, Jochem, Gang, Peter B, Jesper, Zafer, Dilek, Ramon, Zoran, Marina, Elena, Ilona, Peter M, Javier, Sandra, Dimitrije, Rosa, Joe, Egor, Homer, Marjolein, Sandra C, Fang, Antonio, Robin, Pasi, Ara, David, Guusje, Fouad, Hendrik, Inge, Wenhao, JX, Jinbao, Daniel, Rafael, Thomas E, Maren, Nazila, Jovana, Jeroen, Sam, Korneel, Boyang, Camillo, Anton, Julia, Elena V, Rik, Lennart, Wei and Simone. Thirdly, I would like to thank the soccer team for the great matches we have played. Thank you Zoran, Joe, Martin, Peter S, David F, Rene, Ali, Gareth, Moji, Sam, Jens, Carlo, Wouter N, Michele, Antonio, Tom D, Tomas H, Tomas P, Thomas E, Philip, Gonzalo, Rob, Javier, Jamal, Khaled, Jesper, Hendrik, Fouad, Ying and Wenhao. I would like to thank my mountainbike buddies Jesper, Thomas E, Gang and Ramon and my squash buddies Martin and Frederik for the great sport time. I would like to thank everyone for the discussions, 'borrels', birthday parties, paintball, pool games and other social events. Thank you Nynke, Monica, Florian, Sandra P, Laura, Hirsu, Rolf, Matti, Lucian, Manuel, Baira, Jessi, Freddy, Jelle, Sang-ho, Mario, Tao, Diego, Pierre, Yann, Burcu, Thomas H, Özgün, Rogier, Joris, Tom v D, Hebatalla, Donglong, Ivan, Frank H, Ana, Carlos, Katinka, Wouter L, Mark, Marte, Jose, Anne-Eva, Silvia, Petra, Ilse, Nastya, Miguel, Mustafa, Suzanne, Charlotte, Lennart, Evelien, Stefan, Qingyun, Annelie, Upakul, Luis, Piter, Tamara, Davide, Marianna, Selvedin, Anne Mette, Inés (uno and dos), Jan Philipp, Marleen, Reshmi, Sankar, Angeloclaudio, Michal, Suwarno, Mathijs Z, and everyone who I may have unintentionally missed. I would also like to thank Dulce, Nastya, Monalisa and Irene for the nice collaboration with regard to the NIOK PhD Platform.

## Acknowledgments

---

Next to my colleagues, I would also like to thank my friends for showing interest in what I was researching during my PhD. Thank you, Alwin, Michael, Sarah, sailing and wintersport crews, outdoor soccer team and all the others. Nynke, thank you for the support, motivation and nice time you gave me during the final phase of my PhD. I am sure you will be very successful in your research and that great times lie ahead of us. I would also like to thank my family for supporting me through good and bad times. I think dad would be proud and I hope there will be soon two doctors in the family. Special thanks to you, Mama, Joyce and Marco.

## About the Author

Roy van den Berg was born on March 16<sup>th</sup>, 1988 in Nijkerk, The Netherlands. After graduating from the Oldenbarnevelt Gymnasium in Amersfoort, he earned a bachelor degree in Chemistry and a master degree in Nanomaterials: Chemistry and Physics from Utrecht University. He was also a private teacher for secondary school students in the field of natural sciences. He carried out research projects in the fields of



solar energy, hydrogen storage and biomass conversion during his studies. These projects brought his interest to the field of catalysis as essential for the sustainable and efficient conversion of natural resources to energy and materials. He performed his internship in 2011 at Albemarle catalysts in Amsterdam and studied the accessibility of different materials to heavy oil fractions.

After completing his masters in 2011, Roy started his PhD project at the Inorganic Chemistry and Catalysis group at Utrecht University under the supervision of Prof. dr. ir. Krijn de Jong and Prof. dr. Petra de Jongh with financial support from Haldor Topsøe A/S. During four years, he investigated the processes involved in the synthesis of supported copper catalysts, the structural parameters required for maximum methanol synthesis activity, and the influence of different catalyst characteristics on copper particle growth. He conducted this research in collaboration with 10 BSc and MSc students, and colleagues from Utrecht University, Haldor Topsøe A/S, University of Liège and Technical University of Denmark. The main results of his PhD project are described in this thesis, published in internationally renowned journals and presented at (inter)national conferences.

In 2013 and 2014, Roy was secretary at the Dutch Institute in Research and Catalysis PhD Platform and as such was responsible for the general organization of company tours, individual company visits, sports tournaments and social events. In 2014 Roy was selected as a 'Face of Science' by the Royal Netherlands Academy of Arts and Sciences.

